Christian Gösweiner, Dipl.-Ing.

The role of nuclear quadrupole spin resonance in the design of a new class of MRI-contrast agents

DOCTORAL THESIS

to achieve the university degree of

Doctor of Philosophy

submitted to

Graz University of Technology

Supervisor

Ao. Univ.-Prof. Dr. techn. Hermann Scharfetter

Institute of Medical Engineering

Graz, May 2020

AFFIDAVIT

I declare that I have authored this thesis independently, that I have not used other than the declared sources/resources, and that I have explicitly indicated all material which has been quoted either literally or by content from the sources used. The text document uploaded to TUGRAZonline is identical to the present doctoral thesis.

Date	Signature

"Es würde uns gut tun, uns manchmal daran zu erinnern, dass wir zwar in dem Wenigen, das wir wissen, sehr verschieden sein mögen, dass wir aber in unserer grenzenlosen Unwissenheit alle gleich sind."

Karl Popper

Abstract

The role of nuclear quadrupole spin resonance in the design of a new class of MRI-contrast agents

The administration of contrast agents (CAs) in magnetic resonance imaging (MRI) is an indispensable technique to improve image quality and contrast and is thus supporting medical diagnostics for many diseases and pathologies. In September 2015, a research project has been started suggesting a novel contrast agent type, relying upon quadrupole relaxation enhancement (QRE) instead of the currently exploited paramagnetic relaxation enhancement (PRE) effect. The former effect is based on a magnetic dipole-dipole interaction between nuclear spins, the latter between proton and electron spins.

Both techniques aim at enhancing the spin-lattice relaxation rate of proton spins in water molecules sensed by MRI. The enhanced relaxation then leads to an increased contrast in the MRI scan. As the QRE effect is intrinsically selective on the strength of the applied magnetic field in a quantized manner, it is expected that QRE-based CAs have the potential to add several useful methodical features to CA-supported MRI. Also, the QRE effect depends on the electronic structure of the QRE-active molecule, which allows for electronic sensitivity. From these properties, two mechanisms are conceivable: First, on-off switching the contrast effect by an external stimulus i.e. shifting the scanner field. Second, molecular imaging due to modulation of the QRE effect upon electronic alterations. Another argument for alternative CAs is that PRE agents mostly contain Gadolinium (Gd) (encapsulated in stable chelates) and can thus not be administrated to patients with kidney diseases. Lately, it has also been reported that Gd-CAs from particular chelates can be found to remain in the brains of healthy patients.

Central research interest of this work is to support proof-of-concept research for QRE-based contrast agents. In particular, focus is set on the role of nuclear quadrupole resonance within the total magnetization transfer effect from the polarized protons via a close by quadrupole nuclei to the lattice. Mostly by the use of nuclear quadrupole resonance (NQR) spectroscopy, promising compounds containing Bismuth (Bi) are preselected, fulfilling basic requirements of the envisaged application. Also, their spin-spin and spin-lattice relaxation behaviour is studied and assessed with respect to their influence on the QRE effect. To support the structural and morphological design of complete nanoparticle systems, made up of QRE active core compounds and a carrier particle, studies are presented discussing the dependence of NQR transitions upon molecular structure. At the end of this work,

besides first promising results of the QRE effect of triphenylbismuth nanoparticles in aqueous solution, a guideline regarding physical and chemical properties is outlined which shall be considered in further particle design.

Kurzfassung

Die Rolle von Kernquadrupol-Resonanz in der Entwicklung neuartiger MRT Konstrastmittel

Die Verabreichung von Kontrastmittel zur Verbesserung von Bildqualität und Bildkontrast in der Magnetresonanztomographie (MRT) ist eine unverzichtbare Methode um die medizinische Diagnostik verschiedener Krankheiten und Symptome entscheidend zu unterstützen. Im Jahr 2015 wurde ein Forschungs-Projekt gestartet in dem ein völlig neuartiger Kontrastmittel-Typ, basierend auf Kernquadrupol Relaxations-Verstärkung (QRE) anstatt der üblichen paramagnetischen Relaxations-Verstärkung (PRE), vorgeschlagen wird. Beide Effekte zielen darauf ab, die Spin-Gitter Relaxationsrate jener Protonen-Spins in Wassermolekülen zu verstärken, welche mittels MRT detektiert werden. Durch die beschleunigte Relaxation entsteht ein verstärkter Bildkontrast.

Im Unterschied zum PRE Effekt, welche auf magnetische Dipol-Dipol Wechselwirkung zwischen Elektronen- und Protonenspins basiert, wechselwirken bei QRE Protonenspins mit nahegelegenen Quadrupol-Kernspins. Durch die intrinsisch diskrete Selektivität des QRE Effektes im Bezug auf die Stärke des angelegten, äußeren Magnetfeldes ergeben sich neue methodische Möglichkeiten welche herkömmliche, kontrastmittelunterstütze Untersuchungen erweitern können. QRE ist außerdem von der elektronischen Konfiguration und Umgebung des QRE-aktiven Moleküls abhängig, sodass eine molekulare/elektronische Sensitivität der Kontrastverstärkung entsteht. Aufgrund dieser Eigenschaften sind zwei Mechanismen vorstellbar: Erstens, ein von außen getriggerter Ein-Aus Schalter des Kontrasteffektes durch Veränderung des angelegten Scanner-Magnetfeldes. Zweitens ermöglicht die Sensitivität auf elektronische Veränderungen eine Modulierung des QRE Effektes auf molekularer Ebene und könnte so einen Beitrag zu molekularer Bildgebung erbringen. Ein weiteres Argument für die Entwicklung alternativer Kontrastmittelsysteme liefern die verwendeten Materialien bzw. chemischen Elemente. PRE- basierte Kontrastmittel enthalten Gadolinium (Gd) (eingeschlossen in stabile Chelate) und können bei Patienten mit Nierenproblemen nicht eingesetzt werden. Kürzlich wurde außerdem gezeigt, dass sich Gd im Gehirn gesunder Patienten anlagern kann. Auf QRE basierende Kontrastmittel können mit alternativen Elementen realisiert werden.

Zentraler Forschungsinhalt dieser Arbeit ist die Rolle der Kernquadrupol-Resonanz im gesamten Magnetisierung-Transfer Effekt bei QRE; vom polarisierten Proton über benachbarte Quadrupol-Kernspins zum Gitter. Getragen durch Untersuchungen mittels Kernquadrupol-Resonanz Spektroskopie konnten

verschiedene Bi-Verbindungen identifiziert werden, welche einige grundlegende Voraussetzungen für eine spätere Verwendung als Kontrastmittel in medizinischen MRT's erfüllen. Zusätzlich wurden Spin-Spin und Spin-Gitter Relaxationsverhalten dieser Verbindungen untersucht und im Hinblick auf ihren Einfluss auf den QRE Effekt beurteilt. Um einen geeigneten strukturellen und morphologischen Aufbau des Kontrastmittel-Gesamtsystems aus QRE-aktiven Molekülen auf Träger-Nanopartikel zu gewährleisten, wurde der Einfluss molekularer sowie morphologischer Struktur der Verbindungen und ihrer Umgebung auf die quantenmechanischen Kernquadrupol-Übergänge untersucht. Zuletzt werden erste, vielversprechende Beobachtungen des QRE Effektes, erzeugt durch Triphenylbismuth-Nanopartikel in wässriger Lösung, präsentiert. Des Weiteren werden chemische, physikalische sowie dynamische Voraussetzungen und Eigenschaften des Spin-Systems zusammengefasst, welche eine Weiterentwicklung der bisherigen Modellsysteme ermöglichen soll.

Acknowledgements

I wish to thank my supervisor, Prof. Hermann Scharfetter, for his invaluable guidance through any stage of this work. Also, I want to say thank you to all members of the Institute of Medical Engineering for their social as well as professional support; it was a pleasure to work with you!

Many ideas, thoughts, experiments, analysis, derivations and investigations presented in this work were inspired by lively discussions with members of the CONQUER-project team and scientists from the spin-dynamics community across Europe I was lucky to meet; among them I would like to mention Prof. Per-Olof Westlund, Prof. Danuta Kruk, Perttu Lantto and Pär Håkansson.

As a great deal of this work was written during so called free-time, I want to deeply thank my fiancée, friends and family for their infinite understanding and patience whenever I had to skip social events or leisure activities or whenever I was there, but not present.

Preface

This thesis is composed in a cumulative manner, which means that the main body consists of four peer reviewed articles published in different international scientific journals. These works were created during the employment at the Institute of Medical Engineering at Graz University of Technology as well as during short term stays at the University of Oulu and the University of Umeå. Several ideas have also been initialized during scientific meetings and conference attendances in Olsztyn, Turin, Prague and Graz within the EURELAX[1] research network (COST action 15209) which was superbly coordinated by Prof. Danuta Kruk.

To give a better understanding about the interconnection of the publications and their train of though, their context, connection and theory background is given in a frame text surrounding the main articles. Thus, the thesis is organized in three parts: In the first part, an introduction and the motivation is given. Also, relevant basic theory is reviewed on an extended level including historical development which could not be covered within the limited and compact style of journal articles. Then, in the center part, three first-author articles are printed as they were published (accepted manuscripts). Also, one coauthor article is summarized and the results are highlighted. In the final part, a joint, compact conclusion is drawn from all presented papers, where the before mentioned works are referenced. In a subsequent outlook chapter, most recent results from other groups are presented and recommendations for future scientific investigations are given.

[1] http://eurelax.uwm.edu.pl/

Contents

List of Abbreviations

BSA	Bovine serum albumin
CA	Contrast Agent
CEST	Chemical exchange saturation transfer
CONQUER	Contrast by quadrupole enhanced relaxation
D-D	Dipole-Dipole
DFT	Density functional theory
EFG	Electric field gradient
FA	Fluctuating amplitude
FC	Field cycling
FDA	Federal Drug Agency
FFC	Fast field cycling
FFT	Fast Fourier transform
FVA	Fluctuating vibrational amplitude
FWHM	Full width at half maximum
HWHM	Half width at half maximum
IR	Inversion recovery
MD	Molecular dynamics
NMR	Nuclear magnetic resonance
NMRD	Nuclear magnetic relaxation dispersion
MRI	Magnetic Resonance Imaging
NP	Nanoparticle
NQR	Nuclear quadrupole resonance
NQRS	Nuclear quadrupole resonance spectroscopy
PAS	Principal axis system
PR	Pseudo rotational
PRE	Paramagnetic relaxation enhancement
QC	Quantum chemistry
QN	Quadrupole nucleus
QNs	Quadrupole nuclei
QRE	Quadrupole relaxation enhancement
RF	Radio frequency
RT	Room temperature
SE	Spin echo
SO	Spin orbit
SR	Scalar relativistic

Dedicated to my fiancée, family
and friends.

Chapter 1

Introduction and motivation

In September 2015, the European Commission-funded project CONQUER[1] (Contrast by Quadrupole Enhanced Relaxation) was launched with the aim of developing a novel type of contrast agent (CA) for magnetic resonance imaging (MRI). The project team comprises five European universities from Poland, Slovenia, Sweden and Austria and was lead by the Institute of Medical Engineering at Graz University of Technology. Further facts and information on the project can be found here[2].

MRI forms a cornerstone of diagnostic imaging in modern medicine, providing spatially highly resolved scans of human body regions featuring excellent soft tissue contrast. From a physical point of view, MRI relies on detecting the magnetic response of proton spins placed in an externally applied magnetic flux density[3] B_0 by a pick-up coil upon on-resonance excitation by a sequence of short radio-frequency pulses. The resonance condition is given by the proton Larmor frequency ν_L which is determined by the Zeeman interaction of a proton with nuclear spin $I = 1/2$ with the magnetic field B_0 and depends on the proton's gyromagnetic ratio $\gamma_{^1H}$. Applying a field gradient along the scanned region rather than a constant field allows for spatially resolving the signal due to the varying resonance condition. Image contrast evolves from tissue dependent spin relaxation times T_1 (spin-spin) and T_2 (spin-lattice), as well as from the proton density distribution.

Due to the Boltzmann distribution, the energetically rather weak energy splitting of the proton spin states leads to a quite small population difference. In consequence, signal strength in magnetic resonance techniques is generally low. Remedy is found to some degree by the application of relatively high magnetic fields of typically 1.5 T or 3 T in medical scanners. The resulting, still moderate signal strength of MRI can be improved by the administration of exogenous relaxation enhancers that shorten the proton's spin-lattice relaxation times. A larger steady-state magnetization along the z-axis in tissues with faster T_1 relaxation results in larger image intensity and

[1] www.conquer.at, Initiators: Andreas Petrovič, Hermann Scharfetter and Stefan Spirk from Graz University of Technology

[2] https://cordis.europa.eu/project/rcn/196966/factsheet/en: CORDIS EU research results of the European Comission

[3] Further, simply called *magnetic field*, as this is the common term in the MRI community.

contrast [1]. Different strategies for designing such contrast agents are in the focus of researchers ever since the development of MRI [2, 3, 4, 5, 6, 7].

Conventional MRI contrast agents rely on paramagnetic relaxation enhancement (PRE), which is caused by a strong electron-proton dipole dipole (D-D) coupling between the electron spin of the paramagnetic agent and the spin of the water proton detected in MRI [1]. Such PRE-CAs, mostly based on stable chelates containing Gadolinium (Gd), have been proven to support and improve daily medical diagnostics routine for years. Gd-based contrast agents predominantly enhance contrast in T_1-weighted images [1], others, as e.g. nanoparticles made of paramagnetic iron oxides mostly affect T_2 [8].

A review on contrast-enhanced MRI is given by Lohrke *et al.*[9], where it is stated that in 2016 about 25% of all MRI examinations were supported by the administration of CAs. In the work of Alvares *et al.* [10], an overview of different CAs regarding their relaxivity r [L mmol^{-1}s^{-1}] (concentration independent measure of the ability of enhancing the relaxation rate) as well as their sensitivity is given. As an example, r_1 of Gadovist®, a Gd-based CA, is about 5.1 L mmol^{-1}s^{-1}. Administration a concentration of 1.3 mmol/l would lead to an increase of R_1 of blood from about 0.6 s^{-1} to more than 7 s^{-1}.

Without going into any details it is mentioned here, that nowadays the versatility of MRI goes far beyond producing T_1, T_2 or spin density weighted, morphological images of the body only. For example, there is real time imaging of moving objects (e.g. the heart) [11], magnetic resonance spectroscopy [12], functional imaging [13], diffusion and perfusion weighted imaging [14] , magnetic resonance angiography [15] and dynamic contrast-enhanced imaging [16].

Proton relaxation behaviour of different materials is typically captured by measuring R_1 versus B_0 - so called nuclear magnetic relaxation dispersion (NMRD) profiles. This is achieved by means of field cycling relaxometers [17], capable of measuring R_1 at different field strengths. The typical dependence of NMRD profiles in diamagnetic systems, where coupling by D-D interactions to neighbouring nuclear spins is the dominant relaxation mechanism, is a smooth decay with increasing field strength where no noteworthy variation occurs. However, in the presence of paramagnetic compounds (e.g. Gd-based CAs), the proton spins experience a strong relaxation enhancement as well as dependence on the magnetic field strength (PRE, compare relaxation curves in figure 1.1). Reason is the quadratic dependence of the relaxation rate on the electron gyromagnetic ratio, which is about 656 times larger than the gyromagnetic ratio of protons.

Theoretically, NMRD profiles are described by the Solomon-Bloembergen-Morgan equations [18, 19, 20]. The exact form of a relaxation curve depends on the motional conditions of the coupled spin system and is influenced by parameters like the rotational correlation time τ_r of the CA particle in solution. In figure 1.1,

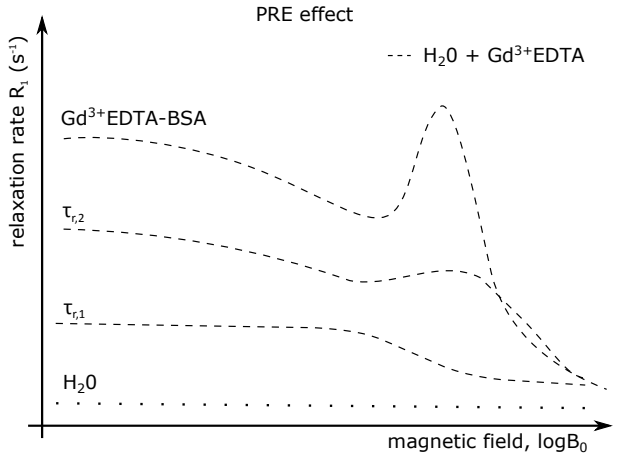

FIGURE 1.1: Schematic behaviour of the proton relaxation rate of pure water and water in the presence of an EDTA-Gd CA. The shape of the curve and the enhancement effect is strongly dependent on the rotational correlation time τ_r of the CA particles ($\tau_{r,2} > \tau_{r,1}$). Upon binding of the CA to e.g. bovine serum albumin (BSA), the strongest enhancement is achieved due to immobilization.

schematic NMRD profiles of pure water and a solution of a paramagnetic CA in water are shown. The enhancement effect of Gd^{3+} encapsulated in ethylenediaminetetraacetic acid (EDTA) is clearly visible as well as the strong dependency on the CA dynamics: the slower τ_r, the stronger the effect. A very interesting phenomenon in this context is what's happening when CA chelates are attached to protein amino acid residues, as for example bovine serum albumin (BSA) [21]: The relaxation curve strongly changes in amplitude and shape due to *de facto* immobilization of the EDTA complex. Unfortunately, PRE-CAs have in common that their enhancement effect becomes weaker for high fields, also the strong bump of the EDTA-BSA curve typically occurs below 3 T. Moreover, safety concerns about the toxicity of Gd-CAs have arisen due to reports on Gd deposition in human brain tissue [22, 23, 24]. In reaction, the FDA has announced respective warnings.

Even though different techniques providing cellular and molecular imaging are increasingly used in MRI [25], compared to radiotracers or optical probes, they are inferior in sensitivity and functionality. For example, it is desirable to switch on and off the contrast by external stimuli. Recently suggested gas-filled protein nanostructures [26] can be deactivated by ultrasound but not be re-established. Chemical exchange saturation transfer (CEST) [27] is a promising technique concerning switching by selective pulses but still has moderate sensitivity. Paramagnetic macromolecules based on nitroxide are free of Gd and shorten T_2 [28], but typically have a short *in vivo* lifetime and cannot be switched.

Another effect capable of enhancing spin-lattice relaxation of protons is based on the so called quadrupole relaxation enhancement (QRE). In contrast to PRE, the resulting enhancement effect exhibits narrow, discrete peaks (QRE-peaks, or dips, when T_1 is plotted) in the NMRD profile (see figure 1.2 (c)). The earliest observation

of such features were made by Woessner and Gutowksy [29] as well as Goldman [30] in p-dichlorobenzene and by Voigt and Kimmich [31] in poly(vinyl chloride) and were attributed immediately to a magnetization transfer effect between the ensemble of protons under observation and neighbouring quadrupole spin nuclei (QNs), exhibiting a spin number $I > 1/2$. Until the CONQUER project, this effect has only been observed in solid samples. QRE results from a coupling of proton spins to close-by quadrupole spins (several Å) by magnetic D-D interactions. The QN acts as an energy sink, taking over the magnetization from the polarized proton and transferring it further to the surroundings (lattice). The discrete nature of the enhancement effect stems from the resonance condition between the Larmor frequency ν_L of the proton spin and one of the QN transition frequencies ν_Q which has to be fulfilled for QRE, as indicated in figure 1.2 (b). While the proton Larmor frequency is determined by the Zeeman interaction only (red curve), the quadrupole transitions (blue curves) result from a superposition of Zeeman and pure quadrupole spin transitions. The frequency positions of the QN transitions at zero field are determined by the nuclear quadrupole resonance (NQR) parameters of the molecule containing the QNs: The quadrupole coupling constant Q_{cc} and the asymmetry parameter η. The origin of NQR transitions and NQR theory is closer discussed in section 2.1. However, it is anticipated already here that these NQR parameters depend on the electric field gradient (EFG) generated by the molecules's electronic configuration at the site of the QN and the QN's quadrupole moment Q.

The QRE effect has been observed also in proton relaxation of biopolymers as e.g. proteins and other biological samples as DNA and muscles due to the presence of ^{14}N-^{1}H groups [32]. In the work of Lurie *et al* [33], this observation is used to produce contrast in *in vivo* MRI images arising from muscle proteins. The authors used a field cycling MRI scanner, able to shift the nominal field strength. In that way, two images could be produced where one is gathered with the scanner field at the QRE peak position and a second image is taken at a field strength where no QRE effect is present. The difference of the two scans then shows contrast due to QRE peaks arising from present ^{14}N-^{1}H groups only. However, QRE peaks from ^{14}N nuclei appear at very low fields, so that the experiment was performed below 100 mT, which - in comparison to standard medical scanners at 1.5 T or 3 T - leads to a quite low sensitivity and resolution.

The core idea of the CONQUER project is thus to facilitate the QRE effect for MRI contrast enhancement at standard medical field strengths of 1.5 T or 3 T. This shall be achieved by the injection of CA particles, carrying QRE-active compounds exhibiting quadrupole spin transition frequencies which cross the proton Larmor frequency at e.g. 3 T. The idea is illustrated in figure 1.2 (a): Nanoparticles act as carriers for QRE-active molecules and allow water exchange so as to relax close by polarized water protons. Exactly this point adds a complication compared to conventional QRE observed in solids, where protons are affected which are bound to the QN containing compound. Here, the goal is to address the protons on water molecules which are

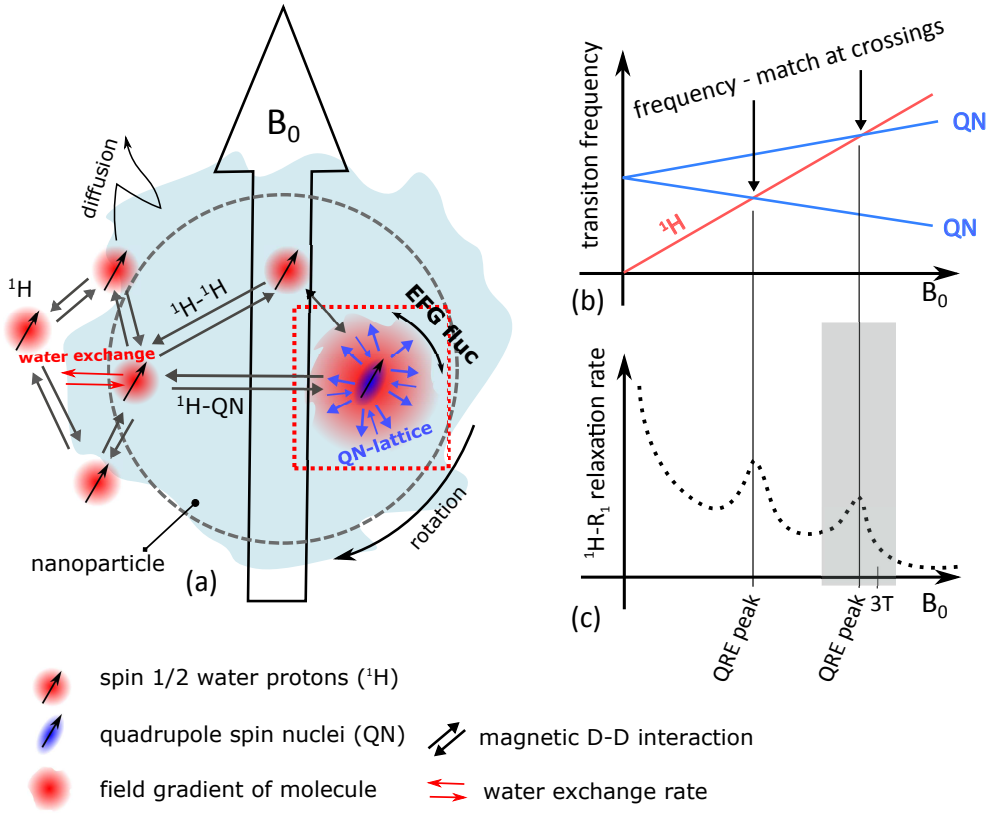

FIGURE 1.2: Schematic overview on the QRE effect acting as MRI contrast agent: Panel a) shows an indefinite carrier nanoparticle containing QNs which can be approached by water protons from the surroundings. Magnetic D-D interactions are indicated by arrows. In panel (b), the behaviour of the proton Larmor frequency and an arbitrary QN transition frequency in an external magentic field is presented. The plot captures only the behaviour of a certain, fixed angle between the EFG of the QRE active compound the the applied magnetic field. In panel c), the hypothetical shape of a resulting NMRD profile is shown. At the crossing points derived from panel b), relaxation enhancement features (QRE peaks) can be expected.

not bound to the dissolved QRE-CA particles. Moreover, the agent must be biocompatible and non-toxic. Also, the QRE active compound must exhibit a quadrupole spin transition frequency spectrum to guaranty level crossing with the proton Larmor frequency close to or at a the scanner frequency e.g. 3 T (see 1.2 (b) and (c)). There are several interactions and coupling effects between all participating spins which can be considered, as magnetic D-D coupling or J coupling. For QRE, most important is the magnetic D-D coupling between QN and proton spins which forms the basis of the QRE magnetization transfer effect (see e.g. [34]).

It must be noted, that the pictures drawn in figure 1.2 are very simplified and shall only demonstrate the basic idea of CONQUER. For example, the transition frequency diagram for the QNs in panel (b) is only valid for a single crystal placed in an external magnetic field, in which all QN are in an electronically equivalent state. In fact, the Zeeman contribution to the QN transitions is angle dependent with respect to the quadrupole spins and dynamics of the particle must be taken into account in liquids. Also, not every crossing will lead to a QRE peak as indicated by the figure as the QRE peak amplitude also depends on the quantum mechanical transition probability of the quadrupole transitions. For high spin QNs, even more transitions are possible than indicated in panel (b).

The advantage of a QRE based CA upon a conventional PRE based CA lies in the discrete character of the NMRD profile. Due to the resonance condition, the enhancement effect is frequency selective and can be switched on and off by (1) either shifting the nominal field of the scanner or by (2) manipulating the position of the quadrupole transition frequencies (compare figure 1.3). The former possibility relies on suitable MRI hardware able to shift the nominal field. Such scanners are in use already at different clinical field strengths for research purposes [35]. The latter way of manipulating the enhancement effect relies on alteration of the electronic structure of the QRE active molecule (more exactly, the EFG at the QN) which determines its quadrupole spin transition frequencies (see chapter 2.1). These, in turn, determine the level-crossings with the proton Larmor frequency and thus the QRE peak positions. In short: The QRE peak position can be shifted by electronic alteration of the QRE active molecule in the CA. This property opens up the possibility of responsive imaging, sensitive to chemical changes. Strategies to enable a contrast effect responsive or sensitive on a molecular level are in the focus of MRI research since a long time [36, 37, 38, 39], and QRE-CAs have the potential to be added as another mechanism.

To compete with conventional CAs, QRE peaks should reach at least a relaxivity of about 5 $\mathrm{mM}^{-1}\mathrm{s}^{-1}$, which is common for PRE-CAs [10]. Or, there must be another unique useful feature which cannot be provided by other mechanisms as the frequency selective nature of the NMRD profiles from QRE active compounds. The QRE peaks should be narrow and appearing at the desired field positions. Two important studies, both based on the stochastic Liouville approach for spin relaxation,

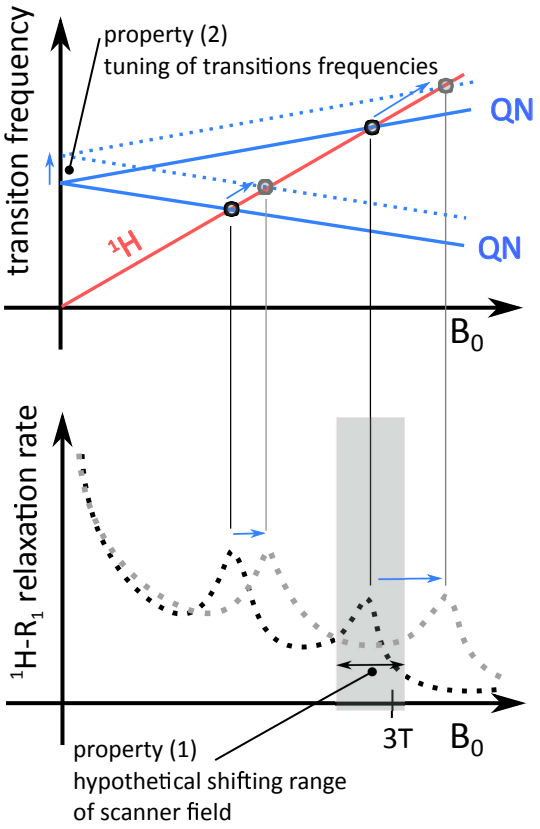

FIGURE 1.3: Schematic illustration of how to make use of the frequency selective character of the NMRD profile from QRE-based CAs. (1) By shifting the scanner field, contrast due to relaxation enhancement can be switched. (2) Alterations of the electronic structure of the QRE compound leads to a shift of the QRE peak positions. In this way, the contrast effect can be modulated by electronic changes of the CA.

are describing the theory of QRE in slow tumbling amide groups [40] and for arbitrary QN spin number and dynamical conditions for molecular crystals [34]. In a more recent study a simple expression for QRE in slowly tumbling molecules valid at low fields is presented [41]. From these works, two requirements for a possible QRE-based CA can already be derived:

- For efficient D-D coupling ($\sim \frac{1}{r^6_{QN-^1H}}$), the interspin distance r_{QN-^1H} between proton and QN should be only a few Ångstroms.
- The rotational correlation time τ_r of the nanoparticle, creating a necessary modulation of the D-D coupling (fluctuations), must be long ($2\pi\nu_Q\tau_r > 1$). This parameter can be controlled by the particle size.

Another important issue, which also plays a role in PRE based CAs, is the water exchange lifetime τ_{ex} and the accessibility of the QNs for protons. This mainly depends on chemistry and structure and must be optimized during the particle design process.

Still, several open questions remain concerning the static and dynamic NQR properties of the QRE active compound so as to be suitable for the envisaged application. The transition spectrum of the QN spins defines the potential appearance of QRE peaks. Another key factor is the quadrupolar relaxation itself and its influence on the width of the QRE peaks and on the additional modulation of the above mentioned D-D coupling.

Central research interest of this work is thus to understand the role of the quadrupole nucleus in the QRE effect with regard to a potential application as contrast agent for MRI. This is indicated also in figure 1.2 (a) by the red square in dashed lines, surrounding the QRE-active QN. The square is emphasizing that focus is set on the second part of the two-step magnetization transfer effect from the proton to the QN and further to the lattice. Model systems of pure quadrupole spin ensembles will be investigated experimentally mainly by the use of nuclear quadrupole resonance spectroscopy (NQRS), i.e. determining NQR parameters as well as spin relaxation behaviour without the application of an external magnetic field. Also, theoretical calculations are performed by the use of quantum mechanical relaxation theory and quantum chemistry (QC) methods. The following research questions are in the focus of the thesis:

- Which molecules and which nuclei are suitable to form the QRE active compound?
- What is a suitable model system that can be studied by NQRS and what are the NQR parameters of this system?
- What is the sensitivity of the frequency positions upon changes of the electronic environment? Can they be tuned to a desired frequency?

- What is the predictive power of *ab initio* quantum chemistry calculations in calculating NQR paramters of the envisaged model systems?
- How strong is the temperature dependence of the frequency positions?
- What are the spin relaxation properties of the model system? Which influence is expected on the QRE effect?
- How can the QRE effect be predicted from the sole nuclear quadrupole resonance parameters of the model system?
- Are there any morphological or structural requirements for the joint system nanoparticle - QRE active compound that should be considered in the design?

It is possible to roughly group the properties of interest of the QRE active compound into *static* and *dynamic* properties, where *static* should be understood as the residual, non-vanishing mean of the always present molecular and nuclear *dynamics*, perceivable on the time scale of the experimental observer. *Static* properties are manifested in constants as the EFG strength or the dimensions the of molecule's structure; they determine resonance conditions as for example the positions of the QRE peaks. *Dynamic* properties comprise the description of fluctuations around the static mean, responsible for relaxation phenomena, transferring excited systems back to the equilibrium condition.

NQR beyond CA research

Apart from the above motivated, very special topic in CA research for MRI, NQRS has a very wide field of applications and can deliver structural and dynamical insights to materials on a molecular level [42]. This is due to the origin of the underlying electric interaction between the quadrupole moment of a QN and the electric field gradient (EFG) at it's location, which is generated by the surrounding electron cloud (see section 2.1). The transition frequency positions are related to the electronic structure of the molecule under observation, their spin relaxation rates are associated with molecule dynamics (EFG fluctuations). By measuring the pure quadrupole relaxation rates using NQRS and applying quantum mechanical relaxation theory, dynamical parameters of the molecule can be extracted. Experimentally determined NQR parameters can be used for material characterization. Of more general relevance is, that relaxation data from quadrupole spins can also be used to validate and test theoretical relaxation models. Equally, experimentally determined NQR parameters can be a reference for theoretical calculations of the electron density distribution of molecules using modern *ab initio* quantum chemistry methods. Thus, throughout this thesis NQRS is considered as a very fruitful method rich in physical information, which can deliver insights into problems beyond CA research.

1.1 Content and structure of the main part

Given the above made general introduction, the content of the main three works of this cumulative thesis is briefly summarized below:
Paper 1 (chapter 3) is dedicated to select promising compounds that can be used in further research on QRE-CAs for MRI. Besides experimental NQR data demonstrating suitable frequency ranges of Bi-aryl compounds, also, a quantum chemistry calculation framework is presented to theoretically predict positions of NQR frequencies of yet unmeasured compounds.
Paper 2 (chapter 4) shows a simple calculation method for predicting the frequency position of QRE peaks in solids, when NQR parameters of the QRE active molecule are known. Due to an assumption made in this work, it is possible to forgo the application of quantum mechanical relaxation theory but still obtaining predictions in accordance with experiments.
Paper 3 (chapter 5) treats the spin-spin relaxation of the pure quadrupole nuclei due to EFG fluctuations in solids and allows to calculate the lineshape of quadrupole transitions. From experimental relaxation data, dynamical parameters of the molecules under observation are determined by the application of Redfield theory. The calcuated lineshape also helps to model the lineshape of QRE peaks, which was only treated phenomenologically in paper 2.
Paper 4 (contribution as coauthor) (chapter 6) discusses aspects of structural order with respect to detection and line broadening of NQR transitions in solids. The question is addressed, if an amorphous solid - produced by melting and shock-freezing a molecular crystal - is still exhibiting a detectable signal. It could be shown, that only in case of a crystalline structure, narrow NQR peaks can be detected, but for an amorphous solid, the signal strength is below the noise floor. By accident, a yet unknown, metastable crystal structure of the investigated sample could be identified.

1.1.1 List of publications

Below, a full list of publications is given where only a coherent selection is part of the thesis (papers 1-4).

1. Gösweiner Christian, Lantto Perttu, Fischer Roland, Sampl Carina, Umut Evrim, Westlund Per-Olof, Kruk Danuta, Bödenler Markus, Spirk Stefan, Petrovic Andreas; Scharfetter Hermann. *Tuning Nuclear Quadrupole Resonance: A Novel Approach for the Design of Frequency-Selective MRI Contrast Agents.*
   In: Phys. Rev. X 8, 021076 (2018), ISSN: 21603308, DOI: 10.1103/PhysRevX.8.021076

2. Gösweiner Christian, Kruk Danuta, Umut Evrim, Masiewicz Elzbieta, Bödenler Markus, Scharfetter Hermann. *Predicting quadrupole relaxation enhancement peaks in proton R1-NMRD profiles in solid Bi-aryl compounds from NQR parameters.*
   In: Molecular Physics, 117:7-8, 910-920 (2018), DOI: 10.1080/00268976.2018.1519201

3. Gösweiner Christian, Westlund Per-Olof, Scharfetter Hermann. *Spin-spin relaxation of nuclear quadrupole resonance coherences and the important role of degenerate energy levels.*
   In: Molecular Physics, 8976, e1743888. DOI: 10.1080/00268976.2020.1743888

4. Scharfetter Hermann, Gösweiner Christian, Krassnig Paul Josef, Sampl Carina, Thonhofer Martin, Fischer Roland, Spirk Stefan, Stana-Kleinschek Karin, Umut Evrim, Kruk Danuta. *Aspects of structural order in 209 Bi-containing particles for potential MRI contrast agents based on quadrupole enhanced relaxation*.
   In: Molecular Physics, 117:7-8, 935-943 (2018), DOI: 10.1080/00268976.2018.1511869

5. Hermann Scharfetter, Roland Fischer, Paul Krassnig, Martin Thonhofer, Felix Theyer and Christian Gösweiner. *Tris(2-Methoxyphenyl)Bismuthine Polymorphism Characterized by Nuclear Quadrupole Resonance Spectroscopy.*
   In: Crystals, 9(9), 446 (2019), DOI: 10.3390/cryst9090446

6. Kruk Danuta, Gösweiner Christian, Masiewicz Elzbieta, Umut Evrim, Sampl Carina and Scharfetter Hermann. *Model – free approach to quadrupole spin relaxation in solid 209Bi-aryl compounds.*
   In: Phys. Chem. Chem. Phys., 2018,20, 23414-23423 (2018), DOI: 10.1039/C8CP03848A

7. D. Kruk, E. Umut, E. Masiewicz, C. Sampl, R. Fischer, S. Spirk, C. Goesweiner and H. Scharfetter. *209Bi quadrupole relaxation enhancement in solids as a step towards new contrast mechanisms in magnetic resonance imaging.*
   In: Phys. Chem. Chem. Phys., 2018,20, 12710-12718 (2018), DOI: 10.1039/C8CP00993G

8. Bödenler Markus, Basini Martina, Casula Francesca Maria, Umut Evrim, Gösweiner Christian, Petrovic Andreas, Kruk Danuta, Scharfetter Hermann. *R1 dispersion contrast at high field with fast field-cycling MRI.*
   In: Journal of Magnetic Resonance 290, 68–75 (2018). DOI: 10.1016/j.jmr.2018.03.010

9. Bödenler Markus, de Rochefort Ludovic, Ross P. James, Chanet Nicolas, Guillot Genevieve, Gareth R. Davies, Gösweiner Christian, Scharfetter Hermann, Lurie David J., Broche Lionel M. *Comparison of fast field-cycling magnetic resonance imaging methods and future perspectives.*
   In: Molecular Physics, 117:7-8, 832-848, DOI: 10.1080/00268976.2018.1557349

1.1.2 Conference participations

- 2^{nd} Workshop of Nuclear Magnetic Resonance Relaxometry, 04.02.2019 - 06.02.2019, Prague, Czech Republic (Talk)
- Conference on NMR Relaxometry and Related Methods, 29.01.2018-31.01.2018, Torino, Italy (Talk)
- 10^{th} Conference on Fast Field-Cycling NMR Relaxometry, 05.06.2017 - 07.06.2017 Mikolajki, Poland (Talk)
- ISMRM 2017 Congress, 22.04.2017-27.04.2017, Honolulu, USA (Poster Session)
- ESMRMB 2016 Congress, 29.09.2016-01.10.2016, Vieanna, Austria (Talk)

Chapter 2

Theory review

Within the limited frame of journal articles, theory parts are typically given in a compact style omitting longer derivations and explanations. Thus, the following sections are meant to review the origin of the used theory just up to the point when they are introduced in the articles. The discussion comprises historical development, approximations and limiting cases of validity.

2.1 Nuclear electric quadrupole Hamiltonian

The first reported observation of zero field quadrupole resonance dates back to 1947, when Nierenberg *et al.* [43] showed ^{23}Na halides (I=3/2) resonance lines with the molecular beam method at very low magnetic field. Pure quadrupole resonance was observed first by Dehmelt and Krüger [44, 45] for the chlorine isotopes ^{35}Cl and ^{37}Cl in solid transdichloroethylene. The theory of nuclear quadrupole interactions in solids was described first by R.V. Pound [46] in 1950 whereas the expression for the scalar nuclear quadrupole moment Q was given much earlier by H. B. G. Casimir [47] in 1936. A first very comprehensive review of the phenomenon summarizing experiments and theory until 1958 is given by T.P. Das and E.L. Hahn [42].

Below, the quantum mechanical Hamilton operator of the interaction associated with a nuclear quadrupole moment in an electric field gradient is derived in condensed form, following the book *Principles of Magnetic Resonance* of C. Slichter [48] and an article of Cohen and Reif [49].

Classically, the interaction energy E associated with a charge distribution $\rho(\mathbf{x})$ of a nucleus with atomic number Z and total electric charge Ze in an external electrostatic potential $V(\mathbf{x})$ is

$$E = \int \rho(\mathbf{x}) V(\mathbf{x}) d^3\mathbf{x}\,, \tag{2.1}$$

integrated over the volume of the nucleus where $\mathbf{x}$ are Cartesian coordinates. Taylor-expanding $V(\mathbf{x})$ about the origin (nuclear center of mass) gives

$$E = V(0) \int \rho(\mathbf{x}) d^3\mathbf{x} + \sum_i V_i \int x_i \rho(\mathbf{x}) d^3\mathbf{x} + \frac{1}{2!} \sum_{i,j} V_{i,j} \int x_i x_j \rho(\mathbf{x}) d^3\mathbf{x} + \ ... \tag{2.2}$$

where x_i $(i = 1, 2, 3)$ stands for cartesian coordinates x, y and z and with $V_i \equiv \frac{\partial V}{x_i}|_0$ and $V_{ij} \equiv \frac{\partial^2 V}{x_i x_j}|_0$. V_{ij} is the electric field gradient (EFG) tensor which must satisfy the Laplace equation $\nabla^2 V = 0$. This has the consequence that V_{ij} is traceless:

$$\sum_i V_{ii} = 0 \, . \tag{2.3}$$

The first term of equation 2.2 corresponds to the electrostatic energy of a point nucleus. The second term contains the electric dipole moment of the nucleus, which is zero. The only term depending on the orientation of the nucleus within the potential (and thus spin dependent) is the third one, containing the nuclear quadrupole moment tensor $Q'_{ij} = \int \rho(\mathbf{x}) x_i x_j \partial^3 \mathbf{x}$ and the EFG tensor V_{ij} (higher order terms can be neglected). Both Q'_{ij} and V_{ij} are symmetric, second rank tensors.

It is convenient to use the definition

$$Q_{ij} = \int \left[3x_i x_j - \delta_{ij}\mathbf{x}^2\right] \rho(\mathbf{x}) \partial^3 \mathbf{x} \, , \tag{2.4}$$

which corresponds to a subtraction of spherically symmetric terms from the quadrupole tensor Q'_{ij} and makes Q_{ij} traceless ($\sum_i Q_{ii} = 0$). Equation 2.4 expressed in Q_{ij} gives

$$\int x_i x_j \partial^3 \mathbf{x} = \frac{1}{3} \left[Q_{ij} + \int \delta_{ij} \mathbf{x}^2 \rho(\mathbf{x}) \partial^3 \mathbf{x} \right] \, . \tag{2.5}$$

which allows to rewrite the remaining, third term of equation 2.2:

$$E = \frac{1}{6} \sum_{ij} \left[V_{ij} Q_{ij} + V_{ij} \delta_{ij} \int \mathbf{x}^2 \rho(\mathbf{x}) \partial^3 \mathbf{x} \right] \tag{2.6}$$

The second term vanishes due to equation 2.3 and one gets

$$E = \frac{1}{6} \sum_{ij} V_{ij} Q_{ij} \, . \tag{2.7}$$

To find the quantum mechanical pedant of the classic energy E (the Hamilton operator $\widehat{H}$), $\rho(\mathbf{x})$ of the nucleus must be replaced by the quantum mechanical operator $\widehat{\rho}(\mathbf{x})$:

$$\widehat{\rho}(\mathbf{x}) = e \sum_{k=1}^{Z} \delta(\mathbf{x} - \mathbf{x}_k) \tag{2.8}$$

Thus, the quadrupole operator $\widehat{Q}_{ij}$ can be found by substituting ρ in equation 2.4 with $\widehat{\rho}$:

$$\begin{aligned} \widehat{Q}_{ij} &= \int \left[3x_i x_j - \delta_{ij}\mathbf{x}^2\right] \widehat{\rho}(\mathbf{x}) \partial^3 \mathbf{x} \\ &= e \sum_{k=1}^{Z} \int \left[3x_i x_j - \delta_{ij}\mathbf{x}^2\right] \delta(\mathbf{x} - \mathbf{x}_k) \partial^3 \mathbf{x} \\ &= e \sum_{k=1}^{Z} \left[3x_{ik} x_{jk} - \delta_{ij} x_k^2\right] \end{aligned} \tag{2.9}$$

The quadrupole Hamiltonian is then:

$$\widehat{H}_Q = \frac{1}{6}\sum_{ij} V_{ij}\widehat{Q}_{ij} \; . \tag{2.10}$$

In the quantum mechanical description, one is interested in finding the matrix elements of $\widehat{H}_Q$ with respect to the nuclear wave functions $|Im\rangle$, characterized by the nuclear spin number I and the magnetic quantum number m, labelling the orientation of the nuclear spin. To describe quantum mechanical spin systems, the established Dirac-notation (Bra-Ket notation) is used throughout the thesis. As a reminder, important eigenvalue and commutation relations for the components of the total nuclear angular momentum operator $\widehat{\mathbf{I}}$ are listed below, where the z-axis is chosen for projecting the orientation of m (quantization axis):

$$\begin{aligned}
\left[\widehat{I}_i, \widehat{I}_j\right] &= i\hbar\epsilon_{ijk}\widehat{I}_k \\
\left[\widehat{I}_i, \widehat{\mathbf{I}}^2\right] &= 0 \\
\widehat{\mathbf{I}}^2|Im\rangle &= \hbar^2 I(I+1)|Im\rangle \\
\widehat{I}_z|Im\rangle &= \hbar m|Im\rangle
\end{aligned} \tag{2.11}$$

For convenience, ladder operators are defined for rising or lowering m of a state for given I:

$$\begin{aligned}
\widehat{I}_\pm &= \widehat{I}_x \pm i\widehat{I}_y \\
\widehat{I}_+|Im\rangle &= \hbar\sqrt{I(I+1) - m(m+1)}|I, m+1\rangle \\
\widehat{I}_-|Im\rangle &= \hbar\sqrt{I(I+1) - m(m-1)}|I, m-1\rangle \\
\left[\widehat{I}_+, \widehat{I}_-\right] = 2\hbar\widehat{I}_z \; , \; \left[\widehat{\mathbf{I}}^2, \widehat{I}_\pm\right] &= 0 \; , \; \left[\widehat{I}_z, \widehat{I}_\pm\right] = \pm\hbar\widehat{I}_\pm
\end{aligned} \tag{2.12}$$

In quadrupole resonance it is sufficient to consider only the nuclear ground state as the separation to the first excited state is much larger than the quadrupolar interaction. This means that it is sufficient to consider only matrix elements $\langle Im|\widehat{H}_Q|Im'\rangle$ diagonal in I and considering only the submatrix $\rho_{mm'}$ to describe the charge denstiy. This argument also makes clear, why the first and second term of the energy in equation 2.2 are of no interest to the quadrupolar interaction: First, the interaction is only depending on m and thus depending on orientation and second, the nuclear ground state wavefunction has definite parity which makes $\rho_{mm'}(-x) = \rho_{mm'}(x)$ and the dipole moment vanishes.

However, the quadrupole operator of equation 2.9 is very complicated to handle as it is containing all nuclear particles (many-particle problem). To overcome this situation, the next step is to express the matrix elements of the quadrupole operator $\widehat{Q}_{ij}$ in components of the angular momentum operators $\widehat{\mathbf{I}}$ instead of

Cartesian coordinates **x**. To achieve this, use is made of the equation

$$\langle Im|\widehat{Q}_{ij}|Im'\rangle = C\langle Im|\frac{3}{2}(\widehat{I}_i\widehat{I}_j + \widehat{I}_j\widehat{I}_i) - \delta_{ij}\widehat{\mathbf{I}}^2|Im'\rangle \tag{2.13}$$

which will not be derived completely here but which shall be sketched briefly:

Central for the derivation of equation 2.13 is the Wigner-Eckart theorem:

$$\langle J'm'|T_{Jm}|J''m''\rangle = C(J''JJ'; m_{J''}mm_{J'})\langle J'\|T_J\|J''\rangle \ , \tag{2.14}$$

where m, m' and m'' are z-components of the total angular momenta J, J' and J'' of a set of wave functions. $C(J''JJ'; m_{J''}mm_{J'})$ are the Clebsch-Gordan coefficients and T_{Jm} are irreducible tensor operators which can be constructed from angular momentum operators obeying the commutation rules

$$\begin{aligned}[J_\pm, T_{Jm}] &= \sqrt{J(J+1) - m(m+1)}T_{Jm\pm1} \\ [J_z, T_{Jm}] &= mT_{Jm}\end{aligned} \tag{2.15}$$

The quantity $\langle J'\|T_J\|J''\rangle$ (sometimes called reduced matrix element) is constant for given J,J',J'' but independent of m, m' and m''. Thus, equation 2.14 states that matrix elements diagonal in I of traceless, symmetric, second rank tensors T_{Jm} are proportional. The Clebsch-Gordan coefficient is the same for all functions T_{Jm} but $\langle J'\|T_J\|J''\rangle$ depends on the variable used to construct T_{Jm}.

An important conclusion from that is, that T_{Jm}'s constructed from different variables q and p can be related via

$$\langle J'm'|T_{Jm}(q)|J''m''\rangle = \langle J'm'|T_{Jm}(p)|J''m''\rangle\frac{\langle J'\|T_J(q)\|J''\rangle}{\langle J'\|T_J(p)\|J''\rangle} \ , \tag{2.16}$$

Practically, this equation allows to relate $T_{Jm}(J)$, constructed from angular momentum operators J, to $T_{Jm}(\mathbf{x})$, constructed from a coordinate **x**. The equation is also valid for linear combinations of the form $\sum a_m T_{Jm}(J)$ and $\sum a_m T_{Jm}(\mathbf{x})$. Derivation of the Wigner-Eckart theorem is given in [48].

An example for a set of irreducible tensor operators $T_{Jm}(J)$ fulfilling equation 2.15 is

$$\begin{aligned}T_{22} &= J_+^2 = (J_x + iJ_y)^2 \\ T_{21} &= -(J_zJ_+ + J_+J_z) \\ T_{20} &= \sqrt{\frac{2}{3}}(3J_z^2 - \mathbf{J}^2) \\ T_{2-1} &= J_zJ_- + J_-J_z \\ T_{2-2} &= J_-^2 = (J_x - iJ_y)^2\end{aligned} \tag{2.17}$$

Recalling the commutator relations of **J**, its components J_x,J_y,J_z and the coordinate **x**:

$$\begin{aligned} [J_x, y] &= iz \\ [J_x, J_y] &= iJ_z \end{aligned} \tag{2.18}$$

makes clear that simply replacing J_x,J_y,J_z in equation 2.17 with x,y,z will produce a new set of irreducible tensor operators $T_{Jm}(\mathbf{x})$ also fulfilling equation 2.15.

$$\begin{aligned} T_{22} &= (x+iy)^2 \\ T_{21} &= -2z(x+iy) \\ T_{20} &= \sqrt{\frac{2}{3}}(3z^2 - \mathbf{x}^2) \\ T_{2-1} &= 2z(x-iy) \\ T_{2-2} &= (x-iy)^2 \end{aligned} \tag{2.19}$$

Caution is necessary only when the components of operators do not commute among themselves, as it is the case for $T_{21}(J)$ where the symmetrized product $J_zJ_+ + J_+J_z$ must be used instead of $2J_+J_z$.

This concept can be applied to the quadrupole operator as derived earlier (equation 2.9)

$$\widehat{Q}_{ij} = e\sum_{k=1}^{Z}\left[3x_{ik}x_{jk} - \delta_{ij}\mathbf{x}_k^2\right] \tag{2.20}$$

depending on Cartesian coordinate **x** and forming a linear combination $F(\mathbf{x}) = \sum a_m T_{Jm}(\mathbf{x})$ of expressions from 2.19. Also functions depending on the components of the total angular momentum $\widehat{\mathbf{I}}$ of the nucleus can be constructed $G(\widehat{\mathbf{I}}) = \sum a_m T_{Jm}(\widehat{\mathbf{I}})$ by simply replacing x, y, z with $\widehat{I}_x$, $\widehat{I}_y$, $\widehat{I}_z$ in the same manner as demonstrated above. This is justified, as also the components of $\widehat{\mathbf{I}}$ fulfil commutator relations similar to equation 2.18. This becomes evident from the definition of their commutation relations with the Cartesian coordinates: $\widehat{I}_i$ is defined as

$$\widehat{I}_i = \sum_{k=1}^{Z}\widehat{l}_{ik} + \widehat{s}_{ik} = \sum_{k=1}^{Z}\widehat{I}_{i,k} \tag{2.21}$$

where $\widehat{l}_{ik}$ and $\widehat{s}_{ik}$ are the i-th components of the orbital and spin angular momentum of the k-th nucleus. They fulfil the following commutation relations, which is leading to a relation similar to equation 2.18:

$$\left[\widehat{l}_{xk}, y_k\right] = iz_k \text{ and } [\widehat{s}_{xk}, y_k] = 0 \longrightarrow \left[\widehat{I}_{xk}, y_k\right] = iz_k \tag{2.22}$$

To finally evaluate the matrix elements of the quadrupole operator as a function of $\widehat{\mathbf{I}}$ instead of $\mathbf{x}$ of equation 2.20, use is made of equation 2.16:

$$\begin{aligned}\langle Im|\widehat{Q}_{ij}|Im'\rangle &= \langle Im|e\sum_{k=1}^{Z}\left[3x_{ik}x_{jk}-\delta_{ij}\mathbf{x}_k^2\right]|Im'\rangle = \langle Im|F(\mathbf{x})|Im'\rangle \\ &= \langle Im|G(\widehat{\mathbf{I}})|Im'\rangle\frac{\langle I\|T_J(\mathbf{x})\|I\rangle}{\langle I\|T_J(\widehat{\mathbf{I}})\|I\rangle} = \langle Im|\frac{3}{2}\left(\widehat{I}_i\widehat{I}_j+\widehat{I}_j\widehat{I}_i\right)-\delta_{ij}\widehat{\mathbf{I}}^2|Im'\rangle C\ ,\end{aligned} \tag{2.23}$$

which is the envisaged expression presented in equation 2.13. As the components $\widehat{I}_i$ do not commute among each other, the symmetrized product $\frac{1}{2}\left(\widehat{I}_i\widehat{I}_j+\widehat{I}_j\widehat{I}_i\right)$ has to be used instead of $\widehat{I}_i\widehat{I}_j$.

The constant C originates from the ratio of the reduced matrix elements in equation 2.23 and still remains to be determined. This can be done by defining the maximum expectation value of the quadrupole moment operator for the case $m = m' = I$ and $i = j = z$ (which is the state in which the component of $\widehat{\mathbf{I}}$ along the z-axis is a maximum) as

$$\langle II|\widehat{Q}_{zz}|II\rangle = \langle II|e\sum_{k=1}^{Z}\left[3z_k-\mathbf{x}_k^2\right]|II\rangle \equiv eQ\ , \tag{2.24}$$

where eQ is the *electric quadrupole moment* of the nucleus in units of the proton charge e. The right hand side of equation 2.23 yields

$$C\langle II|3\widehat{I}_z^2-\widehat{\mathbf{I}}^2|II\rangle = C\left[3I^2-I(I+1)\right] = C\left[I(2I-1)\right]\ , \tag{2.25}$$

combining equations 2.24 and 2.25 one arrives at

$$C = \frac{eQ}{I(2I-1)}\ . \tag{2.26}$$

The quadrupole Hamiltonian of equation 2.10 then reads as:

$$\widehat{H}_Q = \frac{eQ}{6I(2I-1)}\sum_{ij}V_{ij}\left[\frac{3}{2}\left(\widehat{I}_i\widehat{I}_j+\widehat{I}_j\widehat{I}_i\right)-\delta_{ij}\widehat{\mathbf{I}}^2\right] \tag{2.27}$$

It is interesting to note that even though the quadrupole tensor has nine components, in the Hamilton operator only one scalar constant eQ is needed. This is due to the fact that the nucleus can be described by a state of definite angular momentum which is equivalent to the classic statement of cylindrical symmetry. eQ only measures the departure from a spherical symmetry. This can be shown by taking the difference between the charge distribution parallel and transverse to the symmetry axis z:

$$\begin{gathered}\int z^2\rho\partial^3\mathbf{x}-\int x^2\rho\partial^3\mathbf{x} = \int(z^2-x^2)\rho\partial^3\mathbf{x} = \\ \frac{1}{2}\int(2z^2-x^2-y^2)\rho\partial^3\mathbf{x} = \frac{1}{2}\int(3z^2-\mathbf{x}^2)\rho\partial^3\mathbf{x}\end{gathered} \tag{2.28}$$

The last expression corresponds to the classical quadrupole moment as in equation 2.4. eQ can be positive, indicating an elongated cigar-shaped charge distribution along the z-axis. If eQ is negative, it means the charge distribution is flattened along z.

Expression 2.27 can further be simplified by choosing a representation of the EFG tensor V_{ij} in the principal axis system (PAS) where $V_{ij} = 0$ for $i \neq j$ in which the tensor is diagonal:

$$\widehat{H}_Q = \frac{eQ}{6I(2I-1)} \left[V_{xx}(3\widehat{I}_x^2 - \widehat{\mathbf{I}}^2) + V_{yy}(3\widehat{I}_y^2 - \widehat{\mathbf{I}}^2) + V_{zz}(3\widehat{I}_z^2 - \widehat{\mathbf{I}}^2) \right] . \tag{2.29}$$

Making use of equation 2.3 and introducing the definitions

$$\begin{aligned} eq &= V_{zz} \\ \eta &= \frac{V_{xx} - V_{yy}}{V_{zz}} \end{aligned} \tag{2.30}$$

where eq is the strength of the electric field gradient q in units of e and η is called *asymmetry parameter*, equation 2.29 becomes

$$\widehat{H}_Q = \frac{e^2qQ}{4I(2I-1)} \left[(3\widehat{I}_z^2 - \widehat{\mathbf{I}}^2) + \eta(\widehat{I}_x^2 - \widehat{I}_y^2) \right] . \tag{2.31}$$

The term e^2qQ is the so-called *quadrupole coupling constant* Q_{cc} which gives the strength of the quadrupole interaction. The asymmetry parameter η describes the departure of the EFG from cylinder symmetry and can have values from 0 (cylinder symmetric) to 1. These two parameters are enough to describe the electric quadrupole interaction of a $I > 1/2$ nucleus.

If, however, the EFG is spherically symmetric or has cubic symmetry one gets $V_{xx} = V_{yy} = V_{zz}$ and $V_{ij} = 0$, which means the quadrupole interaction vanishes due to equation 2.27. Also, only charges external from the nucleus contribute to the EFG. The traceless EFG tensor is also the reason for averaging of the quadrupole interaction in liquids due to rapid molecular tumbling (see e.g. [50]).

However, the representation of the quadrupole Hamiltonian (equation 2.31) might differ slightly in the following chapters (see equations 3.3 and 4.1a) as it is often necessary to express the Hamiltonian in a non-principal (arbitrary) set of axis relative to a reference frame. This requires rotating the coordinate system using Wigner-matrix elements, which is more conveniently done by using raising and lowering angular momentum operators and writing $\widehat{H}_Q$ in terms of the sum of irreducible tensor products. Also, raising and lowering operators provide useful quantum mechanical selection rules.

Electric field gradient and quadrupole coupling constant

Due to the proportionality of Q_{cc} to the electron distribution $\rho(\mathbf{x})$, no other spectroscopic method (besides microwave spectroscopy) gives such a direct access to chemical bonding as NQR spectroscopy. The variation of the electric field is related to the molecular electronic structure which connects Q_{cc} with structural information of the compound under observation. Provided the quadrupole moment Q of the nucleus is known, the quantity eq, which is related to the EFG, can be derived from experiments and compared with theoretical models. However, exact values of Q are not always available or afflicted with errors. A catalogue is given e.g. by Raghavan [51] and Stone [52]. For the particular case of ^{209}Bi the work of Teodoro and Haiduke [53] presents a calculation of Q as well as summarizes earlier results.

However, the contribution of the EFG (eq in Q_{cc}) can be computed from the charge distribution surrounding the nucleus of interest. The EFG depends on the second derivatives V_{ij} of the potential V which arises from external charges of surrounding electrons and nuclei. From the preceding derivation of the quadrupole Hamiltonian it is known that in the PAS computation of V_{zz} is sufficient. A charge e at a point $\mathbf{x}$ produces a component V_{zz} of the EFG of

$$\begin{aligned} V_{zz} &= e\frac{3z^2 - r^2}{r^5} \\ r^2 &= x^2 + y^2 + z^2 \end{aligned} \tag{2.32}$$

where r is the distance from the origin. In spherical coordinates one gets:

$$V_{zz} = e\frac{3cos^2(\theta) - 1}{r^3} \tag{2.33}$$

From the $1/r^3$ dependence of equation 2.33 it is clear that charges close to the nucleus are most important. This means, that in principle electrons belonging to the atom containing the nucleus should contribute most. This is, however, not true for closed shells where the charge distribution is spherically symmetric. In that case, no quadrupole coupling occurs. Important contributions come from single p-electrons, as calculated e.g. in [48]

$$V_{zz} = -e\frac{4}{15}\overline{\left(\frac{1}{r^3}\right)} \tag{2.34}$$

where $\overline{\left(\frac{1}{r^3}\right)}$ is the average over the p-orbit. Relation 2.34 implies that large Z-atoms ($r \sim \frac{1}{Z}$) will have large field gradients which is confirmed by numerous observations.

For deriving the total electric field gradient arising in a molecule at the nucleus of interest, one must consider the charge density $\rho(\mathbf{x})$ instead of a point charge and integrate equation 2.33 over the whole volume $\partial^3\mathbf{x}$. Also, in quantum mechanical terms $\rho(\mathbf{x})$ is replaced by the use of wave functions $\psi^*\psi$. Additionally, contributions

from external nuclei and electrons are separated and one arrives at [54]:

$$eq = V_{zz} = -e \int \psi^* \left(\frac{3cos^2(\theta) - 1}{r^3} \right) \psi \partial^3 \mathbf{x} + \sum_i Z_i e \left(\frac{3cos^2(\theta_i) - 1}{R_i^3} \right) , \qquad (2.35)$$

where the index i goes over all nuclei in the molecule, treated as point charges. The first therm in equation 2.35 is related to the *electronic* structure of the molecule, whereas the second term is related to the *geometry* only and can be calculated straight forwardly (including averaging over vibrational states might be necessary). From this equation it becomes clear, that any structural change of the compound affecting its electronic structure due to e.g. phase transition, ligand exchange, different lattice site or another alteration, will be visible in NQR spectroscopy. This is why one can speak of a unique "fingerprint" in terms of NQR frequencies for each NQR active compound in a particular state at a particular temperature.

Calculation of the electronic part requires exact knowledge of the atomic and molecular wave functions which still can be a very hard problem to tackle, depending on the system under observation. Roughly, three branches can be distinguished: Molecular crystals, ionic and metallic materials.

For this reason, approximate methods have been used from the early days of NQR spectroscopy, where more familiar chemical parameter as orbital populations, bond hybridization and ionic character are used. Pioneer work on the calculation of EFG's was conducted by Townes and Dailey [55] and are also addressed in [54].

Very often one is only interested in relative changes of Q_{cc} when a compound changes slightly from one situation to another, e.g. due to phase transitions or ligand substitution. Also bond character within similar compounds might be of interest. Weiss and Wigand [56] have studied correlations of NQR parameter and chemical bond parameters as e.g. ionic character, ionicity, electronegativity, bond length and angles.

Modern ab initio quantum chemistry (QC) methods enable the calculation of the electronic charge distribution of a molecular system [57, 58] from which molecular properties, as e.g. the EFG can be derived. QC typically uses the Hartree-Fock method for overcoming the many body problem and solving the Schrödinger equation in combination with the density functional theory (DFT) for treating electron correlations correctly to determine the electronic structure of chemical compounds. However, exact knowledge of appropriate basis sets describing atomic and molecular orbitals are of importance, which can become problematic for high Z atoms. Also, relativistic effects might start to play a role for larger atoms. Of course, also the geometry of the compound should be known as exactly as possible which can be found either by experimental or theoretical optimization methods or both.

There are numerous QC packages available, as e.g. Gaussian, Quantum Espresso, CASTEP, Wien2K, to only mention a few; all of which offering strength and weaknesses for particular applications. Most of them are quite user friendly an

it is not necessary to reconcile all mathematical details or computational methods (but of course understanding of the methods is required for interpretation of the outcomes). Even though computational power is quite impressive nowadays, enabling for accurate results in reasonable time, finding the adequate functional, basis set and corrections for the particular system can become quite cumbersome and requires special expertise in computational chemistry as well as experience. A sophisticated QC study for the calculation of the EFG at the Bi-site of triphenylbismuth will be presented in chapter 3.

Variation of Q_{cc} is very large. Not only the EFGs can be quite different from system to system, also the quadrupole moments (measured in barns, 1 b = 10^{-28} m^2) of the resonant nuclei can differ by several orders. For example, in the quite extensive NQR spectroscopy of the $I = 1$ nucleus ^{14}N (contained in many drugs, medicines or explosives), transition frequencies below 1 MHz down to just a few kHz are observed [59] [60]. In contrast, transition frequencies much beyond 100 MHz are found in high mass, high spin nuclei as e.g. ^{209}Bi or ^{121}Sb and ^{123}Sb [61, 62]. A quite large collection of chemical compounds and the NQR parameters of the contained quadrupole nuclei is given in the Landolt-Börnstein catalogue [63].

2.1.1 The NQR spectrum

Pure quadrupole transition frequencies

Energy levels E_m of the pure quadrupole spin system can be found by calculating the matrix elements of $\widehat{H}_Q$ with respect to quantum states described by a complete set of orthonormal wave functions. An appropriate base is the Zeeman basis $\{|Im\rangle\}$ obeying commutation relations and eigenvalue equations with respect to components of the angular momentum operator $\widehat{\mathbf{I}}$ as already presented in equations 2.11 and 2.12. Additionally, recalling

$$\begin{aligned} \langle I'm'|Im\rangle &= \delta_{mm'}\delta_{II'} \\ \sum |Im\rangle\langle Im| &= 1 \end{aligned} \tag{2.36}$$

holds. A diagonal matrix representation of the Hamiltonian $\widehat{H}_Q$ contains the wanted energy levels

$$\langle Im|\widehat{H}_Q|Im\rangle = E_m \, . \tag{2.37}$$

In case of half-integer spins, the $I + 1/2$ energy levels are doubly degenerate in m, reflecting the symmetry of the quadrupole Hamiltonian. For integer spins, the degeneracy is broken and an odd number of energy levels evolves giving I doubly degenerate levels and one non degenerate level.

For an axially symmetric EFG ($\eta = 0$) $\widehat{H}_Q$ is diagonal with respect to $\{|Im\rangle\}$ and one can easily derive:

$$E_m = \frac{Q_{cc}}{4I(2I-1)}\left(3m^2 - I(I+1)\right) \tag{2.38}$$

Experimentally, transitions between energy levels are usually induced by the application of a short but powerful pulse of an oscillating magnetic field in the radio-frequency (RF) regime produced by a solenoid coil. This can be described by the time dependent operator

$$\widehat{H}_{RF}(t) = -\hbar B_{RF}\gamma \widehat{I}_{\mathbf{x_{RF}}} cos(\omega_{RF}t + \phi) \ , \tag{2.39}$$

where $\mathbf{x_{RF}}$ is the direction of the RF field in the laboratory frame, γ is the gyromagnetic ratio of the nucleus, $\omega_{RF} = 2\pi\nu_{RF}$ is the angular frequency of the magnetic AC field with an amplitude B_{RF} and phase ϕ_{RF}. The pulse represents a time dependent perturbation of the spin system coupling with the magnetic moment of the nucleus which allows for $\Delta m = 0$ and $\Delta m = \pm 1$ transitions only. Thus, observable signals emerge at frequencies $\nu_Q = E_{m+1} - E_m$.

$$\nu_{Q,m,m\pm1} = \frac{3Q_{cc}}{4I(2I-1)}|(2m \pm 1)| \tag{2.40}$$

However, for the general case of $\eta \neq 0$ this selection rule becomes weak as due to the required diagonalization of $\widehat{H}_Q$ there is a mixing between $\Delta m = \pm 2$ Zeeman states. Analytical approximations for this purpose are available, however, diagonalization is most conveniently done by numerical methods, e.g. provided by MATLAB®. The plot in figure 2.1 illustrates the behaviour of pure quadrupole spin transitions for a nuclear spin number I=9/2 depending on η for $Q_{cc} = 668$ MHz. The effect of $\eta \neq 0$ is, that the transitions are not equidistantly separated any more. The color code indicates the Boltzmann-weighted transition probability

$$W_{mm'} = |\langle Im|\widehat{H}_{RF}|Im'\rangle|^2 \tag{2.41}$$

of spins in a powder sample (300 K) under the action of the perturbation H_{RF} (as introduced in equation 4.5) and multiplied by the population difference according to the Boltzmann distribution. The labelling of the transitions in figure 2.1 denotes the involved states in case of $\eta = 0$. For non-zero η, the states are mixed and the selection rule $\Delta m = 1$ becomes weak and so also double quantum coherences can appear.

Typically, experimentalists are interested in the calculation of the compound specific and temperature dependent NQR parameters Q_{cc} and η from measurements of the pure NQR transition frequencies ν_Q. This can be done when at least two transitions at a particular sample temperature have been determined and assigned (as performed e.g. in chapter 3). For the case $I = 3/2$, however, only one transition is available which requires the application of an external magnetic field or the use of 2D nutation spectroscopy [64] to enable the determination of Q_{cc} and η.

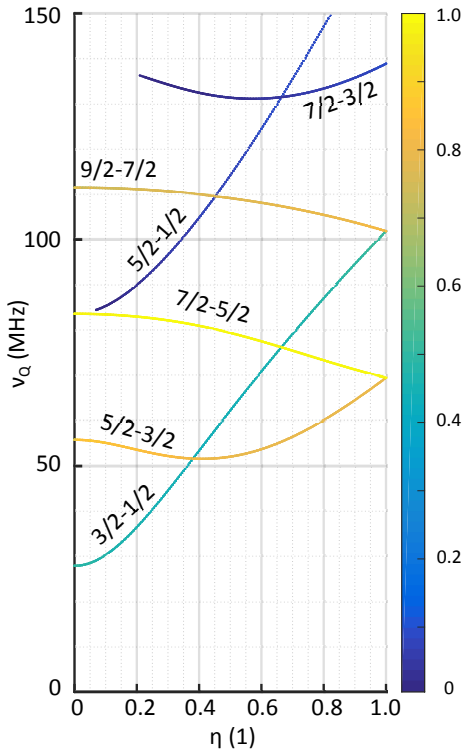

FIGURE 2.1: Plot of ν_Q versus η for a $I = 9/2$ nucleus with an arbitrary $Q_{cc} = 668$ MHz for a powder sample at 300 K. The color indicates the theoretical transition probability with respect to $\widehat{I}_x$ (equation 2.41), multiplied by the population difference according to the Boltzmann distribution and normalized to the maximum value. The labelling of the transitions denotes the involved states in case of $\eta = 0$.

Line broadening and peak shape

As in any spectroscopic method, one expects a certain shape and broadening of the observed resonances which contain valuable information for e.g. materials science, provided their origin can be explained. It is possible to discriminate between static and dynamic contributions to line broadening, depending on its source. Also, homogeneous and inhomogeneous broadening effects can be distinguished if either all nuclei are affected equally or differently. An early review is given in [42] which shall only be summarized briefly here. Also in [65] some aspects are discussed.

The most obvious static contribution to the linewidth are crystal imperfections, leading to a certain distribution of EFGs in the sample from crystal site to crystal site. Sources of this inhomogeneous broadening are impurities, lattice defects and even small temperature gradients across the sample. The resulting randomly distributed EFG variations are inhomogeneous and typically described by a Gaussian distribution.

Also of static nature, but homogeneous, are magnetic interactions between neighbouring nuclei. There is the direct magnetic dipole-dipole interaction between the resonant nucleus and neighbouring nuclei. Also, there is the indirect spin-spin interaction (also called J-coupling) transferred through bonding electrons. These effects can generate hyperfine splitting of the spectra of the resonant nuclei or lead to a line broadening, when the distance between the nuclei is not very close. However, these effects are not in the focus of this work.

Dynamic broadening of the transitions results from the finite lifetime of excited states during excitation and subsequent relaxation of the spin system. The sources for spin relaxation are molecular and lattice dynamics producing fluctuations of the EFG at certain frequencies. These fluctuations can induce transitions between energy levels and thus redistribute the spin population to the equilibrium distribution upon excitation. The line broadening is inversely proportional to the relaxation time which means that fast relaxing (T_2) systems show a broader peak shape. In case of mono exponential decay, the shape will be Lorentzian. This issue is discussed in more detail in chapter 5.

The contributions of each influence to the total linewidth can vary quite strongly when comparing different systems. Typically, for molecular crystals one observes linewidths from below 1 kHz up to several 10 kHz. For example, in high quality crystals, static broadening might play a minor role and broadening is predominantly due to finite lifetime of the excited states and so the lineshape will be Lorentzian. However, also relaxation times do vary a lot (ms to μs), and so also here quite different values are observed. Both linewidth and shape depend very much on the system under investigation and especially the linewidht can be quite sensitive. It is therefore important to have a close look on all possible nuclear interactions and the molecular dynamics of the sample to interpret the lineshape in a reasonable manner. Particular experimental methods (as e.g. different pulse sequences, high resolution

measurements, measurement of the relaxation times, thermostatisation) and careful sample preparation can help to analyse data and apply theoretical models.

Excitation and free magnetic induction decay

The formation of a free magnetic induction decay upon resonant excitation of a quadrupole spin ensemble under the action of a radio frequency (RF) pulse is recapitulated briefly. Using a pulse type spectrometer is not the only possibility to access NQR transitions but by far the most popular one and it also has been used to gather data presented in the following chapters.

One of the earliest descriptions is given by Bloom *et al.* (1955) [66]. Ever since the first descriptions of the NQR theory, comparisons to NMR pulse excitation are drawn. This is, however, a tricky task as the origins of the interactions are quite different. NMR relies on a *magnetic* interaction of the nuclear dipole moment of the nucleus and an external magnetic field, whereas NQR relies on an *electric* interaction of the nuclear quadrupole moment with its surrounding EFG. The similarity arises due to the excitation, which is in both cases coupling of an alternating magnetic field with the magnetic dipole of the nucleus able to manipulate nuclear spin states. Already in [66], the similarity of the solutions for NQR to the two level Zeeman case (as in NMR) is pointed out.

Three different ways to derive an equation for the signal induced in a coil after a single pulse will be sketched briefly in the following paragraphs. The first one (1) follows [66], and uses time dependent perturbation theory to solve the Schrödinger equation for the total Hamiltonian for a I=3/2 spin ensemble with symmetric field gradient (η=0). The second route (2) follows the more recent work of Cordier *et al.* (2005) [67], who applied density matrix theory to derive a signal equation for a I=1 spin system, also for η=0. The third route (3) follows a numerical approach according to Possa *et al.* [68].

In all approaches, the RF-pulse Hamiltonian $\widehat{H}_{RF}$ (see equation 4.5) is treated as a time dependent perturbation of the much larger static (time independent) quadrupole Hamiltonian $\widehat{H}_Q$ (see equation 2.31):

$$\widehat{H}_Q \gg \widehat{H}_{RF} \, . \tag{2.42}$$

This condition is of importance to be able to apply time dependent perturbation theory [69] and for several simplifications applied in the following derivations.

(1) Bloom *et al.* (1955) [66] In time dependent perturbation theory, the Schrödinger equation

$$ih\frac{\partial \psi}{\partial t} = \widehat{H}_{tot} \tag{2.43}$$

is solved for the total Hamiltonian

$$\widehat{H}_{tot}(t) = \widehat{H}_Q + \widehat{H}_{RF}(t) \tag{2.44}$$

for a linearly polarized RF pulse $\widehat{H}_{RF}(t)$ (equation 4.5 in x-direction). Use is then made of the Ansatz for the wave function ψ

$$\psi = \sum_{m=-3/2}^{m=3/2} C_m(t)\phi_m e^{-i(E_m/\hbar)t} , \tag{2.45}$$

where ϕ_m are the eigenfunctions of the time independent Schrödinger equation $\widehat{H}_Q\phi_m = E_m\phi_m$. $C_m(t)$ are time dependent coefficients which are determined by substituting equation 2.45 into 2.43 leading to a set of differential equations for $C_m(t)$. Use is then made of the near-resonance conditions in angular frequencies $\omega = 2\pi\nu$:

$$\omega_{RF} \approx \omega_Q \tag{2.46}$$

Next step is to evaluate the expectation value of $\widehat{I}_x$ which is proportional to the nuclear magnetization in the xy plane which produces the free induction signal.

$$\langle\widehat{I}_x\rangle = \langle\psi^*|\widehat{I}_+|\psi\rangle = (\sqrt{3}/2)sin(\sqrt{3}\omega_1 t_w)sin(\omega_0(t-t_w)) \tag{2.47}$$

where t_w is the pulse length, $\omega_1 = \gamma B_{RF}$ represents the strength of the rf-field with amplitude B_{RF} and the quantity $\sqrt{3}\omega_1 t_w = \beta$ is the flip angle through which the magnetization is rotated from the equilibrium. $\langle\widehat{I}_y\rangle$ and $\langle\widehat{I}_z\rangle$ are zero in case of linear polarized excitation. This result is identical for all quadrupole transitions and differs only in multiplicative constants.

The signal S for a single pulse applied for a duration t_w, taking into account a powder sample with randomly oriented EFGs at an angle θ with respect to the coil as well as the induction law, reads as

$$S \sim \int_0^\pi sin^2\theta sin\left(\sqrt{3}\omega_1 t_w sin(\theta)\right)\partial\theta \tag{2.48}$$

In the later work of Weber and Hahn [70] (1960), the treatment is expanded to circularly polarized RF-pulses, consecutive double pulses and the application of a small external magnetic field.

(2) Cordier *et al.* (2005) [67] A similar result is gained for I=1 but also for $\eta = 0$ in [67], derived via a different route. Starting point is the Liouville von Neumann equation

$$\frac{d\rho}{dt} = i\left[\rho, \widehat{H}_{tot}\right] \tag{2.49}$$

where ρ is the spin density operator. After a rotating frame transformation, similar to the procedure used in NMR, using

$$T = exp(i\omega_{RF}\widehat{I}_z t) \tag{2.50}$$

and the decomposition of the RF-Hamiltonian into two counter rotating terms with half amplitude, an effective total Hamiltonian is found which reads as:

$$\widehat{H}_{eff} = \widehat{H}_Q + \omega_{RF}\widehat{I}_z - \frac{\omega_1}{\sqrt{2}}\widehat{I}_x \ . \tag{2.51}$$

The spin density after the pulse (ap) of length t_w is then found via the equation

$$\rho_{ap} = exp(-i\widehat{H}_{eff}t_w)\rho_{eq}exp(i\widehat{H}_{eff}t_w) \tag{2.52}$$

using the equilibrium spin density ρ_{eq}. After finding a proper basis for a spin $I = 1$ ensemble and expressing ρ_{ap} in matrix representation, use is made of the resonance conditions in equation 2.46. Then, the quantity

$$\langle\widehat{I}_+\rangle = Tr(\rho\widehat{I}_+) \tag{2.53}$$

leads to

$$\langle\widehat{I}_+\rangle = (\omega_0/\sqrt{2})sin(\omega_1 t_w) \tag{2.54}$$

which is the same form as equation 2.47 from above (in the rotating frame). Again, considering averaging over a powder (micro-crystallites with EFG angle θ with respect to the coil) and the induction law, the signal S can be found

$$S \sim \int_0^\pi sin^2\theta sin\left(\omega_1 t_w sin(\theta)\right)\partial\theta \ , \tag{2.55}$$

which differs from equation 2.48 only by a multiplicative factor. This approach is generalized to arbitrary η and spin number in [71].

Physically, the results can be interpreted as a macroscopic oscillating nuclear magnetization along the x axis. Also, the equations are of the same form as for the NMR case except from different flip angles. In [67], it is shown that the NQR flip angle equals the NMR flip angle times a factor of 2. This is due to the fact, that in NMR, $\widehat{I}_z$ is involved in the Hamiltonian, whereas it is $\widehat{I}_z^2$ in the NQR case. The consequence is, that in NQR both oscillation directions of the RF field from the coil contribute to the spin flip (rotation of $\widehat{I}_z^2$), whereas in NMR only one rotation direction is active. A quite similar explanation is given in [66] by using a quasi classical vector model. However, these simple pictures only apply when assuming a symmetric EFG with $\eta = 0$ and no external magnetic field applied. For the more complicated cases one has to trust on the straightforwardly applied equations and the entries in the density matrix.

The description and application of more complicated sequences than a single pulse are given in the literature [42, 72, 73, 74] and follow, in principle, the strategies presented above.

(3) Possa *et al.* (2011) [68] As a third possibility, the work of Possa *et al.* is mentioned here, where a numerical approach is presented. It is universally applicable to different spin numbers, pulse sequences and it is possible to include an external magnetic field. The procedure is based on finding a solution for the spin density operator using the interaction picture and the average Hamiltonian theory [75]. The software, implemented in *Mathematica*, is available freely and can be accessed via a link which can be found in [68]. The software also allows for implementing circularly polarized RF excitation field which are of importance for solid state quantum computing using NQR.

Remarks on the interpretation of signal formation

It is worth mentioning that signal formation in NQR is, for good reasons, often compared to signal formation in NMR, as both can be described by a quantum mechanical two level system. The excitation techniques (pulse sequences) applied in both methods are indeed quite similar and theory shows that also the signal equations are similar- at least for the simplest cases (NQR: axial symmetric field gradient, no external field applied, well separated transitions; NMR: the Bloch equations). However, the visually comfortable, simple and widespread magnetization vector model used in many NMR and MRI introductions is, under a critical look, not satisfying for several applications and sometimes leading to misconceptions. Already the formation of a simple $\pi/2$ pulse rises contradictions when viewed in the vector model and being compared with quantum mechanical laws. Are there really just two possible directions (up and down) of the magnetization? How is it possible to transfer half a quantum? Is there really something like a transition, a sudden quantum jump, as in photon emission, happening? There are several reasons for the misconceptions. Sometimes, the behaviour of a single spin is confused with the behaviour of an ensemble. Also, classical and quantum mechanical explanations and pictures are mixed. Both of them give valuable explanations and for the simplest cases, the classical description is completely sufficient and still must form the fundamental basis of physical understanding (just because, our human perception is set, predominantly, classical).

For a quantum mechanical treatment, an alternative can be the "balls and arrows" explanation, as given in the book of Malcolm Levitt [72], visualizing populations and coherences in the density operator formalism. "Mathematical minds" might be completely happy with the entries of the spin density matrix and do not need any pictures at all [76].

In a very interesting book from 2015, edited by Csaba Szántay, Jr. [77], a clarifying discussion of the classical and quantum mechanical nuclear magnetic resonance phenomena is started, trying to reconcile and straighten misconceptions in visual and narrative explanations.

As one example, the appearance of a quantum state after a $\pi/2$ pulse shall be considered closer. Lets consider a general, arbitrary quantum state $|\psi\rangle$ of the two-level $I = 1/2$ Zeeman spin system expressed by the two eigenstates $\mid 1/2 \rangle$ and $\mid -1/2 \rangle$ associated with the measurement of the spin component in z-direction:

$$|\psi\rangle = a|1/2\rangle + b|-1/2\rangle \tag{2.56}$$

The weighting coefficients of this superposition of eigenstates a and b fulfil $\mid a \mid^2 + \mid b \mid^2 = 1$, as the probabilities of finding one of the eigenstates must sum to 1. An analogue formulation, quite similar to the description of a classical spin, is

$$|\theta, \phi\rangle = cos(\theta/2)|1/2\rangle + sin(\theta/2)|-1/2\rangle exp(i\phi) \ , \tag{2.57}$$

where the polar angle θ reflects the amplitude of the up and down states and the azimuthal angle ϕ their phase difference. While the phase of a single state is without physical relevance, the phase difference in a superposition matters. Expression 2.57 is the so-called Bloch vector which can be defined for any quantum mechanical two-level system. In the NMR case, this Bloch vector is proportional to the magnetic moment in 3-D space. A transversal magnetization along the x-axis at time t=0 right after excitation can be expressed by setting e.g. $\theta = 90^\circ$ and $\phi = 0^\circ$:

$$|\psi(t=0)\rangle = |\theta = 90^\circ, \phi = 0^\circ\rangle = cos(90^\circ/2)|1/2\rangle + sin(90^\circ/2)|-1/2\rangle \ . \tag{2.58}$$

This is a weighted sum of energy eigenstates, also called stationary states. Stationary states $|\psi_E\rangle$ have a well defined energy and the property of not evolving into any other state in time, as long as the interaction does not change. Their time dependence is only a linear phase evolution at the rate of their definite energy E

$$|\psi_E(t)\rangle = exp(-iEt/\hbar)|\psi_E(t=0)\rangle \ . \tag{2.59}$$

If one is now interested in the time evolution of the transversal state in 2.58, it is necessary to apply equation 2.59 to each term in equation 2.58. The result is

$$|\psi(t)\rangle = cos(90^\circ/2)|1/2\rangle + sin(90^\circ/2)|-1/2\rangle exp(-i\omega_0 t) = |\theta = 90^\circ, \phi = \omega_0 t\rangle \tag{2.60}$$

where $\omega_0 = E_{1/2} - E_{-1/2}$ is the energy difference of the two eigenstates representing the precession frequency of the phase. This result is quite interesting, as it shows that the signal detected in an NMR or NQR signal upon an 90° excitation is nothing but the phase evolution of a superposition of eigenstates of the involved energy levels. Therefore, the term *transition*, commonly used for the phenomenon which is borrowed from photon emission, is in fact misleading, as no quantum jump or transition is involved in the detection process. Despite that finding, throughout this work the term "transition" is used, as it is the common expression in the literature and has some practical advantages and carries elements of truth. There is indeed

a statistical redistribution of the single spins in the ensemble, but what is being measured is the oscillating coherence of two stationary energy levels.

Finally, the book of K. Blum [76] on density matrix theory is recommended, where the concept of coherent superposition and its connection with signal formation is described in general for two-level quantum systems ("quantum beats"). Excitation as well as relaxation of quantum systems is demonstrated and discussed by the help of density matrix theory in a detailed and understandable way; besides others, examples from magnetic resonance phenomena are given.

2.1.2 Applications of NQRS

Since its first theoretical description and experimental observation, NQR has inspired numerous ideas and possibilities for applications in different fields. Here, without any deeper treatment, some of these shall be mentioned and references are given. The essence of most of the applications is the outstanding sensitivity of the EFG on the electronic environment created by the molecular structure of the sample under investigation. Molecular or structural changes can be detected quite easily and compounds have an individual NQR "fingerprint", reflected by the frequency position of the observable spin transitions. However, there are several limitations:

- NQRS is applicable only to solid state samples (compare e.g. [78]).
- Only nuclei with a spin number $I > 1/2$ are detectable.
- Crystal symmetry (octahedral molecular configuration) can lead to zero EFG (e.g. BiF_3 [79]).
- Rather weak signal strength and thus need for averaging many measurement cycles.
- Problems for the hardware can arise from the very broad frequency range of occurring transition frequencies (Hz to MHz). This requires the development of spectrometers covering wide fr-bands by the use of resonator circuits (which are narrow-band).
- Possibility of tricky constellations of relaxation times: Long T_1 times require long measurement times (besides the need for averaging). Short T_2 can become a problem due to ring-down effects from the transmit (excitation) circuit.

Still, many creative applications have been developed. A (by far not complete) list of references is given below:

- Identification of pharmaceuticals and drugs: [80] [59] [81] [82]
- Detection of explosives: [82] [80] [83] [60] [84]
- Mining industry: [85] [86] [87]

- Material science, crystallography, polymorphism: [56] [88] [89] [90] [91] [92]
- Quantum computing: [68]
- Atomic clock: [93]
- MRI contrast agent: [61]
- Molecular dynamics: [94]
- Temperature sensor: [95]

2.2 Theory of spin relaxation

Theories for explaining spin relaxation phenomena in magnetic resonance have gone through several steps of extensions and refinements since the first formulation by F. Bloch in 1946 [2]. A first development was contributed by Bloembergen, Purcell and Pound [18], who connected transition rates between energy levels with spectral densities of field fluctuations. The next big step was the use of the density matrix by Wangsness and Bloch [96]. The theory used in this thesis goes back to A. G. Redfield[1] (1965) [97], which is presented also in [48]. A compact review on the results, conclusions and the derivation of the theory is given in a quite recent article (2007)- compared to the first formulation- by the same author [98].

Before introducing the fundamental equations of relaxation theory, it makes sense to start with some general comments about relaxation processes and how thermal equilibrium of an open quantum system in contact with the classically treated surrounding (lattice) is established. In the sense of thermodynamics relaxation is an irreversible process, meaning that the entropy of the total coupled system increases during relaxation. This fact is somewhat problematic, as the quantum mechanical equations of motions (Schrödinger and Liouville equation) - used to describe spin dynamics - are strictly reversible. Therefore, relaxation must be treated as a phenomenon of an ensemble of spins, which differs from the behaviour of a single spin. In the derivation of the master equation (see section 2.2.1), the treatment of this issue will be mentioned.

First, the definition of the thermal equilibrium and the driving force of relaxation in terms of the concept of statistical *microstates* and *macrostates* shall be discussed [2]. Lets start by assuming an ensemble of a large number of N spins μ_1, μ_2,...μ_N occupying N different available states (corresponding to cells) in the following manner: spin 1 can be in cell 1, spin 2 in cell 2, spin 3 in cell 3: $\{\mu_1, \mu_2, \mu_3, ...\}$. This would be one possible configuration- or *microstate*- defining the current state of the system. Another possibility would be $\{\mu_3, \mu_1, \mu_2, ...\}$, which is essentially the same microstate, as the spins are indistinguishable. A different microstate would be $\{\mu_1\mu_2, , \mu_3, ...\}$, where the first cell contains two spins, but the second one none. "Equal" microstates form a macrostate. For a macrostate, the only thing that matters is how many spins are in a certain cell, but not which ones. If one now considers a system where the spins are randomly distributed in time over the cells which are all equally probable, it is easy to realize that some macrostates are compatible with a higher number of microstates than others. If, for example, we consider only 4 spins, the number of configurations Ω of each cell occupied by one spin is $4! = 24$. But there is only one microstate for the macrostate of having all 4 spins in the first cell. A general statement is thus; *the probability of finding a certain macrostate is proportional to*

[1] You may consider the obituary for Alfred G. Redfield, who passed away on July 24, 2019.
[2] The discussion in this paragraph has been extracted from [77].

the number of microstates accessible to that macrostate. The same considerations apply to the lattice, only that there is a much higher number of available states. Further, both for the lattice as well as for the spin system, a Maxwell-Boltzmann distribution is assumed for the number of microstates associated with a distinct energy.[3] The difference is only that there are much more degrees of freedom of the lattice than of the spin system, which leads to a narrower distribution in case of the lattice.

The next issue to consider is the energy of the total, combined system E_{total},

$$E_{total} = \sum E_{\mu}^{pot} + \sum E_{mol}^{kin} \; . \tag{2.61}$$

Here, $\sum E_{\mu}^{pot}$ is the energy of the spin ensemble and $\sum E_{mol}^{kin}$ is the energy of the lattice, made up of the kinetic energy of the molecules. The following applies: (1) the total energy is conserved, (2) spin ensemble and lattice can exchange energy, (3) coupling between the systems is weak and, (4) the lattice has much more degrees of freedom and is much larger than the spin ensemble, so that the lattice remains unchanged no matter how much energy is flowing into or out of the lattice (heat reservoir). Energy transfer is made possible by fluctuating fields $f(t)$

$$\sum E_{\mu}^{pot} \quad \overset{\text{f(t)}}{\longleftrightarrow} \quad \sum E_{mol}^{kin} \; , \tag{2.62}$$

which corresponds to spin-lattice relaxation. The phenomenon of energy transfer only within the spin system is called spin-spin relaxation.

Important is now, that the energy defines the number of available states: The probability of finding the spin ensemble to have the energy $\sum E_{\mu}^{pot}$ is proportional to the number of microstates of the combined system $\Omega_{total}(\sum E_{\mu}^{pot})$. This is a consequence of the principle of *a priori* probabilities that at equilibrium all accessible microstates of the combined system are equally likely. If the spin system has energy $\sum E_{\mu}^{pot}$, it can be in any of its own $\Omega_{spin}(\sum E_{\mu}^{pot})$ microstates. At the same time, the lattice has energy $\sum E_{mol}^{kin} = E_{total} - \sum E_{\mu}^{pot}$ and can be in $\Omega_{lattice}(\sum E_{mol}^{kin})$ microstates. Also, any microstate of the spin system can be combined with every microstate of the lattice. Together, the total number of microstates Ω_{total} compatible with the spin ensemble at energy $\sum E_{\mu}^{pot}$ is

$$\Omega_{total}(\sum E_{\mu}^{pot}) = \Omega_{spin}(\sum E_{\mu}^{pot})\Omega_{lattice}(\sum E_{mol}^{kin}) \; . \tag{2.63}$$

The probability $P(\sum E_{\mu}^{pot})$ of the spin ensemble having energy $\sum E_{\mu}^{pot}$ is proportional to the result of equation 2.63:

$$P(\sum E_{\mu}^{pot}) \sim \Omega_{spin}(\sum E_{\mu}^{pot})\Omega_{lattice}(\sum E_{mol}^{kin}) \; . \tag{2.64}$$

A simple practical example shall illustrate the consequence of this finding. Lets assume a total energy of the system of 10, able to change only in units of 1 among the

[3] Which is only valid for an ideal gas, but the exact shape of this distribution is not of importance here

two systems *spin* and *lattice*. Also, with the energy, a certain number of states Ω is connected. Writing $[(10), 200]_{spin}$ means, that the spin system has energy 10 and is connected with 200 possible microstates. Accordingly, the same accounts for the lattice, where only the number of states is typically much higher. Following equation 2.63, it is possible to write down a fictitious example using very low (and arbitrary) numbers of possible microstates:

$$\begin{aligned}
[(0), 24]_{spin}[(10), 200]_{lattice} &\rightarrow [(10), 4800]_{total} \\
[(-1), 18]_{spin}[(11), 800]_{lattice} &\rightarrow [(10), 14400]_{total} \\
[(-2), 12]_{spin}[(12), 1600]_{lattice} &\rightarrow [(10), 19200]_{total} \\
[(-3), 8]_{spin}[(13), 5000]_{lattice} &\rightarrow [(10), 40000]_{total} \\
[(-4), 3]_{spin}[(14), 9500]_{lattice} &\rightarrow [(10), 28500]_{total}
\end{aligned}$$

Obviously, the most probable macrostate is realised for line 4, where the energy of the spin state is not the lowest, but the number of microstates is the highest of all cases. This means that the equilibrium macrostate of our ensemble has energy (-3). For a system out of equilibrium, the function 2.63 reacts quite sensitive: When the spin system lowers the energy only by a small amount, the number of available microstates will decrease very fast, as it depends on the number of degrees of freedom. As a reaction, the energy of the lattice is raised via the weak coupling (see equation 2.62) and the number of lattice microstates will increase even faster. The result is, that the probability in equation 2.64 has a quite sharp maximum, defining the equilibrium for a certain temperature.

In statistical thermodynamics, the system described above corresponds to a *Canonical ensemble*. A thermodynamic quantity connected with the number of microstates is the Gibbs entropy S:

$$S = -k_B \sum_i p_i \, ln(p_i) \tag{2.65}$$

where k_B is the Boltzmann constant and p_i is the probability of finding the microstate p_i. Irreversible processes, as will be treated here, always increase the entropy of the total system. The driving force of relaxation is thus maximising entropy, not lowering the total energy.

As a result of statistical thermodynamics [99], the thermal equilibrium of the quantum mechanical density operator for a Canonical ensemble can be written as

$$\rho_{eq} = \frac{e^{-\widehat{H}/k_B T}}{tr\left(e^{-\widehat{H}/k_B T}\right)} \, . \tag{2.66}$$

The two main conclusion from the considerations in this section are: (1) Irreversibility must be taken into account in relaxation theory by treating spin ensembles rather than single spins. (2) The thermal equilibrium configuration at a certain temperature

is given by equation 2.66, because according to statistcal physics spins behave like a Canonical ensemble.

2.2.1 Redfield Theory

The theory[4] describes relaxation of an open quantum system S, made up of an ensemble of spins, which is in continuous contact with the lattice L. For such a system it makes sense to use the reduced density operator $\rho_S^*(t)$ [5] for the spin system instead of the density operator $\rho^*(t)$ of the complete system.

$$\rho_S^*(t) = tr_L \{\rho^*(t)\} \tag{2.67}$$

The notation $tr_L \{\}$ means that the trace considers elements diagonal in the lattice states only (averaging over the lattice degrees of freedom). This means, $\rho_S^*(t)$ contains information about the lattice from the viewpoint of the spin system only, and elements having no effect on observables of the spin system are not considered.

When the quantum system S is in a non-equilibrium state, it will gradually be transferred into its thermodynamic equilibrium driven by a weak coupling H_1, enabling energy exchange with the lattice. However, this has no effect on L, as the lattice is assumed to be very large, having many degrees of freedom and resting at constant temperature at all times. The consequence of this assumption is, that the time dependence of the total system $H_S + H_L + H_1$ can be described by a density matrix $\rho^*(t)$ written as a product of the lattice and spin density operators:

$$\rho^*(t) \longrightarrow \overline{\rho^*(t)} = \rho_S^*(t)\rho_L^*(0) \tag{2.68}$$

$H_1(t)$ is small and averages to zero over time. $\rho_L^*(0)$ stays constant for all times and thus S and L are uncorrelated. Also, $\rho_L^*(0) = \rho_{eq}$ applies (see equation 2.66). Equation 2.68 is the basic *condition of irreversibility*.

In consequence, equation 2.67 can be further simplified to

$$\rho_S(t)^* = tr_L \{\rho_S^*(t)\rho_L^*(0)\} \tag{2.69}$$

The below derivation follows mainly [48], where the master equation is developed at first for $\rho_S^*(t)$ considering only spin coordinates (ignoring the lattice density operator in the first place). In a final step, the derived equation for $\rho_S^*(t)$ will be corrected for the lattice influence. Care is taken when lattice operators appear explicitly (as for example in section 2.2.1).

The equation of motion of the spin density $\rho^*(t)$[6] for a large, time-independent Hamiltonian H_0, representing the spin system and a smaller time-dependent

[4] Derivation of the theory follows mostly [48] and [76].
[5] The star symbol * means, this quantity is the interaction frame representation.
[6] Further, the indices S in $\rho_S(t)$ is dropped

perturbation term H_1, representing the coupling to the lattice is

$$\frac{\partial \rho}{\partial t} = \frac{i}{\hbar}\left[\rho, H_0 + H_1(t)\right] \tag{2.70}$$

Rewriting this equation (the *Liouville von Neumann equation*) in the interaction picture by defining

$$\rho(t) = e^{-(i/\hbar)H_0 t}\rho^*(t)e^{(i/\hbar)H_0 t} \tag{2.71}$$

and substituting into the left side of equation 2.70 gives

$$\frac{\partial \rho^*}{\partial t} = \frac{i}{\hbar}\left[\rho^*, H_1^*(t)\right] \tag{2.72}$$

where $H_1^*(t) = e^{(i/\hbar)H_0 t}H_1(t)e^{-(i/\hbar)H_0 t}$.

Preceding integration of equation 2.70 from 0 to time t gives

$$\rho^*(t) = \rho^*(0) + \frac{i}{\hbar}\int_0^t \left[\rho^*(t'), H_1^*(t')\right] dt' \,. \tag{2.73}$$

Performing an iterative step by substitution of $\rho^*(t')$ in equation 2.73 one gets

$$\begin{aligned}\rho^*(t) &= \rho^*(0) + \frac{i}{\hbar}\int_0^t \left[\rho^*(0) + \frac{i}{\hbar}\int_0^{t'} \left[\rho^*(t''), H_1^*(t'')\right] dt'', H_1^*(t')\right] dt' \\ &= \rho^*(0) + \frac{i}{\hbar}\int_0^t \left[\rho^*(0), H_1^*(t')\right] dt' \\ &\quad + \left(\frac{i}{\hbar}\right)^2 \int_0^t \int_0^{t'} \left[\left[\rho^*(t''), H_1^*(t'')\right], H_1^*(t')\right] dt' dt'' \,,\end{aligned} \tag{2.74}$$

which is equivalent to second order perturbation theory. Finally, the derivative of 2.74 is

$$\frac{\partial \rho^*(t)}{\partial t} = \frac{i}{\hbar}\left[\rho^*(0), H_1^*(t)\right] + \left(\frac{i}{\hbar}\right)^2 \int_0^t \left[\left[\rho^*(t'), H_1^*(t')\right], H_1^*(t)\right] dt' \,. \tag{2.75}$$

The integral in equation 2.75 depends on $\rho^*(t')$, which means the behaviour of the system at time t depends on its past from $t' = 0$ until $t' = t$. However, the system S is damped with a characteristic damping constant γ due to its coupling to L. Also, we will later see that $H_1(t)$ acts in a way so that knowledge or memory of any past configuration of $H_1(t)$ is destroyed within a characteristic time τ_c. As one is typically interested in macroscopic timescales much larger than τ_c, the integral can be assumed to depend only on the present value of $\rho^*(t)$. One could also say the system has no memory of its past during time steps at which equation 2.75 is evaluated. This also means, that Redfield theory is only valid when the dynamics of $H_1(t)$, characterized by τ_c is much faster than a typical macroscopic decay of S, characterized by $\frac{1}{\gamma}$:

$$\tau_c \ll \frac{1}{\gamma} \tag{2.76}$$

This is the *Markoff approximation* which allows to replace $\rho^*(t')$ with $\rho^*(t)$ in equation 2.75:

$$\frac{\partial \rho^*(t)}{\partial t} = \frac{i}{\hbar}\left[\rho^*(0), H_1^*(t)\right] + \left(\frac{i}{\hbar}\right)^2 \int_0^t \left[\left[\rho^*(t), H_1^*(t')\right], H_1^*(t)\right] dt' \tag{2.77}$$

Equation 2.77 is the starting point of the derivation of Redfield theory. First, matrix elements of the first term are computed:

$$\langle\alpha|\left[\rho^*(0), H_1^*(t)\right]|\alpha'\rangle = \sum_\beta \langle\alpha|\rho^*(0)|\beta\rangle\langle\beta|H_1^*(t)|\alpha'\rangle - \langle\alpha|H_1^*(t)|\beta\rangle\langle\beta|\rho^*(0)|\alpha'\rangle \tag{2.78}$$

We now assume an ensemble of spins, where each element experiences a different coupling or perturbation $H_1(t)$ which sum up to zero. In contrast, an applied alternating field would act on every spin in an equivalent manner and thus is not vanishing upon averaging. As we are dealing with a stationary perturbation, an ensemble average is the same as a time average and we can write

$$\overline{\langle\alpha|H_1^*(t)|\beta\rangle} = 0\,, \tag{2.79}$$

where the bar indicates ensemble average. A consequence is, that $H_1(t)$ does not produce any frequency shift to the total Hamiltonian $H_0 + H_1(t)$. The first term in equation 2.77 thus vanishes for a spin ensemble and the second term must be computed.

Defining $\tau = t - t'$ and remembering that

$$\langle\alpha|H_1^*(t)|\beta\rangle = e^{i/h(E_\alpha - E_{\alpha'})t}\langle\alpha|H_1(t)|\beta\rangle \tag{2.80}$$

one can find for the second term of equation 2.77 by evaluating the double commutator

$$\begin{aligned}\frac{\partial \rho^*_{\alpha\alpha'}}{\partial t} = \frac{1}{\hbar^2}\sum_{\beta,\beta'}\int_0^t \big[\ &\langle\alpha|H_1(t-\tau)|\beta\rangle\langle\beta'|H_1(t)|\alpha'\rangle e^{-i/h(E_\alpha - E_\beta)\tau} e^{i/h(E_\alpha - E_\beta + E_{\beta'} - E_{\alpha'})t}\rho^*_{\beta\beta'} \\ &+ \langle\alpha|H_1(t)|\beta\rangle\langle\beta'|H_1(t-\tau)|\alpha'\rangle e^{-i/h(E_{\alpha'} - E_{\beta'})\tau} e^{i/h(E_\alpha - E_\beta + E_{\beta'} - E_{\alpha'})t}\rho^*_{\beta\beta'} \\ &- \rho^*_{\alpha\beta}\langle\beta|H_1(t-\tau)|\beta'\rangle\langle\beta'|H_1(t)|\alpha'\rangle e^{i/h(E_{\beta'} - E_{\beta)}\tau} e^{i/h(E_\beta - E_{\alpha'})t} \\ &- \langle\alpha|H_1(t)|\beta\rangle\langle\beta|H_1(t-\tau)|\beta'\rangle e^{i/h(E_{\beta'} - E_\beta)\tau} e^{i/h(E_\alpha - E_{\beta'})t}\rho^*_{\beta'\alpha'}\ \big]\, d\tau\end{aligned} \tag{2.81}$$

Also on equation 2.81 an ensemble average is performed to consider the average contribution of differing $H_1(t)$. This means, an ensemble of particles is considered instead of a single spin and it is possible to find expressions $J_{\alpha\beta\alpha'\beta'}(\nu)$ in equation 2.81

$$J_{\alpha\beta\alpha'\beta'}(\nu) = \int_0^\infty \overline{\langle\alpha|\,H_1(t)\,|\beta\rangle\,\langle\beta'|\,H_1(t+\tau)\,|\alpha'\rangle} e^{-i\nu\tau} d\tau \tag{2.82}$$

where $\nu = 1/h(E_{\beta'} - E_{\alpha'})$. These expression are called *spectral densities* and shall be discussed a bit closer. First, the argument for writing the integral from 0 to ∞ is

the following: As we are discussing stationary perturbations, elements of the form $\overline{\langle\alpha|H_1(t-\tau)|\beta\rangle\langle\beta'|H_1(t)|\alpha'\rangle}$ (*autocorrelation functions* of the fluctuations) are independent of t. Also, they decay quickly to zero when τ exceeds the characteristic decay time of the fluctuations of $H_1(t)$, τ_c. So, for times t greater than τ_c, we are permitted to extend the integration of τ to ∞.

The correlation function contained in equation 2.82 is real and an even function of τ, so real and imaginary parts can be written as:

$$\begin{aligned} ReJ(\nu) &= \frac{1}{2}\int_{-\infty}^{\infty} \overline{\langle\alpha|\, H_1(t)\,|\beta\rangle\,\langle\beta'|\, H_1(t+\tau)\,|\alpha'\rangle} cos(\nu t)d\tau \\ ImJ(\nu) &= -\int_{0}^{\infty} \overline{\langle\alpha|\, H_1(t)\,|\beta\rangle\,\langle\beta'|\, H_1(t+\tau)\,|\alpha'\rangle} sin(\nu t)d\tau \end{aligned} \tag{2.83}$$

Further, only the real part will be considered, as the imaginary part can be shown to lead to a second order frequency shift (sometimes called *dynamical shift*).

From equation 2.81 it becomes also clear, that only elements fulfilling $E_\alpha - E_{\alpha'} = E_\beta - E_{\beta'}$ contribute. Having this in mind and considering only the real part, it is possible to rewrite matrix elements of equation 2.77 as

$$\frac{\partial\rho^*_{\alpha\alpha'}}{\partial t} = \sum_{\beta,\beta'} R_{\alpha\alpha',\beta\beta'} e^{i/h(E_\alpha - E_{\alpha'} - E_\beta + E_{\beta'})t} \rho^*_{\beta\beta'} \ , \tag{2.84}$$

where

$$\begin{aligned} R_{\alpha\alpha'\beta\beta'} = \frac{1}{2\hbar^2}\,[\ & J_{\alpha\beta\alpha'\beta'}(\nu_{\alpha'\beta'}) + J_{\alpha\beta\alpha'\beta'}(\nu_{\beta\alpha}) \\ & - \delta_{\alpha',\beta'}\sum_\gamma J_{\gamma\beta\gamma\alpha}(\nu_{\gamma\beta}) + \delta_{\alpha,\beta}\sum_\gamma J_{\gamma\alpha'\gamma\beta'}(\nu_{\gamma\beta'})\ ] \end{aligned} \tag{2.85}$$

and

$$J_{\alpha\beta\alpha'\beta'}(\nu) = \int_{-\infty}^{\infty} \overline{\langle\alpha|\, H_1(t)\,|\beta\rangle\,\langle\beta'|\, H_1(t+\tau)\,|\alpha'\rangle} e^{-i\nu\tau} d\tau \ . \tag{2.86}$$

It is noted here, that the definition of the indices might differ from textbook to textbook, as their sequence is (to some degree), dependent on the definition of $J_{\alpha\beta\alpha'\beta'}(\nu)$. The derivation above is following Slichter's book [48]. When applying and evaluating these equations, it is of importance to follow one definition consistently.

One can see from equation 2.84 that the elements of the spin density matrix obey a set of linear differential equations, where the elements $R_{\alpha\alpha'\beta\beta'}$ are constant in time. The exponential has the effect, that only terms fulfilling $E_\alpha - E_{\alpha'} = E_\beta - E_{\beta'}$ contribute to spin relaxation. A non-zero exponential would lead to an oscillatory term which is averaging to zero over time.

In the above derivation of equation 2.84 only spin variables are considered and the lattice is ignored. The consequence is, that equation does not describe the approach to an equilibrium at finite temperature. To include the lattice and the consequences of irreversibility, equation 2.69 must be used to consider the total spin density described by a product of spin and lattice density operators.

The derivative for the total spin density can be written as

$$\frac{\partial}{\partial t} tr_L \left\{ \rho_S^*(t) \rho_L^*(0) \right\} = \frac{\partial}{\partial t} tr_L \left\{ \rho_S^*(t) \rho_{eq} \right\} = \rho_{eq} \frac{\partial}{\partial t} \rho_S^*(t) \ , \tag{2.87}$$

where the lattice remains in thermal equilibrium at all times (see equation 2.66). As a result, equation 2.84 must be modified slightly by exchanging $\rho(t)^*$ with $(\rho(t)^* - \rho_{eq})$ which gives

$$\frac{\partial \rho^*_{\alpha\alpha'}(t)}{\partial t} = \sum_{\beta,\beta'} R_{\alpha\alpha',\beta\beta'} e^{i(E_\alpha - E_{\alpha'} - E_\beta + E_{\beta'})t} \left(\rho^*_{\beta\beta'}(t) - \rho^*_{\beta\beta',eq} \right) \ . \tag{2.88}$$

A rigorous treatment of the total density operator and a detailed derivation and discussion of equation 2.88 can be found in [100] and [101].

Finally, a back transform $\rho^* \rightarrow \rho$ can be performed which brings back the static Hamiltonian H_0 into the equation for the spin density elements:

$$\frac{d\rho_{\alpha\alpha'}(t)}{dt} = \sum_{\nu_{\alpha\alpha'} = \nu_{\beta\beta'}}^{\beta,\beta'} \left(i\mathcal{L}^0_{\alpha\alpha'\beta\beta'} - R_{\alpha\alpha'\beta\beta'} \right) \left(\rho^*_{\beta\beta'}(t) - \rho^*_{\beta\beta',eq} \right) \ , \tag{2.89}$$

where $\nu_{\alpha\alpha'} = 1/h(E_\alpha - E_{\alpha'}$ are the transition frequencies of $\hat{H}_0$ and E_α are its Eigenvalues.

The Liouvillian $\mathcal{L}^0$ contains the static transition frequencies and is defined via a commutator relation:

$$i\mathcal{L}^0 \rho(t) = \frac{i}{\hbar} \left[\hat{H}_0, \rho(t) \right] \tag{2.90}$$

The elements of $\mathcal{L}^0$ can be expressed by the difference between two energy levels E_α:

$$\begin{aligned} \mathcal{L}^0_{\alpha\beta\alpha\beta} &= \nu_{\alpha\beta} = 1/h \left(E_\alpha - E_\beta \right) \\ &= \langle \Psi_\alpha | \widehat{H}_0(I) | \Psi_\alpha \rangle \rangle - \langle \Psi_\beta | \widehat{H}_0(I) | \Psi_\beta \rangle \end{aligned} \tag{2.91}$$

Equation 2.89 is the starting point of a study on quadrupole spin relaxation presented in chapter 5.

Correlation function and spectral density

The spectral density function J(ν) presented in equation 2.86 depends on the motional model that generates the stochastic modulation of the Hamiltonian H_1(t). This interaction operator can be written in the form

$$H_1 = \sum_i T_i V_i \tag{2.92}$$

where V_i are time-dependent spatial operators describing the reservoir (thermal bath) and T_i are spin operators acting on the variables of the spin system only. After

inserting expression 2.92 into equation 2.86, J(ν) contains terms of the form:

$$tr_L\{V(t)_i V(t')_j \rho_L(0)\} = \langle V(t)_i V(t')_j \rangle \ . \tag{2.93}$$

It is noted here, that the lattice density operator (which has been ignored during the derivation of equation 2.84) is now considered explicitly. Equation 2.93 describes an expectation value of a physical quantity taken at different times. This is the definition of a correlation function of $V(t)$, which characterizes the correlation existing on average between the interactions occurring at times t and t'. All information on the reservoir (lattice) is contained in the correlation functions. The quantity in equation 2.93 reflects the memory of the reservoir about the interaction at time t at time t'. As the reservoir is assumed to be large, effects of the interaction are dissipating fast which means that interactions become progressively less correlated for $t - t' > \tau$ and uncorrelated for $t - t' \gg \tau$. As the correlation function depends only on $t - t'$, the function is stationary; a property which has been used in the above derivation.

The correlation time τ is a measure of the time during which some memory of the interaction is retained. Figuring out the nature of this quantity is a prime interest of relaxation theory as well as experiments. In case of gases, τ may be given as the mean time between two collisions. Accordingly, for liquids τ can describe diffusion or rotations of molecules or particles. In solids, τ might reflect fluctuations of molecular bonds or lattice vibrations. For example, a motional model for electric field gradient fluctuations in molecular crystals will be given in chapter 5.

If the stochastic process can be described by an exponentially decaying correlation function, a resulting spectral density function is a Lorentzian function. In case of isotropic molecular tumbling, applying the well known rotational diffusion equation leads to a correlation function (see e.g. [101, 102])

$$C_{rot}(t) = \frac{1}{5} e^{-t/\tau_{rot}}. \tag{2.94}$$

The resulting spectral density, expressed in angular frequency $\omega = 2\pi$, gives

$$J_{rot}(\omega) = \frac{1}{5} \frac{\tau_{rot}}{1 + (\omega\tau_{rot})^2}. \tag{2.95}$$

More complex stochastic motions might lead to multiple correlation times. It can be seen from equation 2.95 that the fluctuations are most efficient for $\tau_{rot} \simeq \omega^{-1}$, where their frequency matches the transition energy of the spin system. In case of very fast motions (e.g. fast tumbling of small molecules) $(\omega\tau_c) \ll 1$ leads to $J(\omega) \simeq J(0)$, which is commonly known as *extreme narrowing limit*. In this regime, relaxation is independent of the spin transition frequency (in case of NMR, the applied magnetic field), and no dispersion can be observed.

2.3 Stimulated emission, absorption and relaxation

In sections 2.1 and 2.2.1, excitation and relaxation have been treated separately. During a spin resonance experiment, however, both processes occur simultaneously. For the sake of completeness, this situation is sketched briefly below.

A characteristic of transitions in the microwave and radiofrequency (RF) region is the predominance of stimulated emission upon spontaneous emission. This follows from Einstein's theory of radiation which tells that the ratio between stimulated and spontaneous transitions is proportional to the spectral radiation density $r(\nu)$ and the wavelength λ: $r(\nu)\lambda^3$. In the RF regime, both are large and spontaneous emission can be neglected.

In the absence of spontaneous emission, the transition probabilities for stimulated emission and absorption are equal. An external RF field has thus the effect of equalizing the populations. In contrast, relaxation tends to re-establish thermal distribution of spins among the basis states (according to a Boltzmann distribution). Under the influence of the three processes stimulated emission, absorption, and relaxation, a dynamical equilibrium is established. For the corresponding equation of motion of the spin density, equation 2.89 must be expanded by a term accounting for the excitation:

$$\frac{d\rho_{\alpha\alpha'}(t)}{dt} = \sum_{\nu_{\alpha\alpha'}=\nu_{\beta\beta'}}^{\beta,\beta'} \left(i\mathcal{L}^0_{\alpha\alpha'\beta\beta'} - R_{\alpha\alpha'\beta\beta'}\right)\left(\rho^*_{\beta\beta'}(t) - \rho^*_{\beta\beta',eq}\right) - (i/\hbar)\langle\alpha|\left[H_{IA}(t), \rho_S(t)\right]|\alpha'\rangle\,. \tag{2.96}$$

$H_{IA}(t)$ is the interaction Hamiltonian, representing e.g. an external RF field. Discussion of this equation is out of scope of this work, but further information can be found in [76].

Chapter 3

Tuning Nuclear Quadrupole Resonance - A Novel Approach for the Design of Frequency Selective MRI Contrast Agents

Christian Gösweiner[1*], Perttu Lantto[2], Roland Fischer[3], Carina Sampl[3], Evrim Umut[4], Per-Olof Westlund[5], Danuta Kruk[4], Markus Bödenler[1], Stefan Spirk[6,7], Andreas Petrovič[1] and Hermann Scharfetter[1]

[1]*Institute of Medical Engineering, Graz University of Technology, 8010 Graz, Austria*
[2]*NMR Research Unit, University of Oulu, P.O.Box 3000, 90014 Oulu, Finland*
[3]*Institute of Inorganic Chemistry, Graz University of Technology, 8010 Graz, Austria*
[4]*Faculty of Mathematics and Computer Science, University of Warmia and Mazury in Olsztyn, 10-719 Olsztyn, Poland*
[5]*Departement of Chemistry, UmeåUniversity, 901 87 Umeå, Sweden*
[6]*Institute for Chemistry and Technology of Materials, Graz University of Technology, 8010 Graz, Austria*
[7]*Institute of Paper, Pulp and Fibre Technology, Graz University of Technology, 8010 Graz, Austria*

published in:
Physical Review X 8, 021076 (2018), DOI:10.1103/PhysRevX.8.021076 [61]

Abstract

The interaction between water protons and suitable quadrupolar nuclei (QN) can lead to quadrupole relaxation enhancement (QRE) of proton spins, provided the resonance condition between both spin transitions is fulfilled. This effect could be utilized as a frequency selective mechanism in novel, responsive T_1 shortening contrast agents (CAs) for magnetic resonance imaging (MRI). In particular, the proposed contrast mechanism is depending on the applied external flux density- a property that can be exploited by special field-cycling

MRI scanners. For the design of efficient CA molecules, exhibiting narrow and pronounced peaks in the proton T_1 relaxation dispersion, the nuclear quadrupole resonance (NQR) properties as well as the spin dynamics of the system QN-^{1}H have to be well understood and characterized for compounds in question. In particular, the energy-level structure of the QN is a central determinant for the static flux densities at which the contrast enhancement appears. The energy levels depend both on the QN as well as the electronic environment, i. e. the chemical bonding structure in the CA molecule. In this work, the NQR properties of a family of promising organometallic compounds containing ^{209}Bi as QN have been characterized. Important factors like temperature, chemical structure and chemical environment have been considered by NQR spectroscopy and ab initio quantum chemistry calculations. The investigated Bi-aryl compounds turned out to fulfill several crucial requirements: NQR transition frequency range applicable to clinical 1.5 T and 3 T MRI systems, low temperature dependency, low toxicity as well as tunability in frequency by chemical modification.

3.1 Introduction

Magnetic resonance imaging (MRI) is one of the most powerful diagnostic imaging tools in modern medicine. The technique features high spatial resolution combined with high penetration depth and superb soft tissue contrast without the use of ionizing radiation. Tissue contrast in MRI is essentially based on the distribution of water protons within the body (proton density) as well as their spin-lattice and spin-spin relaxation times (T_1, T_2). To further increase contrast and consequently sensitivity, signal enhancement strategies have been developed involving the use of relaxation enhancers, so-called contrast agents (CA). The most widely used CAs are gadolinium (Gd) based paramagnetic chelates that shorten T_1 of free water protons [1]. In contrast, nanoparticles composed of paramagnetic iron oxides predominantly shorten T_2 [8]. These CAs are administered to patients leading to an improved soft tissue contrast in either T_1 or T_2 weighted sequences. As a consequence, MRI is nowadays employed for both, morphological and functional imaging, such as dynamic contrast enhancement (DCE) in cancer diagnostics [16]. MRI is increasingly used also in the context of cellular and molecular imaging [25], the aim of which is to provide spatially and temporally resolved maps of biomarkers which contain information on pathophysiological processes correlated with cancer and other diseases [103]. This is usually achieved by administration of CAs that respond to their chemical environment. Considerable effort has been directed into the development of MRI CAs exhibiting a significant change in relaxivity upon activation in response to physiological alterations such as temperature, metal ions, redox state, enzyme activity or pH [104, 38]. One representative of such responsive CAs are based on chemical exchange saturation transfer (CEST) [105, 106, 27] which has gained more and more interest in the last years. CEST contrast can be switched on and off using a selective radio frequency (RF) saturation pulse. However, CEST suffers from

low sensitivity, SAR restrictions and saturation spillover effects between bulk protons and protons of the CEST agent, which is due to insufficient frequency separation. Also, new nitroxide-based macromolecules have been reported as T_2 shortening agents [28] which provide a system free of toxic heavy metals. As they contain radicals, their in vivo lifetime may become a limiting factor and they are not inherently switchable. In this paper, we explore a novel alternative approach to the established CAs making use of quadrupole relaxation enhancement (QRE) [31, 107, 32] induced by the interaction of protons with quadrupolar nuclei (i.e. nuclei with spin quantum number $I > 1/2$) [40, 108, 109]. The ability of QRE for enhancing MRI contrasts has been proven for the interaction between endogenous ^1H and ^{14}N in the amide groups of muscle proteins at very low flux densities [33]. However, it is completely unexplored for exogenous CAs at clinical fields such as 1.5 or 3 T. For QRE, the dipole-dipole (D-D) interaction between a proton spin and the nuclear spin of a quadrupolar nucleus (QN) is associated with a transfer of magnetization from the proton to the QN and thus accelerates the proton spin relaxation. Designing a CA based on QRE, however, is a complex task, as several conditions concerning e.g. the ^1H-QN distance and the time scale of the motional dynamics, must be met for the phenomenon to take place. In particular, the process becomes effective when the proton spin transition frequency (i.e. the Larmor frequency) matches to one of the spin transition frequencies of the QN which depend on its quadrupole coupling constant Q_{cc} and the Zeeman splitting. QRE based CAs are selective to B_0 due to the field dependence of this resonance condition. Moreover Q_{cc} is sensitive to the temperature as well as the chemical surrounding of the QN, and subsequently to subtle changes of the bonding structure e.g. by chemical reactions. Thus, contrast can be modulated by e.g. either alterations of the chemical structure of the CA or by shifting the main magnetic field B_0 of a MRI system. Utilizing the combination of fast field cycling (FFC) relaxometry with MRI (FFC-MRI), it is possible to cycle the nominal B_0 field during an imaging sequence [33, 110]. This technique gives access to contrast types arising from the field dependency of the proton relaxation rates $R_1(B_0) = 1/T_1(B_0)$ and $R_2(B_0) = 1/T_2(B_0)$, referred to as nuclear magnetic relaxation dispersion (NMRD). CAs exhibiting a strong R_1 dispersion are especially favourable to be imaged by delta relaxation enhanced magnetic resonance (dreMR) imaging [111, 112], as the R_1 dispersion of healthy tissue is inherently low at clinical fields [113]. QRE is in principle capable of generating narrow peaks instead of just a smooth slope in the proton T_1-NMRD profile and so offering the possibility for modulating contrast by cycling the field of the scanner. The first step of the development of a potential contrast agent is the identification of promising chemical compounds which contain a suitable QN. Basic selection criteria are:

- high gyromagnetic ratio γ_{QN} to provide strong D-D coupling and hence strong QRE
- high nuclear spin I, preferably $I = 9/2$, as the relaxation rate R_1 scales with

I [34], and a higher nuclear spin offers more possible quadrupole transition frequencies that can fulfill the resonance condition

- low toxicity
- high natural abundance
- rich and well-known chemistry
- high Q_{cc}, so that there exist transition frequencies close to the Larmor frequency at clinical field strengths (1.5 T or 3 T). Q_{cc} depends on both the quadrupolar moment of the QN and the electric field gradient (EFG) produced by the electronic environment of the QN, i. e. the chemical bonding structure of the compound.

Among a number of potential QNs, ^{209}Bi with I=9/2 appears particularly favorable because it is considered as comparatively non-toxic and so Bi compounds are expected to have a higher biocompatibility [114] than e. g. Gd based CAs [24, 23]. ^{209}Bi has been suggested [115, 116, 117], also in X-ray contrast agents which makes it an ideal candidate for dual-mode CAs for computer tomography (CT) and MRI with only a single core element. The knowledge of the nuclear quadrupole resonance (NQR) parameter Q_{cc} and η (asymmetry parameter of the EFG, see Appendix A) is of central importance for fulfilling the QRE resonance condition as they determine the NQR transition spectrum. The purpose of this paper is thus to characterize, in terms of these parameters, a set of Bi-aryl compounds which are promising starting candidates for the development of QRE-based contrast agents. Moreover, it is pivotal to identify and, if possible, quantify all relevant mechanisms which can modify these parameters during the development cycle of the final CA. In this context, the aim of this paper is twofold: 1) experimental characterization of Q_{cc} and η of a promising set of quadrupolar compounds in their crystalline state by means of zero-field nuclear quadrupole resonance spectroscopy (NQRS) [42] (see Sec. III.B). As a side-product also the quadrupole spin relaxation times $T_{1,Q}$ and $T_{2,Q}$ are determined. 2) estimation of the influence of structural changes on Q_{cc} and η, when passing from the crystalline state to single isolated molecules in solution (It is not possible to observe NQR-peaks directly in liquids [50] due to temporal averaging of the tumbling molecules). This may serve as a first approximation for the situation in the final CA and is achieved by ab initio quantum chemistry (QC) calculations (see 3.3.3).

The paper is organized as follows: First, the basic theoretical background on QRE in protons (section 3.2) is given. Then, the proposed compounds are introduced as well as the results on the two main points introduced above are discussed (3.3). In 3.4 the main conclusions are summarized and in 3.5 a brief outlook will be given. At the end of the paper, the methods used for QC calculation and NQR spectroscopy (3.6) are described in detail. Appendix A contains the mathematical description of

the NQR transition frequency spectrum. Details to the data analysis and fitting procedure are given in Appendix B. In Appendix C, results and related error estimations are summarized.

3.2 Quadrupole relaxation enhancement in protons

At first, it is important to recollect the basics of NQR. The interaction of a high spin nucleus (I>1/2) with the EFG generated by its surrounding charge distribution gives rise to a quantized energy level system which can be studied by NQRS [42, 65, 54]. The emerging NQR transition frequency spectrum $\nu_{Q,k}$ (pure quadrupole transition frequency, see Appendix A) can be fully described by Q_{cc} and η. The number of transitions depends on the nuclear spin quantum number I; in case of ^{209}Bi, four pure quadrupole peaks (no external field B_0) can be observed (see figure 3.1 (a)). The NQR transitions provide a very direct and highly sensitive insight into the electronic environment of the molecule where the resonant QN is located. The position of the transition frequency is sensitive to chemical or structural changes of the molecule as well as to the temperature. If the relevant influences are well understood, the transition frequency of the QN can be tuned to a desired frequency and its response upon slight chemical changes can be predicted. A more detailed mathematical deduction of the NQR transition frequency spectrum and the origin of its parameters Q_{cc} and η is given in Appendix A. As soon as an external field B_0 is applied, QNs and protons experience a splitting of their energy level systems due to Zeeman coupling (see figure 3.1(b)). In consequence, the degeneracy in the magnetic quantum number m_I is cancelled, which leads to an observable peak at the Larmor frequency ν_L for protons as well as to a splitting of the pure NQR transition frequencies. The Zeeman contribution to the two spin ensembles depends on $\gamma_{^1H}$ and γ_{QN}, respectively. For the QN the angle Ω between its EFG and B_0 has to be considered as well (definition, see Appendix A). So, at particular flux densities it is possible that spin transitions of both ensembles overlap, as indicated by the red area in figure 3.1(b). This is the primary condition for QRE.

There is, however, still another important prerequisite for QRE to occur. As illustrated in figure 3.2 (a), fluctuating D-D interactions must act as a coupling mechanism, because QRE is based on a magnetization transfer from a ^{1}H spin ensemble to a quadrupolar spin ensemble by cross relaxation [34]. Therefore it is required that (1) the ^{1}H-QN distance r_{H-Bi} is small enough and that (2) the spectrum of the D-D fluctuations, which can be described by the spectral density function $J(\nu)$, contains strong components at those frequencies where the resonance condition is met (compare figure 3.1 (b)). The latter condition depends on the time scale and model of the motional dynamics (assuming an exponentially decaying correlation time function). The first condition arises because the D-D interaction strength scales with the distance r_{H-QN} between the proton and the QN as $\frac{1}{r^6}$. The second condition implies

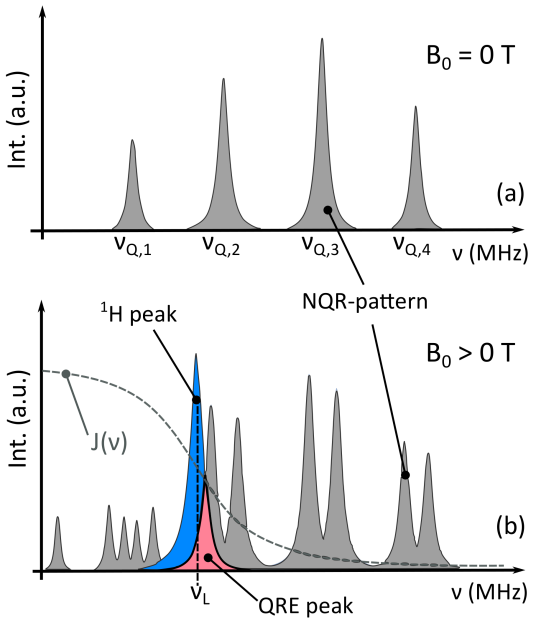

FIGURE 3.1: Simple scheme of transition frequency crossing to produce QRE in protons. For illustration and simplicity, the lineshapes are assumed to be Lorentzian (see Appendix B equation (15)) with equal width for each transition. Intensities in a.u. correspond to Boltzmann weighted transition probabilities (Appendix A, equation (10)). In panel a), the pure NQR pattern of a single crystal is shown (grey pattern). In panel b), $B_0 > 0$T leads to an observable ^{1}H resonance (blue peak) at the Larmor frequency ν_L as well as to a splitting of the NQR pattern (Appendix A equation (9)). The four-line splitting of the lowest transition is a consequence of non-zero off diagonal elements of the Hamiltonian [42]. A transition frequency match at a particular field strength B_0 -indicated by the red highlighted overlap area- as well as the D-D fluctuations $J(\nu)$ at the corresponding frequency, are the main condition for a QRE of the protons.

that the correlation time τ_c of the spin fluctuations has to be long enough to fulfill the condition $2\pi\nu_{Q,k}\tau_c > 1$.

Subsequently, we will focus on the resonance-condition for QRE which can be written as

$$\nu_L = \nu_{0,k}(\Omega), \tag{3.1}$$

where $\nu_L = B_0\gamma_H$ is the Larmor frequency of the protons, and $\nu_0, k(\Omega)$ one of the allowed transition frequencies k of the QN, which result from transitions between the energies levels of the total QN Hamiltonian:

$$H_0(I)(\Omega) = H_Q(I)(\Omega) + H_Z(I). \tag{3.2}$$

H_Q is the pure quadrupole Hamiltonian, H_Z is the Zeeman Hamiltonian (see Appendix A) and I is the nuclear spin of the QN, $I > 1/2$.

According to equation 3.1, the transition crossings occur only at particular flux densities, which is one reason for the frequency selectivity of QRE. This fact is also reflected in figure 3.2(b) (which is just another viewpoint of the situation in figure 3.1), where the qualitative transition patterns of both spin ensembles are shown in dependence on B_0. The pure quadrupole transitions $\nu_{Q,k}$ form transition frequency bands with increasing B_0. The bands are due to the fluctuations of the angle Ω between the EFG and the external field B_0 caused by molecular rotation. For solid powders, all intensity-weighted angles have to be considered. Crossings between the proton Larmor frequency ν_L and the QN-transition bands fulfill the resonance condition and open the possibility for QRE in protons. These regions (highlighted in red) can be shifted to a desired flux density e.g. 3 T, by tuning the pure NQR spectrum (figure 3.2 b)). To accomplish this in a rational manner, a sound understanding of the mechanisms involved in shifting the pure NQR pattern, in particular at the human body core temperature, is of major importance for the application of QRE in MRI CAs.

For convenience, in the following sections and tables pure NQR transitions $\nu_{Q,k}$ are labeled consecutively from transition $'1'$ to transition $'4'$ starting from the lowest $|1/2\rangle - |3/2\rangle$ to the highest $|7/2\rangle - |9/2\rangle$ coherence. It is noted, that as soon as $\eta \neq 0$ or the Zeeman field points into an arbitrary direction with respect to the EFG, the states $|m\rangle$ are no pure Zeeman states anymore and labeling according to m_I becomes impracticable.

3.2.1 Quadrupole relaxation enhancement in protons

Although the description of QRE on protons given above is quite general, the aggregation state (solid or liquid) as well as the exact proton pool (intra- or intermolecular) of the considered system has to be clearly defined and distinguished. An important difference is the source of D-D fluctuations responsible for the transfer of magnetization. Whereas in solids the spectral density of the fluctuations may be due to bond

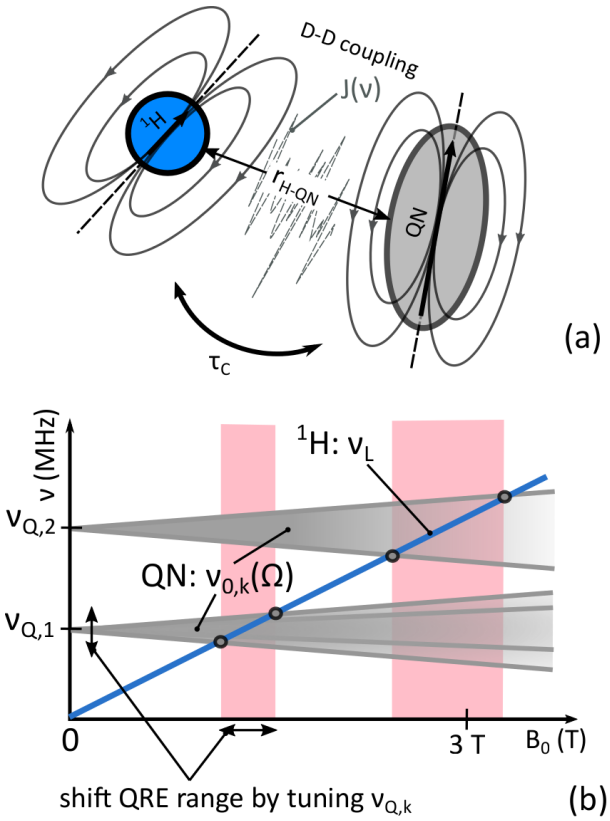

FIGURE 3.2: Panel a) shows the schematic principle of QRE in protons due to the interaction with close-by QN via magnetic D-D coupling. Panel b) shows the transition frequencies of both spin ensembles, ν_L for the protons (blue line) and $\nu_{Q,k}(\Omega)$ for the QNs (grey), depending on an externally applied flux density B_0. Where transitions of both spin ensembles match, QRE can be expected as for the considered case at 3 T. This area is indicated by the vertical red bands. Panel b) also gives an impression of how the QRE peaks are shifted by tuning the pure quadrupole frequency.

vibrations, for solutions containing both protons and QRE based CA particles, diffusion and rotation is the main source (compare figure 3.2(a)). To simulate relaxation dynamics of QRE in the liquid state, the stochastic Liouville approach [34, 118, 119], is necessary, as the dynamical conditions for the Redfield theory [97, 48], as used in solids, are not fulfilled anymore. Both theories necessarily require the knowledge of the NQR parameters Q_{cc} and η. The most direct way for the determination of these parameters is zero-field NQRS in solid powders. For stochastic Liouville-simulations in liquids, however, these parameters are only approximately valid, because they differ slightly [120] between free molecules in solution and molecules bound in a solid crystal. This issue will be discussed in Sec. III.C. Beyond that, the QRE strength and position depends not only on the transition frequency match but also on several additional parameters such as the correlation time of the D-D fluctuations, the water exchange rate and the relaxation behavior of the quadrupole nuclei. In the liquid state, there is no simple relationship such as illustrated in figure 3.1 and figure 3.2, which allows predicting QRE peaks directly from the NQR parameters, but relative changes of Q_{cc} and η are expected to lead to very similar relative shifts of the QRE peaks.

3.3 Results and discussion

3.3.1 Compound selection

As a group of model systems, we chose Bi-aryl compounds (in form of crystalline powders) because of several practical reasons: Their most simple representative, triphenylbismuth, is commercially available and possesses a versatile and comparatively simple organic chemistry with the possibility of incorporating or grafting it onto nanoparticles for blood stream transportation. Moreover, at least partially complete NQR datasets are available for several Bi-aryl molecules [63] and qualify some of them as promising for QRE because they possess NQR transitions close to frequencies which are required at clinical field strengths, i.e. 1.5 and 3 T. The structures of the compounds are shown in figure 3.3 and labeled accordingly throughout the paper. The compounds were synthesized according to established procedures (see Appendix C, table 3.5). In total, eight compounds including triphenylbismuth (1) were investigated; tris(4-fluorophenyl) bismuth (2), tris(4- dimethylaminophenyl) bismuth (3), tris(4-methoxyphenyl) bismuth (4), tris(2-methoxyphenyl) bismuth (5), tris(2-6-dimethoxyphenyl) bismuth (6), triphenylbismuth dichloride (7), and fully deuterated triphenylbismuth (8). For samples 5 and 7 we identified two superimposed spectra corresponding to different Bi-sites in the crystal (5A, 5B and 7A, 7B respectively).

The tricoordinate Bi(III) compounds 1-6 and 8 feature a trigonal pyramidal structure around Bi with sums of angles Σ C-Bi-C between 280° and 296° , where the phenyl rings adopt a tilted conformation with respect to the principal axis of the

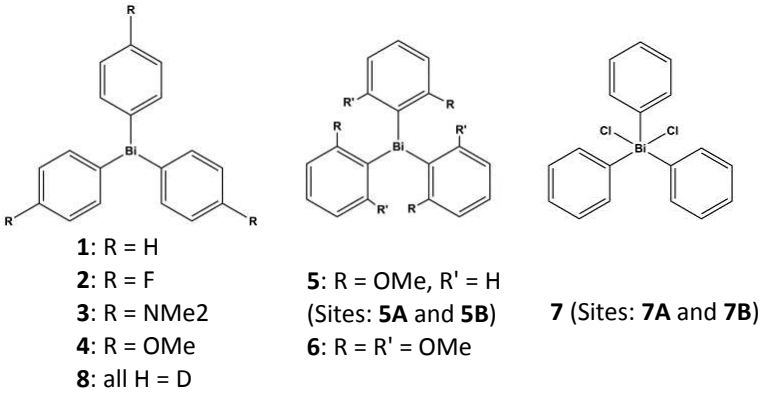

FIGURE 3.3: Overview on Bi-aryl compounds and their structures: triphenylbismuth (1), tris(4-fluorophenyl) bismuth (2), tris(4-dimethylaminophenyl) bismuth (3), tris(4-methoxyphenyl) bismuth (4), tris(2-methoxyphenyl) bismuth (5) (5A and 5B), tris(2-6-dimethoxyphenyl) bismuth (6), triphenylbismuth dichloride (7) (7A and 7B), and fully deuterated triphenylbismuth (8).

molecule (see figure 3.7 and Appendix C, table 3.5). Compound 7, triphenylbismuth dichloride, exhibits a pentacoordinate Bi(V) center adopting a trigonal bipyramidal configuration with Cl in apical position trans to each other, while the ipso-carbon atoms of the phenyl rings form the trigonal base and are in plane with the Bi atom. The phenyl rings are again tilted with respect to the Cl-Bi-Cl vector. Both structure types show almost perfect cylinder symmetry with respect to the pyramid's height axis. Basic structural data as well as structure references of the Bi-aryl compounds are summarized in Appendix C, table 3.5. A rather important selection criterion already at this stage of development is the potential toxicity of the presented molecules. Bismuth compounds are used in therapeutic treatment of gastrointestinal disorders, suggesting a relatively low toxic potential after oral administration [121], with Peptobismoltm being the most prominent example. Although there are a few cases known, where bismuth compounds showed negative side effects (e.g. bismuth subgallate, bismuth tryglycollamate [122]), in general, bismuth compounds are not considered to feature a high degree of toxicity [114]. Particularly, arylbismuth compounds with stable Bi-C bonds have not been reported to have high cytotoxic potential. For instance, triphenylbismuth (1), 1-phenyl-2-trimethlsilyl-1-benzostilyl-1-benzobismepine, tris(4-methylphenyl) bismuth, and tris(2-(methoxymethyl)phenyl) bismuth, did not show cytotoxicity at 10 μM [123]. However, establishing Bi-compounds for intravenous application certainly requires further studies to assess their cytotoxicity also at higher concentrations as e.g. used in conventional Gd-CAs (up to several mM, which corresponds to about 0.1 mmol/kg body weight, according to the Gadovist® product monograph). Promising data in this respect can be found in a study of dextran coated bismuth-iron oxide nanohybrid contrast agents [117]. In this publication, in vivo experiments on mice showed extraction of the degradation products of the CA via kidneys and urine. The experiments were carried out with a dosage of 350 mg Bi per kg body weight, i.e. more than 1.6 mmol/kg body weight. The investigated particles have been identified as being biocompatible

and biodegradable.

3.3.2 NQR spectroscopy

From the eight different crystalline Bi-aryl powder samples introduced above, NQR parameters Q_{cc} and η, relaxation times $T_{1,Q}$ and $T_{2,Q}$ as well as the line width of all accessible transitions were determined and are presented in Appendix C, table 3.6 and table 3.7. Every sample was characterized at 37°C, for some of them measurements were also carried out at the temperature of liquid nitrogen and room temperature (RT). To our knowledge, NQR data have not yet been published for tris(4- dimethylamino) bismuth (3), tris(2-methoxyphenyl) bismuth (4), tris(4-methoxyphenyl) bismuth (5), tris(2-6-dimethoxyphenyl) bismuth (6) and deuterated triphenylbismuth (8). Literature data was confirmed for the transition frequencies determined for triphenylbismuth (1) at RT and 77 K by Robinson et al. [124] and Weaver and Robinson [125] respectively, and for triphenylbismuth dichloride (7) by Brill and Long [126] at 300 K as well as for tris(4-fluorophenyl) bismuth (2) at 300 K by van der Kelen and Ketelaere [127].

NQR spectrum and target frequency

The collected data demonstrate the tuning possibilities of the quadrupole transition frequency by attaching different substituents. Figure 3.4 illustrates the positions of the transition frequencies of each sample measured at 37°C (colored dots) and RT (dots in brackets), respectively. In case that a particular transition could not be measured with the current experimental setup, its frequency was calculated using equation 3.9 of Appendix A, 3.7, and plotted as a grey square. Figure 3.4 shows also a grey-shaded area which highlights the target frequency range for the pure NQR peaks to create a QRE peak at a flux density range defined by a hypothetical FFC MRI scanner (e.g. a standard medical system with nominal static flux density B_0 of 1.5 T or 2.89 T, equipped with an additional insert coil which allows for shifting the flux density by $\pm$ 200 mT). Given that case, all samples have a transition within the required range (see figure 3.4). This field shift was chosen because it is technically feasible as shown by B_0 insert coils as used in Lee et al. [128] and Harris et al. [110]. Another FFC-MRI system has been reported working at a nominal flux density of 2.89 T $\pm$ 100 mT [129].

Of course, it must be kept in mind that a certain shift in transition frequency can be expected when dissolving the solid powders in a solvent or grafting them onto a nanoparticle (NP). There are two important factors influencing the Q_{cc}, namely structure and chemical environment of the compounds (see Sec. III.C). Additionally, the D-D interaction between ^{209}Bi and ^{1}H nuclei, which transfers the magnetization during QRE, is modulated by the relative motion (mainly rotation) between the CA and water protons [34]. These influences can lead to frequency shifts of the QRE

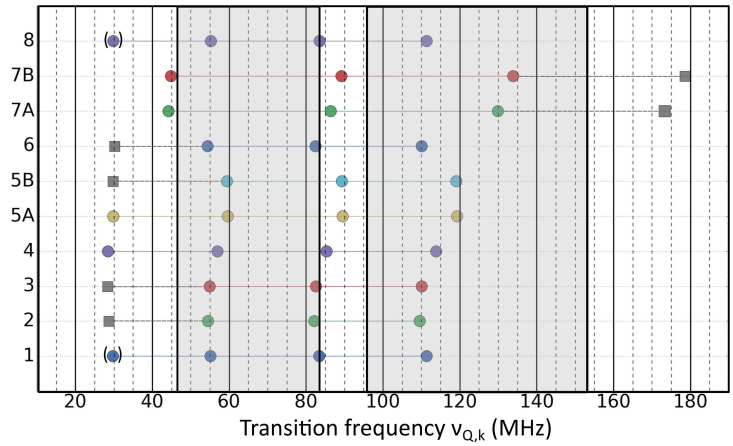

FIGURE 3.4: NQR frequencies of samples 1 to 8. The pure NQR target frequency to create a QRE peak accessible for a FFC MRI scanner with a B_0-shift of 1.5 T $\pm$ 200 mT and 2.89 T $\pm$ 200 mT is marked in grey. This frequency range can be calculated using the resonance condition equation 3.1 and the transition frequency spectrum as in Appendix A,3.7, equation 3.9 (also, compare to figure 3.2(b)). Colored circles have been measured, grey squares mark calculated values (from equation 3.9 Appendix A, 3.7). Dots in brackets are measurements at RT; the rest has been obtained at 37°C.

peaks in liquid with respect to those in solids, depending on the rotational correlation time between the two spin species. The frequency range illustrated in figure 3.4 shall therefore be treated only as a guideline rather than a precise decision rule for pre-selecting promising compounds.

Observed NQR parameter variation

Q_{cc} and η can be calculated from at least two experimentally determined NQR peaks using equation 3.9 of Appendix A. When triphenylbismuth is considered as the reference system (Q_{cc} = 668.3 MHz at 37°C), Q_{cc} shifts of several MHz can be observed when adding particular substituents (see figure 3.5). The strongest impact is observed when changing from three to five coordinate species (by adding two Cl atoms (QN, I=3/2) directly to the Bi center) which leads to an increase in Q_{cc} by about 400 MHz. More subtle changes can be realized, when incorporating substituents at different positions on the phenyl rings. Then Q_{cc} shifts from about +47 MHz (methoxy-group on the ortho position of the phenyl rings) to -11 MHz (F on the para position of the phenyl rings) can be observed. The asymmetry parameter η on the contrary is changing only slightly from sample to sample and ranges between 0 and 0.1 (see Appendix C, table 3.6) since the cylinder-symmetric EFG around Bi is maintained for all compounds. Compound 5 has the highest η with 0.105 whereas all compounds containing mono-methoxyphenyl do not possess any asymmetry. All associated values including the transition frequencies for 37°C as well as some measurements at 77 K can be found in Appendix C, table 3.6.

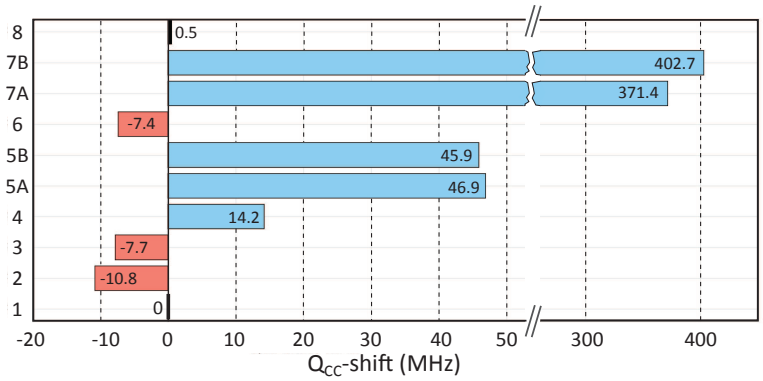

FIGURE 3.5: Q_{cc}-shifts of Bi-aryl compounds with respect to triphenylbismuth (1) @ 37°C (Q_{cc} = 668.3 MHz) depending on the ligand type according to figure 3.3.

For sample 5 and 7 two superimposed ^{209}Bi NQR spectra, labeled $'A'$ and $'B'$ have been observed. This is an indication for two different crystallographic sites within the crystal. In the case of triphenylbismuth dichloride, they correspond to crystallographically independent molecules on different lattice sites A and B [130]. For compound 5 Schuster et al. [131] reported two crystallographically independent molecules in the unit cell where one is located on a threefold crystallographic axis (space group R3), while the second one is located on a general site within the unit cell with occupancies of 0.8802:0.1198. As the full width at half maximum (FWHM) of the peaks in spectrum 'B' is larger than in spectrum 'A' at all transitions (see Appendix C, table 3.7) we assign site B as the disordered species. Noteworthy is the slight Q_{cc} up-shift by 0.5 MHz of deuterated triphenylbismuth (8) due to an isotope effect which is not treated closely here.

The influence of ligands

As the EFG at the QN due to a point charge located at distance r outside of the nucleus is proportional to $1/r^3$ [42, 132], only charge redistributions in the closest vicinity of the nucleus are relevant for shifting the transition frequency. Roughly, two influences on the EFG inducing the observed shifts can be distinguished: First, an additional substituent on whatever site will alter the electron density distribution of the whole molecule to a stronger or lesser degree due to valence orbital forming and charge polarization. This will, however, only have a considerable impact on the quadrupolar coupling strength if these changes affect the closer surrounding of the Bi center. For ligands at the outer position of the phenyl rings, this is expected to play only a minor role. Secondly, ligands introduce a change of both, the molecular as well as the crystalline structure; this fact is in any case likely to have an impact onto the EFG. In figure 3.6, this second influence is visualized by plotting the measured Q_{cc} values versus the average Bi-C bond length (see Appendix, table 3.5) of each sample. The plot indicates a negative trend for Q_{cc} when increasing the average Bi-C distance within each molecule. Notably, tris(4-dimethylamino) bismuth (3) is a little bit off the trend. For this set of compounds the plot in figure 3.6 may serve as a

very rough estimation of what shift can be expected as soon as the structure change is known or vice versa.

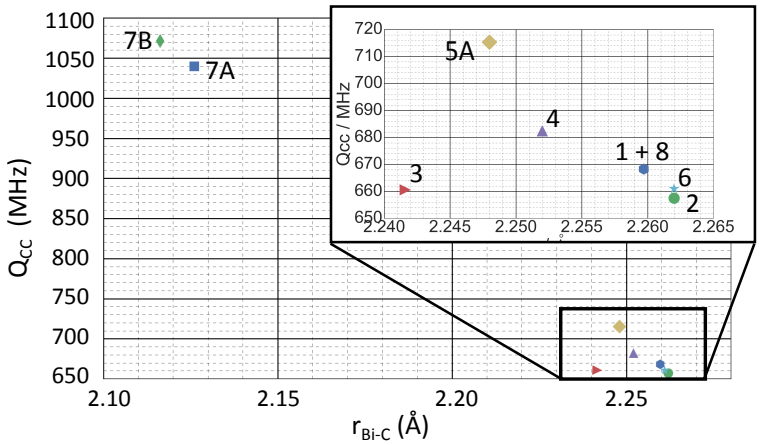

FIGURE 3.6: Q_{cc} versus average Bi-C bond length. A trend for the investigated Bi-aryl compounds can be observed: The closer the Bi-C distance, the higher Q_{cc}.

Temperature sensitivity

The temperature dependency of the NQR-peaks was investigated by temperature-swept NQRS experiments on selected samples. The temperature interval was selected with $\pm$ 5°C around the core temperature of the human body, i.e. 37 °C. For reasons of simplicity, the temperature dependency of the transition frequencies is assumed to be linear in the observed range. The strongest measured temperature coefficient is about -10 kHz/K for transition 4 of compound 1, the weakest temperature coefficient of -3 kHz/K was observed for transition 2 of compound 5A. The results are summarized in Appendix C, table 3.8. The frequency shift within $\pm$1°C is in general lower than a typical NQR-peak width (see Appendix C, table 3.7) and is therefore not expected to play a major role in the application of the compounds as CA.

Quadrupolar relaxation

Though the quadrupolar relaxation rates in the solid state are not of central interest for the scope of this paper, they have been tabulated for completeness because their determination formed part of our standard experimental procedure of the NQR characterization of the compounds. For almost all NQR transitions of the presented compounds, the relaxation times $T_{1,Q}$ and $T_{2,Q}$ were determined at 37°C sample temperature (see Appendix C, table 3.7). This table forms a comprehensive database for deeper analysis in terms of relaxation theory, which is planned in follow-up papers. Moreover it shows potential reasons why for some transitions the peaks could not be identified: $T_{1,Q}$ ranges from as short as 50 μs for transition 4 of sample 7 to as long as 3 ms for transition 1 of sample 1. Also, for T_2 the range is wide and spans from about 30 μs for sample 7 transition 4, up to 700 μs for sample 8 transition 4. $T_{2,Q}$ times

somewhat lower than 30 μs cannot be measured reliably with the current experimental setting. Thus we conclude that some peaks could not be detected, because their $T_{2,Q}$ time is too short. In liquid nitrogen, the relaxation times usually increase considerably thereby facilitating the identification of rapidly dephasing peaks.

3.3.3 Quantum chemistry calculation

As ^{209}Bi is a rather heavy element, the Bi-aryl compounds require careful considerations when performing quantum chemistry (QC) calculations of EFG tensors, especially when it comes to relativistic and electron correlation effects and their coupling [133, 134, 135, 136, 53, 137]. In addition to the scalar relativistic (SR) effects, the influence of relativistic spin-orbit coupling (SO) needs to be taken into account in the heavy element magnetic resonance parameters [136, 137, 138]. While combining relativistic theory with more elaborate electron correlation treatment with hybrid functionals of the Density Functional Theory (DFT) is currently not feasible for periodic solids, we follow closely the approach of Roukala et al. for the nuclear shielding tensor of 195Pt in molecular solids [139]. The following nomenclature is introduced to describe the calculation inputs: 'DFT Functional_Relativistic level_Basis Set' e.g. 'PBE_SO-ZORA_TZ2P' i.e. at SO-ZORA theory using PBE DFT functional and TZ2P basis set, and will be used to discuss the results.

Q_{cc} shift from a solid crystal to the CA

Though the presented data has been gathered from solid crystalline samples, in the final application the QRE effect will be used in CAs dispersed in liquids. These two states are expected to produce slightly different structures as the molecules are integrated in different surroundings. The CA molecules are not embedded into a periodic crystal anymore, which causes what we call a *crystal effect* on the EFG. Also, the molecular structure itself is expected to relax (bond length and angles) in the altered surroundings, thus causing a *structure effect*. As the particular surroundings of the CA are not exactly known at present, an isolated gas-phase structure is assumed as a reasonable approximation.

To figure out the role of these effects, three different cases have been considered at PBE_SO-ZORA_TZ2P level for the reference system sample (1) (triphenylbismuth) which are shown in figure 3.7:

case 1) ... molecule optimized in periodic surrounding + crystalline, periodic surrounding,
case 2) ... molecule optimized in periodic surrounding + isolated state,
case 3) ... molecule in isolated state (gas phase structure) + isolated state.

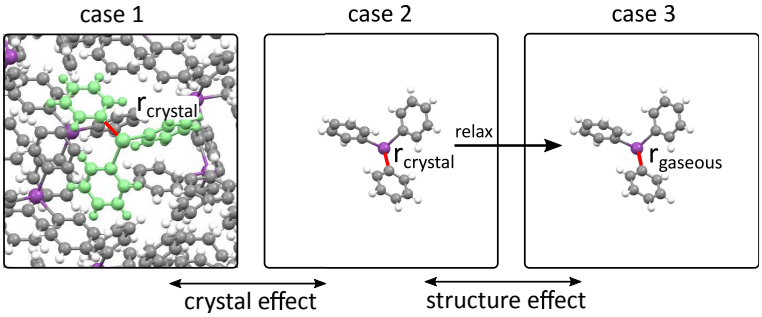

FIGURE 3.7: Cases considered for QC calculations to estimate the crystal effect and the structure effect onto Q_{cc}. The average Bi-C distance of the CASTEP-optimized crystal structure is rcrystal = 2.291 Å, while the distance is $r_{gaseous}$ = 2.263 Åin the gas-phase [140] (see Appendix C table 3.5). 3D models of the molecule structures are supplemented as .cif files [102].

TABLE 3.1: Comparison of QC results at PBE_SO-ZORA_TZ2P level with experimental ones for Q_{cc} and η for triphenylbismuth in different surroundings.

solid - CA comparison	η (1)	Q_{cc} (MHz)
case 1	0.049	661.1
case 2	0.059	539.5
case 3	0.001	557.3
Experiment (crystalline solid)	0.087	668.3
crystal effect (case 1 - case 2)	-0.010	121.6
structure effect (case 2 - case 3)	0.058	-17.9

The sole *crystal* effect makes up the difference between case 1) and 2) whereas the *structure effect* can be determined by taking the difference between case 2) and case 3).

Case 1 corresponds best to the experimental situation except that the QC calculations were performed for static geometries neglecting thermal (vibrational) effects, whereas the experiment was carried out at 37°C. Even though the data in table 3.1 indicates that periodic calculations yield a rather good agreement with experiment, the comparison of absolute values shall be treated with care, as there is room for improvement in both many-electron correlation and one-electron basis set treatments.

The PBE_SO-ZORA_TZ2P results in table 3.1 show that for Q_{cc} the crystal effect of +18.2% is much more important than the structure effect of -2.7% due to the geometry change of the molecule from gas to solid phase. This means that when the triphenylbismuth-molecule undergoes a transition from the solid crystalline to an isolated state, a Q_{cc} shift of about -15% can be expected. The asymmetry parameters η are, in contrast to Q_{cc}, more sensitive to the change of local geometry around Bi than to e.g. 'global' crystal effects. The changes in η are therefore not very strong

TABLE 3.2: Changes of Q_{cc} and η in a single triphenylbismuth molecule (case 2, if not noted otherwise) due to better basis set (QZ4P with respect to TZ2P), hybrid PBE0 functional and relativistic spin-orbit coupling (SO-ZORA, X2C, and DC with respect to SR-ZORA, SF-X2C, and SF-DC, respectively). Nonrelativistic one- (NR) and four-component (LL) results are displayed for comparison.

code	level of theory, see section 3.6.2	η (1)	Q_{cc} (MHz)
ADF	PBE_SO-ZORA_TZ2P	0.059	539.5
	PBE_SO-ZORA_QZ4P	0.069	563.4
	PBE0_NR_QZ4P	0.049	590.5
	PBE0_SR-ZORA_QZ4P	0.060	590.1
	PBE0_SO-ZORA_QZ4P (crystal, case2)	0.062	669.8
	PBE0_SO-ZORA_QZ4P (gas, case3)	0.000	687.5
DIRAC	PBE0_LL_RPF-4Z/cc-pVDZ	0.048	587.9
	PBE0_SF-DC_RPF-4Z/cc-pVDZ	0.053	645.1
	PBE0_DC_RPF-4Z/cc-pVDZ	0.049	674.0
	PBE0_SF-X2C_RPF-4Z/cc-pVDZ	0.053	644.7
	PBE0_X2C_RPF-4Z/cc-pVDZ	0.049	673.2

and the quadrupole tensor is practically cylindrically symmetric ($\eta \approx 0$) in all cases.

QC-parameter study

The roles of different parameter improvements in QC calculations were tested in the case 2 for a single triphenylbismuth molecule. Table 3.2 shows the role of the improved QZ4P basis set, the better electronic correlation treatment with the hybrid PBE0 functional, and the impact of relativistic spin-orbit coupling effect at approximate SO-ZORA and exact two-component (X2C) relativistic theories, as well as at fully relativistic four-component Dirac-Coulomb (DC) level of theory.

When turning from a TZ2P basis set to a QZ4P Q_{cc} changes by +23.95 MHz (4%) (η by +0.009). This indicates that with the lower basis set (TZ2P) the EFG has not fully converged yet and QZ4P should be chosen if possible.

A change from the pure GGA (PBE) to a hybrid DFT functional (PBE0) including 25% of exact Hartree-Fock exchange has a stronger influence onto the Q_{cc} value by an amount of 106.4 MHz (19%) (η by -0.006). According to Teodoro et. al. [53], hybrid DFT functionals provide reasonable but slightly underestimated EFG values for ^{209}Bi in diatomic molecules wrt. high-level ab initio DC-CCSD results. The present magnitude increase due to PBE0 is most probably an improvement and, hence, the hybrid DFT functional is preferred for the estimation of Q_{cc}. The rather large relativistic effect on Q_{cc} of about +80 MHz (+14%, wrt. PBE0_NR_QZ4P) associated with the heavy ^{209}Bi isotope is well described at the best PBE0_SO-ZORA_QZ4P level including both SR and SO relativistic effects. This is confirmed by comparing it with the results from the fully relativistic four-component Dirac-Coulomb (PBE0_DC_RPF-4Z/cc-pVDZ) and it's much lighter exact two-component

(PBE0_X2C_RPF-4Z/cc-pVDZ) approximation. While the ^{209}Bi basis set is presumably well converged in both cases, the small difference in η is probably due to a different basis set of the ligands (TZ2P vs. cc-pVDZ). The seemingly quite large relativistic SO effect (PBE0_SO-ZORA_QZ4P vs. PBE0_SR-ZORA_QZ4P) on Q_{cc}, of about +80 MHz (+14%) is clearly overestimated by the ZORA method. The same effect at fully relativistic DC and approximative X2C level of theory is only about +29 MHz (+4%) when compared to results with the corresponding scalar relativistic SF-DC and SF-X2C results. Actually, the SR-ZORA value for Q_{cc} is very similar with values of both non-relativistic, one- (NR) and four-component (Levy-Leblond, LL), theories. Therefore, for ^{209}Bi in this complex, the so-called ZORA-4 scalar relativistic approximation including a small-component density "picture-change correction "[141] used in ADF gives very small scalar relativistic effect on EFG. This is an example of somewhat arbitrary division of SR and SO relativistic effects by different methods [142]. Therefore, the preferable SR approximation for EFG is obtained with the Dyall's spin-free Hamiltonian [143] used in the SF-DC and SF-X2C calculations with DIRAC code, which provides reasonable estimation close to the fully relativistic value. The methods of choice for the molecular modeling of Bi-complexes would be PBE0_SO-ZORA_QZ4P or PBE0_X2C_RPF-4Z/cc-pVDZ combinations that provide good approximations for the fully relativistic PBE0_DC_RPF-4Z/cc-pVDZ calculation with much lower cost (e.g. X2C takes ca. tenth of the time of DC calculation). However, for the case study in section 3.3.3 we use PBE_SO-ZORA_TZ2P, as for the treatment of a periodic surrounding (ADF-BAND code) no higher basis set is available. The PBE0_SO-ZORA_QZ4P calculation gives a Q_{cc} value of about -17.65 MHz (-2.6%) for the structure correction (see table 3.2, changes from case 3 to case 2). The same relative change was predicted at much lighter PBE_SO-ZORA_TZ2P level (-2.7%) as seen in table 3.1, even though the absolute values are much smaller there. This shows that relative changes can be studied at less advanced method and theory level as well.

3.4 Summary and conclusion

The experimental investigation of eight different Bi-aryl compounds by means of NQR- spectroscopy is an important step towards the rational synthesis of QRE based CAs. The acquired data represents a compendium of promising Bi-compounds with their NQR parameters Q_{cc} and η, quadrupole transition frequencies and associated relaxation times $T_{1,Q}$ and $T_{2,Q}$, mainly at the medically relevant body temperature of 37° C. Depending on the type of ligand and its molecular position, frequency shifts of the quadrupole coupling constant (Q_{cc}) from -10.8 MHz up to 400 MHz with respect to triphenylbismuth (Q_{cc} = 668.3 MHz) have been observed whereas the asymmetry parameter η stays in a range of 0 to 0.1. According to our analysis, this NQR parameter range is especially favorable for the utilization of QRE in clinical 1.5 T or 3 T MRI scanners, provided they are equipped with a fast field cycling insert-coil

(FFC MRI). The temperature dependence of the transition frequencies found at the human body core temperature (typically around 10 kHz/K) is not expected to affect the QRE contrast adversely. The average Bi-C bond distance of each compound, which depends on ligand type and position, has been found to be correlated with Q_{cc}; when increasing the bond distance, a decrease in Q_{cc} is observed (for a bond distance between 2.116 and 2.262 Å, Q_{cc} decreases from 1071 to 675 MHz). From this ligand induced frequency shifts, one can also think of applications for QRE enhancement in fixed field scanners: An EFG change due to chemical interactions (e.g. in the context of ligand targeting) would "tune "or "detune "the QRE peak to or from the scanner frequency, e.g. 1.5 T, thus producing contrast in the image.

As the transition frequencies cannot be expected to be exactly the same in the liquid state, it is of great interest to predict the expected discrepancies. In principle, this can be achieved by calculating the EFG modification with modern ab *initio* quantum chemistry (QC) methods. When modeling the transition of triphenylbismuth from a periodic molecular crystal to an isolated gas-phase molecule our QC simulations predict a Q_{cc} shift of -18.2% due to the *crystal effect* and of 2.7% due to a compensating *structural effect*. These results suggest a possible downshift of the transition frequencies of about 15% when passing from solid to liquid.

Of course, the reliability of these findings depends on the validity of the model. In order to select the best QC settings, a parameter study has been performed. In particular we face the problem of calculating electron distributions in the vicinity of high-mass, high-spin nuclei. It could be shown that the influence of relativistic effects, the chosen basis set and the density functional are of great relevance; the resulting parameter set suggests PBE0_SO-ZORA_QZ4P with ADF code or PBE0_X2C_RPF-4Z/cc-pVDZ with DIRAC code. As an interesting byproduct, the generated NQRS database provides test-data for the validation of EFG calculations with QC methods.

The strong variation of the $T_{1,Q}$ and $T_{2,Q}$ relaxation times for the different samples and NQR transitions point out the experimental difficulties of NQR spectroscopy: At 37°C $T_{1,Q}$ times ranging from 3 ms down to 60 μs and $T_{2,Q}$ times from 700 μs down to 40 μs could be observed, which, on the one hand can lead to very long measurement times and, on the other hand challenge the ring down speed of the spectrometer. In several cases, measurements at low temperature (77 K) helped to increase the signal quality due to slower $T_{2,Q}$ relaxation and an increased population difference of the spin states. The relaxation data is particularly interesting for modeling molecular dynamics and testing relaxation models for high spin systems in the solid state, e.g. based on Redfield theory.

To summarize, the investigation of eight Bi-aryl compounds has identified them as promising candidates for the use as QRE-based contrast agents. Due to their frequency selective character, the compounds may add interesting options in molecular MRI diagnostics in the future. Three of the above investigated solid samples samples, namely tris(2-methoxyphenyl) bismuth (5), tris(2-6-dimethoxyphenyl) bismuth

(6) and triphenylbismuth dichloride (7) have already shown pronounced QRE peaks in yet unpublished proton T_1 relaxometry data at the expected frequencies. Furthermore, the comparatively low toxicity, mostly good stability against hydrolysis and versatile as well as simple chemistry qualifies Bi-aryl compounds as fruitful research objects in the context of MRI contrast agents.

3.5 Outlook

Though the discussion of QRE in solids is out of the scope of this paper, we would like to mention that pronounced QRE peaks have already been observed. As an example, in figure 3.8 the T_1-NMRD profile of solid, crystalline tris(2-methoxyphenyl) bismuth (5) is presented which shows pronounced QRE peaks from inherent protons. These findings are not primarily relevant for the envisaged CAs, nevertheless the data are highly motivating for undertaking the next logical steps: grafting the abovementioned core compounds onto NPs and solubilize them as to act as carriers through the bloodstream. The contrast enhancing effect can then be investigated also on free solvent protons of the system ^1H *containing solvent + NP + CA* core compound by relaxation measurements. In particular, questions concerning size and structure of the carrier particles can then be addressed to shape dynamical conditions and water exchange for optimizing D D coupling and thus magnetization transfer efficiency of the QRE. Another key parameter is the ^{1}H-QN distance during closest approach. However, these questions need to be resolved before the expected increase in relaxivity of protons due to QRE CAs can be reasonably estimated.

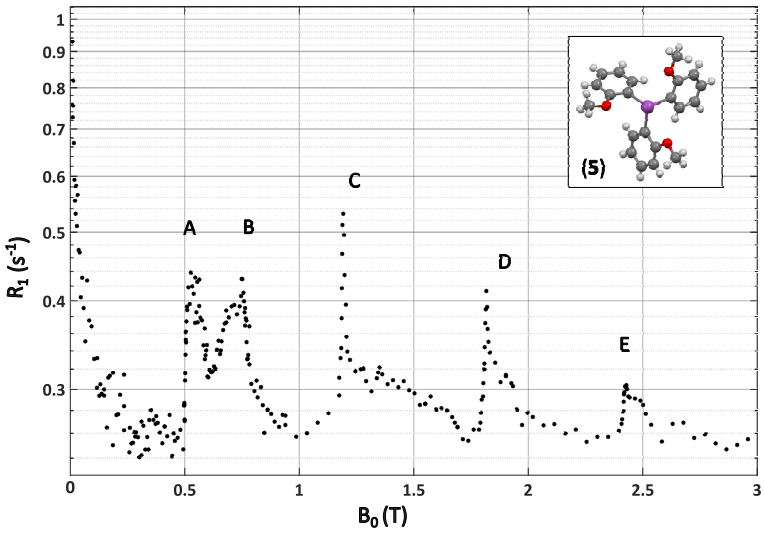

FIGURE 3.8: Proton T_1-NMRD profile of the solid powder-sample (5) at 298 K obtained by a STELAR (Mede, Italy) Spinmaster relaxometer equipped with a magnet operating up to 3 T. Features A-E of the proton R_1 relaxation dispersion can be attributed unambiguously to QRE peaks superimposed on a background due to proton-proton dipolar coupling.

From our current understanding, there are four points which should be focused on in future research in some more detail: Firstly, it can be concluded from NMRD

data in figure 3.8 as well as from theory is that the ^{1}H-QN distance is of great importance for the D-D interaction ($1/r^6$). An average ^{1}H-QN distance of about 3-4 Åis estimated for the solid which can be, at best, also assumed for solution protons exchanging with the coordination sphere of paramagnetic CAs (compare Gd-CAs with about 2.5-4 Å[144]). In this context we expect approximately the same order of magnitude as in paramagnetic CAs. The second important parameter is the water exchange rate which is expected to increase the enhancement per QN considerably when passing from solid to liquid. So far there are no data available about this parameter in Bi-Aryl compounds, which should be investigated also for a possible NP. The third parameter is the gyromagnetic ratio of the QN which is a lot smaller than that of the electrons in paramagnetic CAs. In this aspect QRE CAs are clearly inferior. However, on the other hand the relaxation enhancement seen with paramagnets is known to remain far below the maximum theoretical value because of the fast relaxation of the electrons. Here we find a clear advantage in the QN compounds because the quadrupolar relaxation is usually much slower than that of electrons. This fourth parameter is thus probably essential for making QRE agents competitive.

In future QC studies, a refinement of the molecular surrounding of the CA can be considered. Furthermore, calculations to predict the EFG change of Bi-aryl compounds upon chemical modifications, i.e. different ligand types, can be envisaged. This could improve the CA-design procedure significantly by reducing the experimental workload.

3.6 Methods

3.6.1 NQR spectroscopy

By means of NQR spectroscopy the relaxation of a nuclear spin ensemble to the equilibrium distribution can be detected using a tank circuit. The most common NQR instruments are pulse type FFT spectrometers [65], [145] that excite spin states using an RF-pulse sequence, comparable to standard NMR-sequences but without exposing the sample to an external static flux density. For our investigations we mainly use well known sequences as for example spin echo (SE), free induction decay (FID) and inversion recovery (IR) using rectangular pulses together with phase cycling. Details concerning data analysis and fitting functions can be found in Appendix B, equations 3.13 and 3.14.

Beyond characterizing QN spin systems, NQR spectroscopy has proven its scientific versatility in several applications and studies as for example research on molecular structure [146] [147], superconductor [148], semiconductor [149], phase transition [150] [151], as well as quantum computing [68] or the authentication of medicines [59].

Experiments were done with two pulse-type NQR spectrometer working with two complementary frequency sweep methods both using a variety of transmit/receive coils. The self-built "Graz-NQRS-MK1 "[152] is particularly suitable for fast wide band sweeps up to 30 MHz bandwidth whereas the commercially available "Scout "(Tecmag, Inc., USA) allows for advanced pulse sequence programming. The probe coil is driven during transmit by a 500 W amplifier and enables $\pi/2$ pulses down to 300 ns. In combination, the two systems cover a frequency range of 20 MHz up to 150 MHz with an available temperature range from liquid nitrogen (special cryo coils [153]) up to 50°C (dry-air flow thermostatization). The temperature is measured using a type K thermocouple close to the probe coil. For transportation, storage and measurement the samples are stored in glass vials of 10 mm diameter and 40 mm length in form of a crystalline, solid powder.

3.6.2 QC calculation

First, the ionic positions in a periodic crystal model were optimized at DFT level using CASTEP [154] code keeping lattice parameters in their experimental values of the starting geometry [155]. The PBE functional with TS dispersion correction [156] was used with ultrasoft pseudopotentials [157] a cutoff energy of 240 eV, and Monkhorst-Pack k-point grid 4 X 4 X 1 with spacing < 0.03 Å^{-1} between points in each direction. After optimization, all forces acting on ions were less than 0.05 eV/Å.

The EFG at the site of ^{209}Bi of triphenylbismuth was first computed for solid state structures with the periodic ADF-BAND code of the Amsterdam Density Functional modelling suite [158, 159, 160] using the parameter-free PBE [161] DFT functional at zeroth order regular approximation (ZORA) level of theory including either SR (SR-ZORA) or both SR and SO effects (SO-ZORA). The more detailed study of electron correlations effects with hybrid PBE0 [162, 163] functional was then carried out for a single triphenylbismuth molecule either in its optimized solid state or experimentally found gas phase geometry (gas electron diffraction, GED), by Berger et al. [140]. The relativistic effects on the EFG tensor were also studied at the fully relativistic four-component Dirac-Coulomb (DC) and the exact two-component (X2C) relativistic approximation, as well as their spin-free counterparts (SF-DC and SF-X2C), with PBE0 functional using the DIRAC [164] code.

To estimate how much the EFG of the isolated molecule is affected due to geometry changes, we performed a structure optimization with ADF code at the PBE-D3_SR-ZORA_TZ2P level starting from the experimental gas phase structure [140]. The average changes in molecular geometry (see table 3.5 in Appendix C) due to optimization caused a 1.2% decrease of Q_{cc} (550.4 MHz, η = 0.001) at PBE_SO-ZORA_TZ2P level of theory, which is rather small change compared to other influences (see table 3.1 and table 3.2). In the ADF-BAND calculations of EFG tensors the Slater-type basis sets designed for ZORA calculations were used from the standard ADF basis set library [165]. Both triple-ζ with two (TZ2P) and quadruple-ζ with four (QZ4P) polarization functions basis sets were employed.

In calculations with DIRAC code, Gaussian-type nonrelativistic correlation-consistent polarized valence triple-ζ (cc-pVTZ) basis sets [166] were used for light H and C elements, whereas the relativistic prolapse-free quadruple-ζ (RPF-4Z) basis set [167] was used for ^{209}Bi.

All the calculated nuclear quadrupole coupling constants Q_{cc} were obtained from QC computed EFG tensors by using the most recent value for the nuclear quadrupole moment (NQM) of ^{209}Bi: Q(^{209}Bi) = -415.1 mb, [137] which is within the error bars of the other recent determination of Q(^{209}Bi) = -420(8) mb [53]. One should note that these values differ quite much from the old standard value of Q(^{209}Bi) = -516(15) [168].

Acknowledgements

The authors wish to acknowledge CSC-IT Center for Science, Finland, for computational resources, the European Commission in the frame of the H2020 Programme (FET-open, CONQUER) under grant agreement 665172, COST-STSM-CA1520937391, and the Academy of Finland (project no. 285666) for financial support. P.L. acknowledges Prof. Juha Vaara and Dr. Pär Håkansson for the scientific discussions. Also, we wish to thankfully acknowledge Dr. Eleonore Fröhlich for referencing and summarizing general questions on toxicity of Bi compounds.

3.7 Appendix A: The NQR transition spectrum

There are basically two conditions that have to be met by the molecule under consideration to develop an observable nuclear spin transition spectrum: 1) A nucleus exhibiting a non-spherical charge distribution, so that its Taylor expansion gives a non-zero quadrupolar term (valid for nuclear spin I>1/2), and 2), a non-zero EFG generated by the charges external to the nucleus (derived from the spatial derivative of the corresponding electrostatic potential ϕ: $\phi_{ij} = \frac{\partial^2 \phi}{\partial x_i \partial x_j}$ where x_i, x_j are Cartesian coordinates x,y,z and fulfilling $\Delta\phi = 0$).

The pure quadrupole Hamiltonian in some laboratory frame (LAB) can be expressed as the product of two irreducible rank two tensor operators $T_m^{(2)}$ and $V_m^{(2)}$ [48]:

$$H_Q(I)^{LAB} = \frac{Q_{cc}}{I(2I-1)} \sum_{m=-2}^{2} (-1)^m T_m^{(2)} V_{-m}^{(2)LAB} \tag{3.3}$$

$$\begin{aligned} T_0^{(2)}(I) &= \frac{1}{2}(3\widehat{I}_z^2 - I(I+1)) \\ T_{\pm 1}^{(2)}(I) &= \frac{\sqrt{6}}{4}(\widehat{I}_z\widehat{I}_\pm + \widehat{I}_\pm\widehat{I}_z) \\ T_{\pm 2}^{(2)}(I) &= \frac{\sqrt{6}}{4}\widehat{I}_\pm^2 \end{aligned} \tag{3.4}$$

The product of the EFG strength $eq = \phi_{zz}$ and the quadrupole contribution eq is called the quadrupole coupling constant $Q_{cc} = e^2qQ/\hbar$. The $\widehat{I}$'s denote the usual spin operators. In the principal axis system (PAS, where $\phi_{ij} = 0$ for $i \neq j$), which is a reference frame bound to the molecule, the EFG tensor operator $V_m^{(2)PAS}$ can be written as:

$$\begin{aligned} V_0^{(2)PAS} &= \sqrt{\frac{3}{2}}\phi_{zz} = \sqrt{\frac{3}{2}}eq \\ V_{\pm1}^{(2)PAS} &= 0 \\ V_{\pm2}^{(2)PAS} &= \frac{1}{2}\phi_{zz}\eta = \frac{1}{2}eq\eta \end{aligned} \tag{3.5}$$

$\eta = \frac{\phi_{xx}-\phi_{yy}}{\phi_{zz}}$ is the asymmetry parameter of the EFG, ranges between 0 and 1 and is a measure for the deviation from a cylindrically symmetric (η=0) EFG.

When applying an external flux density B_0 to the spin system, the Zeeman Hamiltonian

$$H_Z(I) = -\gamma_{QN}B_0\hat{I} \tag{3.6}$$

introduces an angle dependency $\Omega = (\alpha, \beta, \gamma)$ of the EFG with respect to the direction of B_0 which has to be considered when adding both quadrupolar and Zeeman interaction to the total Hamiltonian

$$H_0(I)(\Omega) = H_Q(I)(\Omega) + H_Z(I) \tag{3.7}$$

The tensor representation of $H_Q(I)$, equation 3.3, allows rotating the quadrupole interaction by the Euler angles $\Omega = (\alpha, \beta, \gamma)$ into the main quantization axis of the total Hamiltonian, e.g. defined by B_0. The rotation from the PAS to a LAB-system is performed using Wigner-D matrix elements:

$$V_m^{(2)LAB}(\Omega) = \sum_{m'=-2}^{+2} D_{m',m}^{(2)}(\Omega)V_{m'}^{(2)PAS} \tag{3.8}$$

The result of this transformation can be found in Possa *et al.* [68], and in equation 3.11.

The corresponding transition frequencies $\nu_{0,k}$ (in case of $B_0 = 0$, pure NQR transition frequencies $\nu_{Q,k}$) can be calculated straightforwardly by diagonalizing the total Hamiltonian $H_0(I)$ and thereby obtaining the energy levels E_α of the spin system with respect to the eigenfunctions $\{|\Psi_\alpha(\Omega)\rangle\}$:

$$\nu_{0,k} = E_\alpha - E_\beta = \langle\Psi_\alpha|\widehat{H}_0(I)|\Psi_\alpha\rangle - \langle\Psi_\beta|\widehat{H}_0(I)|\Psi_\beta\rangle \tag{3.9}$$

The eigenfunctions $\{|\Psi_\alpha(\Omega)\rangle\}$ can be expressed as linear combinations of the functions $|I, m_I\rangle$ of the Zeeman basis $\{|I, m_I\rangle\}$ with the magnetic quantum number $m_I = -I, -I+1, ..., I$: $|\Psi_\alpha(\Omega)\rangle = \sum_{m=-I}^{2I+1} a_{\alpha,m}(\Omega)|m\rangle$.

In case of ^{209}Bi, the nuclear spin of $I = 9/2$ leads to four transitions with Δm when $B_0 = 0$, as the energy levels are doubly degenerated in m_I. As soon as $B_0 \neq 0$, the energy levels and therefore the transition frequencies split up and form a more complex pattern. The principal behavior of the NQR pattern depending on B_0 is shown in figure 3.1(a) 1(a) and figure 3.1(b). In case of a powder sample, an average across a spherical distribution of Euler angles can be calculated. The intensity of the spectrum in figure 3.1 is proportional to Boltzmann population weighted transition probabilities:

$$I(\nu_{Q,k}) = |\langle \Psi_\alpha(\Omega)|H_{RF}|\Psi_\beta(\Omega)\rangle|^2 \cdot \frac{e^{-\frac{E_\alpha - E_\beta}{k_B T}}}{\sum_{i,j} e^{-\frac{E_i - E_j}{k_B T}}}. \tag{3.10}$$

H_{RF} is the radio frequency excitation Hamiltonian $H_{RF} \sim \widehat{I}_{\overrightarrow{x}} B_{RF}$ where $\overrightarrow{x}$ is the direction of the transmit/receive coil generating an oscillating flux density B_{RF}. T is the temperature and k_B Boltzmann's constant.

In this work, only pure NQR-transitions (no B_0-field) of powder samples are presented where the EFG is chosen to be in the PAS $\alpha = \beta = \gamma = 0$. Q_{cc} and η can be calculated numerically from two experimentally derived transition frequencies using equation 3.9.

Performing the transformation according to equation 3.8 the irreducible tensor operator elements have the form:

$$\begin{aligned}
V_0^{(2)LAB} &= \frac{1}{2}\left[\frac{(3cos^2\beta - 1)}{2} + \frac{\eta}{4} sin^2\beta(e^{-2i\gamma} + e^{-2i\gamma})\right] \\
V_{\pm 1}^{(2)LAB} &= \frac{1}{2}\left[\mp\sqrt{\frac{3}{8}} sin2\beta e^{\pm i\alpha} + \frac{\eta}{\sqrt{6}}\left(-\frac{1 \mp cos\beta}{2} sin\beta e^{\pm i(\alpha \mp 2\gamma)} + \frac{1 \mp cos\beta}{2} sin\beta e^{i(\pm\alpha + 2\gamma)}\right)\right] \\
V_{\pm 2}^{(2)LAB} &= \frac{1}{2}\left[\sqrt{\frac{3}{8}} sin^2\beta e^{\pm 2i\alpha} + \frac{\eta}{\sqrt{6}}\left(\frac{(1 \mp cos\beta)^2}{4} e^{\pm 2i(\alpha \mp \gamma)} + \frac{(1 \pm cos\beta)^2}{4} e^{2i(\pm\alpha + \gamma)}\right)\right]
\end{aligned} \tag{3.11}$$

The matrix-representation of equation 3.3 in the Zeeman basis $\{|I, m_I\rangle\}$, where $V_m^{(2)LAB}(\Omega)$ has to be included from equation 3.11, looks like:

$$H_Q = \begin{pmatrix}
\frac{Q_{cc}V_0}{2} & \frac{Q_{cc}V_{m1}}{\sqrt{6}} & \frac{Q_{cc}V_{m2}}{2\sqrt{6}} & 0 & 0 & 0 & 0 & 0 & 0 & 0 \\
-\frac{Q_{cc}V_{p1}}{\sqrt{6}} & \frac{Q_{cc}V_0}{6} & \frac{Q_{cc}V_{m1}}{\sqrt{6}} & \frac{1}{6}\sqrt{\frac{7}{2}}Q_{cc}V_{m2} & 0 & 0 & 0 & 0 & 0 & 0 \\
\frac{Q_{cc}V_{p2}}{2\sqrt{6}} & -\frac{Q_{cc}V_{p1}}{2\sqrt{6}} & -\frac{Q_{cc}V_0}{12} & \frac{1}{6}\sqrt{\frac{7}{2}}Q_{cc}V_{m1} & \frac{1}{4}\sqrt{\frac{7}{3}}Q_{cc}V_{m2} & 0 & 0 & 0 & 0 & 0 \\
0 & \frac{1}{6}\sqrt{\frac{7}{2}}Q_{cc}V_{p2} & -\frac{1}{6}\sqrt{\frac{7}{2}}Q_{cc}V_{p1} & -\frac{Q_{cc}V_0}{4} & \frac{Q_{cc}V_{m1}}{6} & \frac{5Q_{cc}V_{m2}}{12} & 0 & 0 & 0 & 0 \\
0 & 0 & \frac{1}{4}\sqrt{\frac{7}{3}}Q_{cc}V_{p2} & -\frac{Q_{cc}V_{p1}}{6} & -\frac{Q_{cc}V_0}{3} & 0 & \frac{5Q_{cc}V_{m2}}{12} & 0 & 0 & 0 \\
0 & 0 & 0 & \frac{5Q_{cc}V_{p2}}{12} & 0 & -\frac{Q_{cc}V_0}{3} & -\frac{Q_{cc}V_{m1}}{6} & \frac{1}{4}\sqrt{\frac{7}{3}}Q_{cc}V_{m2} & 0 & 0 \\
0 & 0 & 0 & 0 & \frac{5Q_{cc}V_{p2}}{12} & -\frac{Q_{cc}V_{p1}}{6} & -\frac{Q_{cc}V_0}{4} & -\frac{1}{6}\sqrt{\frac{7}{2}}Q_{cc}V_{p2} & \frac{1}{6}\sqrt{\frac{7}{2}}Q_{cc}V_{m2} & 0 \\
0 & 0 & 0 & 0 & 0 & \frac{1}{4}\sqrt{\frac{7}{3}}Q_{cc}V_{p2} & \frac{1}{6}\sqrt{\frac{7}{2}}Q_{cc}V_{p1} & -\frac{Q_{cc}V_0}{12} & -\frac{Q_{cc}V_{m2}}{\sqrt{6}} & \frac{Q_{cc}V_{m2}}{2\sqrt{6}} \\
0 & 0 & 0 & 0 & 0 & 0 & \frac{1}{6}\sqrt{\frac{7}{2}}Q_{cc}V_{p2} & -\frac{Q_{cc}V_{p1}}{\sqrt{6}} & \frac{Q_{cc}V_0}{6} & -\frac{Q_{cc}V_{m1}}{\sqrt{6}} \\
0 & 0 & 0 & 0 & 0 & 0 & 0 & \frac{Q_{cc}V_{p2}}{2\sqrt{6}} & \frac{Q_{cc}V_{p1}}{\sqrt{6}} & \frac{Q_{cc}V_0}{2}
\end{pmatrix} \tag{3.12}$$

TABLE 3.3: Phase of pulses for SE and IR.

π (only for IR)	117°	117°	117°	117°
$\pi/2$	0	1	2	3
π	1	1	1	1
RX	0	3	2	1

3.8 Appendix B: Data analysis and fitting procedure

The spin-lattice ($T_{1,Q}$) and spin-spin ($T_{2,Q}$) relaxation times of all found transition peaks were experimentally determined using inversion recovery (IR) and spin echo (SE) sequences with variable inversion time T_I and echo time T_E respectively (phase cycling see table 3.3). The data was analyzed using standard fitting procedure of the usual, well known models [169]:

$$M_{IR}(T_I) = M_0(1 - 2 \cdot e^{-\frac{T_I}{T_{1,Q}}}) + B \tag{3.13}$$

$$M_{SE}(T_E) = M_0 \cdot e^{-\frac{T_E}{T_{2,Q}}} + B \tag{3.14}$$

To fit the peak shape, a Lorentzian shape is assumed, which holds true for monoexponential decays:

$$\begin{aligned} L(\nu) &= \frac{I}{1 + (\frac{\nu - \nu_c}{\gamma})^2} + B \\ FWHM &= 2\gamma \end{aligned} \tag{3.15}$$

An example of the application of the models is given in figure 3.9 and table 3.4 for tris(4-methoxyphenyl) bismuth (4), transition 2 at 310 K: $T_{1,Q}$ = 958 μs, $T_{2,Q}$ = 369 μs, ν_C = 56.88 kHz, FWHM = 51 kHz, stepsize ΔT_E = 4 μs , ΔT_I = 10 μs.

The temperature dependency of the transition frequency is assumed to be linear in the range of several degrees ($\Delta T \pm 5$°C) around the target temperature of 310 K (37 °C). The linear temperature coefficient C_{37} is determined by measuring the transition frequency $\nu_{Q,k}$ for several sample temperatures:

$$\nu_{Q,k}(T) = C_{37}\Delta T + \nu_{37} \tag{3.16}$$

Raw data as well as fitting parameters for each measurement are available anytime in detail on request.

3.9 Appendix C: Experimental data and error estimation

General error estimation to the data in table 3.6 and table 3.7:

Temperature accuracy:
0.1 K (accuracy of temperature controller)

TABLE 3.4: Example for fitting result of figure 3.9 including result and standard error according to equations 3.13, 3.14 and 3.15.

IR	M_0 (arb. units)	$T_{1,Q}$ (μs)	B (arb. units)	-
value	$7.8286 \cdot 10^{-1}$	958.3	$1.4471 \cdot 10^{-1}$	-
std. error	$0.027 \cdot 10^{-1}$	7.8	$0.0371 \cdot 10^{-1}$	-
SE	M_0 (arb. units)	$T_{2,Q}$ (μs)	B (arb. units)	-
value	$9.5343 \cdot 10^{-1}$	368.6	$3.346 \cdot 10^{-2}$	-
std. error	$0.0295 \cdot 10^{-1}$	2.5	$0.136 \cdot 10^{-2}$	-
L	γ (kHz)	ν_c (kHz)	I (arb. units)	B (arb. units)
value	25.38	$56.882 \cdot 10^3$	$9.63 \cdot 10^{-1}$	$8.2 \cdot 10^{-3}$
std. error	0.50	$0.00033 \cdot 10^3$	$0.13 \cdot 10^{-1}$	$1.7 \cdot 10^{-3}$

TABLE 3.5: Sample overview; crystal structures, structure info, references and source.

Nr	sample name	crystal structure	average Bi-C distance (Å)	sum of angles C-Bi-C (°)	structure reference	hydrolytic stability	synthesize reference
1	triphenylbismuth	monoclinic C2/c	2.260	281.68	[155]	yes	[170, 171, 172]
2	tris(4-fluorophenyl) bismuth	monoclinic P2(1)/c	2.262	285.38	n.a.	yes	[172]
3	tris(4-dimethylamino) bismuth	triclinic, P-1	2.242	283.04	[173]	yes	[174]
4	tris(4-methoxyphenyl) bismuth	trigonal, R-3	2.252	281.37	[172]	yes	[172]
5A	tris(2-methoxyphenyl) bismuth, site A	rhombohedral R3	2.248	282.62 /277.4	[131, 175]	yes	[176]
5B	tris(2-methoxyphenyl) bismuth, site B	disordered	n.a.	n.a.	[131]	yes	[176]
6	tris(2-6-dimethoxyphenyl) bismuth	monoclinic P21/c	2.262	296.8	[177]	yes	[176]
7A	triphenylbismuth dichloride, site A	orthorhombic P2(1)2(1)2(1)	2.129	n.a.	[130]	no	[171, 178]
7B	triphenylbismuth dichloride, site B	orthorhombic P2(1)2(1)2(1)	2.116	n.a.	[130]	no	[171, 178]
8	triphenylbismuth deuterated	monoclinic C2/c	see Nr.1	see Nr.1	n.a.	yes	n.a.
n.a.	triphenylbismuth, gas phase	n.a.	2.263	284.13	[140], GED structure	n.a.	n.a.
n.a.	triphenylbismuth, ADF optimized, gas phase	n.a.	2.279	282.08	n.a.	n.a.	n.a.
n.a.	triphenylbismuth, CASTEP optimized, periodic	monoclinic, C2/c	2.291	282.62	n.a.	n.a.	n.a.

TABLE 3.6: Measured NQR transition frequencies $\nu_{Q,k}$ and derived NQR parameter Q_{cc} and η at different temperatures (310 K, 300 K and 77 K) for eight Bi-aryl compounds.

		transition frequency $\nu_{Q,k}$ (MHz)[a]						
Nr.	sample name temperature (K)		1	2	3	4	Q_{cc} (MHz)[b]	η (1)[c]
1	triphenylbismuth	310	*29.67*	55.14	83.42	111.32	668.3	0.087
		300	*29.76*	55.21	83.5	111.42	668.9	0.083
		77	30.6	56.45	85.45	114.03	684.6	0.090
2	tris(4-fluorophenyl) bismuth	310	*28.60*	54.51	82.11	109.54	657.5	0.071
		77	28.65	55.86	84.02	112.06	672.5	0.053
3	tris(4- dimethylamino) bismuth	310	*28.34*	54.94	82.52	110.06	660.6	0.058
		77	*28.23*	*56.20*	84.35	112.47	674.8	0.020
4	tris(4-methoxyphenyl) bismuth	310	28.49	56.88	85.34	113.77	682.5	0.000
		77	29.17	n.a.	n.a.	n.a.	n.a.	n.a.
5A	tris(2-methoxyphenyl) bismuth site A	310	(29.82)	59.64	89.47	119.27	715.2	0.000
5B	tris(2-methoxyphenyl) bismuth site B	310	29.76	59.45	89.29	119.06	714.3	0.000
6	tris(2-6-dimethoxyphenyl) bismuth	310	*30.14*	54.40	82.45	110.06	660.90	0.105
7A	triphenylbismuth dichloride site A	310	(44.14)	86.4	129.91	*173.30*	1039.70	0.046
		77	45.51	87.50	*131.80*	*175.80*	1055.3	0.063
7B	triphenylbismuth dichloride site B	310	(44.81)	89.20	133.86	*178.50*	1071	0.020
		77	45.80	91.24	*136.90*	*182.60*	1095.4	0.020
8	triphenylbismuth deuterated	310	*29.68*	55.20	83.49	111.40	668.8	0.086
		300	29.82	55.25	83.58	111.56	669.9	0.098

n.a. : not available, italic values: theoretically predicted and have not been measured yet, values in brackets have larger errors.
[a] $\Delta\nu_{Q,k}$ = ± 10 kHz (310 K), Δ $\nu_{Q,k}$ = ± 30 kHz (300 K and 310 K in brackets), Δ $\nu_{Q,k}$ = ± 5 kHz (77 K)
[b] ΔQ_{cc} = ± 0.4 MHz (310 K), Δ Q_{cc} = ± 0.6 MHz (300 K and 310 K in brackets), Δ Q_{cc} = ± 0.2 MHz (77 K)
[c] $\Delta\eta$ = ± 0.001 (310 K), $\Delta\eta$ = ± 0.004 (300 K and 310 K in brackets), $\Delta\eta$ = ± 0.001 (77 K)

TABLE 3.7: Measured NQR relaxation times $T_{1,Q}$ and $T_{2,Q}$, FWHM of Lorentzian Peak shape and transition frequencies $\nu_{Q,k}$

Nr.	sample name	transition	temperature (K)[a]	$T_{1,Q}$ (μs)[b]	$T_{2,Q}$ (μs)[c]	FWHM (kHz) [d]	$\nu_{Q,k}$ (MHz) [e]
1	triphenylbismuth	2	310	1123	277	4	55.14
		3	310	548	436	15	83.42
		4	310	835	486	5	111.32
		1	300	2915	80	10	29.76
		2	300	1547	222	7	55.21
		3	300	820	396	7	83.50
		4	300	966	434	9	111.42
		1	77	63738	102	27	30.60
		2	77	18000	394	12	56.45
		3	77	16400	802	4	85.45
		4	77	17029	822	5	114.03
2	tris(4-fluorophenyl) bismuth	2	310	201	81	10	54.51
		3	310	91	66	18	82.11
		4	310	89	83	22	109.54
		1	77	11182	48	22	28.65
		2	77	2930	450	8	55.86
		3	77	2322	581	9	84.02
		4	77	1754	546	10	112.06
3	tris(4- dimethylamino) bismuth	2	310	238	109	19	54.94
		3	310	193	108	32	82.52
		4	310	231	115	20	110.06
		3	77	2600	360	poor fit	84348.00
		4	77	3700	400	poor fit	112469.00
4	tris(4-methoxyphenyl) bismuth	1	310	2897	51	17	28.49
		2	310	958	369	51	56.88
		3	310	768	245	43	85.34
		4	310	872	294	66	113.77
		1	77	n.a.	42	14	29.12
5A	tris(2-methoxyphenyl) bismuth site A	1	(310)	1261	57	11	29.82
		2	310	570	370	25	59.64
		3	310	334	284	36	89.47
		4	310	426	315	41	119.27
5B	tris(2-methoxyphenyl) bismuth site B	2	310	64	58	48	59.45
		3	310	64	51	45	89.30
		4	310	61	67	63	119.06
6	tris(2-6-dimethoxyphenyl) bismuth	2	310	122	69	10	54.40
		3	310	50	51	14	82.45
		4	310	78	56	14	110.06
7A	triphenylbismuth dichloride site A	1	(310)	98	52	poor fit	44.14
		2	310	63	50	25	86.40
		3	310	46	44	36	129.91
		2	77	940	310	7	87.50
		1	77	1846	90	16	45.51
7B	triphenylbismuth dichloride site B	1	(310)	241	40	6	44.81
		2	310	108	46	9	89.20
		3	310	54	28	17	133.86
		1	77	985	69	poor fit	45.80
		2	77	397	311	8	91.24
8	triphenylbismuth deuterated	1	300	2381	418	20	29.82
		2	300	1472	525	11	55.25
		3	300	909	636	13	83.58
		4	300	1049	693	16	111.56
		2	310	1104	621	11	55.20
		3	310	646	629	11	83.49
		4	310	725	712	15	111.40

n.a.: not available, poor fit: due to poor frequency resolution, temperatures in brackets have higher uncertainty

[a] temperature accuracy: 0.5 K

[b,c] at 300 K/310 K: For $T_{2,Q} > 200$ μs $\Delta T_{1,Q}$: $< 12\%$, $\Delta T_{2,Q}$: $< 12\%$ For $T_{2,Q} < 200$ μs Δ $T_{1,Q}$: $< 22\%$, $\Delta T_{2,Q}$: $< 22\%$

[b,c] at 77 K: For $T_{2,Q} > 200$ μs Δ $T_{1,Q}$: $< 7\%$, Δ $T_{2,Q}$: $< 7\%$ For $T_{2,Q} < 200$ μs Δ $T_{1,Q}$: $< 12\%$, $\Delta T_{2,Q}$: $< 12\%$

[d] Δ FWHM: $\pm$ 1 kHz, due to fitting, see table 3.4

[e] $\Delta\nu_{Q,k}$ at 310 K = $\pm$ 10 kHz, $\Delta\nu_{Q,k}$ at (310 K) = $\pm$ 30 kHz, $\Delta\nu_{Q,k}$ at 300 K = $\pm$ 30 kHz

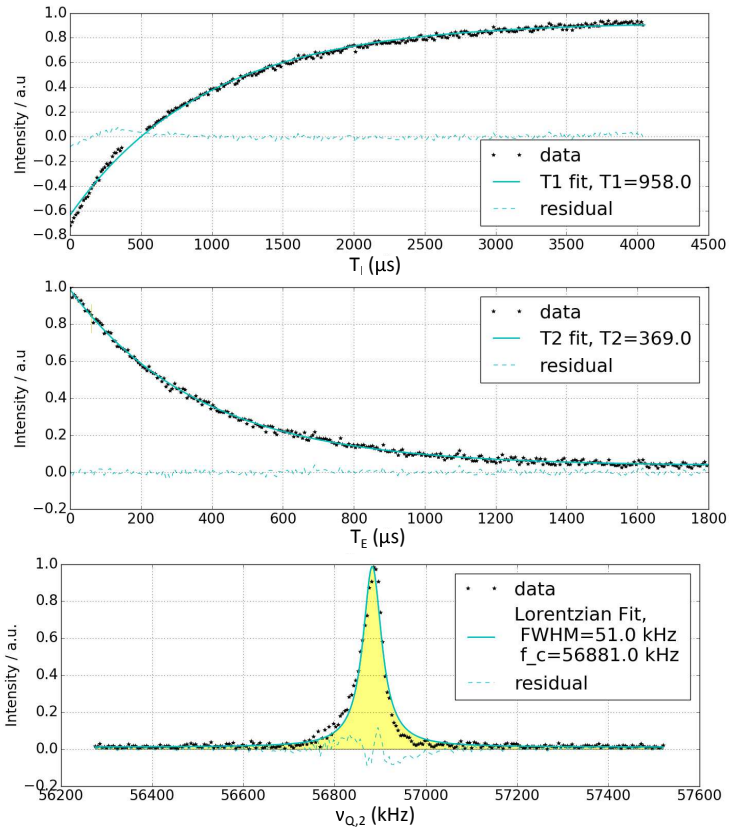

FIGURE 3.9: Example for T_1 and T_2 measurement and fitted models; sample (4), transition 2 at 310 K . Results see table 3.4.

0.5 K (experimental accuracy due to drift and offset (thermocouple position))

NQR-parameter:
at 310 K: $\Delta\nu_{Q,k}$ = ±10 kHz (due to temperature stability during 1 h measurement)
ΔQ_{cc}: ±0.4 MHz (calculation variation within transition frequency limits)
$\Delta\eta$: ±0.001 (calculation variation within transition frequency limits)
at 300 K, at (310 K): $\Delta\ \nu_{Q,k}$ = ± 30 kHz (extended sample-thermocouple distance)
ΔQ_{cc}: ± 0.6 MHz (calculation variation within transition frequency limits)
$\Delta\eta$: ±0.003 (calculation variation within transition frequency limits)
at 77 K: $\Delta\nu_{Q,k}$ = ±5 kHz (spectrometer accuracy)
ΔQ_{cc}: ±0.2 MHz (calculation variation within transition frequency limits)
$\Delta\eta$: ±0.001 (calculation variation within transition frequency limits)

linear temperature coefficient C_{37}
±0.2 kHz/K (due to average deviation in 95% confidence bound)

Relaxation times:
Statistical fitting error:
$\Delta T_{1,Q}$: < 2 % standard error (due to average deviation in 95% confidence bound)

TABLE 3.8: Linear temperature coefficient C_{37} of selected NQR transition frequencies of several Bi-aryl compounds.

Nr.	sample name	transition	C_{37} (kHz/K)[a]
1	triphenylbismuth	3	-9.2
		4	-10.4
2	tris(4-flurophenyl) bismuth	3	-5.9
		4	-6.4
3	tris(4- dimethylamino) bismuth	3	-5.7
		4	-6.4
4	tris(4-methoxyphenyl) bismuth	2	-4.7
		3	-6.2
		4	-7.1
5A	tris(2-methoxyphenyl) bismuth site A	2	-2.9
		3	-4.2
		4	-4.9
7B	triphenylbismuth dichloride site B	1	-8.7
		2	-8.7
		3	-8.9

[a] $\Delta C_{37} = \pm$ 0.2 kHz/K

$\Delta T_{2,Q}$: <2 % standard error (due to average deviation in 95% confidence bound)
Systematic error: (mainly due to temperature drift during the experiment and estimated from repeated T_2 and T_1 determination on a single transition, higher errors for low T_2 measurements due to low SNR)
at 300 K/310 K: For $T_{2,Q}$ > 200 μs $\Delta T_{1,Q}$: $<$ 10%, $\Delta T_{2,Q}$: $<$ 10%
For $T_{2,Q} < 200$ μs $\Delta T_{1,Q}$: $<$ 20%, $\Delta T_{2,Q}$: $<$ 20%
at 77 K: For T_2 > 200 μs $\Delta T_{1,Q}$: $<$ 5 %, $\Delta T_{2,Q}$: $<$ 5%
For $T_2 < 200$ μs $\Delta T_{1,Q}$: $<$ 10 %, $\Delta T_{2,Q}$: $<$ 10%

Chapter 4

Predicting quadrupole relaxation enhancement peaks in proton R_1-NMRD profiles in solid Bi-aryl compounds from NQR parameters

Christian Gösweiner[a*], Danuta Kruk[b], Evrim Umut[b], Elzbieta Masiewicz[b], Markus Bödenler[a] and Hermann Scharfetter[a]

[a]*Institute of Medical Engineering, Graz University of Technology, Graz, Austria*
[b]*Faculty of Mathematics and Computer Science, University of Warmia and Mazury in Olsztyn, Olsztyn, Poland*

published in:
Molecular Physics, 117:7-8, 910-920, DOI: 10.1080/00268976.2018.1519201 [179]

Abstract

We propose a simple method to calculate and predict quadrupole relaxation enhancement (QRE) features in the spin-lattice nuclear magnetic relaxation dispersion (R_1-NMRD) profile of protons (^1H) in solids. The only requirement is the knowledge of the nuclear quadrupole resonance (NQR) parameters of the quadrupole nuclei in a molecule. These NQR parameters- the quadrupole coupling constant Q_{cc} and the asymmetry parameter η - can be determined by NQR spectroscopy or using quantum chemistry calculations. As there is an increasing interest in using molecules producing high field QRE features as e.g. for contrast enhancing agents in magnetic resonance imaging, the experimental efforts of seeking for suitable compounds can be reduced by pre-selecting molecules via calculations. Also, the method can be used to extract NQR parameter, and thus structural information, from R_1-NMRD profiles showing QRE features. In this article, we describe the calculation procedure and present examples of comparing the result to experimental R_1-NMRD data of two different solid ^{209}Bi-aryl compounds.

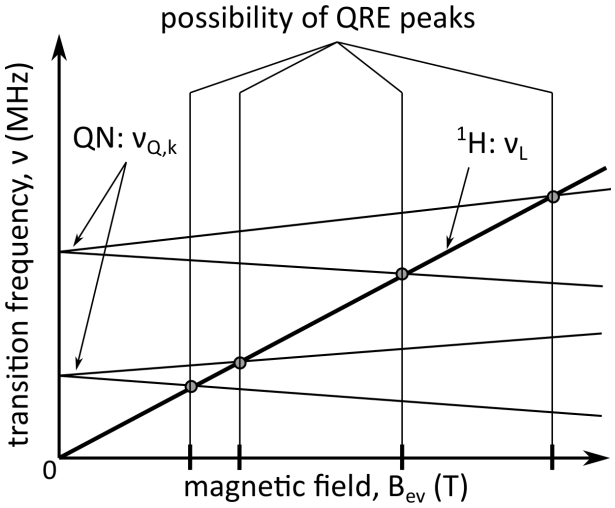

FIGURE 4.1: Scheme of the nuclear spin transition frequency for a proton ν_L and a QN ν_Q with I=5/2 versus the magnetic evolution field. At the B_{ev} field positions of the level crossings, QRE features can be expected in case that there is a D-D coupling present between QN and proton originating from spin fluctuations due to molecular motions.

4.1 Introduction

An application of nuclear magnetic resonance (NMR), forming a field of research by its own, is the measurement of spin-lattice relaxation rates R_1 of nuclear spins. Experiments can be performed on a great variety of materials from condensed matter to liquids. As one is typically interested in molecular motions, such measurements are done temperature and/or field dependent by means of NMR field cycling (FC) relaxometry [180]. This method allows to study $R_1(\nu_L)$ of protons on a broad band Larmor frequency scale ν_L which is achieved by stepping the external magnetic field value B_{ev} (evolution field) applied to the sample at different cycles during a dispersion measurement. The experimental procedure uses an elaborate way of cycling the magnetic field in a sequence for enabling polarization, evolution and detection of a nuclear spin ensemble. The evolution field can typically be varied to create proton Larmor frequencies from as low as 10 kHz to about 40 MHz. The experiments presented later in this article, however, are conducted between 20 MHz up to 128 MHz by the use of an additional superconducting 3 T magnet [94]. An early detailed description of the method can be found in the work of F. Noack [181], a more recent review is given in reference [180]. FC-NMR relaxometry nowadays is a standard analysis method and is applied to a wide range of research fields as e.g. ionic crystals [182], liquid crystals [183], lipids [184], polymer dynamics [185], porous media [186] or, as formulated quite generally in another review [17], to *molecular dynamics in complex media*. The resulting measurements of the frequency dependence of R_1 is often referred to as nuclear magnetic relaxation dispersion (NMRD) profile. A method for gaining insight into molecular dynamics from analysing NMRD profiles is e.g. the Redfield relaxation theory [97].

However, not only dynamical properties but also structural information from solids is accessible from NMRD measurements. The quadrupole relaxation enhancement (QRE, [29, 31, 119, 40, 34]) effect can create pronounced and prominent features (peaks) in the R_1-NMRD profile, depending on the type of quadrupole nuclei (QN, $I > 1/2$) and structure of their electronic surrounding. This so called QRE-peaks (also called quadrupolar dips in case of a $T_1 = 1/R_1$ dispersion representation) emerge due to a magnetization transfer from the protons to nearby (only several Å) QN via magnetic dipole dipole (D-D) coupling which is manifested in an increase of the relaxation rate R_1 of the proton spins. The effect is frequency (magnetic field) dependent, because QRE can only occur where both the transition frequencies ν_L of the protons (their Larmor frequency) and ν_Q of a coupled pool of quadrupole nuclei match (see figure 4.1). One of the first articles demonstrating this effect is dealing with powdery polyvinylchloride containing ^{35}Cl and ^{37}Cl nuclei (I=3/2)[31]. Also, studies on solids containing ^{14}N [187, 188] were reported. Cases were presented, where ^{14}N (I=1) nuclei produce QRE peaks in the NMRD profile of biological systems e.g. proteins in muscles [189, 32]. Lurie *et al.* [33] have utilized this effect for magnetic resonance imaging (MRI) and could demonstrate a contrast enhancement in $T_1 = 1/R_1$ weighted images using a special field cycling MRI systems at low magnetic field strengths (< 200 mT). Field cycling MRI has also been successfully demonstrated at clinical field strengths of 1.5 T [128, 112, 110] and 3 T [129]. Recently, strong and pronounced QRE peaks have been observed in NMRD measurements of different Bi-aryl compounds [94]. The experimental data of this article will be used to evaluate the herein presented simulation.

Aim of this work is to predict the location of QRE peaks in proton R_1-NMRD profiles of solids from the nuclear quadrupole resonance (NQR) parameters of the QRE-active nuclei by calculating NQR transition probabilities. As we do not directly include relaxation processes the approach is fairly simple to calculate and gives, as is shown later, reliable results. This is especially favorable when considering the increasing interest in QN compounds creating QRE peaks in proton R_1-NMRD profiles at high fields (e.g. 3 T) to use them as MRI contrast agents [61] while the measurements of such is not yet straightforward and connected with technical challenges. Also, the availability of such systems is not yet very high. The NQR parameters on the contrary are accessible with NQR spectrometers working in the radio frequency regime and to some degree also through quantum chemistry (QC) calculations. Of course, the approach can also be used for the other way round: determining NQR parameters from NMRD profiles showing QRE peaks which could be used to double check NQR results or to support the determination of NQR parameters where NQR spectroscopy is problematic.

The central idea can be summarized by formulating four assumptions:

Assumption (1): As in solid powders the nuclei cannot rotate freely their energy level structure is essentially static and determines the NQR powder spectra $\nu_Q(B_{ev})$ in the presence of an external magnetic field by applying the unperturbed

total Hamiltonian as a sum of quadrupole and Zeeman Hamiltonian. From that, the transition probability $p_Q(B_{ev})$ can be calculated by summing up all contributions over all orientations of the crystallites.

Assumption (2): QRE can only occur at magnetic fields B_{ev} at which $\nu_L(B_{ev})$ matches a QN transition frequency $\nu_Q(B_{ev})$.

Assumption (3) states, that the QRE amplitude at B_{ev} depends on the joint transitions probability between eigenstates of the spin system of the QN - ^{1}H pair mediated by D-D coupling. As we neglect the proton relaxation, the sole QN transitions probability $p_Q(B_{ev})$ is considered. This has the consequence, that the QRE amplitudes will not be reproduced completely correct.

Assumption (4) proposes, that the relaxation of NQR transitions due to perturbations of the QN energy level structure (which acts as the mechanism in the QRE process for dissipating the magnetization to the lattice) can be regarded as small and enters the calculation only phenomenological by the assumption of a certain linewidth for zero field transitions.

4.2 Theory

4.2.1 The calculation procedure

Details of how to calculate the NQR powder spectrum will be matter of the following sections, but to understand the calculation procedure, one has to know that a QN can already exhibit excitable spin transitions $\nu_{Q,k}$ at zero magnetic field [42]. Depending on its nuclear spin quantum number I, one can observe- in case of half integer spins- $I + 1/2 - 1$ transitions k. As ν_L is given by the product of the proton's gyromagnetic ratio γ_p times the applied field B_{ev} in qualitatively the same way as the splitting of quadrupole transitions is given by γ_{QN} times B_{ev}, the only determinant of the frequency locations of the transition crossings are the pure quadrupole transition frequencies of the QN at zero magnetic field (see figure 4.1). These are the result of an electrical interaction between the electric field gradient (EFG) at the nucleus of interest and its quadrupole moment Q being present in the QN containing molecule.

Keeping this in mind, the calculation procedure can best be explained by an extension of figure 4.1 towards a more general case where the EFG is not aligned with B_{ev} but randomly uniformly distributed, thus leading to a powder spectrum at each B_{ev} (see figure 4.2). Also, the intensity of the NQR powder spectrum is included. Again, the nuclear spin transition frequencies of a proton and a QN in the presence of a magnetic evolution field B_{ev} are plotted in the transversal plane. On the z-axis additionally the intensity of the NQR powder spectrum is drawn. So, figure 4.2 shows the spectral NQR intensity as a function of frequency in dependence on the magnetic field. In particular six selected NQR spectra are drawn and labelled with colours from dark red to yellow, the brightness indicating the increasing B_{ev}. The

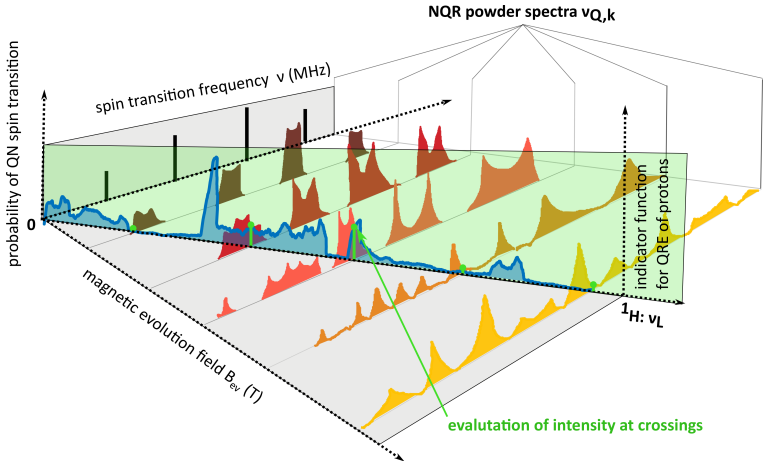

FIGURE 4.2: Scheme to illustrate the calculation procedure for predicting QRE peak positions in NMRD measurements. The x-y plane of the 3D plot is spanned by the spin transition frequency versus the magnetic field B_{ev} which is applied to a proton and a QN. The z-axis gives the intensity of the NQR powder spectrum which depends on the QN spin transition probability p_Q. When following the proton Larmor frequency along the x-y plane, the NQR spectrum intensity can be evaluated at a set of points along the magnetic evolution field. Some evaluation positions, which correspond to the transition crossings, are marked in green color. The thereby generated intensity profile in blue gives an estimate for the probability of a QRE feature in an R_1-NMRD profile of slowly rotating or static (in solids) systems.

oblique plane is aligned with the proton Larmor frequency ν_L and thus acts as an indicator function which cuts out the quadrupole transition probability exactly at the corresponding crossover points, as indicated exemplary by the vertical light green lines ("evaluation points"). The resulting pattern along this indicator plane is used for predicting the QRE transition probability and thus those bands where QRE most likely can be expected. As it does not account for lineshapes or spectral densities of the D-D fluctuations it must not be interpreted quantitatively, i.e. in terms of QRE strength.

4.2.2 NQR powder spectrum

The required theory in order to obtain the quadrupole transition frequencies ν_Q and their expectable NQRS intensities $I_{NQR}(\nu_Q)$ in the presence of an external static magnetic field B_0 is well described in references [42, 48, 68] and will be adapted and summarized in the following section.

The interaction of nuclei exhibiting a quadrupole moment Q (for $I > 1/2$) with an electric field gradient (EFG, $V_{ij} = \frac{\partial^2 V}{\partial x_i \partial x_j}$) resulting from surrounding binding electrons forming the electrostatic potential V, gives rise to discrete energy levels of the nuclear spin. A nucleus with e.g. spin number $I = 5/2$ has $2I + 1 = 6$ energy levels denoted with $m = -I ... + I$.

The interaction can be fully described by just two parameters: the quadrupole coupling constant Q_{cc} and the asymmetry parameter η which appear in the pure

NQR Hamiltonian $\widehat{H}_Q(I)$ in the laboratory frame (LAB):

$$\widehat{H}_Q(I)^{LAB} = \frac{Q_{cc}}{I(2I-1)} \sum_{m=-2}^{2} (-1)^m T_m^{(2)} V_{-m}^{(2)LAB} \tag{4.1a}$$

$$\begin{aligned} T_0^{(2)}(I) &= \frac{1}{2}(3\widehat{I}_z^2 - I(I+1)) \\ T_{\pm1}^{(2)}(I) &= \frac{\sqrt{6}}{4}(\widehat{I}_z\widehat{I}_\pm + \widehat{I}_\pm\widehat{I}_z) \\ T_{\pm2}^{(2)}(I) &= \frac{\sqrt{6}}{4}\widehat{I}_\pm^2 \end{aligned} \tag{4.1b}$$

$Q_{cc} = e^2qQ/\hbar$ is made up of the product of the EFG strength eq and the quadrupole contribution eQ with the quadrupole moment Q. The asymmetry parameter $\eta = \frac{V_{xx}-V_{yy}}{V_{zz}}$ is a measure for the deviation of the EFG from cylinder symmetry. The $\widehat{I}$'s denote the usual spin angular momentum operators.

As we are applying an external static magnetic field, the Zeeman Hamiltonian $\widehat{H}_Z(I)$ has to be added to the total Hamiltonian $\widehat{H}_0(I)(\Omega)$:

$$\widehat{H}_0(I)(\Omega) = \widehat{H}_Z(I) + \widehat{H}_Q(I)(\Omega). \tag{4.2a}$$

$$\widehat{H}_Z(I) = -\gamma_{QN}\,\overrightarrow{B}_{ev} \cdot \overrightarrow{\widehat{I}} \tag{4.2b}$$

$\widehat{H}_Z(I)$ introduces an angle dependency $\Omega = (\alpha, \beta, \gamma)$ between the direction of the EFG and the applied magnetic field $\overrightarrow{B}_{ev}$. γ_{QN} is the gyromagnetic ratio of the quadrupole nucleus under investigation.

In order to account for the required rotation into the same coordinate system (LAB), the spatial tensor operators $V_m^{(2)}$ have to be written in the following form [68]:

$$\begin{aligned} V_0^{(2)LAB} &= \frac{1}{2}\left[\frac{(3cos^2\beta - 1)}{2} + \frac{\eta}{4}sin^2\beta(e^{-2i\gamma} + e^{-2i\gamma})\right] \\ V_{\pm1}^{(2)LAB} &= \frac{1}{2}\left[\mp\sqrt{\frac{3}{8}}sin2\beta e^{\pm i\alpha} + \frac{\eta}{\sqrt{6}}\left(-\frac{1 \mp cos\beta}{2}sin\beta e^{\pm i(\alpha\mp2\gamma)} + \frac{1 \mp cos\beta}{2}sin\beta e^{i(\pm\alpha+2\gamma)}\right)\right] \\ V_{\pm2}^{(2)LAB} &= \frac{1}{2}\left[\sqrt{\frac{3}{8}}sin^2\beta e^{\pm2i\alpha} + \frac{\eta}{\sqrt{6}}\left(\frac{(1 \mp cos\beta)^2}{4}e^{\pm2i(\alpha\mp\gamma)} + \frac{(1 \pm cos\beta)^2}{4}e^{2i(\pm\alpha+\gamma)}\right)\right] \end{aligned} \tag{4.3}$$

To finally obtain the transition frequencies ν_Q, the total Hamiltonian from (4.2a) is being diagonalized numerically and we end up with the energy levels E_α of the spin system with respect to the eigenfunctions $|\Psi_\alpha(\Omega)\rangle = \sum_{m=-1}^{2I+1} a_{\alpha,m}(\Omega)|I,m\rangle$, where $\{|I,m\rangle\}$ is the orthonormal Zeeman basis, in short, written as $\{|m\rangle\}$. The angle dependent NQR transition frequencies $\nu_Q(\Omega)$ at an external magnetic field B_{ev} can

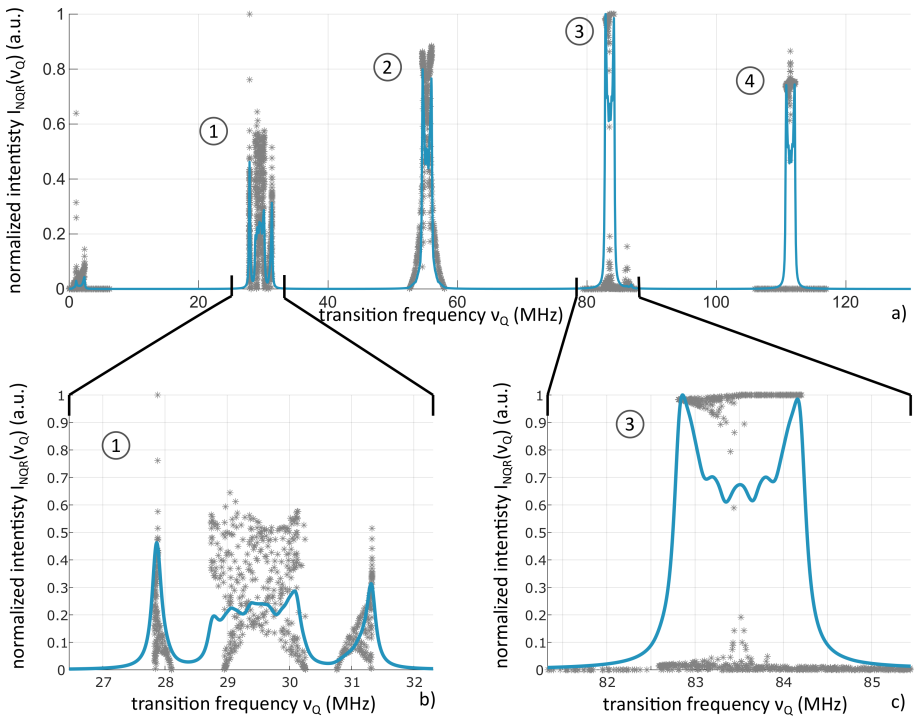

FIGURE 4.3: Simulated NQR powder spectrum at an external magnetic field of 100 mT for triphenylbismuth according to equation (4.7). The grey dots in the background correspond to the result of equation (4.6) evaluated for a single angle Ω. The blue line gives the normalized summation of all grey points according to equation (4.7). Panel a) shows the whole spectrum from 0 to 120 MHz. Panel b) and c) zoom into two selected bands which show the splitting of transition 1 and 3, respectively. While transition 3 shows a typical Pake-pattern, the low-frequency pattern corresponding to transition 1 is comparatively complex. The reason for this shape has been described elsewhere [42]. Input parameters for triphenylbismuth from reference[61]: Q_{cc} = 668.87 MHz, η = 0.08, I = 9/2, γ_{Bi} = 6.95 MHz/T, FWHM of single intensity = 40 kHz. N = 200.

be expressed by the difference between two energy levels E:

$$\nu_Q(\Omega, B_{ev}) = E_\alpha - E_\beta = \langle \Psi_\alpha(\Omega)|\widehat{H}_0(I)(\Omega)|\Psi_\alpha(\Omega)\rangle - \langle \Psi_\beta(\Omega)|\widehat{H}_0(I)(\Omega)|\Psi_\beta(\Omega)\rangle \tag{4.4}$$

4.2.3 Intensity of the NQR powder spectrum

A NQR experiment can be performed by exciting a QN spin transition with an oscillating magnetic field with amplitude $\overrightarrow{B}_{RF}$ in an arbitrary direction (x,y,z) at angular frequency ω_{RF} and phase ϕ_{RF} described by the RF-Hamiltonian [68]

$$\widehat{H}_{RF} = -\gamma_{QN}\overrightarrow{B}_{RF} \cdot \overrightarrow{I} \cdot cos(\omega_{RF}t - \phi_{RF}). \tag{4.5}$$

The expected relative intensity for each transition $\nu_Q(\Omega)$ when an evolution field B_{ev} is applied can be written as a product of the quantum mechanical transition probability p_{NQR} times the Boltzmann population difference p_T of the energy levels

at the ensemble temperature T:

$$I_{NQR}(\nu_Q)(\Omega, B_{ev}) = p_{NQR} \cdot p_T = |\langle \Psi_\alpha(\Omega)|\widehat{H}_{RF}|\Psi_\beta(\Omega)\rangle|^2 \cdot \frac{e^{\frac{E_\alpha - E_\beta}{k_B T}}}{\sum_{i,j} e^{\frac{E_i - E_j}{k_B T}}}, \tag{4.6}$$

where k_B is Boltzmann's constant.

To describe a powder spectrum, the frequencies from equation (4.4) and their corresponding intensities (equation (4.6)) are being evaluated for a set of N random, uniformly distributed angles Ω on a sphere. Then, each intensity value is assumed to represent a Lorentzian peak with an experimentally determined and constant full width at half maximum (FWHM) derived from zero-field NQR measurements. The Lorentzians with $\gamma = FWHM/2$ are then summed up and averaged according to equation (4.7).

$$\bar{I}_{NQR}(\nu_Q)(B_{ev}) = \sum_{\Omega} \left[\frac{I_{NQR}(\nu_Q)(\Omega, B_{ev})}{1 + \frac{\nu - \nu_Q(\Omega, B_{ev})}{\gamma}} \right] / N \tag{4.7}$$

In figure 4.3, the result of such a procedure is demonstrated for triphenylbismuth in a field B_{ev} of 100 mT. The clouds of single grey stars in the background represent the intensity values for each of the randomly chosen angles Ω on a unit sphere according to equation (4.6), the blue solid line is the average according to (4.7) and shows the calculated NQR spectrum at a field strength of 100 mT. The noisy, oscillatory shape of the spectrum is a result of the random input parameters and the frequency step size. For higher number of angles N and a smaller step size the lineshape of the spectrum becomes smoother.

4.2.4 The relevant intensity of the NQR powder spectrum

The intensity $\bar{I}_{NQR}(\nu_Q)(B_{ev})$ as described in section 4.2.3 is the intensity that can be expected from a measurement using a NQR spectrometer. Typically, $\widehat{H}_{RF}$ in equation (4.6) reduces to $\widehat{I}_x$, when the RF field oscillates perpendicular to the applied magnetic field. But we are interested in the QRE effect which is manifested in magnetic field selective R_1-relaxation enhancement features in NMRD profile measurements. In this case two spin species and their corresponding transitions are involved. To figure out what are the allowed transitions, we should have a closer look at what is happening at the level crossings: Assuming that the proton with I=1/2 in a magnetic field is performing a transition from $|-1/2\rangle$ to $|+1/2\rangle$ during spin-lattice relaxation, the angular momentum changes by $\Delta m = +1$. To act like an energy sink and take over the corresponding magnetization, the QN has to perform a spin transition with the same energy by $\Delta m = -1$ (e.g. $|-3/2\rangle$ to $|-5/2\rangle$), which corresponds to an excitation. The operator that can mediate such a transition within the QN energy level system is the lowering operator $\widehat{I}_-$. In that case, the intensity of

NQR transitions available for the protons for performing QRE can be written as:

$$I_{QRE}(\nu_Q)(\Omega, B_{ev}) = p_{QRE} \cdot p_T = |\langle \Psi_\alpha(\Omega)|\widehat{I}_-|\Psi_\beta(\Omega)\rangle|^2 \cdot \frac{e^{\frac{E_\alpha - E_\beta}{k_B T}}}{\sum_{i,j} e^{\frac{E_i - E_j}{k_B T}}}$$
$$\overline{I}_{QRE}(\nu_Q)(B_{ev}) = \sum_{\Omega} \left[\frac{I_{QRE}(\nu_Q)(\Omega, B_{ev})}{1 + \frac{\nu - \nu_Q(\Omega, B_{ev})}{\gamma}} \right] / N, \tag{4.8}$$

where the angle averaged intensity $\overline{I}_{QRE}(\nu_Q)$ is formed assuming Lorentzian peaks of constant width γ.

From the simulation's point of view, the definition of the direction of the applied evolution field B_{ev} decides whether raising operator $\widehat{I}_+$ or the lowering operator $\widehat{I}_-$ should be used. In our case, B_{ev} points into the positive z direction, which means that the proton state $|+1/2\rangle$ has lower energy and R_1-relaxation therefore is connected with an angular momentum change by $\Delta m = +1$. Therefore, the operator of choice to calculate the NQR spectra is the lowering operator $\widehat{I}_-$. However, as shown in section 4.3.2, this is not a strict rule for all transitions.

4.2.5 The indicator function for QRE peaks

Taking together the above derived equations (4.4) and (4.9), we are ready to write down an indicator function f_{QRE} for the potential of finding QRE peaks in a R_1-NMRD measurement of protons coupled to a QN in solids:

$$f_{QRE}(\nu_L) = \overline{I}_{QRE}(\nu_Q(B_{ev}))\ |_{\nu_L}, \tag{4.9}$$

which simply means, that the intensity of the NQR powder spectrum $\overline{I}_{QRE}$ seen by a proton ^{1}H coupled to a QN at a particular magnetic field B_{ev} is evaluated at the corresponding proton Larmor frequency ν_L.

In principle, equation (4.9) can also be used to consider double quantum transitions by using $\widehat{I}_-\widehat{I}_-$ and involving two protons.

4.3 Results

Equation (4.9) is evaluated for tris(2-6-dimethoxyphenyl) bismuthine and tris(2-methoxyphenyl) bismuthine based on their NQR parameters taken from [61]. The used input parameter Q_{cc}, η, γ and the step sizes for B_{ev} and ν_Q for the calculations are summarized in table 4.1. Simultaneously, the results are compared to experimental R_1-NRMD profiles which can be found in reference [94]. The molecular structure of the Bi-aryl compounds is included as an insert in figures 4.4 and 4.5.

As already addressed in section 4.2.1, the result of the QRE simulation is somewhat noisy due to the random character in the calculation of the NQR spectrum.

TABLE 4.1: Simulation input parameters for Bi-aryl compounds tris(2-6-dimethoxyphenyl) bismuthine and tris(2-methoxyphenyl) bismuthine. NQR parameter Q_{cc}, η and linewidth $\gamma = FWHM/2$ at 310 K from reference [61].

Compound	molecular formula	Q_{cc} (MHz)	η (1)	γ (kHz)[a]	smoothing span[b]	step size B_{ev} (mT)	step size ν_Q (kHz)
tris(2-6-dimethoxyphenyl) bismuthine	$BiPh_3(DiOMe)_3$ ortho	660.9	0.105	20	11	2.1 ($\widehat{=}$ 88 kHz)	13.8
tris(2-methoxyphenyl) bismuthine site A	$BiPh_3(OMe)_3$ ortho A	715.3	0	20	15	2.8 ($\widehat{=}$ 120 kHz)	15.4
tris(2-methoxyphenyl) bismuthine site B	$BiPh_3(OMe)_3$ ortho B	714.2	0	20	15	2.8 ($\widehat{=}$ 120 kHz)	15.4

[a] an average value has been assumed for all transitions
[b] low pass filter with coefficients equal to $1/span$ with $span$ in percentage of number of data points

Because of that, a post processing step is performed by smoothing the result using a moving average filter (filter parameters for coefficients see table 4.1).

4.3.1 Tris(2-6-dimethoxyphenyl) bismuthine

The result for $BiPh_3(DiOMe)_3$ ortho is illustrated in figure 4.4. The upper panel shows the experimental NMRD data at 295 K with many pronounced QRE peaks A-E. The positions of peaks C-E are well reproduced by the simulation according to equation (4.9) (input parameters see table 4.1) in the lower panel. Also, their shape (shoulder to higher frequencies) is reproduced well. For the low frequency features (< 40 MHz) A and B on the contrary, no such good correspondence can be found.

4.3.2 Tris(2-methoxyphenyl) bismuthine

$BiPh_3(OMe)_3$ ortho has two crystal sites A and B with their Q_{cc} only differing by about 1 MHz and a similar η (see table 4.1). Correspondingly, the NMRD profile (at 295 K) shows single peaks (A-E), where both nuclei contribute on the same frequency (within experimental accuracy). This is illustrated in figure 4.5, where the lower panel shows the simulation for both sites in blue and green solid line according to equation (4.9) and using the input parameters of table 4.1. The locations and shapes of peaks C-E are well reproduced by the calculation. The low frequency features (< 40 MHz) A and B, on the contrary, are very strong in the experiment, but are estimated weaker by the simulation. Reasons for that will be discussed in addressed in section 4.4.3. Also, a frequency match is only present for feature A. Peak B has no correspondence in the simulation.

4.3.3 Double quantum transitions

Calculations were performed to look for double quantum transitions using the $\widehat{I}_-\widehat{I}_-$ operator and also allowing double proton transitions (crossings with $2 \cdot \nu_L$). Equation (4.9) is therefore applied using $\widehat{I}_-\widehat{I}_-$ instead of $\widehat{I}_-$ and evaluated at $2 \cdot \nu_L$ with the input parameter of table 4.1.

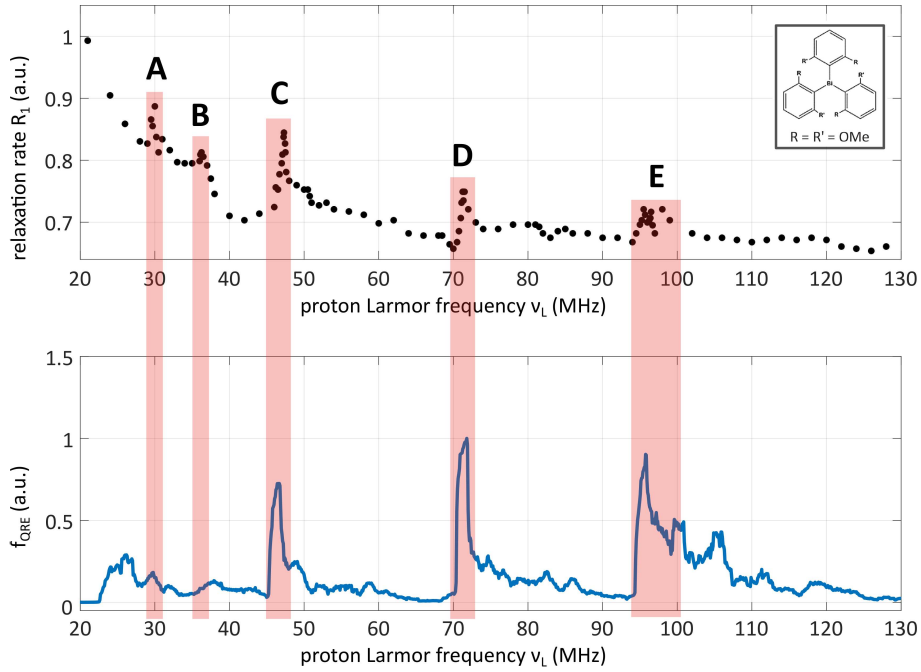

FIGURE 4.4: Comparison of QRE prediction calculation according to equation (4.9) (lower panel) at 310 K with experimental R_1-NMRD profile of tris(2-6-dimethoxyphenyl) bismuthine (upper panel) at 295 K.

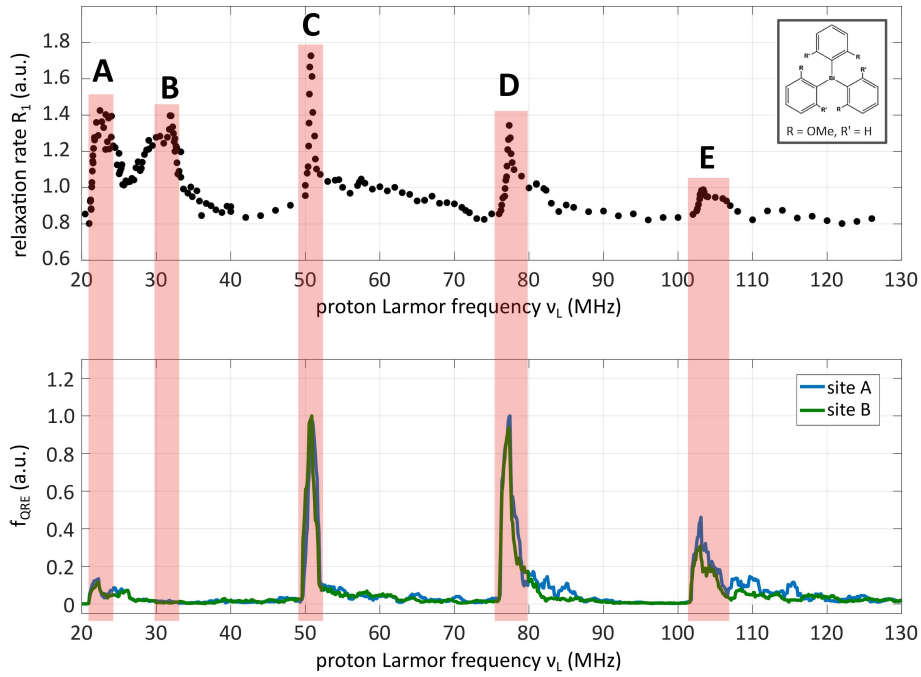

FIGURE 4.5: Comparison of QRE prediction calculation according to equation (4.9) (lower panel) at 310 K with experimental R_1-NMRD profile of tris(2-methoxyphenyl) bismuthine site A and B (upper panel) at 295 K.

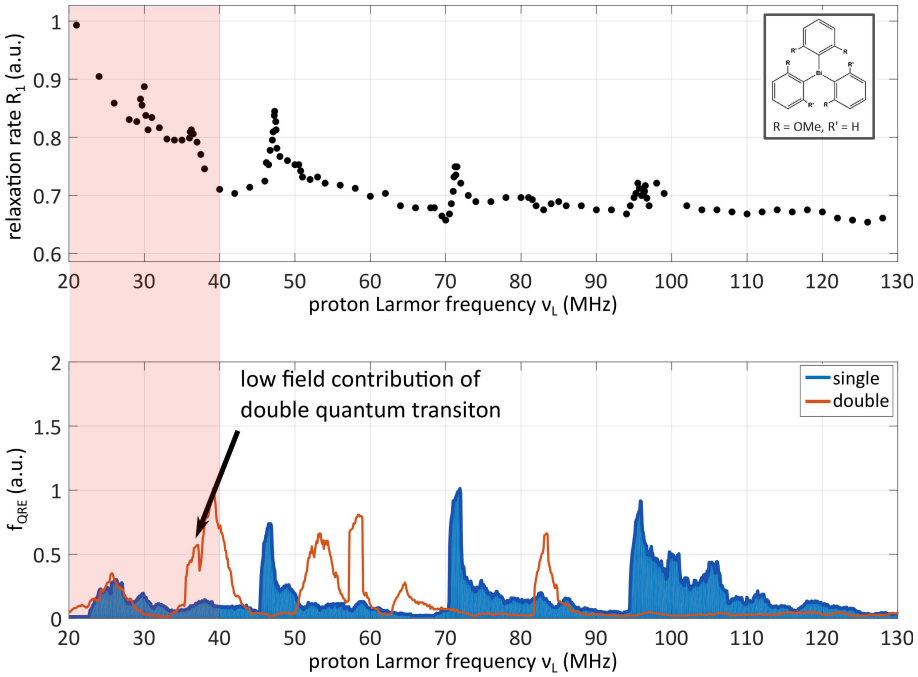

FIGURE 4.6: Comparison of QRE prediction calculation according to equation (4.9) (lower panel) at 310 K with experimental R_1-NMRD profile of tris(2-6-dimethoxyphenyl) bismuthine (upper panel) at 295 K. In blue, the calculation based on single quantum transitions is shown, for the red solid line, the calculation is based on double quantum transitions

The results are shown in figures 4.6 and 4.7, where the low field features are marked in red in the upper panel with simulations for both cases in the lower panel. The blue line corresponds to the simulation using $\widehat{I}_-$, the red line to the simulation using $\widehat{I}_-\widehat{I}_-$. An overlay of both procedures suggests a slightly better match in the low field region to the experimental data than the sole $\widehat{I}_-$ calculation.

Possible reasons for the comparably poor reproduction of the low field features and the meaning of the additional peaks in the simulation in the high field region are addressed in section 4.4.

4.4 Discussion

The proposed procedure for predicting the appearance of QRE peaks in ^{1}H-NMRD profiles of the R_1 relaxation rate of molecular crystals performs well for several experimentally investigated Bi-aryl compounds in the higher field range, though a couple of assumptions have been applied. In some sense the method represents an extension to the QRE peak allocation of a previous work [94], where rather broad frequency bands attributed to QRE locations could be defined.

4.4.1 The low field regime <1 T

As the correspondence between simulation and experiment in the low field regime is not satisfactory when considering only single quantum transitions (figures 4.4 and

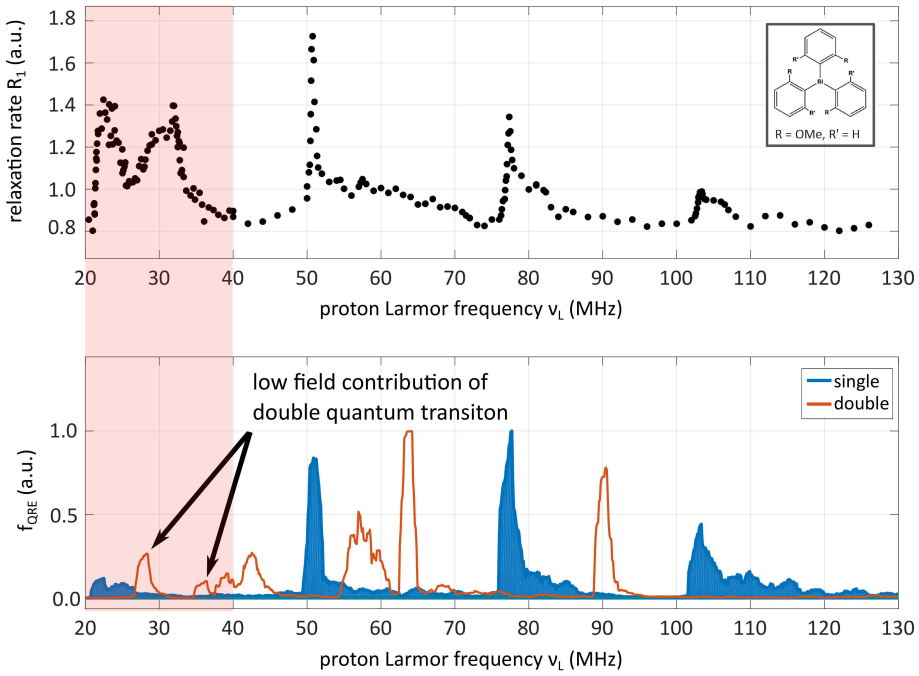

FIGURE 4.7: Comparison of QRE prediction calculation according to equation (4.9) (lower panel) at 310 K with experimental R_1-NMRD profile of tris(2-methoxyphenyl) bismuthine site A (upper panel) at 295 K. In blue, the calculation based on single quantum transitions is shown, for the red solid line, the calculation is based on double quantum transitions

4.5), also the role of possible double quantum transitions is discussed.

The low field features A and B in the NRMD profiles of the two Bi-aryl species most likely originate from the lowest NQR transitions, $|\pm 3/2\rangle$ to $|\pm 1/2\rangle$, similar to the spectrum shown in figure 4.3 panel b). This is a special transition compared to higher ones, as in case of Zeeman-splitting, the corresponding Hamiltonian $\hat{H}_0(I)(\Omega)$ (equation 4.2a) exhibits large off-diagonal elements which induce a mixing of the $|+1/2\rangle$ and $|-1/2\rangle$ states [42]. Due to that mixing, the selection rule due to the conversion of angular momentum is not restricted to $\Delta m = -1$ any more. In that case, also double quantum transitions $\Delta m = -2$ are allowed and the simulation should also include contributions from the $\hat{I}_-\hat{I}_-$ operator. Also, one must take into account, that for such a transition, two protons have to be involved to maintain angular momentum.

The result when including double quantum transitions is shown in figures 4.6 and 4.7. The data suggest that double quantum transitions can contribute to QRE in the frequency range/field range associated with the lowest NQR transition.

4.4.2 The high field regime >1 T

QRE peaks occurring at ν_L >40 MHz can be predicted well both in location and shape by assuming only single quantum transition. This is demonstrated in figures 4.4 and 4.5

The slight mismatch in frequency (down-shifted simulation) can be attributed to the temperature difference (simulation at 310 K, experiment at 295 K) and experimental errors both in the R_1-NMRD profile and in the used NQR parameter for the simulation. As has been shown in [61], the temperature coefficient of NQR transitions around 310 K is expected about 10 kHz/K, at worst. For an assumed temperature difference of about 20 K , this means one can expect a shift of 0.2 MHz for the QRE peaks, which is of the order of the experimental resolution.

However, the exact relative intensities of the QRE features and the baseline shape due to a relaxation background cannot be reproduced. This is not surprising as corresponding models have not yet been included.

The additional peaks at higher frequencies from the simulation of double quantum transitions (red lines in figures 4.6 and 4.7) do not originate from such special conditions as addressed above and are thus also not observed in the experiment (as such transitions are forbidden). Although, in principle also these higher states are subjected to a mixing due to non-zero η and the angle dependency of the Zeeman Hamiltonian, this effect is significantly lower than for the lowest transition. Therefore corresponding features cannot be observed in the experiment.

4.4.3 Possible improvements

Most worth mentioning is the fact that the actual D-D coupling mechanism between QNs and protons has not been included into the formulation. Also, no other relaxation mechanism, as e.g. the proton D-D background, has been considered. The method is solely based on the probability of the QN NQR transitions which are available for the QRE effect.

One attempt to include relaxation processes could be a model based on D-D coupling between heterogeneous nuclei extended by a suitable model for the quadrupolar spin fluctuations. This could increase the accuracy of the simulation of predicting also the exact intensities of possible QRE features, which are not perfectly reproduced by the current method. Also, a model for the proton relaxation background based on dipolar coupling could be used to add a more realistic baseline to the presented calculations.

In particular, a high spectral density at the matching frequency enabling efficient QRE can be responsible for the strong mismatch in predicting the relative QRE peak intensities (see figure 4.4 and 4.5) between low field and high field QRE peaks.

The next step would be to consider the whole spin system and all relaxation effects directly in a Redfield theory [97] approach, which is considerably more complex and requires more computational resources.

Another point for improvement is the calculation of the static NQR powder spectrum depending on an external magnetic field. Instead of assuming a constant width for all transitions, a proper model based on Redfield theory can be applied to calculate the lineshape throughout the whole spectrum. In that way, the actual peak

widths, which are different for each transition, could be included which would certainly better resolve the experimentally observed QRE peak shape.

4.4.4 Conclusion

The comparison between experiment and simulation is satisfactory in the high field region (>1 T) and so the presented method can be used to plan R_1-NMRD measurements in advance by predicting QRE peak positions in QN and ^{1}H containing molecular crystals. The necessary NQR parameters Q_{cc}, η and the linewidth can be determined either experimentally from NQRS measurements or by ab *initio* QC calculations as already has been shown to give reasonable results [61].

As the actual relaxation effect between ^{1}Hs and QNs is not included, the procedure does not provide quantitative information and shall therefore be treated as a prediction tool for frequencies where QRE peaks are likely to occur. More precisely, the presented procedure shows at which field strengths there is no or little chance for a QRE peak and so states a necessary condition that can serve as a basis for further considerations.

When it comes to an application of the presented method we would like to mention that the tool can support ongoing research on MRI contrast agents based on the QRE effect [34, 61, 94] which is especially suitable for FFC-MRI systems [129]. Of course, the requirements and conditions for a particle acting as MRI contrast agent in biological tissue are rather complex and not straightforward to fulfill. However, in a rational particle design process it makes sense to start with the simplest system and extracting promising compound candidates already from the solid state. By doing so, to some degree the frequency (magnetic field) positions where the QRE effect most likely occurs can already be restricted. In a next step, the selected particles can be brought into solution (water) by e.g. incorporate them in a nano particle acting as blood stream carrier. For this overall particle system further properties, as e.g. water exchange, rotational dynamics and solubility have to be shaped. This topics are matter of ongoing work where further research is desirable. In a quite recent work aspects of structural order of QRE active particles based on ^{209}Bi are discussed with the outcome, that also in solution, particles with a highly ordered molecular structure are beneficial [91].

Acknowledgement(s)

This work was supported by the European Commission (Horizon 2020 Program) under Grant number 665172 (FET-open CONQUER) and under Grant number 15209 (COST Action European Network on NMR Relaxometry).

Disclosure statement

No potential conflict of interest was reported by the authors.

Chapter 5

Spin-spin relaxation of nuclear quadrupole resonance coherences and the important role of degenerate energy levels

Christian Gösweiner[a], Per-Olof Westlund[b] and Hermann Scharfetter[a]

[a]*Institute of Medical Engineering, Graz University of Technology, Stremayrgasse 16/3, 8010 Graz, Austria;*

[b]*Department of Chemistry, Umeå University KB.A4, Linnaeus väg 10, 901 87 Umeå, Sweden*

published in:
Molecular Physics, 8976, e1743888. DOI: 10.1080/00268976.2020.1743888 [190]

Abstract

*We present an extension of a Redfield approach for calculating spin-spin relaxation rates of zero-field nuclear quadrupole resonance (NQR) coherences, which was published in [Kruk et al., PCCP, 2018, **20**, 23414-23426]. The oversimplification of the secular approximation made in the recent paper makes the calculation invalid for zero-field NQR and has led to partially large deviations between predicted and experimental data from ^{209}Bi-containing molecular crystals. Furthermore, these deviations led to speculations about an additional dipole-dipole relaxation mechanism besides the main electric field gradient (EFG) fluctuations. Here, we demonstrate how a complete application of the Redfield relaxation expression eliminates the deviation from experimental data without the need for additional assumptions. In particular, we point out the important role of off-diagonal elements in the Redfield relaxation matrix within the 3/2-1/2 block appearing due to degenerate energy levels. The resulting coupling between single and double coherence spin density elements leads to a faster coherence decay than for all other transitions. The pseudo rotational model for EFG fluctuations, as proposed in the earlier publication and usually applied for isotropic liquids, is*

extended in a second analysis by introducing a vibrational mode to account for the case of crystalline solids.

5.1 Introduction

Nuclear spin relaxation phenomena in condensed matter offer a rich source of information on the molecular dynamics of the system under observation [101, 48, 191, 102]. Measurements of spin-lattice (R_1) and spin-spin relaxation rates (R_2) encode information on the type of fluctuations leading to relaxation and the shape of their spectral density. This fact is extensively used e.g. by field cycling relaxometry on protons [17], where the molecular dynamics of complex, often liquid samples can be revealed by acquiring a nuclear magnetic relaxation dispersion (NMRD) profile. Typically, such measurements are also performed at different temperatures.
In nuclear magnetic resonance (NMR) spectroscopy, relaxation measurements are used for the assignment of molecular groups, to investigate exchange processes and to study the influence of different quantum mechanical interactions that can be a source for relaxation [192]. One of the most prominent applications of proton relaxation is magnetic resonance imaging (MRI). Of major interest in that field are techniques and mechanisms able to enhance or manipulate image contrast by the application of chemical agents that influence the relaxation process [104, 38].

Another, less popular method to access nuclear spin relaxation is nuclear quadrupole resonance (NQR) spectroscopy [45, 42]. In contrast to NMR, where mostly protons are in the center of interest, in NQR nuclei with spin number $I > 1/2$ in solids are addressed directly and the application of an external magnetic field is not necessary. Instead, an electric interaction between the quadrupole moment of the nucleus and an electric field gradient (EFG), produced from the surrounding atoms and molecules, is the origin of discrete spin states. Though, the measurement procedure is closely related to NMR where the application of a sequence of radio frequency pulses redistributes the occupation of spin states. High spin nuclei exhibit a richer, but also more complex energy level system which requires a very careful treatment when applying quantum mechanical models as e.g. Redfield theory [97]. As NQR is much less extensively used than NMR techniques, there are no standard procedures available as e.g. the intensively used Solomon-Bloembergen-Morgan (SBM) equation for the field dependent R_1 relaxation of protons in paramagnetic systems [18, 19, 20]. Several works treat temperature dependence of R_1 relaxation of pure NQR transitions [193, 194, 195, 196], but less studies were performed on the coherence decay (R_2) or the lineshape of NQR spectra [197]. Though, the total experimental lineshape carries information of quite practical nature as e.g. crystal homogeneity, or nanoparticle size, which is connected with the EFG distribution [198, 199, 200, 201]. However, one can only address this issue trustfully when

the portion of line broadening due to dephasing and finite lifetime of spin states is exactly known.

In this work, we present an extension of an earlier article [94] where spin-spin relaxation rates of quadrupole transitions at zero field where calculated for I=9/2 nuclei using Redfield theory [97, 98]. In [94], fluctuations of the electric field gradient according to the simple two parameter pseudo rotational (PR) model are assumed, which is originally used for modelling fluctuations of the zero field splitting interaction in electron spin relaxation [202]. The calculation includes only single coherence elements of the spin density and no possible off-diagonal elements of the Redfield matrix are considered, leading to uncoupled equations of motions for each transition. Comparison with and fitting to experimental data from deuterated and non-deuterated triphenylbismuth in powder form were not completely satisfactory, as for the lowest transition the errors are high. This discrepancy was attributed to an additional relaxation mechanism resulting from dipole-dipole interactions between the quadrupole nuclei (^{209}Bi) and surrounding protons.

However, in the zero field case and for half-integer spin nuclei, NQR states are doubly degenerate and the secular approximation is not restricted to the diagonal elements any more. Only in case of very small off-diagonal elements, they can be ignored which we show here, is not the case. Including the complete relaxation matrix according to the Redfield theory complicates the calculations slightly, as more elements of the spin density must be included and the equations can become coupled. Performing a Fourier-Laplace transform of the spin density equation of motion allows to evaluate the decoherence-broadened NQR spectrum including any coupling. Also, a closed form solution for each single quantum coherence is given. From the linewidth of the resonance peaks, their spin-spin relaxation rate can be extracted. The respective Redfield relaxation matrix elements are calculated analytically for two different motional models for the fluctuations of the electric field gradient (EFG) at the ^{209}Bi-site.

It is not an easy task to capture all features of motion of molecular crystals [203, 204], as treated in this study, and how these affect the EFG at the site of a particular nucleus. In general, in such a solid lattice and molecular motions are expected. Lattice motions comprise phonon modes while molecular motions comprise molecular torsional oscillations as well as intra molecular and molecular reorientations [194]. As we do not intend to discuss in detail all possible motions in a molecular crystal, we formulate, in a heuristic manner, an as simple as possible model for the EFG fluctuations to keep the number of parameters low while maintaining physical reasoning. Instead of the PR model used in [94], we introduce a so called flickering amplitude (FA) model [205], using a monoexponetial correlation function for the EFG amplitude which is extended in a second step with a vibrational mode to form the flickering vibrational amplitude (FVA) model. For the assumption of an isotropic distribution of fluctuation directions, the FA model becomes equivalent with the PR model.

Experimental relaxation data are discussed from three different Bi-aryl compounds at two different temperatures (77 K and 310 K) (mostly taken from [61]). The applied spin echo measurements provide spin-spin relaxation rates from homogeneous effects only. The two dynamical models are tested on these data and so dynamical parameters reflecting time-scale and amplitude of the EFG fluctuations are determined. It should be noted, that the presented method is not applicable to very slow molecular motions, as in this case the Redfield condition is not fulfilled and the stochastic Liouville approach must be applied (see e.g. [206]).

5.2 Methods

5.2.1 Lineshape calculation

The concept of the spin density operator [76] and the semi classical model for relaxation developed by Bloch, Wangsness and Redfield are summarized and discussed extensively in several works [96, 97, 101, 48]. Thus, here only a brief collection of the used equations and the derivation of the lineshape function adjusted to our case is given. A great deal of the equations is defined in appendix 5.5.

The time evolution of a spin ensemble is described by the stochastic Liouville equation for the spin density operator $\hat{\rho}$

$$\frac{d}{dt}\hat{\rho}(t) = -i\left[\hat{H}(t), \hat{\rho}(t)\right] \,, \tag{5.1}$$

which can be solved for a stochastic time dependent Hamiltonian $\hat{H}(t) = \hat{H}_0 + \hat{H}_1(t)$ by applying second order time dependent perturbation theory and following the approximations of Redfield relaxation theory. From the result [97, 48, 100, 98] it follows that equation 5.1 can be written in Liouville space as

$$\frac{d}{dt}\rho(t) = \left(-i\mathcal{L}^0 - \Gamma\right)\rho(t)\,, \tag{5.2}$$

where $\mathcal{L}^0$ is the Liouvillian generated by the time independent Hamiltonian $\hat{H}_0$ and Γ is the relaxation superoperator which is generated by the stochastic Hamiltonian $\hat{H}_1(t)$. In Liouville space formulation, an operator basis projection $\{|\alpha\rangle\langle\alpha'|\}$ is used where $|\alpha\rangle$ are the usual Zeeman states with the magnetic spin quantum number $\alpha \in [-I, I]$ and the spin quantum number I. Using such an operator basis, the spin density operator can be expanded in the complete set of operators $|\alpha\rangle\langle\alpha'|$ as $\hat{\rho} = \sum_{\alpha,\alpha'} \rho_{\alpha\alpha'} |\alpha\rangle\langle\alpha'|$ and thus forms a column vector in equation 5.2 with the elements $\rho_{\alpha\alpha'} = \langle\alpha|\hat{\rho}|\alpha'\rangle$, while the Liouvillian and relaxation superoperators become matrices. Their elements are defined in appendix 5.5, equations 5.25 and 5.26a. Equation 5.2 written element-wise reads as

$$\frac{d}{dt}\rho_{\alpha\alpha'}(t) = \sum_{\nu_{\alpha\alpha'}=\nu_{\beta\beta'}}^{\beta,\beta'} \left(-i\mathcal{L}^0_{\alpha\alpha'\beta\beta'} - \Gamma_{\alpha\alpha'\beta\beta'}\right)\rho_{\beta\beta'}(t)\,, \tag{5.3}$$

where $\nu_{\alpha\alpha'} = E_\alpha - E_{\alpha'}$ are the transition frequencies of $\hat{H}_0$ and E_α are its Eigenvalues. The condition for the sum results from the secular approximation which can best be understood by looking at equation 5.2 in the interaction frame, where $\rho^*_{\alpha\alpha'} = e^{i\mathcal{L}_0 t}\rho_{\alpha\alpha'}$:

$$\frac{d}{dt}\rho_{\alpha\alpha'}(t)^* = \sum_{\beta\beta'} \Gamma_{\alpha\alpha'\beta\beta'} e^{i(E_\alpha - E_{\alpha'} - E_\beta + E_{\beta'})t} \rho_{\beta\beta'}(t)^* \tag{5.4}$$

Any terms for which $E_\alpha - E_{\alpha'} \neq E_\beta - E_{\beta'}$ give oscillating contributions and thus do not contribute to the relaxation of $\rho(t)$. In the absence of degenerate terms this leads to diagonal single and double coherence blocks in the relaxation matrix and so no cross relaxation between off-diagonal elements can occur [48, 207]. We will see that for NQR this is different. In NQR, the energy levels of the $|\pm\alpha\rangle$ quantum states are doubly degenerate in case of half integer spins and no external field is applied. This means that more elements fulfill the secular approximation than e.g. in nuclear magnetic resonance (NMR) phenomena. As a consequence, (1) equation 5.26a for calculating the elements of Γ has been altered slightly compared to the standard formulation (see appendix 5.5), (2) more elements are entering $\rho(t)$ and (3), it is possible that also off-diagonal elements appear in the single and double coherence blocks of the relaxation matrix.

As we are interested in spin-spin relaxation, we have to evaluate the expectation value of the $\hat{I}_x$ and $\hat{I}_x\hat{I}_x$ operators $\langle \hat{I}_x \rangle$ and $\langle \hat{I}_x\hat{I}_x \rangle$ respectively, that encode single and double quantum coherences (transversal component of the magnetization). A corresponding signal $G(t)$ can then be written as

$$G(t) \sim \langle \hat{I}_x \rangle + \langle \hat{I}_x\hat{I}_x \rangle = \frac{tr\left\{\rho(t)\hat{I}_x\right\}}{tr\left\{\hat{I}_x^2\right\}} + \frac{tr\left\{\rho(t)\hat{I}_x\hat{I}_x\right\}}{tr\left\{\hat{I}_x^2\hat{I}_x^2\right\}} \,. \tag{5.5}$$

The equation picks out the right elements from the spin density vector $\rho(t)$ containing the signal. A convenient way to solve this coupled system of differential equations is by applying Fourier-Laplace transform and solve the equation in frequency domain [208]. First, the transform $L[\rho(t)] = \tilde{\rho}(s)$ is applied and the differential equation is solved. Then, a variable transformation $s \to i\nu$ is performed to produce the Fourier transform (see appendix 5.5 equation 5.27).

$$\rho(\nu) = \left(i\nu\mathbb{1} + i\mathcal{L}^0 + \Gamma\right)^{-1}\rho(0) \tag{5.6}$$

$\rho(\nu)$ can be identified as the spin density in frequency domain. For evaluating equation 5.6, the matrices $\mathcal{L}^0$ and Γ need to be calculated according to appendix 5.5, equations 5.25 and 5.26a. $\rho(0)$ is the initial condition which follows the Boltzmann equilibrium distribution of the spin system.

Instead of calculating the signal in time domain from equation 5.5, we can now

evaluate the lineshape $F(\nu)$ (NQR spectrum) which is just its Fourier transform:

$$F(\nu) = \frac{tr\left\{\rho(\nu)\hat{I}_x\right\}}{tr\left\{\hat{I}_x^2\right\}} + \frac{tr\left\{\rho(\nu)\hat{I}_x\hat{I}_x\right\}}{tr\left\{\hat{I}_x^2\hat{I}_x^2\right\}} = \sum_{\alpha\alpha'} \frac{\langle\alpha|\,\rho(\nu)\,|\alpha'\rangle\,\langle\alpha'|\,\hat{I}_x\,|\alpha\rangle}{tr\left\{\hat{I}_x^2\right\}} + \sum_{\alpha\alpha'} \frac{\langle\alpha|\,\rho(\nu)\,|\alpha'\rangle\,\langle\alpha'|\,\hat{I}_x\hat{I}_x\,|\alpha\rangle}{tr\left\{\hat{I}_x^2\hat{I}_x^2\right\}} \tag{5.7}$$

Using equation 5.7 together with 5.6, the NQR spectrum can be calculated which eventually contains information on the spin-spin relaxation rates R_2 in the linewidth of the transitions.

5.2.2 Quadrupole interaction

The static part of the total Hamiltonian, $\hat{H}_0$, in equation 5.1 is the usual quadrupole Hamiltonian expressed in spherical tensor operators (see 5.28a). Two parameters are enough to fully describe the interaction between a nuclear quadrupole ($I > 1/2$) and it's local electric field gradient (EFG) generated by the surrounding molecule: The quadrupole coupling constant $Q_{cc} = e^2qQ/\hbar$ is formed by the product of the EFG strength $V_{zz} = eq$ and the quadrupole contribution eQ with the quadrupole moment Q. The asymmetry parameter $\eta = \frac{V_{xx}-V_{yy}}{V_{zz}}$ describes the deviation of the EFG from cylinder symmetry. $\hat{H}_0$ is responsible for the transition frequencies of the quadrupole spin resonance and enters the lineshape calculation via the elements of the Liouvillian $\mathcal{L}^0$ (appendix 5.5, equations 5.25 and 5.32). As solid powders of molecular crystals are treated, in some cases a powder average has to be considered. Reasons could be the presence of an external magnetic field or if one is interested in the intensity of a spin transition that can be detected by the solenoid coil of a spectrometer also creating the RF field for excitation. This requires a transformation of the principal axis system (P) of the EFG with respect to the laboratory system (L), defined by the spectrometer coil or an external field. However, in the presented case, no external field is applied and no intensity analysis is performed so it is convenient to use the (P) representation of the quadrupole Hamiltonian (see appendix 5.5, equations 5.28a-5.28d and explanations).

As the main source of relaxation in pure NQR spin ensembles we consider fluctuations of the quadrupole Hamiltonian (defining the spin states) due to fluctuations of the EFG itself. This EFG fluctuation is connected with the molecular fixed frame (M) and has to be transformed into the (P) frame defined by the static part of the EFG. According to this assumption, the total Hamiltonian $\hat{H}$ carries a time and angle depending part $\hat{H}_1(t)(\Omega_{MP})$ describing random, stochastic fluctuations of the EFG. To fulfill the conditions of Redfield theory, this Hamiltonian has to average to zero in a time period much faster than a typical relaxation time of the spin system under observation. The choice of the explicit time dependence of the EFG tensors $V_m^{(2)}$ (rank 2 spherical tensor operators) is discussed in section 5.2.3.

$\hat{H}_1(t)(\Omega_{MP})$ formally has the same form as $\hat{H}_0$ and enters the relaxation matrix Γ via equations 5.26a and 5.26b. In order to display the transformations between coordinate systems (L) Lab, (M) molecular fixed and (P) the principal coordinate system of the EFG it may be written:

$$L \rightarrow^{\Omega_{PL}} P \leftarrow^{\Omega_{MP}} M \tag{5.8}$$

5.2.3 Motional model of the EFG fluctuations

As the main source of fluctuations that induce quadrupole spin relaxation in the addressed Bi-aryl molecular crystals, we assume that the EFG at the ^{209}Bi nucleus experiences changes due to random motions from the surrounding phenyl groups and ligands and, probably of less importance, from the motions of neighbouring molecules. The main contribution to the EFG origins from the binding orbitals at the Bi nucleus which are not considered as reorienting groups, so the transient fluctuating magnitude can be considered to be only a small fraction of the total Hamiltonian. As a second mechanism modulating the EFG fluctuations, wagging and rocking motions of covalent bonds and torsional motions of the whole molecule are considered. From the point of view of the total EFG, this might lead to an oscillating or vibrating amplitude of the fluctuations. This type of modulation can be described by periodically modulated EFG tensor elements. Also phonons of the crystal lattice might account for such a periodically modulated EFG. A review summarizing different contributions of motions to relaxation is given in [194].

On the basis of the introduced mechanisms, we present two ways of describing the EFG fluctuations: The first one (concept (1)) corresponds to the widely used pseudo rotational (PR) model [101, 209, 210, 102] and will only be summarized briefly. It assumes time dependent reorientations via rotations of the EFG tensor at constant amplitude and has been applied for example in [202] for proton relaxation in metal aquo complexes due to zero field splitting as well as to describe EFG fluctuations in solids [94]. The second derivation (concept (2)), on the contrary, assumes a time dependent amplitude of the EFG fluctuations along certain directions with respect to the main EFG. It will be discussed in more detail and represents the motional model for the EFG used in this work. A quite similar model was presented by Friedman et al. [205] (flickering model) for electron paramagnetic resonance (EPR) relaxation of Ni^{2+} ions.

Figure 5.1 helps to visualize the concepts. For both, a fluctuating, time dependent portion of the total EFG (blue arrows) forming $\hat{H}_1(t)(\Omega_{MP})$ is assumed which can be rotated at a certain angle with respect to the main, averaged EFG that produces $\hat{H}_0$ (red arrow). Addition of both EFG's gives the total Hamiltonian of equation 5.1. In case of concept (1), the angles are time dependent and the amplitude is constant. For concept (2), a certain constant distribution of directions of the fluctuations with time dependent magnitudes is assumed. From figure 5.1 also the term pseudo rotational becomes clear as only the fluctuation, but not the total Hamiltonian is performing

rotations. In both cases, the EFG fluctuations are of stochastic nature and can be described by their autocorrelation function. It's Fourier transform (compare equation 5.26b) is proportional to the envisaged spectral density $J(\nu)$ of $\hat{H}_1(t)(\Omega_{MP})$.

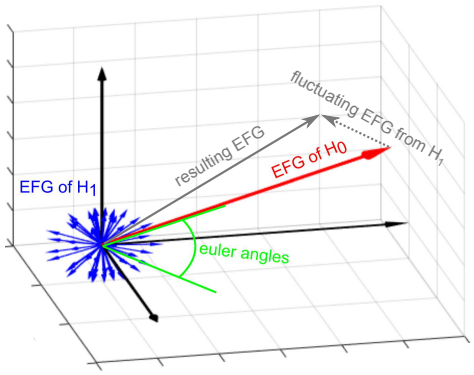

FIGURE 5.1: Visualization of the EFG fluctuations (blue, small arrows) with respect to the main molecule EFG (red, large arrow). To add both Hamiltonians correctly, Wigner rotations by Euler angles Ω_{MP} have to be performed to rotate the fluctuating Hamiltonian $\hat{H}_1(t)(\Omega_{MP})$ into the PAS system defined by the static Hamiltonian $\hat{H}_0$. A possible instantaneous EFG is indicated by the black arrow. A spherical, random distribution of the fluctuation directions is assumed. Such an isotropic distribution averages to zero in space and so no asymmetric contribution has to be added to the static Hamiltonian.

Concept (1): Rotational reorientation. We start with a general description of the fluctuating tensor elements $V_m^{(2)P}$ depending on time and some internal coordinates (q_i) [202]. We simplify this approach and consider only a dependence due to one component q:

$$V_m^{(2)P}(q(t)) = V_m^{(2)P}(q^0) + \Delta q(t)\frac{\partial V_m^{(2)P}}{\partial q} + \textit{higher order terms} \tag{5.9}$$

The first term $V_m^{(2)P}(q^0)$ is the low symmetry part of the EFG which is fluctuating due to motions of the molecule and the second term $\frac{\partial V_m^{(2)P}}{\partial q}$ represents the coupling of the EFG to the lattice coordinate q.

An angular reorientation of the EFG of equation 5.9 can be described by a transform of the tensor components $V_m^{(2)}$ from a molecular fixed frame (M) to the principal axis system (P) of the main Hamiltonian using the Wigner rotation matrix $D^{(2)}_{m',m}(\Omega_{MP}(t))$ [211] and time dependent Euler angles $\Omega_{MP}(t)$.

$$V_m^{(2)M}(\Omega_{MP}(t)) = \sum_{m'=-2}^{+2} D^{(2)}_{m',m}(\Omega_{MP}(t))V_{m'}^{(2)P} \tag{5.10}$$

This transform is needed to be able to add the static and the stochastic Hamiltonian to a total Hamiltonian (see figure 5.1). Inserting equation 5.9 into 5.10 gives

$$\begin{aligned} V_m^{(2)M}(t) &= \sum_{m'} D^{(2)}_{m,m'}(\Omega_{MP}(t)) V_{m'}^{(2)P} \\ &= \sum_{m'} D^{(2)}_{m,m'}(\Omega_{MP}(t)) \left[V_{m'}^{(2)P}(q^0) + \Delta q(t) \frac{\partial V_{m'}^{(2)P}}{\partial q} \right] \\ &= \sum_{m'} \left[D^{(2)}_{m,m'}(\Omega_{MP}(t)) V_{m'}^{(2)P}(q^0) + D^{(2)}_{m,m'}(\Omega_{MP}(t)) \Delta q(t) \frac{\partial V_{m'}^{(2)P}}{\partial q} \right] \end{aligned} \tag{5.11}$$

To form the autocorrelation function of equation 5.11, $\langle V_m^{(2)M*}(t) V_n^{(2)M}(t+\tau) \rangle$, a couple of assumptions are made. The only non-zero tensor element is V_0^P and advantage is taken of the relation $\langle D^{(2)*}_{n,m}(\Omega_{MP}(t)) D^{(2)}_{n',m'}(\Omega_{MP}(t+\tau)) \rangle = \delta_{m,m'} \delta_{n,n'} \frac{1}{5} e^{-t/\tau_r}$ which is only valid for isotropic rotational diffusion [191, 102] with the reorientation correlation time τ_r. But as the averaged motion of the angles in a solid might not be isotropic, a non-zero average term $\overline{D^{(2)}_{0,m}(\Omega_{MP}(t))} \neq 0$ has to be considered and relaxation is due to $\Delta D^{(2)}_{0,m}(\Omega_{MP}(t)) \equiv D^{(2)}_{0,m}(\Omega_{MP}(t)) - \overline{D^{(2)}_{0,m}(\Omega_{MP}(t))}$. Altogether, an expression for the spectral density according to equation 5.26b of the first term of equation 5.11 reads as:

$$J_{\alpha\beta\alpha'\beta'}(\nu) \sim \langle |\Delta D^{(2)}_{0,m}(\Omega_{MP}(t))|^2 \rangle (V_0^P(q^0))^2 \frac{1}{5} \frac{\tau_r}{1+\nu^2\tau_r^2}, \tag{5.12}$$

which is the PR model. For the second term in equation 5.11 it is further assumed that the coupling term $\frac{\partial V_0^{(2)P}}{\partial q}$ is constant and the internal coordinate $q(t)$ is proportional to a normal mode of the harmonic oscillator Hamiltonian that describes vibrations in a lattice with frequency ν_v, amplitude $\langle \Delta q^2 \rangle$ and relaxation time τ_v: $\langle \Delta q^*(t)\, \Delta q(t+\tau) \rangle \sim \langle \Delta q^2 \rangle \cos(\nu_v t) e^{-t/\tau_v}$. Thus it can be found that

$$J_{\alpha\beta\alpha'\beta'}(\nu) \sim \langle |\Delta D^{(2)}_{0,m}(\Omega_{MP}(t))|^2 \rangle (\frac{\partial V_0^{(2)P}}{\partial q})^2 \langle \Delta q^2 \rangle \frac{1}{5} \frac{\tau_{eff}}{1+(\nu-\nu_v)^2\tau_{eff}^2}, \tag{5.13}$$

where $\frac{1}{\tau_{eff}} = \frac{1}{\tau_r} + \frac{1}{\tau_v}$. With all the mentioned approximations, the spectral density of the rotational reorientations model is a simple Lorentzian (equation 5.12). With the inclusion of a vibrational mode from the lattice a shifted Lorentzian is formed (equation 5.13). This result corresponds to the model presented in [202]. However, the core of the derivation is the solution of the three dimensional diffusion equation which is mostly used for molecules in liquids. Also, the properties of Wigner matrix elements can only be utilized for an isotropic case. This concept appears somewhat ad hoc and may not be adequate for solid as it is quite restricted and makes use of a couple of assumptions.

Concept (2): Fluctuating EFG amplitude. Instead of a time dependent orientation of the EFG, we assume that the directions Ω_{MP} of the fluctuations are constant but their magnitudes $q_{cc}(t)$ are stochastically fluctuating (see equations 5.29a and 5.29b). We call this the flickering amplitude (FA) model. Again, a transform of the EFG tensor components $V_m^{(2)}$ from a molecular fixed frame (M) to the principal axis system (P) of the main Hamiltonian is needed to describe a certain fluctuation direction:

$$V_m^{(2)M}(t,\Omega_{MP}) = \sum_{m'=-2}^{+2} D^{(2)}_{m',m}(\Omega_{MP}) V_{m'}^{(2)P}(t) = q_{cc}(t) d_m(\Omega_{MP}) \tag{5.14}$$

This time, the transform is performed explicitly and the result can be found in equation 5.29b. For the last relation in equation 5.14, time and spatial dependence of $V_m^{(2)M}(t,\Omega_{MP})$ is separated into the time dependent amplitude $q_{cc}(t)$ of $\hat{H}_1(t,\Omega_{MP})$ and an angle dependent factor $d_m(\Omega_{MP})$. Forming the autocorrelation function of the time dependent tensor elements $V_m^{(2)M}(t,\Omega_{MP})$ yields:

$$\begin{aligned} \langle V_m^{(2)M*}(0) V_n^{(2)M}(t)\rangle &= d_m(\Omega_{MP}) d_n(\Omega_{MP}) \langle q_{cc}(t)^* q_{cc}^0\rangle \\ &= d_m(\Omega_{MP}) d_n(\Omega_{MP}) \langle q_{cc}^2\rangle e^{-t/\tau_c} \end{aligned} \tag{5.15}$$

The only assumption made is that the autocorrelation function of the amplitude of the fluctuations is mono exponential and independent of direction: $\langle q_{cc}(t)^* q_{cc}^0\rangle = \langle q_{cc}^2\rangle e^{-t/\tau_c}$, with fluctuation amplitude q_{cc} and correlation time τ_c. This is justified as the amplitude's motion can be approximated by a damped mass-spring system excited by the environment. Such systems frequently occur in nature and are often described by a Lorentzian. Beyond that, e.g. molecular dynamics (MD) simulations of the electron proton dipole-dipole correlation time of hydrated Gd ions support a mono exponential behavior [212]. The spectral density for the FA model is:

$$\begin{aligned} J_{\alpha\beta\alpha'\beta'}(\nu) &\sim \langle q_{cc}^2\rangle \frac{\tau_c}{1+\nu^2\tau_c^2} d_m(\Omega_{MP}) d_n(\Omega_{MP}) \\ &= \widetilde{J}(\nu) d_m(\Omega_{MP}) d_n(\Omega_{MP}) \end{aligned} \tag{5.16}$$

Coupling of the EFG to a lattice mode introduces a vibrational mode to the amplitude fluctuations. This is in accordance with the result of concept (1) with the only difference that instead of the angles, the amplitude of the EFG is oscillating: $\langle q_{cc}(t)^* q_{cc}^0\rangle = \langle q_{cc}^2\rangle \cos(\nu_v t) e^{-t/\tau_c}$, with frequency ν_v, amplitude q_{cc} and correlation time τ_c. The oscillating contribution is a consequence of the inclusion of the second term of equation 5.9. It considers possible vibrational modes in solids that can modulate the EFG amplitude. We call this flickering vibrational amplitude (FVA) model and the spectral density reads as:

$$\begin{aligned} J_{\alpha\beta\alpha'\beta'}(\nu) &\sim \langle q_{cc}^2\rangle \frac{\tau_c}{1+(\nu-\nu_v)^2\tau_c^2} d_m(\Omega_{MP}) d_n(\Omega_{MP}) \\ &= \widetilde{J}(\nu) d_m(\Omega_{MP}) d_n(\Omega_{MP}) \end{aligned} \tag{5.17}$$

The resulting spectral densities are again a simple Lorentzian and a shifted Lorentzian, respectively (equations 5.16 and 5.17). In contrast to concept (1), however, it was not necessary to make use of the orthogonal properties of Wigner matrices and no assumption is made about the EFG tensor elements. Their influence is encoded in $d_m(\Omega_{MP})$ which can be evaluated explicitly (equation 5.29b). This also means, that the fluctuation needs not necessarily be assumed isotropic as it is possible to average over a certain arbitrary set of Euler angles $\{\Omega_{MP}\}$. In case of spherical distribution of this angles, concept (1) and concept (2) are essentially equal with the only difference, that the elements $V_{\pm 1}$ and $V_{\pm 2}$ of the fluctuation Hamiltonian $\hat{H}_1$ need not be assumed zero. A downside of course is, that with concept (2) it is necessary to calculate the relaxation matrix Γ for all assumed directions $\{\Omega_{MP}\}$ numerically and form the average which is leads to larger computation time.

The two above introduced mechanism (FA and FVA model) and the derived mathematical expressions for the correlation functions of the EFG motions shall be seen as the result of considering the sum of all possible molecular motions in the solid and their effect on the EFG in a very simplified manner. A sophisticated treatment would require the inclusion of e.g. different torsional modes of the molecule, states of vibrations of covalent bonds as well as a density of states for the phonon dispersion and their interaction with the nuclear spin system via Raman processes [193, 194, 195, 196]. Therefore, we also forgo an explicit description of the temperature dependence of the introduced parameters, which is quite elaborate for this system and would introduce even more unknowns. Even though, the free parameters fluctuation amplitude q_{cc}, correlation time τ_c and vibration frequency ν_v are expected to be temperature dependent.

5.2.4 Explicit evaluation

As we have now defined the formalism of the lineshape calculations, included the assumed interactions and formulated the motional model of the stochastic Hamiltonian, the question remains which elements of the spin density $\rho(\nu)$ have to be considered. To do so, equation 5.7 can be evaluated formally for an ensemble with nuclear spin number $I = 9/2$ (see appendix 5.5 equation 5.30 and 5.31). Thus, all together 17 elements (9 single coherence and 8 double coherence terms) are picked out and the corresponding set of Liouville basis operator states is:

$$\begin{aligned}\{\ &|\tfrac{1}{2},\tfrac{3}{2}\rangle, |-\tfrac{1}{2},-\tfrac{3}{2}\rangle, |-\tfrac{1}{2},\tfrac{3}{2}\rangle, |\tfrac{1}{2},-\tfrac{3}{2}\rangle, |-\tfrac{1}{2},\tfrac{1}{2}\rangle, |\tfrac{3}{2},\tfrac{5}{2}\rangle,\\ &|-\tfrac{3}{2},-\tfrac{5}{2}\rangle, |\tfrac{5}{2},\tfrac{7}{2}\rangle, |-\tfrac{5}{2},-\tfrac{7}{2}\rangle, |\tfrac{7}{2},\tfrac{9}{2}\rangle, |-\tfrac{7}{2},-\tfrac{9}{2}\rangle, |\tfrac{3}{2},\tfrac{7}{2}\rangle,\\ &|-\tfrac{3}{2},-\tfrac{7}{2}\rangle, |\tfrac{5}{2},\tfrac{9}{2}\rangle, |-\tfrac{5}{2},-\tfrac{9}{2}\rangle, |\tfrac{1}{2},\tfrac{5}{2}\rangle, |-\tfrac{1}{2},-\tfrac{5}{2}\rangle\ \}\end{aligned} \tag{5.18}$$

In all further treatments, the order of the operator states given above is maintained for the vectors and matrices contained in equation 5.7.

The evaluation of the Liouville matrix $\mathcal{L}^0$ and the relaxation matrix Γ has been performed according to equations 5.25 and 5.26a for the operator states of equation 8.1 and the spectral densities formulated in equations 5.16 and 5.17. The analytical results are presented in appendix 5.5, equations 5.33, 5.34 and 5.35 and were calculated with the help of a Mathematica code (see supplemental materials) supported by the SpinDynamica toolbox [213]. The found elements $\Gamma_{\alpha\alpha'\beta\beta'}$ are depending on the directions of the fluctuations with respect to the main Hamiltonian via the angle dependent factors $d_m(\Omega_{MP})$. These factors can be interpreted as angle depending weighting factors for the efficiency of a certain direction inducing relaxation. We have chosen a set of N_Ω Euler angles $\{\Omega_{MP}\}$ describing a spherical distribution (see figure 5.1) and calculated an averaged relaxation matrix $\Gamma = \sum_\Omega \Gamma(\Omega)/N_\Omega$ thus representing the chosen distribution.

A closer look at the $\Gamma_{\alpha\alpha'\beta\beta'}$ elements illustrates the typical features of spin-spin relaxation: It is possible to identify non-adiabatic fluctuations that cause transitions between states which results in a finite lifetime and thus lead to the decay of coherences due to an uncertainty in the energy levels. Such fluctuation also lead to a redistribution and equilibration of populations (R_1 decay). These terms contain the angle dependent part of the tensor operators $V_m^{(2)M}(t, \Omega_{MP})$, d_{+1}, d_{-1} and spectral densities $\widetilde{J}(\nu_{\Delta m=1})$ for single, and d_{+2}, d_{-2} and $\widetilde{J}(\nu_{\Delta m=2})$ for double quantum transitions. Adiabatic fluctuations are represented by terms containing d_0 and zero quantum transitions at $J(0)$. These terms generate variations in the energy levels of the spins which lead to random fluctuations of the transition frequencies and so, over time, coherences are running out of phase. This contribution only acts on R_2, and not on R_1 relaxation as it cannot induce transitions for redistributing populations [214].

As the analytical expressions for the elements of the Liouvillian and the relaxation matrix are rather long, matrix plots containing the evaluated elements for a particular set of parameters are given in figure 5.2. The relaxation matrix on the

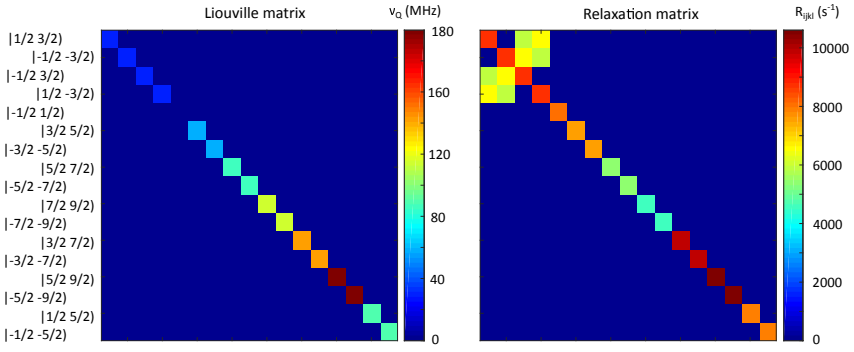

FIGURE 5.2: Matrix plot of the evaluation of the Liouvillian (according to equation 5.25) and the relaxation matrix (according to equation 5.26a). The labeling of rows and columns is given on the lefthand side according to the operators of equation 8.1. The secular approximation (see equation 5.4) has already been applied. An interesting feature is the appearence of off diagonal elements in the relaxation matrix as a result of degenerate energy levels and double coherence elements. Parameters: $I = 9/2$ $Q_{cc} = 668.8$, $\eta = 0.086$, $q_{cc} = 4.46$ MHz, $\tau_c =$ 4e-9 s/rad, $\nu_v = 0$, $N_\Omega = 150$, T = 310 K. Analytical expressions can be found in equations 5.33, 5.34 and 5.35.

right hand side determines the lineshapes of the spin transitions with center frequencies determined by the Liouvillian (left hand side matrix). The 4x4 block in the upper left corner of Γ, determining the lineshape of the lowest, 3/2-1/2 transition, contains off-diagonal elements which have to be considered when calculating its R_2 relaxation rate. The relaxation rates of the higher transitions are, however, determined directly by the relaxation rate elements on the diagonal. The consequence of this issue is discussed closer in section 5.3.1.

5.2.5 Lineshape analysis and fitting procedure

The NQR-spectrum obtained from the procedure above can be plotted by evaluating equation 5.7. This numerical task is performed in Matlab. The following parameters have to be defined:

- NQR parameter: Q_{cc}, η and nuclear spin number I (defined by the sample)
- Sample temperature: T (for ρ_0)
- Dynamics: EFG fluctuation amplitude q_{cc} and correlation time τ_c for the FA model, additionally the vibration frequency ν_v for the FVA model; Number of angles considered for the spherical distribution of fluctuations N_Ω.

The lineshape of a particular sample, deuterated triphenylbismuth at 310 K (see table 5.1), is given in figure 5.3. The dynamical parameters are the same as used in figure 5.2, where the structures of the underlying matrices $\mathcal{L}^0$ and Γ are displayed. In accordance with spin number $I = 9/2$, four single coherence transitions can be distinguished. The transitions are labeled from $t1$ (which is the lowest) to $t4$ (which is the highest). Also, one quite small double quantum coherence transition is visible at 84.88 MHz (labelled DQ), arising due to $\eta \neq 0$. This transition was not observed experimentally, but might be detectable with a two-photon excitation method as described by Eles and Michal [215, 216]. The peaks are all of Lorentzian shape (which is confirmed by spin-echo NQRS experiments [61]) but their widths, which are the result of spin-spin relaxation, are different. As a measure for the spin-spin relaxation rate suggested by the simulation, the half width at half maximum (HWHM) $\delta^{(i)}$ is determined from the plot in figure 5.3 and we get

$$R^{(i)}_{2,sim}(q_{cc}, \tau_c, \nu_v) = \delta^{(i)}, \tag{5.19}$$

where (i) denotes the number of the transition. For the FVA model, there are three free parameters, in case of the FA model, the frequency ν_v is zero. A sweep through parameter space gives an example for the behavior of $R^i_{2,sim}$ on the free dynamical parameter τ_c and ν_v (see figure 5.4). The amplitude $\langle q^2_{cc} \rangle$ is just a scale factor and is fixed for the examples. The plot in panel (a) has been derived by evaluating a spectrum like the one presented in figure 5.3 for different correlation times τ_c and picking out the widths $\delta^{(i)}$ of each single coherence transition which are the relaxation rates

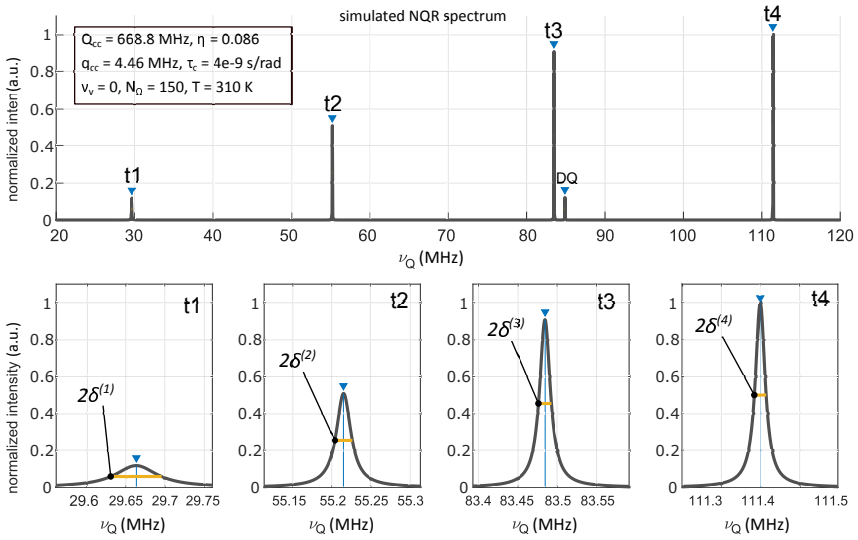

FIGURE 5.3: Example of a simulated NQR spectrum (equation 5.7) for deuterated triphenylbismuth at 310 K for arbitrary EFG dynamics (parameters see insert). In the upper panel an overview is given and in the lower panels the four single quantum coherences are zoomed out. Their lineshape is Lorentzian but the width at half maximum (yellow line $= 2\delta^{(i)}$) is different in each case. The intensity distribution is additionally modulated by the initial condition $\rho(0)$ that contains the Boltzmann distribution differences. However, to get the intensities of an actual NQR experiment, the resonances must be weighted with their associated transition probability with respect to an applied excitation field produced by a coil (placed in a certain direction in the laboratory frame (L)). Also, the induction law for detecting the signal must be applied. Crystal defects lead to inhomogeneous broadening which is not considered here.

$R^{(i)}_{2,sim}(\tau_c)$. The overall tendency shows, that the relaxation rates become higher for slower EFG dynamics. Clearly, a modulation of the strength of the relaxation rates over the correlation time is visible which is different for each transition due to their different transition frequencies. Interesting to see from the plot is also, that $R^{(1)}_{2,sim}$ is decaying faster than all other transitions. The same procedure can be performed when including vibration ν_v of the amplitude (FVA model), which is shown in panel (b) of figure 5.4. For slow vibrations (ν_v = 10^5 MHz and below), a cut through the surface plot along the τ_c axis will give quite the same result as in panel (a). But as soon as the vibration frequency reaches the order of frequencies of the nuclear spin transitions, the relaxation rates can be drastically altered. To demonstrate this effect more clearly, in panel (c) a cut through the surface plot at constant $\tau_c = 2 \cdot 10^{-8}$ s/rad along ν_v is presented. Whenever ν_v matches one of the spin transition frequencies, the corresponding relaxation rate is enhanced strongly (indicated by the red arrows labeled with the transition number). Interestingly, not only the rate of the associated transition is enhanced but also all other transitions are enhanced to a lesser or stronger extent. This is due to the occurrence of different spectral densities $J(\nu)$ in each relaxation matrix element (see appendix 5.5, equations 5.33, 5.34 and 5.35). Each element of the relaxation matrix eventually is a weighted sum of relaxation terms from all spin states. The parameters that are fitted to the experimental data

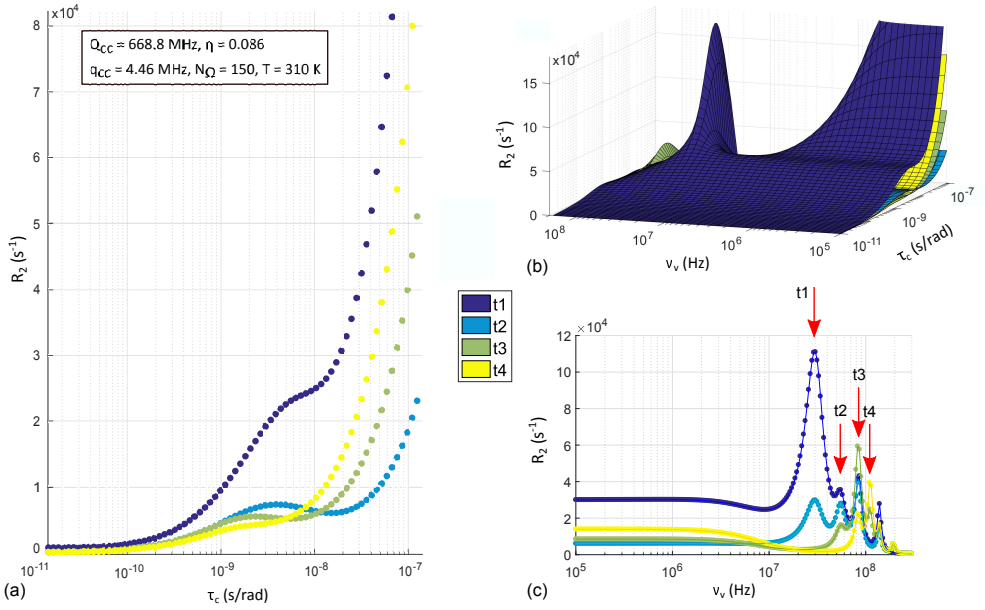

FIGURE 5.4: Behavior of the relaxation rates $R^i_{2,sim}$ of the four single quantum coherences when sweeping through parameter space of the two EFG dynamics at fixed fluctuation amplitude q_{cc}. Panel (a) shows $R^i_{2,sim}(\tau_c)$ for the FA model. Panel (b) shows a surface plot for $R^i_{2,sim}(\tau_c, \nu_v)$ of the FVA model. The colors denote the spin transitions: Dark blue: $t1$, light blue: $t2$, green: $t3$ and yellow: $t4$. In panel (c) a cut through the 3D surface plot for the FVA model at τ_c = 2e-8 s/rad is shown to demonstrate the effect of a vibrational EFG fluctuation. At the position of the red arrows, the vibration frequency of the EFG fluctuation coincides with the frequency of a spin transition. At resonance, the relaxation rates are enhanced strongly.

are q_{cc}, τ_c and ν_v. The experimental relaxation $R^{(i)}_{2,exp}$ rates are provided by NQR

relaxation measurements (see section 5.2.7). To get rid of q_{cc} (which is just a scaling factor), the ratios between the relaxation times of all available transitions are calculated and compared to the ratios suggested by the experiment. Thus, the cost function for a least squares optimization is:

$$S(\tau_c) = \sum_{i \neq j}^{n} \left(\frac{R_{2,sim}^{(i)}(\tau_c, \nu_v)}{R_{2,sim}^{(j)}(\tau_c, \nu_v)} - \frac{R_{2,exp}^{(i)}}{R_{2,exp}^{(j)}} \right)^2 \tag{5.20}$$

where n is the total number of transitions per sample from which the relaxation rate has been determined. The minimum of this cost function, found by an exhaustive search algorithm, gives the best fit parameters.

5.2.6 Closed form solution

The calculation of the lineshape using the complete Liouville and Redfield matrix according to the above presented procedure covers the most general case. Any form of coupling will be considered. However, it is worth to have a closer look at the particular form of the matrices and derive analytical expressions for the observable single quantum coherences. Obviously, for the transitions $t2$ to $t4$, both the Liovillian and the Redfield matrices are diagonal (compare figure 5.2). Thus, their R_2 relaxation rates are not coupled and the respective matrix elements can be calculated from equation 5.33. Based on equation 5.6, the lineshapes of transitions $t2$ to $t4$ follow a simple Lorentzian:

$$\begin{aligned} L(\nu)_{t2} &= Re\left[\left[i\left(\nu - \nu_{Q,t2}\right) + \Gamma_{\frac{3}{2}\frac{5}{2}\frac{3}{2}\frac{5}{2}}\right]^{-1}\right] \\ L(\nu)_{t3} &= Re\left[\left[i\left(\nu - \nu_{Q,t3}\right) + \Gamma_{\frac{5}{2}\frac{7}{2}\frac{5}{2}\frac{7}{2}}\right]^{-1}\right] \\ L(\nu)_{t2} &= Re\left[\left[i\left(\nu - \nu_{Q,t4}\right) + \Gamma_{\frac{7}{2}\frac{9}{2}\frac{7}{2}\frac{9}{2}}\right]^{-1}\right] \end{aligned} \tag{5.21}$$

The situation is different for transition $t1$, where off-diagonal elements appear in the Redfield matrix. Taking advantage of the symmetry of the 4x4 submatrix (comprising only relevant $\pm 3/2 \leftrightarrow \pm 1/2$ states), a Wang transform can be applied to form a block symmetric shape. The total lineshape is then a sum of $\rho_{1/2,3/2}$ and $\rho_{-1/2,-3/2}$ (see appendix 5.5)

$$L(\nu)_{t1} = Re\left[\frac{(-1)\cdot(\Gamma_{-\frac{1}{2}\frac{3}{2}\frac{1}{2}\frac{1}{3}} + \Gamma_{\frac{1}{2}-\frac{3}{2}\frac{1}{2}\frac{3}{2}}) + \left(i(\nu - \nu_{Q,t1}) + \Gamma_{-\frac{1}{2}\frac{3}{2}-\frac{1}{2}\frac{3}{2}}\right)}{-(\Gamma_{-\frac{1}{2}\frac{3}{2}\frac{1}{2}\frac{1}{3}} + \Gamma_{\frac{1}{2}-\frac{3}{2}\frac{1}{2}\frac{3}{2}})^2 + \left(i(\nu - \nu_{Q,t1}) + \Gamma_{\frac{1}{2}\frac{3}{2}\frac{1}{2}\frac{3}{2}}\right)\left(i(\nu - \nu_{Q,t1}) + \Gamma_{-\frac{1}{2}\frac{3}{2}-\frac{1}{2}\frac{3}{2}}\right)}\right] \tag{5.22}$$

The relaxation matrix elements can be found in equations 5.33 to 5.35. In the presented case $\Gamma_{\frac{1}{2}\frac{3}{2}\frac{1}{2}\frac{3}{2}} = \Gamma_{-\frac{1}{2}\frac{3}{2}-\frac{1}{2}\frac{3}{2}}$ applies which means equation 5.22 simplifies to:

$$L(\nu)_{t1} = Re\left[\left[i\left(\nu - \nu_{Q,t1}\right) + \Gamma_{\frac{1}{2}\frac{3}{2}\frac{1}{2}\frac{3}{2}} + \Gamma_{-\frac{1}{2}\frac{3}{2}\frac{1}{2}\frac{1}{3}} + \Gamma_{\frac{1}{2}-\frac{3}{2}\frac{1}{2}\frac{3}{2}}\right]^{-1}\right] \tag{5.23}$$

Equation 5.23 is again a Lorentzian where the relaxation rate is a sum of three Redfield elements. Equations 5.21 and 5.23 give the same spectrum and lineshapes as presented in figure 5.3.

5.2.7 Experimental relaxation rates and materials

Experimental data for testing the introduced model for quadrupole spin-spin relaxation is mostly taken from [61], where spin-spin and spin-lattice relaxation times, $T_2 = 1/R_2$ and $T_1 = 1/R_1$, have been presented for a set of Bi-aryl compounds in powder form. The ^{209}Bi nucleus has nuclear spin I=9/2 and thus gives rise to four observable spin resonances. We have decided to only discuss samples and temperatures for which relaxation times of all four transitions are available. For triphenylbismuth, deuterated triphenylbismuth and tris(4-flourophenyl)bismuth complete data sets are available at 310 K and 77 K. However, for all three samples, T_2 of $t1$ at 310 K was measured within this work to complement the data sets and has not been published yet. The relaxation measurements were performed with a pulse type NQR spectrometer (Tecmag, USA, "Scout") using a spin-echo sequence with variable echo time so that T_2 is connected with homogeneous broadening only. T_2 was determined by fitting a mono-exponential model to the signal. For all discussed samples the NQR parameters Q_{cc} and η as well as the experimentally found spin-spin relaxation rates $R^{(i)}_{2,exp}$ are presented in table 5.1.

The selected Bi-aryl samples are monoclinic molecular crystals. The molecule has a trigonal pyramidal structure with tilted phenyl rings forming the basis and the tricoordinated Bi is at the top. Structure and synthesis information has been published in [155, 172] and is summarized in [61], where also a 3D structure file for triphenylbismuth is available. Standard safety precautions have to be met when handling the mentioned chemicals according to their respective safety data sheet.

5.3 Results

5.3.1 The role of off-diagonal elements

The impact of the inclusion of off-diagonal elements via the lineshape treatment compared to a calculation of only the diagonal single coherence relaxation rates is illustrated in figure 5.5. Panel (a) shows $R^{(i)}_{2,sim}(\tau_c)$ for the FA model, where $R^{(i)}_{2,sim}$ has been derived from the widths $\delta^{(i)}$ of the single spin resonances according to the above presented procedure (same set of parameters as figure 5.4). In panel (b), however, each $R^{(i)}_{2,sim}(\tau_c)$ is directly calculated from equation 5.26a for each observable

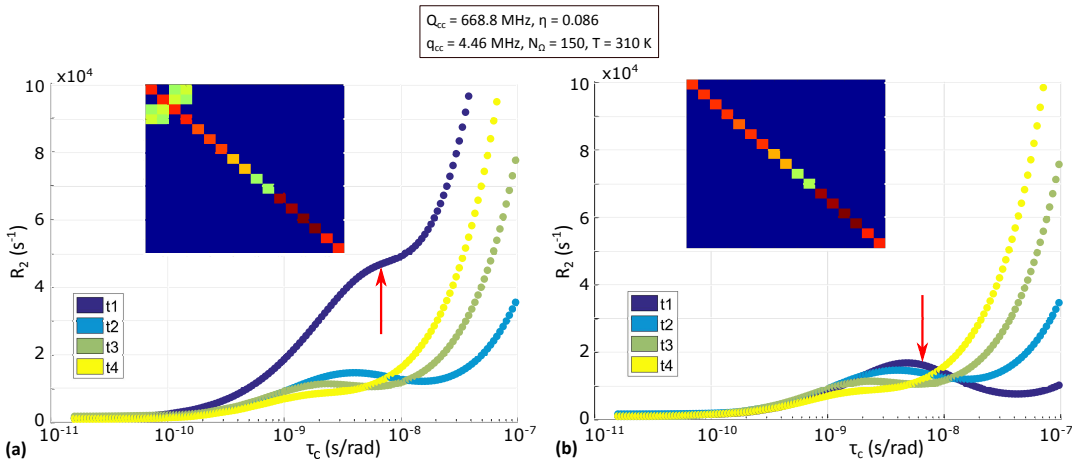

FIGURE 5.5: In panel a), $R^{(i)}_{2,sim}(\tau_c)$ is calculated from the widths of the lineshape calculated from equation 5.7 as also shown in figure 5.4 a). For the same set of NQR parameter, in panel b) $R^{(i)}_{2,sim}(\tau_c)$ are just the diagonal elements of the relaxation matrix Γ of the associated transition according to equation 5.33, without using the lineshape approach (as in [94]). The relaxation rate for $t1$ is much larger in panel a) then in panel b) due to the incorporation of off diagonal elements in the Redfield matrix, which is indicated by the inserts. This behavior is marked with a red arrow. Transitions $t2$ to $t4$ are not affected.

single coherence transition (see $\Gamma_{\frac{1}{2}\frac{3}{2}\frac{1}{2}\frac{3}{2}}$, $\Gamma_{\frac{3}{2}\frac{5}{2}\frac{3}{2}\frac{5}{2}}$, $\Gamma_{\frac{5}{2}\frac{7}{2}\frac{5}{2}\frac{7}{2}}$ and $\Gamma_{\frac{7}{2}\frac{9}{2}\frac{7}{2}\frac{9}{2}}$ in equation 5.33), which is the same procedure as in [94] and corresponds to the assumption of a diagonal Redfield matrix without including double quantum coherence terms. A strong difference occurs for $R^{(1)}_{2,sim}$ (dark blue) which is much larger in panel (a) than in panel (b) (indicated by the red arrow). Transitions $t2$ to $t4$ are not affected, as all off diagonal elements in the relaxation matrix next to these transitions are zero. For $t1$, however, the non-zero off diagonal elements open up another relaxation route via $|-1/2, 3/2)$ and $|-3/2, 1/2)$ double coherence states which are at the same frequency as the single coherence terms (see figure 5.2). These non-zero off diagonal terms are a consequence of degenerate energy levels in pure NQR as well as the consideration of double coherences. The matrix equation 5.6 mixes these terms into the single expressions for the spin density elements, in particular $\rho_{\pm 3/2,\pm 1/2}(\nu)$.

When an external magnetic field is applied, these additional relaxation pathways and the enhanced relaxation disappear, as in that case degeneracy of $\pm$m states is cancelled. The reason is, that zero-field NQR energy levels as well as the resonance peaks are split and the secular approximation (see equation 5.4) prohibits off diagonal elements. This effect is expected to lead to a prolongation of the T_2 relaxation time and thus might contribute to a signal enhancement in NQR experiments when a small magnetic field is applied, as reported e.g. by Lehmann-Horn et al. on ^{75}As in $FeAs_2$ [147].

TABLE 5.1: Sample name, NQR parameter, experimental relaxation rates and simulation results with best fit parameter for the FA and the FVA model

Experimental sample	NQR parameter		tr.	ν_Q (MHz)	$R_{2,exp}$ (s^{-1})	FA model $R_{2,sim}$ (s^{-1})	deviation (%)	best fit parameter		FVA model $R_{2,sim}$ (s^{-1})	deviation (%)	best fit parameter	
	T (K)	77	t1	30.64	9803.9	7322	-33.9	q_{cc} (MHz)	1.136	9533	-2.8	q_{cc} (MHz)	2.081
triphenyl	Q_{cc} (MHz)	684.6	t2	56.45	2538.1	2317	-9.5	τ_c (s/rad)	$4.92{\cdot}10^{-9}$	2616	3.0	τ_c (s/rad)	$1.90{\cdot}10^{-8}$
bismuth	η (1)	0.09	t3	85.45	1246.9	1584	21.3			1149	-8.5	ν_v (MHz)	17.01
			t4	114.03	1216.6	1564	22.2			1328	8.4		
	T (K)	310	t1	29.72	11770.0[2]	10560	-11.5	q_{cc} (MHz)	1.680	11300	-4.2	q_{cc} (MHz)	2.114
triphenyl bismuth	Q_{cc} (MHz)	668.3	t2	55.14	3610.1	3415	-5.7	τ_c (s/rad)	$4.69{\cdot}10^{-9}$	3655	1.2	τ_c (s/rad)	$5.83{\cdot}10^{-9}$
	η (1)	0.087	t3	83.42	2293.6	2413	4.9			2286	-0.3	ν_v (MHz)	17.01
			t4	111.32	2057.6	2346	12.3			2127	3.3		
	T (K)	77	t1	30.72	1612.9	1305	-23.6	q_{cc} (MHz)	0.207	1620	0.4	q_{cc} (MHz)	0.214
triphenyl bismuth	Q_{cc} (MHz)	685.6	t2	56.52	508.7	424	-19.9	τ_c (s/rad)	$4.57{\cdot}10^{-9}$	498.9	-2.0	τ_c (s/rad)	$7.39{\cdot}10^{-9}$
deuterated	η (1)	0.095	t3	85.56	231.6	293	20.8			239.2	3.2	ν_v (MHz)	19.78
			t4	114.19	215.3	278	22.7			211.9	-1.6		
	T (K)	310	t1	29.78	3759.4[2]	3623	-3.8	q_{cc} (MHz)	1.664	3651	-3.0	q_{cc} (MHz)	1.44
triphenyl bismuth	Q_{cc} (MHz)	668.8	t2	55.25	1610.3	1717	6.2	τ_c (s/rad)	$7.76{\cdot}10^{-10}$	1719	6.3	τ_c (s/rad)	$9.54{\cdot}10^{-10}$
deuterated	η (1)	0.086	t3	83.49	1589.8	1695	6.2			1687	5.8	ν_v (MHz)	4.84
			t4	111.40	1404.5	1293	-8.6			1288	-9.0		
	T (K)	77	t1	28.65	20833.0	11370	-83.2	q_{cc} (MHz)	1.676	17940	-16.1	q_{cc} (MHz)	1.71
tris(4-fluorophenyl)	Q_{cc} (MHz)	672.5	t2	55.86	2222.2	3464	35.8	τ_c (s/rad)	$5.54{\cdot}10^{-9}$	4869	54.4	τ_c (s/rad)	$1.67{\cdot}10^{-8}$
bismuth	η (1)	0.053	t3	84.02	1721.2	2293	24.9			1442	-19.4	ν_v (MHz)	20.24
			t4	112.06	1831.5	2364	22.5			1540	-18.9		
	T (K)	310	t1	28.35	19608.0[2]	25210	22.2	q_{cc} (MHz)	49.860	19490	-0.6	q_{cc} (MHz)	6.572
tris(4-fluorophenyl)	Q_{cc} (MHz)	657.5	t2	54.51	12346.0	12830	3.8	τ_c (s/rad)	$1.70{\cdot}10^{-10}$	12170	-1.4	τ_c (s/rad)	$3.71{\cdot}10^{-9}$
bismuth	η (1)	0.071	t3	82.11	15152.0	13520	-12.1			15880	4.6	ν_v (MHz)	95.41
			t4	109.54	12048.0	10580	-13.9			11750	-2.5		

5.3.2 EFG dynamics

For the FA and the FVA model (equations 5.16 and 5.17) using isotropic fluctuations, the best fit parameters for most fluctuation amplitudes q_{cc} are found around 1 MHz, which is about 0.15 % of a typical static Q_{cc}. The timescales of the EFG fluctuations τ_c give values between 1 ns/rad and 10 ns/rad. At low temperature (77 K) the amplitudes are smaller and the correlation times are longer than at elevated temperatures (310 K). Details of all best fit parameters can be found in table 5.1 and are graphically presented in figure 5.6. These findings are in accordance with the observations in

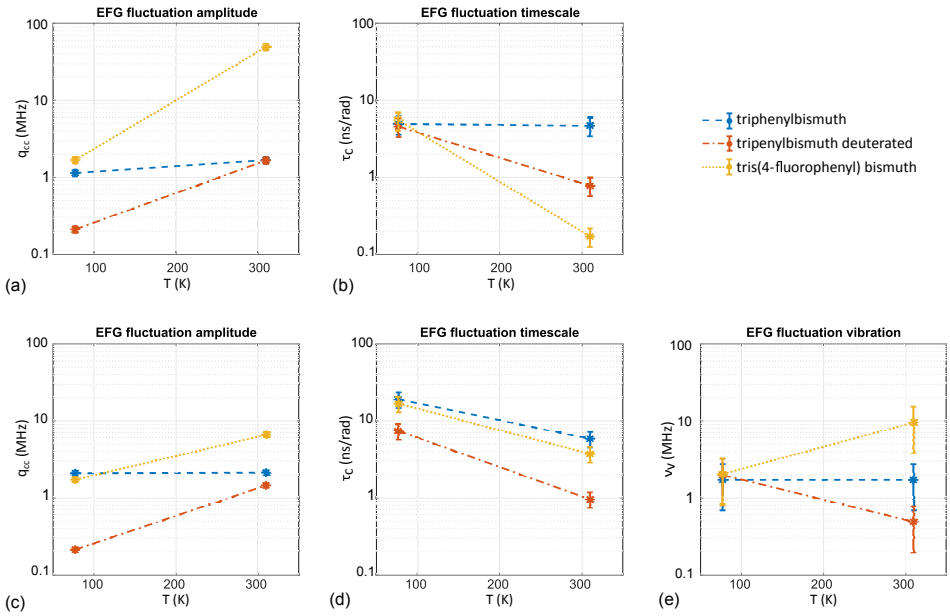

FIGURE 5.6: Summary of the best fit results for the parameters of the FA model (panels (a) and (b)) and the FVA model (panels (c)-(e)) applied to three different Biaryl compounds at two different temperatures (77 K and 310 K). The single fitting results can be found in appendix 5.5 figures 5.8 and 5.9. Errorbars are discussed in the supplemental materials. A dashed line serves as a guide to the eye.

the earlier work [94]. However, for tris(4-flourophenyl)bismuth at 310 K the best

fit for the FA model gives an amplitude of 50 MHz in combination with a very fast fluctuation of only 0.1 ns/rad. This result deviates from all the other examples as the fluctuations are almost as strong as the static interaction itself and indicates that the FA model cannot capture the experimental observation for this case. Only with the help of a third parameter in the FVA model (the vibrational mode with frequency ν_v), also for this case a reasonable amplitude and timescale for the fluctuations could be found. Not surprisingly, the inclusion of ν_v as third parameter improves the averaged deviation between experimental and simulated R_2 from about 18 % for the FA to 7 % for the FVA model (exact deviations see table 5.1). The values for ν_v settle between 5 MHz and 100 MHz. For most of the samples ν_v takes a value about 20 MHz, which is about the frequency of the lowest ($t1$) spin transition. This enhances R_2 of the $t1$ transitions even further.

This behavior is illustrated in figure 5.7, where deuterated triphenyl bismuth at 77 K has been picked out to present one result in more detail: The black dots with errorbars are the experimentally found values plotted versus the corresponding transition frequency. The dashed lines serve as a guide to the eye. This pattern is

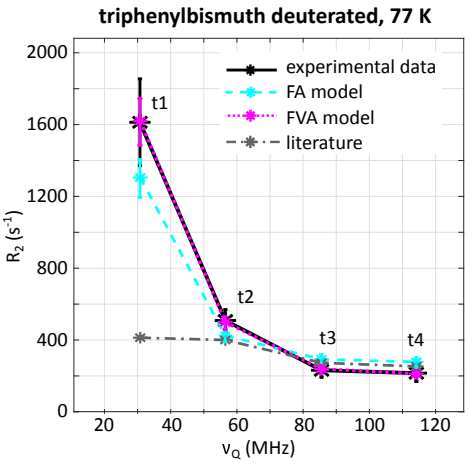

FIGURE 5.7: Experimental and fitted relaxation rates for deuterated triphenylbismuth at 77 K plotted versus the transition frequency. Data can be found in table 5.1, errorbars are discussed in the supplemental materials. Dashed line serves as a guide to the eye. Both best fit results for the FA (cyan) and the FVA model (magenta) can reproduce the experimental observation (black). The FVA model uses an additional parameter and performs better. For comparison, the literature result (grey) from [94] is included, where the relaxation rates are calculated directly without the use of lineshape calculation. For transitions $t2$ to $t4$, the results match with the FA model as it uses an equivalent motional model, the PR model. Only a constant shift is present due to different scaling, but $t1$ is clearly underestimated.

quite a usual result shared by all of the investigated samples: The lowest transitions decays at a much higher rate than all other transitions. The cyan stars show the result for the best fit of the FA model, the magenta stars for the FVA model. Even though the FA model already fits relatively well, in the FVA model the additional parameter shifts $R^{(1)}_{2,sim}$ even higher up. For comparison, another result from the literature [94] (grey stars), which applies the PR model, has been added and gives the same result as the FA model for transitions $t2$ to $t4$ (only shifted slightly down by

a constant term of about 24 s^{-1} due to a different mean value). This is expected, as both approaches employ the same dynamical model for the EFG. However, in [94] $t1$ was not simulated satisfactorily, where $R^{(1)}_{2,sim}$ is generally underestimated since off-diagonal elements of the relaxation matrix block were not included (see section 5.3.1). The rest of the results from table 5.1 are illustrated in appendix 5.5 figures 5.8 and 5.9.

5.4 Conclusions

There are two key findings which appear from this work that should be considered when applying Redfield relaxation theory to zero-field NQR: (1) In case of spin relaxation due to EFG fluctuations, the complete set of Liouville basis operators for single and double coherences should be considered when constructing the relaxation matrix. The reason is that EFG fluctuations can also induce double coherence terms, which becomes evident from the appearance of the $\widehat{I}^2_+$ operator in the quadrupole Hamiltonian. (2) The secular approximation must be applied correctly for the pure NQR case as the degenerate energy levels lead to non-zero off diagonal terms. A comparable situation due to degeneracy occurs for two equivalent coupled $I = 1/2$ spins, where also additional secular terms occur in the relaxation matrix [217]. The additional off-diagonal elements resulting from (1) and (2) are naturally considered by the proposed lineshape method which is a convenient way to solve the coupled differential equations for the spin density operator. Also, closed form analytical expressions could be derived for each single quantum coherence (see section 5.2.6). In the particular case presented here, for the lowest observable quadrupole transition between $\pm 3/2$ and $\pm 1/2$ states, the degeneracy opens additional relaxation pathways via double coherences which are not restricted via the secular approximation. The consequence is, that R_2 for this transition is enhanced by about a factor of 2 at typically observed dynamical conditions (e.g. 5 ns/rad). The correct treatment of this issue improves the result of an earlier work [94] considerably (see figure 5.7), where a reduced spin density matrix was used. The large discrepancy between experimental and theoretical relaxation rate for the lowest transition was attributed to an additional relaxation mechanism due to magnetic D-D coupling between protons and ^{209}Bi nuclei, which is sometimes considered as mechanism of line broadening in pure NQR transitions [218, 194]. However, in the Bi containing molecular crystals treated in this work (see section 5.2.7), this effect is considered as being small compared to EFG fluctuations. An estimation of the dipolar coupling constant between ^{209}Bi and the closest ^{1}H atom (~ 3.3 Å see [155]) gives about 550 Hz. In comparison, a typical value for Q_{cc} for the Bi-aryl compounds considered here is about 670 MHz and results of this work show, that fluctuations are of the order of 1 MHz (see table 5.1). In conclusion, and supported by the results of this work, no other relaxation

[2]Data acquired within this work. All other experimental relaxation rates and frequencies are taken from [61].

mechanism besides EFG fluctuations needs to be involved to account for the experimentally observed spin-spin relaxation rates.

The special case of the 3/2-1/2 transition is already pointed out in the earliest works on NQR (see [42]), where a small external magnetic field splits the lowest transition into four peaks while all other transition are only split into double lines. This finding is particularly important, as lots of NQR studies are performed on I=3/2 nuclei where no comparison to the relaxation of higher transitions can be made and this fact might be overlooked when e.g. analyzing the lineshape to reveal crystal inhomogeneities [219, 200]. Knowledge of the finite lifetime NQR resonance lineshape, as it is presented here, might also be interesting for predicting the correct lineshape of the quadrupole resonance enhancement (QRE) effect in solids [29, 31]. This issue has been addressed in [179] using only an approximated ad-hoc NQR lineshape and could be improved.

The presented motional models (FA and FVA) for the EFG fluctuations are alternatives to the pseudo rotational (PR) model used in [94] (typically used for isotropic rotations of molecules in liquids). Due to the explicit inclusion of spatial directions of the fluctuations, also anisotropic motions can be considered in principle (e.g. in case of linear molecules). Also, a vibrational mode is considered which is more adequate for solids. The FA and the FVA model, both based on the assumption that isotropic fluctuations of the EFG amplitude are the main source for nuclear quadrupole spin relaxation, were able to capture the main features of the experimental R_2 relaxation rates quite well, whereby the FVA model performed better especially at elevated temperatures (see section 5.3.2).

For discussing in more detail the fluctuation mechanism leading to R_2 relaxation, it helps also to have a look at the experimental R_1 (spin-lattice) results, published in [61]. At low temperature (77 K), R_1 and R_2 differ from each other quite significantly (R_2 is much higher than R_1). As R_1 relaxation is governed by phonon coupling [193, 194, 195, 196], inefficient R_1 relaxation is a hint for little vibrations present in the solid. So, fluctuations of the energy levels due to EFG changes according to the FA model are the most efficient relaxation mechanism. The model can reproduce the experimental observations quite well. At elevated temperature (310 K), however, the FA model does not perform so well any more. In that regime, R_2 and R_1 are closer together indicating that R_1 becomes more efficient and vibrations becoming more important governing both relaxation phenomena. In that regime, the FVA model, which allows a vibrational mode to modulate the EFG fluctuations, is able to reproduce the experimental data better than the FA model. However, in the supplemental material we propose an experiment that could demonstrate the role of vibrations and thus support or oppose the FVA model. Whether phonons, torsional oscillations or stochastic EFG fluctuations contribute most to the relaxation can only be distinguished when temperature profiles of R_2 and R_1 are known over a wider range and with small spacing. R_2 decay comprises adiabatic and non-adiabatic contributions from EFG fluctuations whereas R_1 decay is only due to non-adiabatic transitions.

By measuring both temperature profiles, the contributions can be separated when adequate models for the temperature dependency of the spectral densities of fluctuations due to the different motions in molecular crystals are found [194, 210].

To generate a better understanding of the EFG fluctuations and their connection to molecular motions, we encourage to perform ab-*initio* MD simulations for the presented compounds, as e.g. has been done for solid and molten $CHCl_3$ [220]. For triphenylbismuth, to our knowledge only static EFG tensor calculations have been reported using ab-*initio* quantum chemistry methods [61]. MD simulations could be used to review the assumed spherical distribution of the fluctuations. This also applies to the assumption of a mono exponentially decaying autocorrelation function, which is, however, supported by experimentally found quadrupole transitions using a spin-echo sequence which show a Lorentzian lineshape [61].

In conclusion, it has been shown that it is worth the efforts to apply relaxation theory to NQR spectroscopy for studying molecular motions in solids. The method expands the amount of accessible solid materials where no protons are present or other, NQR active nuclei are in the center of interest. An advantage is also, that the experimental expenses for operating an NQR device are much lower than for typical NMR machines or field-cycling relaxometers due to the lack of a magnet.

Disclosure statement

There are no conflicts to declare.

Funding details

This work was supported by the European Commission (Horizon 2020 Program) under grant [665172] (Future and Emerging Technologies (FET)-open CONQUER) and under grant [15209] (Cooperation in Science and Technology (COST) Action "European Network on NMR Relaxometry").

Notes

If the reader is interested closer in the Mathematica code programmed for evaluating the symbolic expressions for the elements of Γ (equation 5.26a and results in 5.33, 5.34 and 5.35), please consider the code provided in the supplemental materials and/or contact the corresponding author.

5.5 Appendix

Definitions and equations

The Liouvillian of equation 5.2 is defined as

$$-i\mathcal{L}^0\rho(t) = \frac{-i}{\hbar}\left[\hat{H}_0, \rho(t)\right] \tag{5.24}$$

In Liouville space formulation $\mathcal{L}_0$ and Γ of equation 5.2 become matrices and their elements can be written as:

$$\mathcal{L}^0_{\alpha\alpha'\beta\beta'} = tr\left\{|\alpha'\rangle\langle\alpha|\left[\hat{H}_0, |\beta\rangle\langle\beta'|\right]\right\} \tag{5.25}$$

and

$$\begin{aligned}\Gamma_{\alpha\alpha'\beta\beta'} = &-J_{\alpha\beta\alpha'\beta'}(\nu_{\alpha\beta}) - J_{\alpha\beta\alpha'\beta'}(\nu_{\beta'\alpha'}) \\ &+ \delta_{\alpha',\beta'}\sum_\gamma J_{\gamma\beta\gamma\alpha}(\nu_{\gamma\beta}) + \delta_{\alpha,\beta}\sum_\gamma J_{\gamma\alpha'\gamma\beta'}(\nu_{\beta'\gamma}) \\ &+ \delta_{\alpha',-\beta'}\sum_\gamma J_{\gamma\beta\gamma\alpha}(\nu_{\gamma\beta}) + \delta_{\alpha,-\beta}\sum_\gamma J_{\gamma\alpha'\gamma\beta'}(\nu_{\beta'\gamma})\end{aligned} \tag{5.26a}$$

$$J_{\alpha\alpha'\beta\beta'}(\nu) = \int_0^\infty \overline{\langle\alpha| H_1(t) |\alpha'\rangle\langle\beta'| H_1(t+\tau) |\beta\rangle} e^{-i\nu\tau} d\tau \tag{5.26b}$$

$J_{\alpha\beta\alpha'\beta'}(\nu)$ is the spectral density function of the stochastic Hamiltonian responsible for the relaxation process. In general, the relaxation matrix Γ is complex. It's real part $Re\{\Gamma\}$ contains the relaxation elements whereas it's imaginary part $Im\{\Gamma\}$ is often called dynamical shift and its contributions add to the static term $\mathcal{L}_0$. Equation 5.26a deviates slightly from the standard formulation found in most books when treating NMR phenomena. The last two terms are additionally entering the equation as the secular approximation is fulfilled for more elements than e.g. in the NMR case.

Transformation of the Liouville von Neumann equation (equation 5.2) into frequency domain and formulation of the lineshape function:

$$\begin{aligned}\frac{d}{dt}\rho(t) &= \left(-i\mathcal{L}^0 - \Gamma\right)\rho(t) && |L[\,] \\ s\tilde{\rho}(s) - \rho(0) &= \left(-i\mathcal{L}^0 - \Gamma\right)\tilde{\rho}(s) \\ \tilde{\rho}(s) &= \left(s + i\mathcal{L}^0 + \Gamma\right)^{-1}\rho(0) && |s \to i\nu \\ \tilde{\rho}(\nu) &= \left(i\nu + i\mathcal{L}^0 + \Gamma\right)^{-1}\rho(0)\end{aligned} \tag{5.27}$$

For further considerations we are dropping the tilde and can identify $\rho(\nu)$ as the spin density in frequency domain.

The static part of the Hamiltonian in equation 5.1 is the usual quadrupole Hamiltonian expressed in spherical tensor operators $T^{(2)}_m$ for the spin and spatial

tensors $V_m^{(2)}$ for the EFG with respect to some possible laboratory (L) system:

$$\hat{H}_0(\Omega_{LP}) = \frac{Q_{cc}}{I(2I-1)} \sum_{m=-2}^{2} (-1)^m T_m^{(2)} V_{-m}^{(2)L}(\Omega_{LP}) \; . \tag{5.28a}$$

$$\begin{aligned} T_0^{(2)}(I) &= \frac{1}{2}(3\hat{I}_z^2 - I(I+1)) \\ T_{\pm 1}^{(2)}(I) &= \mp\frac{\sqrt{6}}{4}(\hat{I}_z\hat{I}_\pm + \hat{I}_\pm\hat{I}_z) \\ T_{\pm 2}^{(2)}(I) &= \frac{\sqrt{6}}{4}\hat{I}_\pm^2 \end{aligned} \tag{5.28b}$$

$$\begin{aligned} V_0^{(2)L}(\Omega_{LP}) &= \frac{1}{2}\left[\frac{(3cos^2\beta - 1)}{2} + \frac{\eta}{4}sin^2\beta(e^{-2i\gamma} + e^{-2i\gamma})\right] \\ V_{\pm 1}^{(2)L}(\Omega_{LP}) &= \frac{1}{2}\left[\mp\sqrt{\frac{3}{8}}sin2\beta e^{\pm i\alpha} + \frac{\eta}{\sqrt{6}}\left(-\frac{1 \mp cos\beta}{2}sin\beta e^{\pm i(\alpha \mp 2\gamma)}\right.\right. \\ &\quad \left.\left. + \frac{1 \mp cos\beta}{2}sin\beta e^{i(\pm\alpha + 2\gamma)}\right)\right] \\ V_{\pm 2}^{(2)L}(\Omega_{LP}) &= \frac{1}{2}\left[\sqrt{\frac{3}{8}}sin^2\beta e^{\pm 2i\alpha} + \frac{\eta}{\sqrt{6}}\left(\frac{(1 \mp cos\beta)^2}{4}e^{\pm 2i(\alpha \mp \gamma)}\right.\right. \\ &\quad \left.\left. + \frac{(1 \pm cos\beta)^2}{4}e^{2i(\pm\alpha + \gamma)}\right)\right] \end{aligned} \tag{5.28c}$$

The $\hat{I}$'s denote the usual angular momentum operators and I is the nuclear spin number. Euler angles $\Omega_{LP} = \{\alpha, \beta, \gamma\}$ allow for a rotation of the Hamiltonian with respect to a L system defined by e.g. an excitation/detection coil or an external magnetic field. As no further interaction comparable in size is present in our case, the principal axis representation (P) of $\hat{H}_0$ will be used which corresponds to the case $\alpha = \beta = \gamma = 0$. In the (P) frame, the EFG tensor is traceless and diagonal. The corresponding spherical tensor operators are:

$$\begin{aligned} V_0^{(2)P} &= \frac{1}{2} \\ V_{\pm 1}^{(2)P} &= 0 \\ V_{\pm 2}^{(2)P} &= \frac{1}{2}\frac{\eta}{\sqrt{6}} \end{aligned} \tag{5.28d}$$

The stochastic, time dependent quadrupole Hamiltonian $\hat{H}_1(t)(\Omega_{MP})$ is defined as

$$\hat{H}_1(t)(\Omega_{MP}) = \frac{1}{I(2I-1)} \sum_{m=-2}^{2} (-1)^m T_m^{(2)} V_{-m}^{(2)M}(t, \Omega_{MP}) \; , \tag{5.29a}$$

in a molecular fixed frame (M), where $T_m^{(2)}$ are similar to the ones defined in equation 5.28b and $V_m^{(2)M}$ can be found in equation 5.29b where rotations are defined by Euler angles Ω_{MP}. The time dependent amplitude $q_{cc}(t)$ of $\hat{H}_1(t)(\Omega_{MP})$ is contained in the

expressions of $V_m^{(2)M}(t)$ and follows an autocorrelation function $\langle V_m^{(2)M}(t)V_n^{(2)M}(t+\tau)\rangle$ defined in equations 5.16 and 5.17, respectively.

$$
\begin{aligned}
&V_0^{(2)M}(t,\Omega_{MP}) = \frac{q_{cc}(t)}{2}\left[\frac{(3cos^2\beta-1)}{2}+\frac{\eta}{4}sin^2\beta(e^{-2i\gamma}+e^{-2i\gamma})\right]\\
&= q_{cc}(t)\cdot d_0(\Omega_{MP})\\
&V_{\pm1}^{(2)M}(t,\Omega_{MP}) = \frac{q_{cc}(t)}{2}\left[\mp\sqrt{\frac{3}{8}}sin2\beta e^{\pm i\alpha}\right.\\
&\left.+\frac{\eta}{\sqrt{6}}\left(-\frac{1\mp cos\beta}{2}sin\beta e^{\pm i(\alpha\mp2\gamma)}+\frac{1\mp cos\beta}{2}sin\beta e^{i(\pm\alpha+2\gamma)}\right)\right]\\
&= q_{cc}(t)\cdot d_{\pm1}(\Omega_{MP})\\
&V_{\pm2}^{(2)M}(t,\Omega_{MP}) = \frac{q_{cc}(t)}{2}\left[\sqrt{\frac{3}{8}}sin^2\beta e^{\pm2i\alpha}+\frac{\eta}{\sqrt{6}}\left(\frac{(1\mp cos\beta)^2}{4}e^{\pm2i(\alpha\mp\gamma)}\right.\right.\\
&\left.\left.+\frac{(1\pm cos\beta)^2}{4}e^{2i(\pm\alpha+\gamma)}\right)\right] = q_{cc}(t)\cdot d_{\pm2}(\Omega_{MP})
\end{aligned}
\tag{5.29b}
$$

Equation 5.29a is inserted in equation 5.26b for the spectral density $J(\nu)$. Equation5.26a then leads to the analytical expressions for the relaxation matrix elements $\Gamma_{\alpha\alpha'\beta\beta'}$ (equations 5.33, 5.34 and 5.35). In the latter equations, also the spatial, angle dependent factors $d_m(\Omega_{MP})$ (depending on the direction of the fluctuation with respect to the (P) frame) can be identified.

Formally evaluating parts of equation 5.7 gives for single quantum transitions:

$$
\begin{aligned}
&\sum_{\alpha\alpha'}\langle\alpha|\,\rho\,|\alpha'\rangle\,\langle\alpha'|\,I_x\,|\alpha\rangle = \frac{3}{2}\rho_{9/2,7/2}+2\rho_{7/2,5/2}+\frac{\sqrt{21}}{2}\rho_{5/2,3/2}\\
&+\sqrt{6}\rho_{3/2,1/2}+\frac{5}{2}\rho_{1/2,-1/2}+\sqrt{6}\rho_{-1/2,-3/2}+\frac{\sqrt{21}}{2}\rho_{-3/2,-5/2}\\
&+2\rho_{-5/2,-7/2}+\frac{3}{2}\rho_{-7/2,-9/2}\,,
\end{aligned}
\tag{5.30}
$$

and for double quantum transitions one obtains:

$$
\begin{aligned}
&\sum_{\alpha\alpha'}\langle\alpha|\,\rho\,|\alpha'\rangle\,\langle\alpha'|\,I_xI_x\,|\alpha\rangle = 3\rho_{9/2,5/2}+\sqrt{21}\rho_{7/2,3/2}+3\sqrt{\frac{7}{2}}\rho_{5/2,1/2}\\
&+5\sqrt{\frac{3}{2}}\rho_{3/2,-1/2}+5\sqrt{\frac{3}{2}}\rho_{1/2,-3/2}+3\sqrt{\frac{7}{2}}\rho_{-1/2,-5/2}\\
&+\sqrt{21}\rho_{-3/2,-7/2}+3\rho_{-5/2,-9/2}
\end{aligned}
\tag{5.31}
$$

The elements of the Liouvillian $\mathcal{L}^0$ (equation 5.25) are calculated for the static Hamiltonian (equation 5.28a) with respect to the set of basis operators presented in equation 8.1. This gives a 17x17 matrix with the spin transition frequencies $\nu_{Q,\alpha\beta}$

on the diagonal $\mathcal{L}^0_{\alpha\beta\alpha\beta}$. These are obtained by diagonalized numerically the static Hamiltonian 5.28a in the PAS and we end up with the energy levels E_α of the spin system with respect to the Eigenfunctions $|\Psi_\alpha\rangle = \sum_{m=-1}^{2I+1} a_{\alpha,m}|I,m\rangle$, where $\{|I,m\rangle\}$ is the orthonormal Zeeman basis written as $\{|m\rangle\}$. The NQR transition frequencies $\nu_{Q,\alpha\beta}$, and thus the elements of $\mathcal{L}^0$, can be expressed by the difference between two energy levels E:

$$\begin{aligned}\mathcal{L}^0_{\alpha\beta\alpha\beta} &= \nu_{Q,\alpha\beta} = E_\alpha - E_\beta \\ &= \langle\Psi_\alpha(\Omega)|\widehat{H}_0(I)(\Omega)|\Psi_\alpha\rangle - \langle\Psi_\beta(\Omega)|\widehat{H}_0(I)(\Omega)|\Psi_\beta\rangle\end{aligned} \tag{5.32}$$

The elements of the relaxation matrix Γ (equation 5.26a) are calculated for the stochastic Hamiltonian (equation 5.29a) with respect to the set of basis operators presented in equation 8.1. As the expressions of the single elements are rather long, only the first column of the 17x17 matrix is presented here. A matrix-plot, representing the value of each element for a particular plot is shown for a particular case in figure 5.2 panel b). Evaluating equation 5.26a gives for the single coherence

terms on the diagonal:

$$
\begin{aligned}
\Gamma_{\frac{1}{2}\frac{3}{2}\frac{1}{2}\frac{3}{2}} &= \frac{1}{36}d_0^2\widetilde{J}(\nu_{\frac{1}{2},\frac{1}{2}}) - \frac{1}{48}d_0^2\widetilde{J}(\nu_{\frac{3}{2},\frac{3}{2}}) - \frac{1}{36}d_{-1}d_{+1}\widetilde{J}(\nu_{\frac{1}{2},\frac{3}{2}}) \\
&- \frac{1}{36}d_{-1}d_{+1}\widetilde{J}(\nu_{\frac{3}{2},\frac{1}{2}}) - \frac{7}{72}d_{-1}d_{+1}\widetilde{J}(\nu_{\frac{5}{2},\frac{3}{2}}) \\
&+ \frac{25}{144}d_{-2}d_{+2}\widetilde{J}(\nu_{-\frac{3}{2},\frac{1}{2}}) + \frac{25}{144}d_{-2}d_{+2}\widetilde{J}(\nu_{-\frac{1}{2},\frac{3}{2}}) \\
&+ \frac{7}{48}d_{-2}d_{+2}\widetilde{J}(\nu_{\frac{5}{2},\frac{1}{2}}) + \frac{7}{72}d_{-2}d_{+2}\widetilde{J}(\nu_{\frac{7}{2},\frac{3}{2}}) = \Gamma_{-\frac{1}{2}-\frac{3}{2}-\frac{1}{2}-\frac{3}{2}} \\
\Gamma_{\frac{3}{2}\frac{5}{2}\frac{3}{2}\frac{5}{2}} &= \frac{1}{24}d_0^2\widetilde{J}(\nu_{\frac{3}{2},\frac{3}{2}}) - \frac{1}{72}d_0^2\widetilde{J}(\nu_{\frac{5}{2},\frac{5}{2}}) - \frac{1}{36}d_{-1}d_{+1}\widetilde{J}(\nu_{\frac{1}{2},\frac{3}{2}}) \\
&- \frac{7}{72}d_{-1}d_{+1}\widetilde{J}(\nu_{\frac{3}{2},\frac{5}{2}}) - \frac{7}{72}d_{-1}d_{+1}\widetilde{J}(\nu_{\frac{5}{2},\frac{3}{2}}) - \frac{1}{6}d_{-1}d_{+1}\widetilde{J}(\nu_{\frac{7}{2},\frac{5}{2}}) \\
&+ \frac{25}{144}d_{-2}d_{+2}\widetilde{J}(\nu_{-\frac{1}{2},\frac{3}{2}}) + \frac{7}{48}d_{-2}d_{+2}\widetilde{J}(\nu_{\frac{1}{2},\frac{5}{2}}) \\
&+ \frac{7}{72}d_{-2}d_{+2}\widetilde{J}(\nu_{\frac{7}{2},\frac{3}{2}}) + \frac{1}{24}d_{-2}d_{+2}\widetilde{J}(\nu_{\frac{9}{2},\frac{5}{2}}) = \Gamma_{-\frac{3}{2}-\frac{5}{2}-\frac{3}{2}-\frac{5}{2}} \\
\Gamma_{\frac{5}{2}\frac{7}{2}\frac{5}{2}\frac{7}{2}} &= \frac{1}{48}d_0^2\widetilde{J}(\nu_{\frac{5}{2},\frac{5}{2}}) + \frac{1}{24}d_0^2\widetilde{J}(\nu_{\frac{7}{2},\frac{7}{2}}) - \frac{7}{72}d_{-1}d_{+1}\widetilde{J}(\nu_{\frac{3}{2},\frac{5}{2}}) \\
&- \frac{1}{6}d_{-1}d_{+1}\widetilde{J}(\nu_{\frac{5}{2},\frac{7}{2}}) - \frac{1}{6}d_{-1}d_{+1}\widetilde{J}(\nu_{\frac{7}{2},\frac{5}{2}}) - \frac{1}{6}d_{-1}d_{+1}\widetilde{J}(\nu_{\frac{9}{2},\frac{7}{2}}) \\
&+ \frac{7}{48}d_{-2}d_{+2}\widetilde{J}(\nu_{\frac{1}{2},\frac{5}{2}}) + \frac{7}{72}d_{-2}d_{+2}\widetilde{J}(\nu_{\frac{3}{2},\frac{7}{2}}) \\
&+ \frac{1}{24}d_{-2}d_{+2}\widetilde{J}(\nu_{\frac{9}{2},\frac{5}{2}}) = \Gamma_{-\frac{5}{2}-\frac{7}{2}-\frac{5}{2}-\frac{7}{2}} \\
\Gamma_{\frac{9}{2}\frac{7}{2}\frac{9}{2}\frac{7}{2}} &= -\frac{1}{18}d_0^2\widetilde{J}(\nu_{\frac{7}{2},\frac{7}{2}}) + \frac{1}{6}d_0^2\widetilde{J}(\nu_{\frac{9}{2},\frac{9}{2}}) - \frac{1}{6}d_{-1}d_{+1}\widetilde{J}(\nu_{\frac{5}{2},\frac{7}{2}}) \\
&- \frac{1}{6}d_{-1}d_{+1}\widetilde{J}(\nu_{\frac{7}{2},\frac{9}{2}}) - \frac{1}{6}d_{-1}d_{+1}\widetilde{J}(\nu_{\frac{9}{2},\frac{7}{2}}) \\
&+ \frac{7}{72}d_{-2}d_{+2}\widetilde{J}(\nu_{\frac{3}{2},\frac{7}{2}}) + \frac{1}{24}d_{-2}d_{+2}\widetilde{J}(\nu_{\frac{5}{2},\frac{9}{2}}) = \Gamma_{-\frac{9}{2}-\frac{7}{2}-\frac{9}{2}-\frac{7}{2}} \\
\Gamma_{-\frac{1}{2}\frac{1}{2}-\frac{1}{2}\frac{1}{2}} &= -\frac{1}{36}d_{-1}d_{+1}\widetilde{J}(\nu_{-\frac{3}{2},-\frac{1}{2}}) - \frac{1}{36}d_{-1}d_{+1}\widetilde{J}(\nu_{\frac{3}{2},\frac{1}{2}}) \\
&+ \frac{7}{48}d_{-2}d_{+2}\widetilde{J}(\nu_{-\frac{5}{2},-\frac{1}{2}}) + \frac{25}{144}d_{-2}d_{+2}\widetilde{J}(\nu_{-\frac{3}{2},\frac{1}{2}}) \\
&+ \frac{25}{144}d_{-2}d_{+2}\widetilde{J}(\nu_{\frac{3}{2},-\frac{1}{2}}) + \frac{7}{48}d_{-2}d_{+2}\widetilde{J}(\nu_{\frac{5}{2},\frac{1}{2}})
\end{aligned}
\tag{5.33}
$$

For the double coherence terms on the diagonal equation 5.26a gives:

$$
\begin{aligned}
\Gamma_{\frac{1}{2}\frac{5}{2}\frac{1}{2}\frac{5}{2}} &= \frac{1}{12}d_0^2\widetilde{J}(\nu_{\frac{1}{2},\frac{1}{2}}) - \frac{1}{48}d_0^2\widetilde{J}(\nu_{\frac{5}{2},\frac{5}{2}}) - \frac{1}{36}d_{-1}d_{+1}\widetilde{J}(\nu_{\frac{3}{2},\frac{1}{2}}) \\
&- \frac{7}{72}d_{-1}d_{+1}\widetilde{J}(\nu_{\frac{3}{2},\frac{5}{2}}) - \frac{1}{6}d_{-1}d_{+1}\widetilde{J}(\nu_{\frac{7}{2},\frac{5}{2}}) + \frac{25}{144}d_{-2}d_{+2}\widetilde{J}(\nu_{-\frac{3}{2},\frac{1}{2}}) \\
&+ \frac{7}{48}d_{-2}d_{+2}\widetilde{J}(\nu_{\frac{1}{2},\frac{5}{2}}) + \frac{7}{48}d_{-2}d_{+2}\widetilde{J}(\nu_{\frac{5}{2},\frac{1}{2}}) \\
&+ \frac{1}{24}d_{-2}d_{+2}\widetilde{J}(\nu_{\frac{9}{2},\frac{5}{2}}) = \Gamma_{-\frac{1}{2}-\frac{5}{2}-\frac{1}{2}-\frac{5}{2}} \\
\Gamma_{\frac{3}{2}\frac{7}{2}\frac{3}{2}\frac{7}{2}} &= \frac{5}{48}d_0^2\widetilde{J}(\nu_{\frac{3}{2},\frac{3}{2}}) + \frac{5}{72}d_0^2\widetilde{J}(\nu_{\frac{7}{2},\frac{7}{2}}) - \frac{1}{36}d_{-1}d_{+1}\widetilde{J}(\nu_{\frac{1}{2},\frac{3}{2}}) \\
&- \frac{7}{72}d_{-1}d_{+1}\widetilde{J}(\nu_{\frac{5}{2},\frac{3}{2}}) - \frac{1}{6}d_{-1}d_{+1}\widetilde{J}(\nu_{\frac{5}{2},\frac{7}{2}}) - \frac{1}{6}d_{-1}d_{+1}\widetilde{J}(\nu_{\frac{9}{2},\frac{7}{2}}) \\
&+ \frac{25}{144}d_{-2}d_{+2}\widetilde{J}(\nu_{-\frac{1}{2},\frac{3}{2}}) + \frac{7}{72}d_{-2}d_{+2}\widetilde{J}(\nu_{\frac{3}{2},\frac{7}{2}}) \\
&+ \frac{7}{72}d_{-2}d_{+2}\widetilde{J}(\nu_{\frac{7}{2},\frac{3}{2}}) = \Gamma_{-\frac{3}{2}-\frac{7}{2}-\frac{3}{2}-\frac{7}{2}} \\
\Gamma_{\frac{5}{2}\frac{9}{2}\frac{5}{2}\frac{9}{2}} &= \frac{7}{144}d_0^2\widetilde{J}(\nu_{\frac{5}{2},\frac{5}{2}}) + \frac{7}{24}d_0^2\widetilde{J}(\nu_{\frac{9}{2},\frac{9}{2}}) - \frac{7}{72}d_{-1}d_{+1}\widetilde{J}(\nu_{\frac{3}{2},\frac{5}{2}}) \\
&- \frac{1}{6}d_{-1}d_{+1}\widetilde{J}(\nu_{\frac{7}{2},\frac{5}{2}}) - \frac{1}{6}d_{-1}d_{+1}\widetilde{J}(\nu_{\frac{7}{2},\frac{9}{2}}) + \frac{7}{48}d_{-2}d_{+2}\widetilde{J}(\nu_{\frac{1}{2},\frac{5}{2}}) \\
&+ \frac{1}{24}d_{-2}d_{+2}\widetilde{J}(\nu_{\frac{5}{2},\frac{9}{2}}) + \frac{1}{24}d_{-2}d_{+2}\widetilde{J}(\nu_{\frac{9}{2},\frac{5}{2}}) = \Gamma_{-\frac{5}{2}-\frac{9}{2}-\frac{5}{2}-\frac{9}{2}} \\
\Gamma_{-\frac{1}{2}\frac{3}{2}-\frac{1}{2}\frac{3}{2}} &= \frac{1}{36}d_0^2\widetilde{J}(\nu_{-\frac{1}{2},-\frac{1}{2}}) - \frac{1}{48}d_0^2\widetilde{J}(\nu_{\frac{3}{2},\frac{3}{2}}) - \frac{1}{36}d_{-1}d_{+1}\widetilde{J}(\nu_{-\frac{3}{2},-\frac{1}{2}}) \\
&- \frac{1}{36}d_{-1}d_{+1}\widetilde{J}(\nu_{\frac{1}{2},\frac{3}{2}}) - \frac{7}{72}d_{-1}d_{+1}\widetilde{J}(\nu_{\frac{5}{2},\frac{3}{2}}) \\
&+ \frac{7}{48}d_{-2}d_{+2}\widetilde{J}(\nu_{-\frac{5}{2},-\frac{1}{2}}) + \frac{25}{144}d_{-2}d_{+2}\widetilde{J}(\nu_{-\frac{1}{2},\frac{3}{2}}) \\
&+ \frac{25}{144}d_{-2}d_{+2}\widetilde{J}(\nu_{\frac{3}{2},-\frac{1}{2}}) + \frac{7}{72}d_{-2}d_{+2}\widetilde{J}(\nu_{\frac{7}{2},\frac{3}{2}}) = \Gamma_{\frac{1}{2}-\frac{3}{2}\frac{1}{2}-\frac{3}{2}}
\end{aligned}
\tag{5.34}
$$

The remaining non-zero off diagonal elements are:

$$\begin{aligned}
\Gamma_{\frac{1}{2}\frac{3}{2}-\frac{1}{2}\frac{3}{2}} &= \frac{1}{16}d_0^2\widetilde{J}(\nu_{\frac{3}{2},\frac{3}{2}}) - \frac{1}{36}d_{-1}d_{+1}\widetilde{J}(\nu_{\frac{1}{2},\frac{3}{2}}) - \frac{7}{72}d_{-1}d_{+1}\widetilde{J}(\nu_{\frac{5}{2},\frac{3}{2}}) \\
&+ \frac{5}{72}d_{-2}d_{+1}\widetilde{J}(\nu_{-\frac{3}{2},-\frac{1}{2}}) - \frac{5}{72}d_{-2}d_{+1}\widetilde{J}(\nu_{\frac{3}{2},-\frac{1}{2}}) \\
&+ \frac{25}{144}d_{-2}d_{+2}\widetilde{J}(\nu_{-\frac{1}{2},\frac{3}{2}}) + \frac{7}{72}d_{-2}d_{+2}\widetilde{J}(\nu_{\frac{7}{2},\frac{3}{2}}) \\
\Gamma_{\frac{1}{2}\frac{3}{2}\frac{1}{2}-\frac{3}{2}} &= \frac{1}{9}d_0^2\widetilde{J}(\nu_{\frac{1}{2},\frac{1}{2}}) - \frac{1}{36}d_{-1}d_{+1}\widetilde{J}(\nu_{\frac{3}{2},\frac{1}{2}}) \\
&+ \frac{25}{144}d_{-2}d_{+2}\widetilde{J}(\nu_{-\frac{3}{2},\frac{1}{2}}) + \frac{7}{48}d_{-2}d_{+2}\widetilde{J}(\nu_{\frac{5}{2},\frac{1}{2}}) \\
&+ \frac{5}{72}d_{+1}d_{+2}\widetilde{J}(\nu_{-\frac{1}{2},-\frac{3}{2}}) - \frac{5}{72}d_{+1}d_{+2}\widetilde{J}(\nu_{\frac{1}{2},-\frac{3}{2}}) \\
\Gamma_{-\frac{1}{2}-\frac{3}{2}-\frac{1}{2}\frac{3}{2}} &= \frac{1}{9}d_0^2\widetilde{J}(\nu_{-\frac{1}{2},-\frac{1}{2}}) - \frac{5}{72}d_{-1}d_{-2}\widetilde{J}(\nu_{-\frac{1}{2},\frac{3}{2}}) \\
&+ \frac{5}{72}d_{-1}d_{-2}\widetilde{J}(\nu_{\frac{1}{2},\frac{3}{2}}) - \frac{1}{36}d_{-1}d_{+1}\widetilde{J}(\nu_{-\frac{3}{2},-\frac{1}{2}}) \\
&+ \frac{7}{48}d_{-2}d_{+2}\widetilde{J}(\nu_{-\frac{5}{2},-\frac{1}{2}}) + \frac{25}{144}d_{-2}d_{+2}\widetilde{J}(\nu_{\frac{3}{2},-\frac{1}{2}}) \\
\Gamma_{-\frac{1}{2}-\frac{3}{2}\frac{1}{2}-\frac{3}{2}} &= \frac{1}{16}d_0^2\widetilde{J}(\nu_{-\frac{3}{2},-\frac{3}{2}}) - \frac{7}{72}d_{-1}d_{+1}\widetilde{J}(\nu_{-\frac{5}{2},-\frac{3}{2}}) \\
&- \frac{1}{36}d_{-1}d_{+1}\widetilde{J}(\nu_{-\frac{1}{2},-\frac{3}{2}}) - \frac{5}{72}d_{-1}d_{+2}\widetilde{J}(\nu_{-\frac{3}{2},\frac{1}{2}}) \\
&+ \frac{5}{72}d_{-1}d_{+2}\widetilde{J}(\nu_{\frac{3}{2},\frac{1}{2}}) + \frac{7}{72}d_{-2}d_{+2}\widetilde{J}(\nu_{-\frac{7}{2},-\frac{3}{2}}) \\
&+ \frac{25}{144}d_{-2}d_{+2}\widetilde{J}(\nu_{\frac{1}{2},-\frac{3}{2}})
\end{aligned} \tag{5.35}$$

Analytical lineshape

The following derivation concerns the solution of a coupled subset from equation 5.6, comprising $|\pm 1/2 \pm 3/2)$ elements only (the first four basis operators of equation 8.1). For convenience, the matrix elements are labelled the following way:

$A = i(\nu - \nu_{Q,t1}) + \Gamma_{\frac{1}{2}\frac{3}{2}\frac{1}{2}\frac{3}{2}} = i(\nu - \nu_{Q,t1}) + \Gamma_{-\frac{1}{2}-\frac{3}{2}-\frac{1}{2}-\frac{3}{2}}$
$B = i(\nu - \nu_{Q,t1}) + \Gamma_{-\frac{1}{2}\frac{3}{2}-\frac{1}{2}\frac{3}{2}} = i(\nu - \nu_{Q,t1}) + \Gamma_{\frac{1}{2}-\frac{3}{2}\frac{1}{2}-\frac{3}{2}}$
$C = \Gamma_{\frac{1}{2}\frac{3}{2}-\frac{1}{2}\frac{3}{2}} = \Gamma_{-\frac{1}{2}\frac{3}{2}\frac{1}{2}\frac{3}{2}} = \Gamma_{-\frac{1}{2}-\frac{3}{2}\frac{1}{2}-\frac{3}{2}} = \Gamma_{\frac{1}{2}-\frac{3}{2}-\frac{1}{2}-\frac{3}{2}}$
$D = \Gamma_{\frac{1}{2}\frac{3}{2}\frac{1}{2}-\frac{3}{2}} = \Gamma_{\frac{1}{2}-\frac{3}{2}\frac{1}{2}\frac{3}{2}} = \Gamma_{-\frac{1}{2}-\frac{3}{2}-\frac{1}{2}\frac{3}{2}} = \Gamma_{-\frac{1}{2}\frac{3}{2}-\frac{1}{2}-\frac{3}{2}}$

$$\left(i\nu\mathbb{1} + i\mathcal{L}^0 + \Gamma\right) = M_{sub} = \begin{pmatrix} A & 0 & C & D \\ 0 & A & D & C \\ C & D & B & 0 \\ D & C & 0 & B \end{pmatrix} \xrightarrow{rearrange} M_{sub} = \begin{pmatrix} A & C & D & 0 \\ C & B & 0 & D \\ D & 0 & B & C \\ 0 & D & C & A \end{pmatrix} \tag{5.36}$$

$$W = \begin{pmatrix} \frac{1}{2} & \frac{1}{2} & \frac{1}{2} & \frac{1}{2} \\ \frac{1}{2} & -\frac{1}{2} & \frac{1}{2} & -\frac{1}{2} \\ \frac{1}{2} & \frac{1}{2} & -\frac{1}{2} & -\frac{1}{2} \\ \frac{1}{2} & -\frac{1}{2} & -\frac{1}{2} & \frac{1}{2} \end{pmatrix} \tag{5.37}$$

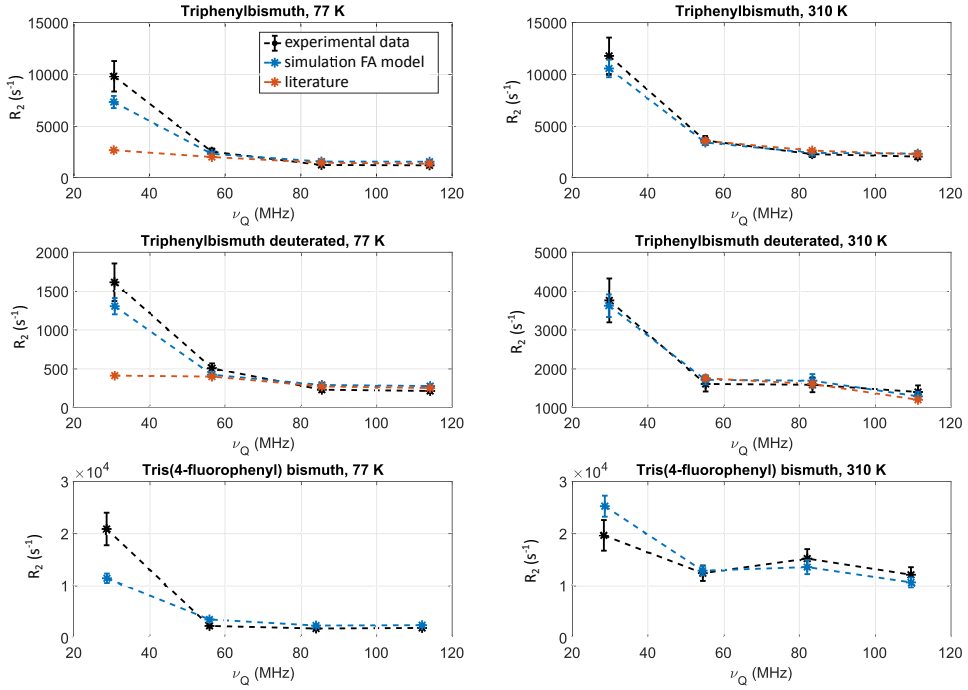

FIGURE 5.8: Fitting results for the relaxation rates $R_{2,sim}^{(i)}$ (blue stars) for the FA model applied to the experimental data (black stars) of three different Bi-aryl compounds at two different temperatures. The red stars are literature results for comparison taken from [94]. Dashed line serves as a guide to the eye. Errorbars are discussed in the supplemental materials.

$$
\begin{aligned}
M_{trans} &= W^{-1} \cdot M_{sub} \cdot W \\
&= \begin{pmatrix}
\frac{1}{2}(A+B+2(C+D)) & 0 & 0 & \frac{A-B}{2} \\
0 & \frac{1}{2}(A+B-2C+2D) & \frac{A-B}{2} & 0 \\
0 & \frac{A-B}{2} & \frac{1}{2}(A+B+2C-2D) & 0 \\
\frac{A-B}{2} & 0 & 0 & \frac{1}{2}(A+B-2(C+D))
\end{pmatrix}
\end{aligned} \tag{5.38}
$$

M_{trans} is block symmetric and only a 2x2 submatrix is used further:

$$
M_{bloc} = \begin{pmatrix}
\frac{1}{2}(A+B+2(C+D)) & \frac{A-B}{2} \\
\frac{A-B}{2} & \frac{1}{2}(A+B-2(C+D))
\end{pmatrix} \tag{5.39}
$$

$$
\rho(\nu) = M_{bloc}^{-1} \cdot \rho = \begin{pmatrix}
-\frac{-B+C+D}{AB-(C+D)^2} \\
\frac{B+C+D}{AB-(C+D)^2}
\end{pmatrix} \tag{5.40}
$$

The first element of equation 5.40 corresponds to $\rho_{1/2,3/2} + \rho_{-1/2,-3/2}$ and thus to the single quantum coherence lineshape of transition $t1$, as it is presented in equation 5.22.

Best fit results

All best fit results from table 5.1 are presented in figures 5.8 and 5.9 and compared with experimental data. Error estimation is given in the supplemental materials.

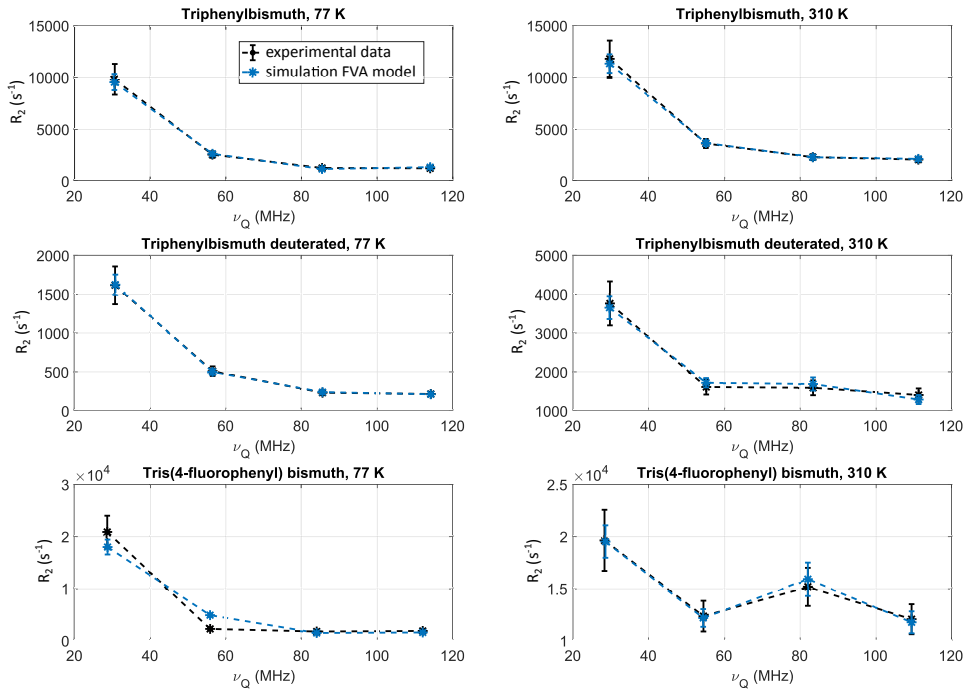

FIGURE 5.9: Fitting results for the relaxation rates $R_{2,sim}^{(i)}$ (blue stars) for the FVA model applied to the experimental data (black stars) of three different Bi-aryl compounds at two different temperatures. Dashed line serves as a guide to the eye. Errorbars are discussed in the supplemental materials.

Supplemental Materials [1]

Error estimation of best fit parameters

As the evaluated cost function (equation 5.20) is not based on a simple linear or polynomial model and the minimum is found via an exhaustive search, error estimation of the fitting result and their best fit parameters is not straight forward. Based on the assumption that the found best fit result (from table 5.1 is correct, random, Gaussian distributed, synthetic data (SD) was generated with the best fit result as the mean values and a standard deviation s corresponding to the error bars of the experimental values (about 10 % experimental error). The fitting procedure has been performed on NSD simulated data sets to obtain NSD fitting results and parameters which are then used to estimate s (see [1]). Representative for all data sets presented in table 5.1, the above described procedure was performed on triphenylbismuth at 310 K for a number of NSD simulated data sets for the FA (NSD=30) and the FVA (NSD=15) model (see figure 5.10). The respective statistic for triphenylbismuth at 310 K is summarized in table 5.2, where the standard deviation s of the results and their corresponding fitting parameters is given in % relative to the respective mean of the set. The found values are considered as a valid estimation for all presented samples, as their experimental errors and cost functions are very similar.

[1] References are given separately at the end of the section

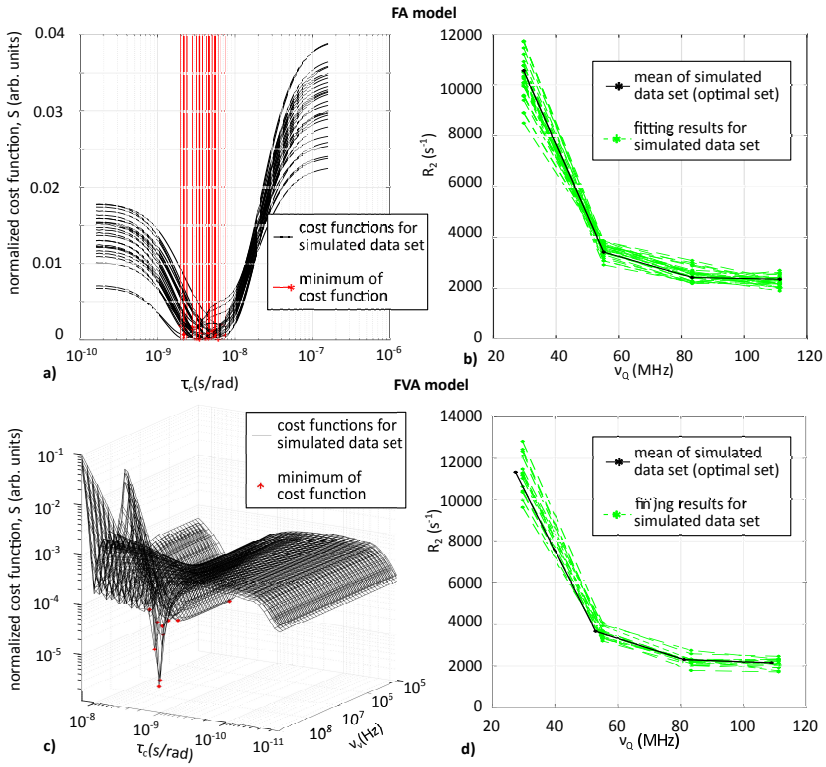

FIGURE 5.10: Visualized error estimation for simulation results and fitting parameters demonstrated for triphenylbismuth at 310K. Panels a) and b) show the cost functions and fitting results for a simulated, Gaussian distributed data set for the FA model, panels c) and d) for the FVA model. From the gathered fitting parameters and relaxation rates, the standard deviation has been calculated.

TABLE 5.2: Summary of the estimation of the standard deviation s of the simulated relaxation rates $R_{2,sim}$ for triphenylbismuth at 310 K and their corresponding fitting parameters for the FA and the FVA model. s is given in % of the mean of the NSD fitting results

s in % of mean	τ_c	q_{cc}	ν_v	$R^1_{2,sim}$	$R^2_{2,sim}$	$R^3_{2,sim}$	$R^4_{2,sim}$
FA	27	7	-	8	7	10	9
FVA	23	10	63	8	8	10	11

Comments on the lineshape procedure and the provided Mathematica code

The presented approach for calculating the lineshape of NQR spectra is rather flexible and can also be applied to other related problems. The fluctuating quadrupole Hamiltonian can be replaced by magnetic dipole-dipole (D-D) fluctuations. The elements of the relaxation matrix Γ can be found quite fast by using the provided Mathematica code. Choosing another dynamical model for the spectral densities of the fluctuations can be done as long as general conditions of Redfield theory [2] are met. A particular strength of the flickering amplitude (FA) model compared to the frequently applied pseudo rotational (PR) model is the explicit consideration of the spatial distribution of the fluctuations and their subsequent numerical averaging. In that way, also non-spherical distributions of the fluctuations can be assumed which generally can be expected in solids. This might also be interesting for e.g. linear molecules. However, any anisotropy must be added to the static, main part of the quadrupole Hamiltonian which will produce a shift of the quadrupole resonance frequencies. Not much alterations are needed to simulate spin-lattice relaxation R_1: Instead of the expectation value for I_x, $\langle I_z \rangle$ has to be calculated which only means that other elements of the spin density are picked out. The operator basis (as in equation 18) is then formed by the populations of the spin density matrix instead of the coherences. Calculation of Γ is straightforward but equation 3 has to be solved in time-domain which requires diagonalization as well as time-domain evolution of the populations. Also, the motional model for the EFG shall be adapted by e.g. explicitly considering lattice vibrations. However, this topic is beyond the scope of this work.

Proposed experiment

It is possible to apply vibrations to the crystal lattice or the molecules from outside, e.g. using a piezoelectric crystal, at the frequency of the spin transitions (here about 20 MHz up to 120 MHz) and thus, according to the FVA model it should be possible to enhance the relaxation rate significantly. This is already done in nuclear acoustic resonance (also known as paramagnetic absorption of sound) [3,4,5]. Say, if the excitation is at the frequency of t2, the relaxation rate should be enhanced strongly as the mechanism is very efficient. As the relaxation rates contain spectral density contributions at many transition frequencies, this would be observable also at t3 (compare figure 4, panel (c)). So, while sweeping the ultrasound excitation frequency around t2, the resonance becomes visible while measuring e.g. t3 using NQRS due to line broadening. This would be a means of detection of resonant absorption of coherent acoustic energy from an external source that can be used to demonstrate coupling between spin transitions. For this experiment, a single crystal is needed to maintain sound coupling and propagation. Something quite similar has been done by Proctor and Tantilla [6], they have shown acoustic nuclear quadrupole excitation on ^{35}Cl,

which has nuclear spin 3/2. Later, acoustic excitation of nuclear spin resonance was also shown on metallic tantalum [7].

References in Supplemental Materials

[1] W. H. Press, S. A. Teukolsky, W. T. Vetterling and B. P. Flannery, *Numerical Recipes in C + +: The Art of Scientific Computing*, Cambridge University Press, Cambridge, 2002, p. 1002.
[2] A. Redfield, *The Theory of Relaxation Processes*, Advances in Magnetic and Optical Resonance, 1965, vol. 1, pp. 1-32.
[3] D. Bolef, *Interaction of Acoustic Waves with Nuclear Spins in Solids*, Physical Acoustics, Vol. 4 Part A, 1966, pp. 113–182.
[4] S. Al'tshuler, B. Kochelaev and A. Leushin, *Paramagnetic absorption of sound*, Uspekhi Fizicheskih Nauk, 1961, 75, 459–499.
[5] R. K. Sundfors, *Exchange and Quadrupole Broadening of Nuclear Acoustic Resonance Line Shapes in the III-V Semiconductors*, Physical Review, 1969, 185, 458–472.
[6] W. G. Proctor and W. H. Tanttila, *Saturation of Nuclear Electric Quadrupole Energy Levels by Ultrasonic Excitation*, Physical Review, 1955, 98,1854–1854.
[7] E. H. Gregory and H. E. Bömmel, *Acoustic excitation of nuclear spin resonance in single-crystal metallic tantalum*, Physical Review Letters,1965, 15, 404–406.

Chapter 6

Aspects of structural order in ^{209}Bi-containing particles for potential MRI contrast agents based on quadrupole enhanced relaxation

Hermann Scharfetter[a], Christian Gösweiner[a], Paul Josef Krassnig[a], Carina Sampl[b], Martin Thonhofer[c], Roland Fischer[d], Stefan Spirk [b], Rupert Kargl[c], Karin Stana-Kleinschek[c], Evrim Umut[e] and Danuta Kruk[e]

[a]*Institute of Medical Engineering, Graz University of Technology, Graz, Austria*
[b]*Institute of Paper, Pulp and Fiber Technology and Institute for Chemistry and Technology of Materials, Graz University of Technology, Graz, Austria*
[c]*Laboratory for Characterization and Processing of Polymers (LCPP), Faculty of Mechanical Engineering, University of Maribor, Maribor, Slovenia*
[d]*Institute of Inorganic Chemistry Graz University of Technology, Graz, Austria*
[e]*Faculty of Mathematics and Computer Science, University of Warmia and Mazury in Olsztyn, Olsztyn, Poland*

published in:
Molecular Physics, 117:7-8, 935-943, DOI: 10.1080/00268976.2018.1511869 [91]

Abstract

Quadrupole relaxation enhancement (QRE) has been suggested as the key mechanism for a novel class of field-selective, potentially responsive magnetic resonance imaging contrast agents. In previous publications, QRE has been confirmed for solid compounds containing ^{209}Bi as the quadrupolar nucleus (QN). For QRE to be effective in aqueous dispersions, several conditions must be met, i.e. high transition probability of the QN at the ^{1}H Larmor frequency, water exchange with the bulk and comparatively slow motion of the Bi-carrying

particles. In this paper, the potential influence of structural order within the compounds ('crystallinity') on QRE was studied by nuclear quadrupole resonance (NQR) spectroscopy in one crystalline and two amorphous preparations of Triphenylbismuth (BiPh3). The amorphous preparations comprised (1) a shock-frozen melt and (2) a granulate of polystyrene which contained homogeneously distributed BiPh3 after common dissolution in THF and subsequent evaporation of the solvent. In contrast to the crystalline powder which exhibits strong, narrow NQR peaks the amorphous preparations did not reveal any NQR signals above the noise floor. From these findings, we conclude that the amorphous state leads to a significant spectral peak broadening and that for efficient QRE in potential contrast agents structures with a high degree of order (near crystalline) are required.

6.1 Summary of motivation and results

In this section, only a brief summary of the above outlined work, containing the most important results and consequences, shall be given. The full paper is available open access [91] and contains complete, detailed information, as for example on experimental methods and the analysis procedure.

The main motivation of this work is to address the importance of structural order of the QRE-active core compound within a carrier nanoparticle. For the investigation, NQRS measurements were performed on different preparations of triphenylbismuth (BiPh3), which comprise crystalline and amorphous solid state samples. As a reference, BiPh3 is available in crystalline powder form. Further, two amorphous preparations have been produced: (1) A shock-frozen melt of the original powder sample and, (2) homogeneously distributed BiPh3 in a polystyrene matrix. Both amorphous samples did not show any observable NQR peak (7/2-5/2 transition of the ^{209}Bi nuclear spin) above the noise level. This indicates a strong broadening of the signal due to an increased EFG distribution.

For preparation (1), the evolution of the NQR signal has also been tracked over time (see figure 6.1): The original sample produces a narrow and pronounced resonance peak at room temperature (RT). From this sample, a supercooled melt is produced by melting and subsequent immersion into liquid nitrogen. Then, the evolution of the NQR signal is traced during recrystallization of the supercooled melt at RT. In the amorphous state, the sample produces no signal. Reason is, that in the amorphous state the distribution of EFG's of each molecule is assumed to be much broader than in the crystalline state. Thus, due to the broad distribution of EFG's, the signal is strongly dispersed in the frequency domain and remains below the noise floor of the spectrometer. Over time, recrystallization of the molecules in the sample sets in which results in re-establishing an ordered structure. Surprisingly, the first signal appears at a shifted frequency (compared to the original peak), which is due to the formation of a different crystal structure as in the original sample. However, this polymorphous state (which has not been reported until this

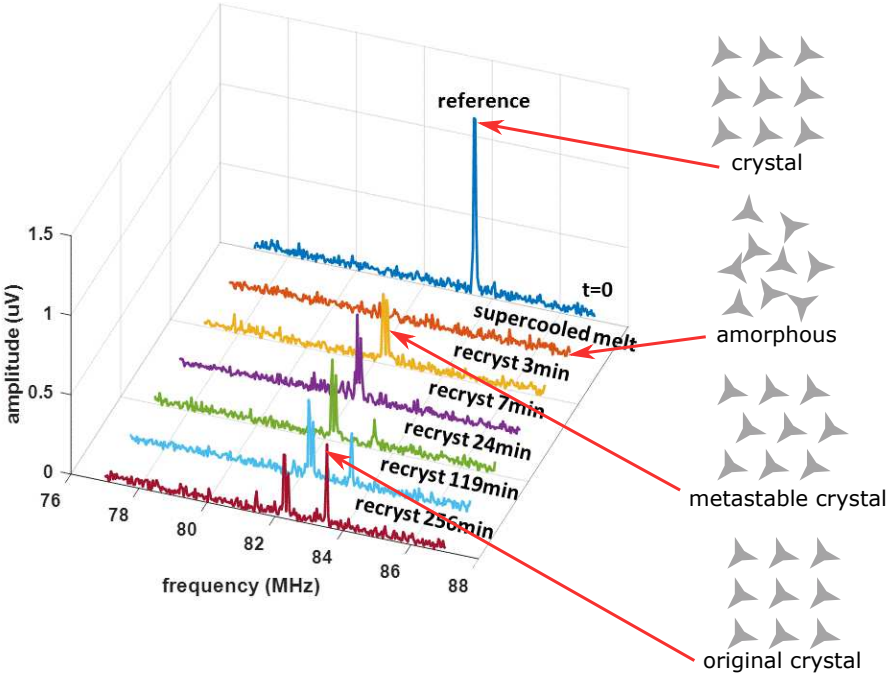

FIGURE 6.1: NQRS experiment on crystalline and amorphous triphenylbismuth. The NQRS signal is used to trace the recrystallization process over time: At the beginning (light red, supercooled melt), the amorphous sample shows no signal. During crystallization, a metastable polymorphous crystal lattice is formed before the original configuration is re-established. The upper most curve (dark blue) shows the reference signal at RT to which the sample has returned after about 24 h. Parts of the figure reproduced with permission from the authors of [91].

publication) is not stable. After several minutes, recrystallization to the original state sets in- which is indicated by the re-appearance of the original NQR signal. With progress of time, the metastable signal disappears and the original crystal structure is re-established.

The findings of this work support the design process of a possible QRE-based CA. It is expected, that a highly ordered structure which produces narrow NQR peaks is beneficial to also produce narrow QRE peaks. This is indicated in figure 6.2, where possible CA particle systems and their expected, resulting NMRD profiles in aqueous solutions are shown. "Highly ordered" does not necessarily mean crystalline, as it is for example possible to graft the QRE active core compounds onto larger, symmetric molecules (e.g. cyclodextrine). This possibility is indicated in the upper right panel of 6.2. Every QRE active molecule in the particle should have a similar surrounding and bonding structure. Such a situation can also be achieved by functionalizing surfaces of crystalline nanoparticles (e.g. silica nanoparticles).

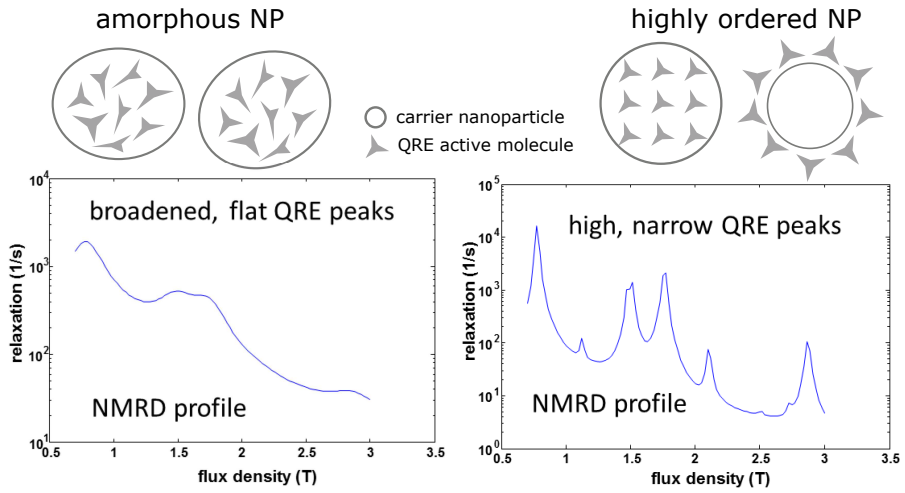

FIGURE 6.2: Schematic NMRD profiles resulting from different nanoparticle preparations. In case of amorphous systems, not every molecule is expected to exhibit the same EFG. This is indicated by the distorted an not-ordered QRE active molecules in the left panel. Such a condition is expected to produce broadened QRE peaks. Ordered structures, as shown on the right panel, have the ability to produce narrow QRE peaks. Parts of the figure reproduced with permission from the authors of [91].

6.2 Contributions of the author

The main contributions of the author were conceptualization of the work in close reconcilement with the first author as well as experiment design and performing NQRS measurements.

Chapter 7

Summarized conclusion

The first step in a systematic system design to realize the idea of a QRE-based MRI contrast agent is to identify suitable molecules (compare figure 1.2). Most important, besides bio-compatibility, is that these molecules contain quadrupole nuclei located in an EFG produced by the surrounding molecular electron orbitals. The values of the resulting NQR parameters Q_{cc} and η must be in a range so as to provide a nuclear spin transition near or at a certain frequency which is defined by the scanner's Larmor frequency. This requirement is fulfilled by most of the ^{209}Bi-Aryl compounds presented in chapter 3 (eight in total), which were investigated by NQR spectroscopy in the form of solid powders. At the human body temperature, their Q_{cc} ranges between 657 MHz and 668 MHz with η around 0.1 (see table 3.6). As ^{209}Bi has I=9/2, it is possible to observe four single quantum coherences where two of them have the potential to facilitate QRE at 1.5 T and 3 T nominal scanner fields. Their temperature dependence of about -10 kHz/K around $37°C$ is not critical for the planned application (see table 3.8).

As it is not yet clear in which condensed form the selected molecules will appear in the final system (e.g. as crystalline nanoparticles or embedded in an amorphous matrix), the dependence of the NQR parameters on the molecules' surroundings has been investigated. This was done by calculating the EFG of one representative compound (triphenylbismuth) using ab-initio quantum chemistry (QC) methods. At first, the crystalline case was considered for developing and refining the QC approach. The theoretical results could be compared with the experimentally determined NQR parameters and are in close agreement (see table 3.1). In a second step, the EFG of an isolated molecule was calculated by removing the crystalline surroundings. In this way it is possible to estimate the contribution from the crystal lattice to the EFG (crystal effect). Finally, the molecule itself was allowed to relax in the isolated state which leads to a slight change of bond length and angles. Also for this case, the EFG changed slightly which gives an estimation of what can happen when the molecule is confined in different surroundings (structure effect). The results of the QC simulations predict a Q_{cc} shift of -18.2% due to the crystal effect and of +2.7 % due to a compensating structural effect, which in total gives a shift of about -15% when the molecule is taken out of the crystalline structure and considered in its isolated gas-phase (see table 3.1). This result is important for the design of contrast

agents from the suggested compounds, as possible shifts due to e.g. surface effects or different embedding of the molecules can be predicted by calculations. The performed QC simulation is interesting also from the point of model and method validation. In case of ^{209}Bi, one is confronted with a high mass, high spin nucleus which makes calculations of the electron distribution quite elaborate. All presented QC results were obtained from a parameter framework found by a preceding parameter study which can also be used in future calculations. In this study, the influence of the chosen basis set and density functional as well as consideration of electron correlation and relativistic spin-orbit coupling was investigated (see table 3.2).

For particle and application design it is of interest to be able to control the frequency position of the quadrupole transitions. This is, to some extent, possible by the use of substituents or ligands to alter the electron distribution in close vicinity of the QRE active nucleus. In case of the investigated Bi-Aryl compounds, manipulations at different positions of the phenyl rings e.g. by methoxy groups or atoms like fluorine influence both the molecule's structure (bond length and angles) as well as electron density. The relation between the length of the C-Bi bond and the experimentally determined Q_{cc} is illustrated for several Bi-Aryl compounds in figure 3.3.2. Ligands which create a smaller C-Bi bond length tend to increase Q_{cc}. With the finding from the QC-study, it is in principle also possible to calculate and predict not only different surroundings of the molecule and its influence on the NQR parameters, but also what happens when different ligands are attached to the molecules. This might help to reduce the experimental efforts, as the success of "tuning" the NQR frequencies by different ligands can be anticipated before synthesising and measuring the compounds (which can be very time consuming).

In a short paragraph in chapter 3, section 3.3.1, several studies on toxicity of Bi-containing materials are collected which predict a relatively low cytotoxic potential. However, this point certainly requires intensive research on the final CA system, made up of a QRE-active core and a nanoparticle acting as carrier. One important point is stability of the agent to avoid release of Bi, which makes covalently bound systems preferable.

Besides experimentally determining Q_{cc} and η of eight Bi-Aryl compounds, the NQR study was complemented by measuring also the spin relaxation times T_1 and T_2 by most of the observed transitions (table 3.7). Quadrupole relaxation forms the second step in the two-step magnetization transfer effect of QRE from the protons via QN to the molecular lattice. From the proton perspective, the relaxation of the QN appears as an additional modulation of the proton-QN D-D coupling and can thus be expected to have an impact on the total process. Also, an impact on the QRE-peak lineshape is expected. Relaxation data thus can serve as input parameters for simulating QRE with relaxation theory as presented in [34].

After selecting suitable QRE active compounds, as a next important step, strong and pronounced QRE peaks were experimentally demonstrated on intrinsic protons

by field cycling (FC) relaxometry on tris(2-methoxyphenyl) bismuth (see figure 3.8). FC relaxometry means measuring the spin-lattice relaxation rate R_1 of protons in the sample at different magnetic fields strengths and is thus the most important verification method for QRE before transferring the system to a MRI scanner. For the intended contrast agent application, it is important to be able to predict the field positions of the QRE peaks. This issue is addressed in chapter 4, where a simple calculation procedure is presented which allows to calculate the appearance of QRE peaks from protons when the NQR parameters at zero field of the involved QN's are known. The approach does not rely on relaxation theory, but uses quantum mechanical probabilities for single quantum coherences of nuclear quadrupole spins in an external magnetic field. The calculation evaluates the NQR spectrum at different field strength and extracts the probability value at the corresponding proton Larmor frequency (see figure 4.2) i.e. at the crossings between Larmor frequency and quadrupole transition frequency (compare figure 4.1). The shape of the QRE peaks is phenomenologically introduced as Lorentzian distribution with an estimated width taken from the spin-spin relaxation data found in chapter 3. The calculations could reproduce well the QRE features measured in solid tris(2-6-dimethoxyphenyl) bismuthine and tris(2-methoxyphenyl) bismuthine appearing above 1 T (see figures 4.4 and 4.5). The developed calculation tool supports contrast agent design as it is possible to accurately determine the frequency position of possible QRE peaks from any compound, where NQR parameters at zero field are known from experiments or have been calculated. It should be noted, that the presented procedure has been shown to work well for intrinsic protons in solids, but to simulate the effect of QRE on external protons in liquid systems, the application of sophisticated relaxation theory- based on the stochastic Liouville equation- is necessary.

An important contribution for a better understanding of the required CA particle morphology is given by the work summarized in chapter 6. The study investigates the impact of structural order of different sample preparations of Bi-aryl compounds on the appearance of zero-field NQR transitions. It could be shown that solid, amorphous preparations containing triphenylbismuth (a shock frozen melt and a granulate from polystyrene-substrate serving as matrix) do not lead to measurable NQR signals above the noise level of the spectrometer. In contrast, crystalline samples in powder form give rise to strong and narrow NQR features. Reason for this observation is the differing width of the EFG distribution in the samples. The result implies that QRE-active compounds in CA particles should appear in a highly ordered form, so as to maintain a narrow EFG distribution and, in turn, produce narrow QRE peaks (see figure 6.2).

As a side discovery, the study presents a yet unknown metastable polymorphic crystal structure of triphenylbismuth detected by NQR spectroscopy. The structure is formed during thermalization of the shock-frozen melt but is transferred into the original structure after a few minutes (see figure 6.1).

Most of the aspects considered up to here are dealing with the static, average EFG of the compound which is responsible for the position of the transition frequencies. Dynamics of the EFG, however, become visible from the relaxation behaviour of the different spin transitions. In case of excited nuclear spins spontaneous emission, as it occurs for photons, is negligible and the decay to equilibrium is due to induced relaxation. Thus, relaxation times are always connected with fluctuations of the system capable of inducing transitions and can be used to obtain dynamical parameters of molecular motions. The theory of choice to model spin relaxation is commonly known as Redfield theory and has been applied in chapter 5 to explain for the NQR relaxation data observed in chapter 3. Analysing field dependent spin-lattice relaxation data from protons (NMRD profiles) in the indicated manner is a very popular method to gain insights into dynamics of solids and liquids. The study presented in chapter 5 shows how NQRS data- which is connected with much less experimental costs and efforts than FC-relaxometry- can be used to learn something about the dynamics of QN containing molecules in the solid state.

The presented calculation assumes fluctuations of the EFG to be the most important source for relaxation. In the particular case of Bi-aryl compounds, the nuclear spin number I is $9/2$ which leads to a higher complexity of the calculations than for typically treated protons with $I = 1/2$. Moreover, due to the zero-field case, the energy levels are degenerate in m. Especially these aspects must be considered when correctly applying Redfield theory to model the relaxation behaviour of the four observable single quantum coherences. A key finding of the study is the important role of degenerate energy levels for the lowest, 3/2-1/2 transition, which leads to a much faster relaxation than for all other transitions. The degeneracy opens additional relaxation pathways via double quantum coherences enabled by the appearance of off-diagonal elements in the Relaxation matrix (see figure 5.5). With this observation, an earlier publication [94] could be corrected in which speculation about additional relaxation mechanisms were made.

The presented findings have contributed to the design of different nanoparticle systems containing selected, above suggested Bi-aryl compounds. The particles were dissolved in different solvents and tested regarding their ability to enhance the spin-lattice relaxation of solvent protons by means of FC-relaxometry. In chapter 8, two of theses samples- which have shown first promising results- are discussed closer.

Chapter 8

Outlook

8.1 QRE in liquids

Following several confirmations of QRE peaks from the suggested Bi-aryl compounds in the solid state for tris(2-methoxyphenyl) bismuthane, tris(2,6-dimethoxyphenyl) bismuthane, triphenylbismuth dichloride and phenylbismuth dichloride [221, 222, 179], encouraging proof-of-principle results were presented for aqueous solutions containing particle preparations of triphenylbismuth [223, 224]. The nanoparticles were produced by a nanoprecipitation method in the presence of a polymer (polyvinyl pyrrolidone, PVP) for stabilization. From these polymer-coated, crystalline nanoparticles, two samples with an average hydrodynamic diameter (HDD) of 400 nm and 750 nm were dissolved in water at a concentration range of 1-2 mg/ml and measured by FC-relaxometry at 295 K. The gained NMRD profiles exhibit significant peaks which can be attributed to relaxation-enhanced bulk protons (see figure 8.1). In accordance with the theory, slower tumbling particles (larger in size) produce larger relaxation rates. Also, the peaks appear in the expected field region which would be suitable for e.g. 3 T scanners. Unfortunately, the current relaxation rates are not large enough for testing the enhancement effect with regard to image contrast by the use of suitable FC-MRI scanners [129, 35].

The results are promising but far from optimal which has, concluding from some of the above made findings, several reasons:

- Shapes and sizes of the produced nanoparticles are not well characterized and exhibit a wide distribution.
- The water accessibility and exchange lifetime with Bi-centres is unclear, must be investigated and, where applicable, optimized.
- Structural order of the QRE compounds on the nanoparticle must be high to produce a narrow EFG distribution. This point is yet unclear for the surfaces of the investigated particles.

Another liquid system, where QRE-peaks have been observed, is a saturated solution of tris(2-methoxyphenyl) bismuthane dissolved in tetrahydrofuran (THF) which is presented by Kruk et al. [225] as well as in [223, 224] . In the former publication, the authors have investigated the potential of QRE to compete with current

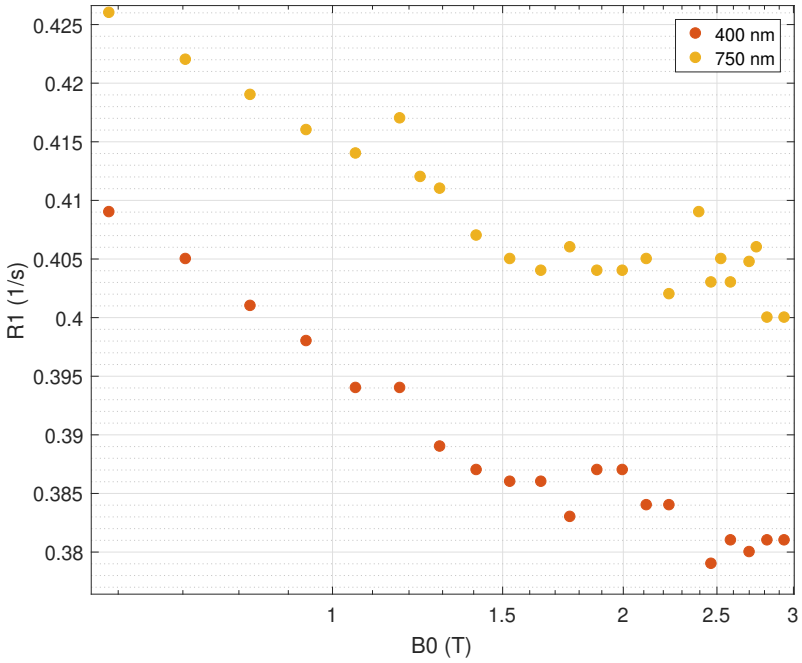

FIGURE 8.1: ^{1}H NMRD profiles of aqueous solutions containing crystalline, PVP coated nanoparticles of triphenylbismuth with average hydrodynamic diameters of 400 nm and 750 nm. Reproduced with permission from the authors of [223].

PRE based systems using the presented NMRD data as well as spin relaxation theory. At the moment, relaxivity of the observed QRE-peaks is about ten times lower then for typical Gd- based agents (3-5.4 $mM^{-1}s^{-1}$). It is hypothesized, that the observed QRE-peaks are produced by clusters of tris(2- methoxyphenyl) bismuthane of about 4 nm in size as single molecules would be rotating too fast. In the closing section of their work several points are emphasized which should be considered for a further particle optimization. Besides the already addressed structural and morphological issues (which are predominantly chemical aspects), prerequisites concerning the dynamics of potential QRE-CAs and the role of quadrupole spin relaxation are discussed [225]:

- The rotational correlation time of the particle τ_r must be in a range so as to produce strong QRE peaks and at the same time a high enough spectral density $J(\omega)$ for mediating ^{1}H-^{209}Bi fluctuations. The value of τ_r should be slower than $2e^{-8}$ s. However, for very slow tumbling, $J(\omega)$ might be too weak at high magnetic fields.

- In QRE, the spin-lattice relaxation time $T_{1,Q}$[1] of the quadrupole nucleus appears as contribution to the D-D rotational correlation time τ_r forming an effective correlation time $1/\tau_{eff} = 1/\tau_r + 1/T_{1,Q}$. So, $T_{1,Q}$ should be slower than τ_r not to dominate $1/\tau_{eff}$.

[1]The subscript "Q" emphasizes that the spin-lattice relaxation of the QN is meant, and not of the proton.

- The exchange lifetime τ_{ex} has a double role as it modulates ^{1}H-^{209}Bi D-D coupling in the same manner as $T_{1,Q}$ described before (so it should be slower than τ_r), and is a measure for how many protons approach the QN in a certain amount of time (with a faster τ_r more protons can be addressed). So, it might be a parameter which has a certain optimum.

In chapter 3, $T_{1,Q}$ values of tris(2- methoxyphenyl) bismuthane and triphenylbismuth at different temperatures are presented which have a range from about 100 μs to a few ms. Event though these values have been determined at zero field for crystalline solids, typically $T_{1,Q}$ is expected to be slower than τ_r.

The spin-spin relaxation time $T_{2,Q}$ of the QN, as discussed in chapter 5, should also be slow so as to keep the contribution of lifetime-broadening to the widht of QRE peaks low. Only narrow NQR peaks are able to produce the desired narrow QRE peaks. The method presented in chapter 5 (based on Redfield relaxation theory) to simulate the QN's spin-spin relaxation $T_{2,Q}$ can also be used for a better understanding of it's spin-lattice relaxation $T_{1,Q}$. In particular, such simulations can become important for the complete CA system, as in a nanoparticle molecular dynamics and thus relaxation behaviour might deviate from the experimental observations made in chapter 3. A possible extension of the calculation presented in chapter 5 from $T_{2,Q}$ to $T_{1,Q}$ is discussed in section 8.2.

When looking at the ^{1}H-NMRD profiles in figure 8.1, it becomes evident that a thorough reconsideration of the triphenylbismuth nanoparticles is necessary to come closer to a QRE-CA system which is capable to fulfil the desired requirements: (1) An "overall" relaxivity which is comparable to state-of-the-art PRE-CAs, and (2) narrow, discrete QRE features. Only when achieving both requirements, QRE based CAs can add valuable novel modalities to conventional MRI. A field selective QRE-CA in combination with a FC-MRI scanner could realize molecular imaging as well as contrast switching by an external trigger; two features which are expected to improve daily medical diagnostic routine significantly. Thus, a continuation of research based on the presented findings is recommended.

8.2 Spin-lattice relaxation of zero field NQR

The approach presented in chapter 5 for calculating spin-spin relaxation R_2[2] and lineshape of NQR spectra is rather flexible and can also be applied to other related problems. Only a few alterations are needed to simulate spin-lattice relaxation R_1: $\langle I_z \rangle$ must be calculated instead of $\langle I_x \rangle$, which means that other elements of the spin density are picked out than in chapter 5. The operator basis (as in equation 8.1) is then formed by the populations of the spin density matrix instead of the coherences. Calculation of Γ is according to equation 5.26a but the Liouville - von Neumann

[2] in this section, the "Q" subscript is dropped

equation (equation 5.3) has to be solved in time-domain which requires diagonalization as well as time-domain evolution of the populations. An example, based on the same model for EFG fluctuations as used in section 5.2.3 is given in figure 8.2. Starting condition at t=0 for the populations of the assumed I=9/2 nucleus is following a Boltzmann distribution where the populations of the levels m=5/2 and m=7/2 are exchanged (figure 8.2, left panel). This non-equilibrium situation corresponds to the distribution right after the application of an inversion-pulse at the 5/2-7/2 resonance condition. In the simulation it is further assumed that only 5/2-7/2 is affected and the (-5/2) - (-7/2) levels remain unchanged (such a situation can only be achieved by circular polarised RF pulses [70, 68]). As evolving over time, the populations restore their equilibrium values under the influence of the time dependent relaxation Hamiltonian (EFG fluctuations). In particular, it is interesting to see that not only the exchanged populations are involved in the relaxation process, but also neighbouring states are "kicked" out of equilibrium for a short moment and eventually relax back to their equilibrium as well. In the right panel of figure 8.2, the population difference is shown which is proportional to a hypothetical NQR signal that could be gained by a T_1 measurement (inversion recovery).

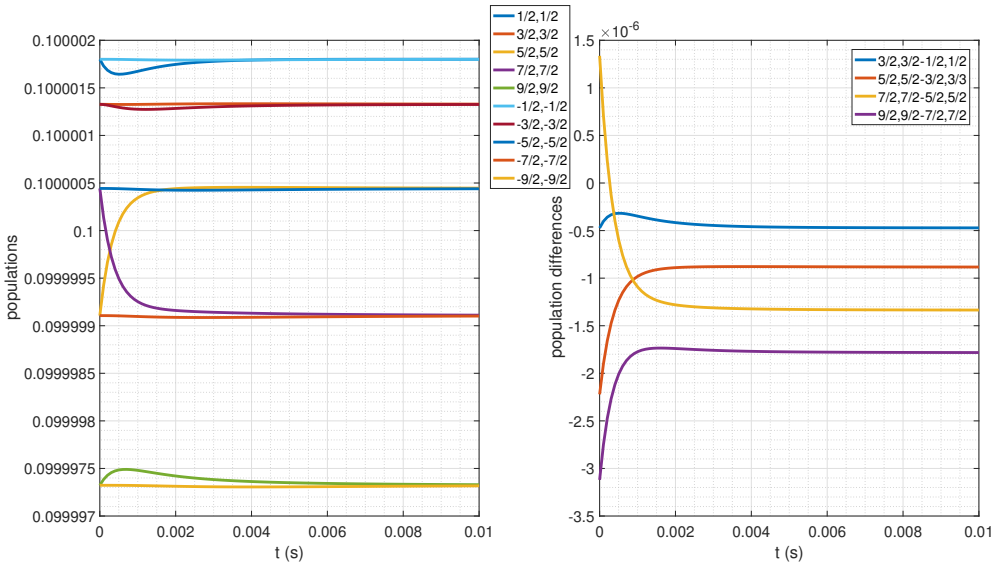

FIGURE 8.2: Preliminary result for the time evolution of out-of-equilibrium populations of a quadrupolar nucleus with I=9/2. The starting condition corresponds to Boltzmann distribution at 300 K, where the occupations of m=7/2 and m=5/2 states are interchanged. Parameters: Q_{cc}=668.87 MHz, $\eta = 0.083$, q_{cc}=6.68 MHz, τ_c=1e-9 s. Assumed is a powder sample using N=150 spherically distributed Euler angles (defining direction of the single EFG's)

To be able to calculate the time evolution of the populations, it is necessary to determine the Redfield relaxation matrix elements according to equation 5.26a. In

case of zero-quantum transitions, the following operator states are involved:

$$\{\ |\frac{1}{2},\frac{1}{2}\rangle, |\frac{3}{2},\frac{3}{2}\rangle, |\frac{5}{2},\frac{5}{2}\rangle, |\frac{7}{2},\frac{7}{2}\rangle, |\frac{9}{2},\frac{9}{2}\rangle, \\ |-\frac{1}{2},-\frac{1}{2}\rangle, |-\frac{3}{2},-\frac{3}{2}\rangle, |-\frac{5}{2},-\frac{5}{2}\rangle, |-\frac{7}{2},-\frac{7}{2}\rangle, |-\frac{9}{2},-\frac{9}{2}\rangle\ \}\ . \tag{8.1}$$

This set leads to a 10x10 Redfield matrix. The coupled differential equation for the density operator elements (equation 5.3) can be solved by finding the eigenvalues and using an Ansatz. The presented approach is not yet tested against experimental findings but should only sketch how one could proceed. One reason is, that in case of spin-lattice relaxation, the stochastic Hamiltonian should be extended by phonons first to account for a more realistic dynamical model.

There are several applications for a complete relaxation model, where both T_1 and T_2 are considered. One is the support of QRE contrast agent design to predict realistic dynamical parameters. Another one is the simulation of NQR based quantum computers, as discussed in [68], where excitation is treated quantum mechanically but relaxation is considered phenomenologically only. Also, further insights into molecular dynamics from NQR spectroscopy can be expected when investigating T_1- which has already been demonstrated for T_2 measurements in chapter 5.

Bibliography

[1] Randall B Lauffer. "Paramagnetic metal complexes as water proton relaxation agents for NMR imaging: theory and design". In: *Chemical Reviews* 87.5 (1987), pp. 901–927. ISSN: 0009-2665. DOI: 10.1021/cr00081a003[doi].

[2] F. Bloch. "Nuclear Induction". In: *Physical Review* 70.7-8 (1946), pp. 460–474. ISSN: 0031-899X. DOI: 10.1103/PhysRev.70.460. URL: https://link.aps.org/doi/10.1103/PhysRev.70.460.

[3] P. C. Lauterbur. "Image Formation by Induced Local Interactions: Examples Employing Nuclear Magnetic Resonance". In: *Nature* 242.5394 (1973), pp. 190–191. ISSN: 0028-0836. DOI: 10.1038/242190a0. URL: http://www.nature.com/articles/242190a0.

[4] Paul C. Lauterbur. "Magnetic Resonance Zeugmatography". In: *Pure and Applied Chemistry* 40.1-2 (1974), pp. 149–157. ISSN: 13653075. DOI: 10.1351/pac197440010149.

[5] Paul C. Lauterbur, M. Helena Mendonça Dias, and Andrew M. Rudin. "AUGMENTATION OF TISSUE WATER PROTON SPIN-LATTICE RELAXATION RATES BY IN VIVO ADDITION OF PARAMAGNETIC IONS". In: *Electrons to Tissues*. 1978, pp. 752–759. DOI: 10.1016/b978-0-12-225401-7.50093-x.

[6] I R Young et al. "Enhancement of relaxation rate with paramagnetic contrast agents in NMR imaging". In: *Journal of Computed Tomography* 5.6 (1981), pp. 543–547. ISSN: 0149-936X. DOI: https://doi.org/10.1016/0149-936X(81)90089-8. URL: http://www.sciencedirect.com/science/article/pii/0149936X81900898.

[7] D. H. Carr et al. "Intravenous Chelated Gadolinium As a Contrast Agent in Nmr Imaging of Cerebral Tumours". In: *The Lancet* 323.8375 (1984), pp. 484–486. ISSN: 01406736. DOI: 10.1016/S0140-6736(84)92852-6.

[8] Gustav J Strijkers et al. "MRI Contrast Agents: Current Status and Future Perspectives". In: *Anti-Cancer Agents in Medicinal Chemestry* 7 (2007), pp. 291–305.

[9] Jessica Lohrke et al. "25 Years of Contrast-Enhanced MRI: Developments, Current Challenges and Future Perspectives". In: *Advances in Therapy* 33.1 (2016), pp. 1–28. ISSN: 18658652. DOI: 10.1007/s12325-015-0275-4.

[10] Rohan D.A. Alvares, Daniel A. Szulc, and Hai Ling M. Cheng. "A scale to measure MRI contrast agent sensitivity". In: *Scientific Reports* 7.1 (2017), pp. 1–9. ISSN: 20452322. DOI: 10.1038/s41598-017-15732-8. URL: http://dx.doi.org/10.1038/s41598-017-15732-8.

[11] Martin Uecker et al. "Real-time MRI at a resolution of 20 ms". In: *NMR in Biomedicine* 23.8 (2010), pp. 986–994. ISSN: 09523480. DOI: 10.1002/nbm.1585.

[12] Karl Landheer et al. "Theoretical description of modern 1H in Vivo magnetic resonance spectroscopic pulse sequences". In: *Journal of Magnetic Resonance Imaging* (2019), pp. 1–22. ISSN: 15222586. DOI: 10.1002/jmri.26846.

[13] Peter Jezzard, Paul M. Matthews, and Stephen M. Smith. *Functional Magnetic Resonance Imaging*. Ed. by Peter Jezzard, Paul M. Matthews, and Stephen M. Smith. Oxford University Press, 2001, p. 432. ISBN: 9780192630711. DOI: 10.1093/acprof:oso/9780192630711.001.0001. URL: http://www.oxfordscholarship.com/view/10.1093/acprof:oso/9780192630711.001.0001/acprof-9780192630711-chapter-3http://www.oxfordscholarship.com/view/10.1093/acprof:oso/9780192630711.001.0001/acprof-9780192630711.

[14] Roland Bammer. "Basic principles of diffusion-weighted imaging". In: *European Journal of Radiology* 45.3 (2003), pp. 169–184. ISSN: 0720048X. DOI: 10.1016/S0720-048X(02)00303-0. URL: https://doi.org/10.1016/S0720-048X(02)00303-0https://linkinghub.elsevier.com/retrieve/pii/S0720048X02003030.

[15] Claudia Prieto et al. "Cardiac MR Angiography". In: *Protocols and Methodologies in Basic Science and Clinical Cardiac MRI*. Cham: Springer International Publishing, 2018, pp. 399–432. DOI: 10.1007/978-3-319-53001-7_13. URL: http://link.springer.com/10.1007/978-3-319-53001-7{_}13.

[16] Anwar R. Padhani. "Dynamic contrast-enhanced MRI in clinical oncology: Current status and future directions". In: *Journal of Magnetic Resonance Imaging* 16.4 (2002), pp. 407–422. ISSN: 10531807. DOI: 10.1002/jmri.10176.

[17] Rainer Kimmich and Esteban Anoardo. *Field-cycling NMR relaxometry*. Vol. 44. 3-4. 2004, pp. 257–320. ISBN: 4973150231. DOI: 10.1016/j.pnmrs.2004.03.002.

[18] N. Bloembergen, E. M. Purcell, and R. V. Pound. "Relaxation effects in nuclear magnetic resonance absorption". In: *Physical Review* 73.7 (1948), pp. 679–712. ISSN: 0031899X. DOI: 10.1103/PhysRev.73.679.

[19] I. Solomon. "Relaxation Processes in a System of Two Spins". In: *Physical Review* 99.2 (1955), pp. 559–565. ISSN: 0031-899X. DOI: 10.1103/PhysRev.99.559. URL: https://link.aps.org/doi/10.1103/PhysRev.99.559.

[20] N. Bloembergen and L. O. Morgan. "Proton Relaxation Times in Paramagnetic Solutions. Effects of Electron Spin Relaxation". In: *The Journal of Chemical Physics* 34.3 (1961), pp. 842–850. ISSN: 0021-9606. DOI: 10.1063/1.1731684. URL: http://aip.scitation.org/doi/10.1063/1.1731684.

[21] Randall B. Lauffer et al. "1/T1 NMRD profiles of solutions of Mn2+ and Gd3+ protein-chelate conjugates". In: *Magnetic Resonance in Medicine* 3.4 (1986), pp. 541–548. ISSN: 07403194. DOI: 10.1002/mrm.1910030407. URL: http://doi.wiley.com/10.1002/mrm.1910030407.

[22] Tomonori Kanda et al. "High signal intensity in the dentate nucleus and globus pallidus on unenhanced T1-weighted MR images: Relationship with increasing cumulative dose of a gadoliniumbased contrast material". In: *Radiology* 270.3 (2014), pp. 834–841. ISSN: 15271315. DOI: 10.1148/radiol.13131669.

[23] Tyler J. Fraum et al. "Gadolinium-based contrast agents: A comprehensive risk assessment". In: *Journal of Magnetic Resonance Imaging* 46.2 (2017), pp. 338–353. ISSN: 10531807. DOI: 10.1002/jmri.25625. URL: http://doi.wiley.com/10.1002/jmri.25625.

[24] Robert J. McDonald et al. "Gadolinium Deposition in Human Brain Tissues after Contrast-enhanced MR Imaging in Adult Patients without Intracranial Abnormalities". In: *Radiology* 285.2 (2017), pp. 546–554. ISSN: 0033-8419. DOI: 10.1148/radiol.2017161595. URL: http://pubs.rsna.org/doi/10.1148/radiol.2017161595.

[25] M.M.J. Modo, J.W.M. Bulte, and E. E. Kim. "Molecular and Cellular MR Imaging". In: *Journal of Nuclear Medicine* 48.12 (2007), pp. 2087–2087. ISSN: 0161-5505. DOI: 10.2967/jnumed.107.045369. URL: http://jnm.snmjournals.org/cgi/doi/10.2967/jnumed.107.045369.

[26] George J. Lu et al. "Acoustically modulated magnetic resonance imaging of gas-filled protein nanostructures". In: *Nature Materials* 17.5 (2018), pp. 456–463. ISSN: 14764660. DOI: 10.1038/s41563-018-0023-7. URL: http://dx.doi.org/10.1038/s41563-018-0023-7.

[27] Elena Vinogradov, A. Dean Sherry, and Robert E. Lenkinski. "CEST: From basic principles to applications, challenges and opportunities". In: *Journal of Magnetic Resonance* 229 (2013), pp. 155–172. ISSN: 10907807. DOI: 10.1016/j.jmr.2012.11.024. arXiv: NIHMS150003. URL: http://dx.doi.org/10.1016/j.jmr.2012.11.024.

[28] Hung V.T. Nguyen et al. "Nitroxide-Based Macromolecular Contrast Agents with Unprecedented Transverse Relaxivity and Stability for Magnetic Resonance Imaging of Tumors". In: *ACS Central Science* 3.7 (2017), pp. 800–811. ISSN: 23747951. DOI: 10.1021/acscentsci.7b00253.

[29] D. E. Woessner and H. S. Gutowsky. "Spin Exchange and Spin-Lattice Relaxation Induced by Mechanical Rotation of Solids". In: *J. Chem. Phys.* 29.4 (1958), p. 804. ISSN: 00219606. DOI: 10.1063/1.1744594. URL: http://link.aip.org/link/JCPSA6/v29/i4/p804/s1{\&}Agg=doi.

[30] Maurice Goldman. "Croisement des frequencies de resonance nucleaire des chlores et des protons dans le paradichlorobenzene". In: *Comptes Rendus Physique* 246 (1958), pp. 1038–1040. URL: https://gallica.bnf.fr/ark:/12148/bpt6k3198s/f1046.item.r=1038.

[31] G. Voigt and R. Kimmich. "Quadrupolar dip in proton relaxation dispersion of poly(vinyl chloride)". In: *Journal of Magnetic Resonance (1969)* 24.1 (1976), pp. 149–154. ISSN: 00222364. DOI: 10.1016/0022-2364(76)90240-7.

[32] R. Kimmich et al. "Interactions and fluctuations deduced from proton field-cycling relaxation spectroscopy of polypeptides, DNA, muscles, and algae". In: *Journal of Magnetic Resonance (1969)* 68.2 (1986), pp. 263–282. ISSN: 00222364. DOI: 10.1016/0022-2364(86)90243-X.

[33] David J. Lurie et al. "Fast field-cycling magnetic resonance imaging". In: *Comptes Rendus Physique* 11.2 (2010), pp. 136–148. ISSN: 16310705. DOI: 10.1016/j.crhy.2010.06.012. URL: http://dx.doi.org/10.1016/j.crhy.2010.06.012https://linkinghub.elsevier.com/retrieve/pii/S1631070510000605.

[34] Danuta Kruk et al. "Quadrupole relaxation enhancement–application to molecular crystals." In: *Solid state nuclear magnetic resonance* 40.3 (2011), pp. 114–20. ISSN: 1527-3326. DOI: 10.1016/j.ssnmr.2011.08.003. URL: http://www.sciencedirect.com/science/article/pii/S0926204011000816.

[35] Markus Bödenler et al. "Comparison of fast field-cycling magnetic resonance imaging methods and future perspectives". In: *Molecular Physics* 117.7-8 (2019), pp. 832–848. ISSN: 0026-8976. DOI: 10.1080/00268976.2018.1557349. URL: https://www.tandfonline.com/doi/full/10.1080/00268976.2018.1557349.

[36] R. Weissleder. "Molecular imaging: Exploring the next frontier". In: *Radiology* 212.3 (1999), pp. 609–614. ISSN: 00338419. DOI: 10.1148/radiology.212.3.r99se18609.

[37] Ralph Weissleder and Mikael J. Pittet. "Imaging in the era of molecular oncology". In: *Nature* 452.7187 (2008), pp. 580–589. ISSN: 14764687. DOI: 10.1038/nature06917.

[38] Dina V. Hingorani, Adam S. Bernstein, and Mark D. Pagel. "A review of responsive MRI contrast agents: 2005-2014". In: *Contrast Media and Molecular Imaging* 10.4 (2015), pp. 245–265. ISSN: 15554317. DOI: 10.1002/cmmi.1629.

[39] Michelle L. James and Sanjiv S. Gambhir. "A molecular imaging primer: Modalities, imaging agents, and applications". In: *Physiological Reviews* 92.2 (2012), pp. 897–965. ISSN: 00319333. DOI: 10.1152/physrev.00049.2010.

[40] Per Olof Westlund. "The quadrupole enhanced1H spin-lattice relaxation of the amide proton in slow tumbling proteins". In: *Physical Chemistry Chemical Physics* 12.13 (2010), pp. 3136–3140. ISSN: 14639076. DOI: 10.1039/b922817a.

[41] Pascal H Fries and Elie Belorizky. "Simple expressions of the nuclear relaxation rate enhancement due to quadrupole nuclei in slowly tumbling molecules". In: *The Journal of Chemical Physics* 143.4 (2015), p. 044202. ISSN: 0021-9606. DOI: 10.1063/1.4926827. URL: http://aip.scitation.org/doi/10.1063/1.4926827.

[42] Tara P Das and Erwin Louis Hahn. *Nuclear quadrupole resonance spectroscopy*. Solid state physics. Supplement 1. New York: Academic Press, 1958, ix, 223 p. URL: http://catalog.hathitrust.org/Record/001482078http://hdl.handle.net/2027/mdp.39015001335077http://hdl.handle.net/2027/mdp.39015001328387(v.1).

[43] W. A. Nierenberg, N. F. Ramsey, and S. B. Brody. "Measurements of Nuclear Quadrupole Moment Interactions". In: *Physical Review* 70.9-10 (1946), pp. 773–775. ISSN: 0031-899X. DOI: 10.1103/PhysRev.70.773.2. URL: https://link.aps.org/doi/10.1103/PhysRev.70.773.2.

[44] Hans-Georg Dehmelt and Hubert Krüger. "Kernquadrupolfrequenzen in festem Dichloräthylen". In: *Die Naturwissenschaften* 37.5 (1950), pp. 111–112. ISSN: 0028-1042. DOI: 10.1007/BF00623717. URL: http://link.springer.com/10.1007/BF00623717.

[45] H. G. Dehmelt and H. Krüger. "Quadrupol-Resonanzfrequenzen von Cl- und Br-Kernen in kristallinem Dichloräthylen und Methylbromid". In: *Zeitschrift für Physik* 129.4 (1951), pp. 401–415. ISSN: 14346001. DOI: 10.1007/BF01379591.

[46] R V Pound. "Nuclear Electric Quadrupole Interactions in Crystals". In: *Phys. Rev.* 79.4 (1950), pp. 685–702. DOI: 10.1103/PhysRev.79.685. URL: https://link.aps.org/doi/10.1103/PhysRev.79.685.

[47] H. B. G. Casimir. "On the Interaction between Atomic Nuclei and Electrons". In: *On the Interaction between Atomic Nuclei and Electrons*. Dordrecht: Springer Netherlands, 1936, pp. 201–283. DOI: 10.1007/978-94-017-6067-6_1. URL: http://link.springer.com/10.1007/978-94-017-6067-6{_}1.

[48] Charles P. Slichter. *Principles of Magnetic Resonance*. Vol. 1. Springer Series in Solid-State Sciences. Berlin, Heidelberg: Springer Berlin Heidelberg, 1990, p. 658. ISBN: 978-3-642-08069-2. DOI: 10.1007/978-3-662-09441-9. URL: http://www.springer.com/de/book/9783540501572http://link.springer.com/10.1007/978-3-662-09441-9.

[49] M. H. Cohen and F. Reif. "Quadrupole Effects in Nuclear Magnetic Resonance Studies of Solids". In: *Solid State Physics - Advances in Research and Applications* 5.C (1957), pp. 321–438. ISSN: 00811947. DOI: 10.1016/S0081-1947(08)60105-8.

[50] Gregory B. Furman, Victor M. Meerovich, and Vladimir L. Sokolovsky. "Nuclear electric quadrupole interactions in liquids entrapped in cavities". In: *Hyperfine Interactions* 237.1 (2016), pp. 3–8. ISSN: 15729540. DOI: 10.1007/s10751-016-1360-z. URL: http://dx.doi.org/10.1007/s10751-016-1360-z.

[51] Pramila Raghavan. "Table of nuclear moments". In: *Atomic Data and Nuclear Data Tables* 42.2 (1989), pp. 189–291. ISSN: 10902090. DOI: 10.1016/0092-640X(89)90008-9.

[52] N. J. Stone. "Table of nuclear magnetic dipole and electric quadrupole moments". In: *Atomic Data and Nuclear Data Tables* 90.1 (2005), pp. 75–176. ISSN: 0092640X. DOI: 10.1016/j.adt.2005.04.001.

[53] Tiago Quevedo Teodoro and Roberto Luiz Andrade Haiduke. "Nuclear electric quadrupole moment of bismuth from the molecular method". In: *Physical Review A - Atomic, Molecular, and Optical Physics* 88.5 (2013), pp. 12–15. ISSN: 10502947. DOI: 10.1103/PhysRevA.88.052504.

[54] J. A. S. Smith. "Nuclear quadrupole resonance spectroscopy. General principles". In: *Journal of Chemical Education* 48.1 (1971), p. 39. ISSN: 0021-9584. DOI: 10.1021/ed048p39. URL: http://pubs.acs.org/doi/abs/10.1021/ed048p39.

[55] C. H. Townes and B. P. Dailey. "Determination of Electronic Structure of Molecules from Nuclear Quadrupole Effects". In: *The Journal of Chemical Physics* 17.9 (1949), pp. 782–796. ISSN: 0021-9606. DOI: 10.1063/1.1747400. URL: http://aip.scitation.org/doi/10.1063/1.1747400.

[56] Alarich Weiss and Silvia Wigand. "Correlation of NQR and Chemical Bond Parameter". In: *Zeitschrift fur Naturforschung - Section A Journal of Physical Sciences* 45.3-4 (1990), pp. 195–212. ISSN: 18657109. DOI: 10.1515/zna-1990-3-403.

[57] Andrew Leach. *Molecular Modelling: Principles and Applications, 2nd Edition*. Pearson Education, 2001, p. 744. ISBN: 9780582382107. URL: https://www.pearson.com/us/higher-education/program/Leach-Molecular-Modelling-Principles-and-Applications-2nd-Edition/PGM251961.html?tab=order.

[58] Robert Withnall et al. "Computational Chemistry Using Modern Electronic Structure Methods". In: ... *of Chemical Education* 84.8 (2007), p. 1364. ISSN: 0021-9584. DOI: 10.1021/ed084p1364. URL: http://pubs.acs.org/doi/

abs/10.1021/ed084p1364{\%}5Cnpapers3://publication/doi/10.1021/ed084p1364.

[59] Cheng Chen et al. "Authentication of Medicines Using Nuclear Quadrupole Resonance Spectroscopy". In: *IEEE/ACM Transactions on Computational Biology and Bioinformatics* 13.3 (2016), pp. 417–430. ISSN: 1545-5963. DOI: 10.1109/TCBB.2015.2511763. URL: http://ieeexplore.ieee.org/document/7364213/{\%}0Ahttps://search.proquest.com/docview/1856597643?accountid=14116{\%}0Ahttp://suprimo.lib.strath.ac.uk/openurl/SU/SUVU01?genre=article{\&}atitle=Authentication+of+medicines+using+nuclear+quadrupole+resonance+spectrosc.

[60] John A.S. Smith et al. "14N NQR, relaxation and molecular dynamics of the explosive TNT". In: *Solid State Nuclear Magnetic Resonance* 71 (2015), pp. 61–66. ISSN: 09262040. DOI: 10.1016/j.ssnmr.2015.09.009. URL: http://linkinghub.elsevier.com/retrieve/pii/S0926204015300229https://linkinghub.elsevier.com/retrieve/pii/S0926204015300229.

[61] Christian Gösweiner et al. "Tuning Nuclear Quadrupole Resonance: A Novel Approach for the Design of Frequency-Selective MRI Contrast Agents". In: *Physical Review X* 8.2 (2018), p. 021076. ISSN: 2160-3308. DOI: 10.1103/PhysRevX.8.021076. URL: https://link.aps.org/doi/10.1103/PhysRevX.8.021076.

[62] L A Zemnukhova and R L Davidovich. "121,123Sb and 209Bi Nuclear Quadrupole Resonance Study of Complex Compounds of Antimony(III) and Bismuth(III) in the Temperature Range 77-400 K". In: *Zeitschrift für Naturforschung A* 53.6-7 (1998). ISSN: 1865-7109. DOI: 10.1515/zna-1998-6-749. URL: https://www.degruyter.com/view/j/zna.1998.53.issue-6-7/zna-1998-6-749/zna-1998-6-749.xml.

[63] Landolt-börnstein I I I Nuclear and Quadrupole Resonance. "Substances Containing C10H16 ... Zn". In: 48B.2474 (2010), pp. 5–6. DOI: 10.1007/978-3-642-02943-1. URL: http://materials.springer.com/bp/docs/978-3-642-02943-1.

[64] N. Velikite, N. Sinyavsky, and M. Maćkowiak. "Lineshape analysis of 2D NMR and NQR nutation spectra of integer and half-integer quadrupolar nuclei". In: *Zeitschrift fur Naturforschung - Section A Journal of Physical Sciences* 54.6-7 (1999), pp. 351–357. ISSN: 09320784. DOI: 10.1515/zna-1999-6-701.

[65] Bryan H Suits. "Nuclear quadrupole resonance spectroscopy". In: *Handbook of Applied Solid State Spectroscopy*. Ed. by D. R. Vij. Springer, New York, 2006. Chap. Chapter 2.

[66] M. Bloom, E. L. Hahn, and B. Herzog. "Free magnetic induction in nuclear quadrupole resonance". In: *Physical Review* 97.6 (1955), pp. 1699–1709. ISSN: 0031899X. DOI: 10.1103/PhysRev.97.1699.

[67] B. Cordier et al. “14N pulsed nuclear quadrupole resonance. 1. Nutation experiments in the case of an axially symmetric electric field gradient tensor”. In: *Molecular Physics* 103.19 (2005), pp. 2593–2598. ISSN: 00268976. DOI: 10.1080/00268970500217170.

[68] Denimar Possa, Anderson C. Gaudio, and Jair C C Freitas. “Numerical simulation of NQR/NMR: Applications in quantum computing”. In: *Journal of Magnetic Resonance* 209.2 (2011), pp. 250–260. ISSN: 10907807. DOI: 10.1016/j.jmr.2011.01.020. URL: http://dx.doi.org/10.1016/j.jmr.2011.01.020.

[69] J. J. Sakurai and Jim Napolitano. *Modern Quantum Mechanics*. Cambridge University Press, 2017. ISBN: 9781108499996. DOI: 10.1017/9781108499996. URL: https://www.cambridge.org/core/product/identifier/9781108499996/type/book.

[70] M. J. Weber and E.L. Hahn. “Selective Spin Excitation and Relaxation in Nuclear Quadrupole Resonance”. In: *Physical Review* 120.2 (1960), pp. 365–375.

[71] Daniel Canet et al. “14N Pulsed nuclear quadrupole resonance. 2. Effect of a single radio-frequency pulse in the general case”. In: *Molecular Physics* 104.9 (2006), pp. 1391–1399. ISSN: 00268976. DOI: 10.1080/00268970500465290.

[72] Malcolm H Levitt. *Malcolm H. Levitt*. 2000, p. 744. ISBN: 9780470511183.

[73] M. Ferrari et al. “14N pulsed nuclear quadrupole resonance. 3. Effect of a pulse train. Optimal conditions for data averaging”. In: *Molecular Physics* 105.23-24 (2007), pp. 3005–3012. ISSN: 00268976. DOI: 10.1080/00268970701730088.

[74] Maude Ferrari and Daniel Canet. “¹⁴ N Pulsed nuclear quadrupole resonance. 4. Two-pulse sequences for the determination of T ₁ and T ₂ relaxation times”. In: *Molecular Physics* 107.22 (2009), pp. 2419–2430. ISSN: 0026-8976. DOI: 10.1080/00268970903352327. URL: http://www.tandfonline.com/doi/abs/10.1080/00268970903352327.

[75] U. Haeberlen and J. S. Waugh. “Coherent Averaging Effects in Magnetic Resonance”. In: *Phys. Rev.* 175 (1968). URL: https://journals.aps.org/pr/abstract/10.1103/PhysRev.175.453.

[76] Karl Blum. *Density Matrix Theory and Applications*. Vol. 64. Springer Series on Atomic, Optical, and Plasma Physics. Berlin, Heidelberg: Springer Berlin Heidelberg, 2012. ISBN: 978-3-642-20560-6. DOI: 10.1007/978-3-642-20561-3. URL: http://link.springer.com/10.1007/978-3-642-20561-3.

[77] Jr. Csaba Szántay, ed. *Anthropic Awareness*. Elsevier, 2015. ISBN: 9780124199637. DOI: 10.1016/C2013-0-06828-4. URL: https://linkinghub.elsevier.com/retrieve/pii/C20130068284.

[78] Gregory B. Furman, Victor M. Meerovich, and Vladimir L. Sokolovsky. "Nuclear electric quadrupole interactions in liquids entrapped in cavities". In: *Hyperfine Interactions* 237.1 (2016), p. 140. ISSN: 0304-3843. DOI: 10.1007/s10751-016-1360-z. URL: http://link.springer.com/10.1007/s10751-016-1360-z.

[79] L A Zemnukhova, S I. Kuznetsov, and R L Davidovich. "209Bi NQR study of bismuth(III) complexes". In: *Russian Chemical Bulletin* 47.11 (1998), pp. 2169–2172. ISSN: 1066-5285. DOI: 10.1007/BF02494274. URL: http://link.springer.com/10.1007/BF02494274.

[80] Vadim S Grechishkin and Nikolai Ya Sinyavskii. "New technologies: nuclear quadrupole resonance as an explosive and narcotic detection technique". In: *Physics-Uspekhi* 40.4 (1997), pp. 393–406. ISSN: 1063-7869. DOI: 10.1070/PU1997v040n04ABEH000229. URL: http://stacks.iop.org/1063-7869/40/i=4/a=A04?key=crossref.64710d2e58dba1f28ea16d330e13b1a3.

[81] Jolanta N Latosinńska. "Applications of nuclear quadrupole resonance spectroscopy in drug development". In: *Expert Opinion on Drug Discovery* 2.2 (2007), pp. 225–248. ISSN: 1746-0441. DOI: 10.1517/17460441.2.2.225. URL: http://www.tandfonline.com/doi/full/10.1517/17460441.2.2.225.

[82] R. Blinc, T. Apih, and J. Seliger. "Nuclear quadrupole double resonance techniques for the detection of explosives and drugs". en. In: *Applied Magnetic Resonance* 25.3-4 (2004), pp. 523–534. ISSN: 0937-9347. DOI: 10.1007/BF03166546. URL: http://link.springer.com/10.1007/BF03166546.

[83] A.N. Garroway et al. "Remote sensing by nuclear quadrupole resonance". In: *IEEE Transactions on Geoscience and Remote Sensing* 39.6 (2001), pp. 1108–1118. ISSN: 01962892. DOI: 10.1109/36.927420. URL: http://ieeexplore.ieee.org/document/927420/.

[84] T N Rudakov, V T Mikhaltsevich, and O P Selchikhin. "The use of multi-pulse nuclear quadrupole resonance techniques for the detection of explosives containing rdx". In: *J.Phys-D-Appl.Phys.* 30.9 (1997), pp. 1377–1382.

[85] J. A. Lehmann-Horn, D. G. Miljak, and T. J. Bastow. "75As, 63Cu NMR and NQR characterization of selected arsenic minerals". In: *Solid State Nuclear Magnetic Resonance* 54 (2013), pp. 8–12. ISSN: 09262040. DOI: 10.1016/j.ssnmr.2013.05.001. URL: http://dx.doi.org/10.1016/j.ssnmr.2013.05.001.

[86] J. A. Lehmann-Horn et al. "Rapid detection of arsenic minerals using portable broadband NQR". en. In: *Geophysical Research Letters* 41.19 (2014), pp. 6765–6771. ISSN: 19448007. DOI: 10.1002/2014GL061386.

[87] T. J. Bastow, J. A. Lehmann-Horn, and D. G. Miljak. "121,123Sb and 75As NMR and NQR investigation of the tetrahedrite (Cu12Sb4S13) - Tennantite (Cu12As4S13) system and other metal arsenides". In: *Solid State Nuclear Magnetic Resonance* 71 (2015), pp. 55–60. ISSN: 09262040. DOI: 10.1016/j.ssnmr.2015.09.010. URL: http://dx.doi.org/10.1016/j.ssnmr.2015.09.010.

[88] R.R. Gainov et al. "Determination of the Local Crystal-Chemical Features of Complex Chalcogenides by Copper, Antimony, and Arsenic NQR". In: *Superconductor*. Vol. 4. Sciyo, 2010. DOI: 10.5772/46939. URL: http://www.intechopen.com/books/superconductor/determination-of-the-local-crystal-chemical-features-of-complex-chalcogenides-by-copper-antimony-and.

[89] Janez Seliger, Veselko Žagar, and Tetsuo Asaji. "NQR investigation and characterization of cocrystals and crystal polymorphs". In: *Hyperfine Interactions* 222.1-3 (2013), pp. 1–13. ISSN: 0304-3843. DOI: 10.1007/s10751-012-0665-9. URL: http://link.springer.com/10.1007/s10751-012-0665-9.

[90] Silvina C. Pérez et al. "Dynamic characterization of crystalline and glass phases of deuterated 1,1,2,2 tetrachloroethane". In: *Journal of Chemical Physics* 143.13 (2015). ISSN: 00219606. DOI: 10.1063/1.4931824. URL: http://dx.doi.org/10.1063/1.4931824.

[91] Hermann Scharfetter et al. "Aspects of structural order in 209 Bi-containing particles for potential MRI contrast agents based on quadrupole enhanced relaxation". In: *Molecular Physics* 8976 (2018), pp. 1–9. ISSN: 0026-8976. DOI: 10.1080/00268976.2018.1511869. URL: https://www.tandfonline.com/doi/full/10.1080/00268976.2018.1511869.

[92] Scharfetter et al. "Tris(2-Methoxyphenyl)Bismuthine Polymorphism Characterized by Nuclear Quadrupole Resonance Spectroscopy". In: *Crystals* 9.9 (2019), p. 446. ISSN: 2073-4352. DOI: 10.3390/cryst9090446. URL: https://www.mdpi.com/2073-4352/9/9/446.

[93] P. Dessovic et al. "229Thorium-doped calcium fluoride for nuclear laser spectroscopy". In: *Journal of Physics Condensed Matter* 26.10 (2014). ISSN: 09538984. DOI: 10.1088/0953-8984/26/10/105402.

[94] Danuta Kruk et al. "Model-free approach to quadrupole spin relaxation in solid 209 Bi-aryl compounds". In: *Physical Chemistry Chemical Physics* 20.36 (2018), pp. 23414–23423. ISSN: 1463-9076. DOI: 10.1039/C8CP03848A. URL: http://xlink.rsc.org/?DOI=C8CP03848A.

[95] A. Ohte et al. "Accurate calibration of a new NQR thermometer (203 K to 398 K range calibration at the NRLM)". In: *Metrologia* 15.4 (1979), pp. 195–199. ISSN: 00261394. DOI: 10.1088/0026-1394/15/4/004.

[96] Wangsness and Bloch. "The Dynamical Theory of Nuclear Induction". In: *Physical Review* 89.4 (1953).

[97] A.G. Redfield. "The Theory of Relaxation Processes". In: *Advances in Magnetic and Optical Resonance*. Vol. 1. C. 1965, pp. 1–32. ISBN: 1057-2732. DOI: 10.1016/B978-1-4832-3114-3.50007-6. URL: http://linkinghub.elsevier.com/retrieve/pii/B9781483231143500076https://linkinghub.elsevier.com/retrieve/pii/B9781483231143500076.

[98] Alfred G Redfield. "Relaxation Theory: Density Matrix Formulation". In: *Encyclopedia of Magnetic Resonance*. Major Reference Works. Chichester, UK: John Wiley & Sons, Ltd, 2007. ISBN: 9780470034590. DOI: 10.1002/9780470034590.emrstm0463. URL: https://doi.org/10.1002/9780470034590.emrstm0463http://doi.wiley.com/10.1002/9780470034590.emrstm0463.

[99] J.C. Slater. *Introduction to chemical physics*. Internatio. McGraw-Hill Book Company, Inc., 1939, p. 521. DOI: 10.1002/jctb.5000591106. URL: http://doi.wiley.com/10.1002/jctb.5000591106.

[100] Maurice Goldman. "Formal Theory of Spin-Lattice Relaxation". In: *Journal of Magnetic Resonance* 149.2 (2001), pp. 160–187. ISSN: 10907807. DOI: 10.1006/jmre.2000.2239.

[101] Anatole Abragam and L. C. Hebel. "The Principles of Nuclear Magnetism". In: *American Journal of Physics* 29.12 (1961), pp. 860–861. ISSN: 0002-9505. DOI: 10.1119/1.1937646. URL: http://aapt.scitation.org/doi/10.1119/1.1937646.

[102] Danuta Kruk. *Understanding Spin Dynamics*. Jenny Stanford Publishing, 2015, p. 260. ISBN: 9780429090738. DOI: 10.1201/b19179. URL: https://www.taylorfrancis.com/books/9789814463508.

[103] Zhi-Yi Chen et al. "Advance of Molecular Imaging Technology and Targeted Imaging Agent in Imaging and Therapy". eng. In: *BioMed Research International* 2014 (2014), pp. 1–12. ISSN: 2314-6133. DOI: 10.1155/2014/819324. URL: http://www.hindawi.com/journals/bmri/2014/819324/.

[104] Gemma-Louise Davies, Iris Kramberger, and Jason J. Davis. "Environmentally responsive MRI contrast agents". In: *Chemical Communications* 49.84 (2013), p. 9704. ISSN: 1359-7345. DOI: 10.1039/c3cc44268c. URL: http://xlink.rsc.org/?DOI=c3cc44268c.

[105] K.M Ward, A.H Aletras, and R.S Balaban. "A New Class of Contrast Agents for MRI Based on Proton Chemical Exchange Dependent Saturation Transfer (CEST)". In: *Journal of Magnetic Resonance* 143.1 (2000), pp. 79–87. ISSN: 10907807. DOI: 10.1006/jmre.1999.1956. URL: http://linkinghub.elsevier.com/retrieve/pii/S1090780799919560.

[106] P van Zijl and NN Yadav. "Chemical exchange saturation transfer (CEST): what is in a name and what isn't?" In: *Magnetic Resonance in Medicine* 65.4 (2011), pp. 927–948. DOI: 10.1002/mrm.22761.Chemical. URL: http://onlinelibrary.wiley.com/doi/10.1002/mrm.22761/full.

[107] F Winter and R Kimmich. "Spin lattice relaxation of dipole nuclei (I = 1/2) coupled to quadrupole nuclei (S = 1)". In: *Molecular Physics* 45.1 (1982), pp. 33–49. ISSN: 0026-8976. DOI: 10.1080/00268978200100031. URL: http://dx.doi.org/10.1080/00268978200100031.

[108] Erik P. Sunde and Bertil Halle. "Mechanism of 1H-14N cross-relaxation in immobilized proteins". In: *Journal of Magnetic Resonance* 203.2 (2010), pp. 257–273. ISSN: 10907807. DOI: 10.1016/j.jmr.2010.01.008. URL: http://dx.doi.org/10.1016/j.jmr.2010.01.008.

[109] P. O. Westlund. "Theoretical reason for the lack of influence of 1H- 14N cross-relaxation on the water proton T 1 NMRD profile in slow tumbling proteins". In: *Molecular Physics* 110.18 (2012), pp. 2251–2255. ISSN: 00268976. DOI: 10.1080/00268976.2012.674566.

[110] Chad T. Harris et al. "Development and optimization of hardware for delta relaxation enhanced MRI". In: *Magnetic Resonance in Medicine* 72.4 (2014), pp. 1182–1190. ISSN: 15222594. DOI: 10.1002/mrm.25014.

[111] Jamu K. Alford et al. "Delta relaxation enhanced mr: Improving activation - Speeificity of molecular probes through R 1 dispersion imaging". In: *Magnetic Resonance in Medicine* 61.4 (2009), pp. 796–802. ISSN: 07403194. DOI: 10.1002/mrm.21933.

[112] Uvo Christoph Hoelscher et al. "Quantification and localization of contrast agents using delta relaxation enhanced magnetic resonance at 1.5 T". In: *Magnetic Resonance Materials in Physics, Biology and Medicine* 25.3 (2012), pp. 223–231. ISSN: 09685243. DOI: 10.1007/s10334-011-0291-6.

[113] Yonathan T. Araya et al. "Nuclear magnetic relaxation dispersion of murine tissue for development of T 1 (R 1) dispersion contrast imaging". In: *NMR in Biomedicine* 30.12 (2017), e3789. ISSN: 09523480. DOI: 10.1002/nbm.3789. URL: http://doi.wiley.com/10.1002/nbm.3789.

[114] G G Briand and N Burford. "Bismuth compounds and preparations with biological or medicinal relevance". In: *Chemical Reviews* 99.9 (1999), pp. 2601–2657. ISSN: 1520-6890. DOI: 10.1021/cr980425s.

[115] Oded Rabin et al. "An X-ray computed tomography imaging agent based on long-circulating bismuth sulphide nanoparticles". en. In: *Nature Materials* 5.2 (2006), pp. 118–122. ISSN: 1476-1122. DOI: 10.1038/nmat1571. URL: http://www.nature.com/articles/nmat1571.

[116] A. Brown. "Bismuth Nanoparticles as Medical X-ray Contrast Agents: Synthesis, Characterization and Applications". In: *Dissertations Thesis* (2013).

[117] Pratap C. Naha et al. "Dextran coated bismuth-iron oxide nanohybrid contrast agents for computed tomography and magnetic resonance imaging". In: *J. Mater. Chem. B* 2.46 (2014), pp. 8239–8248. ISSN: 2050-750X. DOI: 10.

1039/C4TB01159G. arXiv: NIHMS150003. URL: http://xlink.rsc.org/?DOI=C4TB01159G.

[118] Ryogo Kubo. "Stochastic Liouville Equations". In: *Journal of Mathematical Physics* 4.2 (1963), pp. 174–183. ISSN: 0022-2488. DOI: 10.1063/1.1703941. URL: http://aip.scitation.org/doi/10.1063/1.1703941.

[119] Per-Olof Westlund and Håkan Wennerstrom. "Spin-lattice relaxation of a nucleus coupled to a quadrupolar spin-1 nucleus. The quadrupolar dip". In: *Journal of Magnetic Resonance* 63.2 (1985), pp. 280–286. ISSN: 00222364. DOI: 10.1016/0022-2364(85)90317-8. URL: http://linkinghub.elsevier.com/retrieve/pii/0022236485903178.

[120] G.K. Semin. "On solving secular equations for half-interger spins (I=5/2, 7/2, and 9/2)". In: *Russian Journal of Physical Chemistry* 81.1 (2007), pp. 38–46. ISSN: 0036-0244. DOI: 10.1134/S0036024407010104.

[121] Michael A. Mcguigan. "Chronic Poisoning". In: *Goldman's Cecil Medicine*. Elsevier, 2012. Chap. 21, pp. 88–95. DOI: 10.1016/B978-1-4377-1604-7.00021-X. URL: http://linkinghub.elsevier.com/retrieve/pii/B978143771604700021Xhttps://linkinghub.elsevier.com/retrieve/pii/B978143771604700021X.

[122] Samuel Karelitz and Aaron D Freedman. "Hepatitis and nephrosis due to soluble bismuth". In: *Pediatrics* 8.6 (1951), 772 LP –777. URL: http://pediatrics.aappublications.org/content/8/6/772.abstract.

[123] Y. Fujiwara et al. "An Organobismuth Compound that Exhibits Selective Cytotoxicity to Vascular Endothelial Cells in vitro". In: *Journal of Health Science* 51.3 (2005), pp. 333–340. ISSN: 1344-9702. DOI: 10.1248/jhs.51.333.

[124] Walter Robinson, H. G. and Dehmelt, H. G. and Gordy. "Pure Nuclear Quadrupole Spectrum of Bi209 in Bismuth-Triphenyl". In: *Physical Review* 89 (1952), p. 1305. URL: https://journals.aps.org/pr/abstract/10.1103/PhysRev.89.1305.

[125] J. Weaver and F. N.H. Robinson. "Nuclear quadrupole resonance of bismuth and the quadrupole Hamiltonian". In: *Physics Letters A* 85.6-7 (1981), p. 389. ISSN: 03759601. DOI: 10.1016/0375-9601(81)90339-X.

[126] T. B. Brill and G. G. Long. "Studies of Pentavalent Organoarsenic, -antimony, and -bismuth Halide Compounds by Nuclear Quadrupole Resonance Spectroscopy". In: *Inorganic Chemistry* 9.9 (1970), pp. 1980–1985. ISSN: 1520510X. DOI: 10.1021/ic50091a005.

[127] R. F. van der Kelen, G. P., de Ketelaere. "Organo group VB chemistry . Part IV : On the NQR spectra of tertiary aryl groub VB compounds (35Cl, 75As,121Sb,209Bi)". In: *Journal of Molecular Structure* 23 (1974), pp. 329–335.

[128] Eddy SM Lee et al. "Next Generation Delta Relaxation Enhanced MRI with 0.36T ΔB". In: *Proc. Intl. Soc. Mag. Reson. Med.* 20 (2012), p. 2877.

[129] Markus Bödenler et al. "R 1 dispersion contrast at high field with fast field-cycling MRI". In: *Journal of Magnetic Resonance* 290 (2018), pp. 68–75. ISSN: 10907807. DOI: 10.1016/j.jmr.2018.03.010. URL: http://linkinghub.elsevier.com/retrieve/pii/S1090780718300934https://linkinghub.elsevier.com/retrieve/pii/S1090780718300934.

[130] David M. Hawley and George Ferguson. "The Stereochemistry of Some Organic Derivatives of Group VB Elements. Part ll. The Crystal and Molecular Structure of Triphenylbismuth Dichloride". In: *J. Chem. Soc. A* (1968).

[131] Oliver Schuster, Annette Schier, and Hubert Schmidbaur. "The Quest for Complexes with a Coordinative Gold - Bismuth Bond". In: 11 (2003), pp. 4079–4083.

[132] Alarich Weiss and Silvia Wigand. "Correlation of NQR and Chemical Bond Parameter". In: *Zeitschrift fur Naturforschung - Section A Journal of Physical Sciences* 45.3-4 (1990), pp. 195–212. ISSN: 18657109. DOI: 10.1515/zna-1990-3-403.

[133] Perttu Lantto and Juha Vaara. "Calculations of nuclear quadrupole coupling in noble gas-noble metal fluorides: Interplay of relativistic and electron correlation effects". In: *Journal of Chemical Physics* 125.17 (2006). ISSN: 00219606. DOI: 10.1063/1.2363371.

[134] Michal Straka et al. "Theoretical predictions of nuclear magnetic resonance parameters in a novel organo-xenon species: Chemical shifts and nuclear quadrupole couplings in HXeCCH". In: *Journal of Chemical Physics* 127.23 (2007). ISSN: 00219606. DOI: 10.1063/1.2805389.

[135] Leonardo Belpassi et al. "Nuclear electric quadrupole moment of gold". In: *Journal of Chemical Physics* 126.6 (2007). ISSN: 00219606. DOI: 10.1063/1.2436881.

[136] Lan Cheng, Stella Stopkowicz, and Jürgen Gauss. "Spin-free Dirac-Coulomb calculations augmented with a perturbative treatment of spin-orbit effects at the Hartree-Fock level". In: *Journal of Chemical Physics* 139.21 (2013). ISSN: 00219606. DOI: 10.1063/1.4832739.

[137] Avijit Shee, Lucas Visscher, and Trond Saue. "Analytic one-electron properties at the 4-component relativistic coupled cluster level with inclusion of spin-orbit coupling". In: *Journal of Chemical Physics* 145.18 (2016). ISSN: 00219606. DOI: 10.1063/1.4966643.

[138] Lan Cheng and Jürgen Gauss. "Perturbative treatment of spin-orbit coupling within spin-free exact two-component theory". In: *The Journal of Chemical Physics* 141.16 (2014), p. 164107. ISSN: 0021-9606. DOI: 10.1063/1.4897254. URL: http://aip.scitation.org/doi/10.1063/1.4897254.

[139] Juho Roukala et al. "Experimental and First-Principles NMR Analysis of Pt(II) Complexes with O,O-Dialkyldithiophosphate Ligands". In: *Journal of Physical Chemistry A* 120.42 (2016), pp. 8326–8338. ISSN: 15205215. DOI: 10.1021/acs.jpca.6b09586.

[140] R.J.F. Berger et al. "Relativistic effects in triphenylbismuth and their influence on molecular structure and spectroscopic properties". In: *Physical Chemistry Chemical Physics* 14.44 (2012), pp. 15520–15524. ISSN: 14639076. DOI: 10.1039/c2cp43471g.

[141] Erik Van Lenthe and Evert Jan Baerends. "Density functional calculations of nuclear quadrupole coupling constants in the zero-order regular approximation for relativistic effects". In: *Journal of Chemical Physics* 112.19 (2000), pp. 8279–8292. ISSN: 00219606. DOI: 10.1063/1.481433.

[142] Lucas Visscher and Erik van Lenthe. "On the distinction between scalar and spin–orbit relativistic effects". In: *Chemical Physics Letters* 306.5-6 (1999), pp. 357–365. ISSN: 00092614. DOI: 10.1016/S0009-2614(99)00458-3. URL: http://www.sciencedirect.com/science/article/pii/S0009261499004583.

[143] Kenneth G. Dyall. "An exact separation of the spin-free and spin-dependent terms of the Dirac-Coulomb-Breit Hamiltonian". In: *The Journal of Chemical Physics* 100.3 (1994), pp. 2118–2127. ISSN: 0021-9606. DOI: 10.1063/1.466508. URL: http://aip.scitation.org/doi/10.1063/1.466508.

[144] Oleg V. Yazyev and Lothar Helm. "Nuclear Spin Relaxation Parameters of MRI Contrast Agents - Insight from Quantum Mechanical Calculations". In: *European Journal of Inorganic Chemistry* 2008.2 (2008), pp. 201–211. ISSN: 14341948. DOI: 10.1002/ejic.200701013. URL: http://doi.wiley.com/10.1002/ejic.200701013.

[145] Taray N Rudakov. "Nuclear Quadrupole Resonance, Instruments". In: *Encyclopedia of Spectroscopy and Spectrometry*. Elsevier Ltd., 2010, pp. 1966–1974.

[146] R R Gainov et al. "Determination of the Local Crystal-Chemical Features of Complex Chalcogenides by Copper , Antimony , and Arsenic NQR". In: 4 (2009).

[147] J.A. Lehmann-Horn et al. "75As NQR studies on FeAs2". In: *Solid State Nuclear Magnetic Resonance* 71 (2015), pp. 87–90. ISSN: 09262040. DOI: 10.1016/j.ssnmr.2015.07.002. URL: http://linkinghub.elsevier.com/retrieve/pii/S0926204015300084.

[148] G. Koutroulakis et al. "Extended nuclear quadrupole resonance study of the heavy-fermion superconductor PuCoGa5". In: *Physical Review B* 94.16 (2016), p. 165115. ISSN: 2469-9950. DOI: 10.1103/PhysRevB.94.165115. URL: http://link.aps.org/doi/10.1103/PhysRevB.94.165115.

[149] A.p. Reyes et al. "209Bi NMR and NQR investigation of the small-gap semiconductor Ce3Bi4Pt3". In: *Phys. Rev. B* 49.23 (1994).

[150] N. Sinyavsky, E. Korotey, and M. Maćkowiak. "Determination of the electric field gradient asymmetry from Berry's phase in NQR of powder samples". In: *Journal of Molecular Structure* 830.1-3 (2007), pp. 131–138. ISSN: 00222860. DOI: 10.1016/j.molstruc.2006.07.009.

[151] Hirokazu Nakayama, Taro Eguchi, and Nobuo Nakamura. "Phase Transitions in 4,4'-Dichlorobenzophenone as Studied by 3 SC1FT-NQR *". In: *Zeitschrift fur Naturforschung - Section A Journal of Physical Sciences* 2.49a (1994), pp. 267–272.

[152] Hermann Scharfetter. "An electronically tuned wideband probehead for NQR spectroscopy in the VHF range". In: *Journal of Magnetic Resonance* 271.August (2016), pp. 90–98. ISSN: 10907807. DOI: 10.1016/j.jmr.2016.08.008. URL: http://dx.doi.org/10.1016/j.jmr.2016.08.008.

[153] Hermann Scharfetter, Markus Bödenler, and Dominik Narnhofer. "A cryostatic, fast scanning, wideband NQR spectrometer for the VHF range". In: *Journal of Magnetic Resonance* 286 (2018), pp. 148–157. ISSN: 10907807. DOI: 10.1016/j.jmr.2017.12.004. URL: http://linkinghub.elsevier.com/retrieve/pii/S1090780717302963.

[154] C. J. Pickard et al. "First principles methods using CASTEP". In: *Zeitschrift für Kristallographie* 220 (2005), pp. 567–570.

[155] P. Jones, A. Blaschette, and D. Henschel. "Redetermination of the crystal structure of triphenylbismuth, (C6H5)3Bi". In: *Zeitschrift für Kristallographie* 210.5 (1995). DOI: https://doi.org/10.1524/zkri.1995.210.5.377.

[156] Alexandre Tkatchenko and Matthias Scheffler. "Accurate molecular van der Waals interactions from ground-state electron density and free-atom reference data". In: *Physical Review Letters* 102.7 (2009), pp. 6–9. ISSN: 00319007. DOI: 10.1103/PhysRevLett.102.073005.

[157] David Vanderbilt. "Soft self-consistent pseudopotentials in a generalized eigenvalue formalism". In: *Physical Review B* 41.11 (1990), pp. 7892–7895. ISSN: 01631829. DOI: 10.1103/PhysRevB.41.7892. arXiv: arXiv:1011.1669v3.

[158] *ADF2017, SCM, Theoretical Chemistry, Vrije Universiteit, Amsterdam, The Netherlands*, URL: http://www.scm.com.

[159] Célia Fonseca Guerra et al. "Towards an order-N DFT method". In: *Theoretical Chemistry Accounts* 99 (1998), pp. 391–403. ISSN: 1432-881X. DOI: 10.1007/s002149800m26.

[160] G.te Velde et al. "Chemistry with ADF". In: *Journal of Computational Chemistry* 22.931 (2001).

[161] John P. Perdew, Kieron Burke, and Matthias Ernzerhof. "Generalized Gradient Approximation Made Simple". In: *Physical Review Letters* 77.18 (1996), pp. 3865–3868. ISSN: 0031-9007. DOI: 10.1103/PhysRevLett.77.3865. arXiv: 0927-0256(96)00008 [10.1016]. URL: https://link.aps.org/doi/10.1103/PhysRevLett.77.3865.

[162] Matthias Ernzerhof and Gustavo E. Scuseria. "Assessment of the Perdew-Burke-Ernzerhof exchange-correlation functional". In: *The Journal of Chemical Physics* 110.11 (1999), pp. 5029–5036. ISSN: 0021-9606. DOI: 10.1063/1.478401. URL: http://aip.scitation.org/doi/10.1063/1.478401.

[163] Carlo Adamo and Vincenzo Barone. "Toward reliable density functional methods without adjustable parameters: The PBE0 model". In: *J. Chem. Phys.* 110.13 (1999).

[164] H. J. Aa. Jensen et al. *DIRAC, a relativistic ab initio electronic structure program, Release DIRAC16 (2016)*. 2016. URL: http://www.diracprogram.org.

[165] E. Van Lenthe and E. J. Baerends. "Optimized Slater-type basis sets for the elements 1-118". In: *Journal of Computational Chemistry* 24.9 (2003), pp. 1142–1156. ISSN: 01928651. DOI: 10.1002/jcc.10255.

[166] Thom H. Dunning. "Gaussian basis sets for use in correlated molecular calculations. I. The atoms boron through neon and hydrogen". In: *The Journal of Chemical Physics* 90.2 (1989), pp. 1007–1023. ISSN: 00219606. DOI: 10.1063/1.456153.

[167] Tiago Quevedo Teodoro, Albérico Borges Ferreira Da Silva, and Roberto Luiz Andrade Haiduke. "Relativistic prolapse-free gaussian basis set of quadruple-ζ quality: (aug-)RPF-4Z. II. The d-block elements". In: *Journal of Chemical Theory and Computation* 10.11 (2014), pp. 4761–4764. ISSN: 15499626. DOI: 10.1021/ct500804j.

[168] Jacek Bieroń and Pekka Pyykkö. "Nuclear quadrupole moments of bismuth". In: *Physical Review Letters* 87.13 (2001), pp. 133003/1–133003/4. ISSN: 00319007. DOI: 10.1103/PhysRevLett.87.133003.

[169] Malcolm H. Levitt. *Spin Dynamics: Basics of Nuclear Magnetic Resonance*. Second Edi. Wiley, 2007, p. 740. ISBN: 978-0-470-51117-6.

[170] Ahmad Luqman et al. "The Importance of Heterolepticity in Improving the Antibacterial Activity of Bismuth(III) Thiolates". In: *European Journal of Inorganic Chemistry* 2016.17 (2016), pp. 2738–2749. ISSN: 10990682. DOI: 10.1002/ejic.201600076.

[171] Hitomi Suzuki et al. *Organobismuth Chemistry*. Amsterdam: Elsevier Science, 2001, p. 636. ISBN: 9780444205285.

[172] Martin Hébert et al. "Synthesis of highly functionalized triarylbismuthines by functional group manipulation and use in palladium- and copper-catalyzed arylation reactions". In: *Journal of Organic Chemistry* 81.13 (2016), pp. 5401–5416. ISSN: 15206904. DOI: 10.1021/acs.joc.6b00767.

[173] Abdi Hassan et al. " Organobismuth(III) and Organobismuth(V) Complexes Containing Pyridyl and Amino Functional Groups. Syntheses and Characterizations of Bi III Ar 3 (Ar = p -C 6 H 4 (NMe 2), p -C 6 H 4 CH 2 (NPr i 2), p -C 6 H 4 [CH 2 N(2-Py) 2]), Bi V Ar 3 L 2 , [Bi V A". In: *Organometallics* 15.26 (1996), pp. 5613–5621. ISSN: 0276-7333. DOI: 10.1021/om960641w.

[174] Jay P. Parrish et al. "Establishing the Parabolic Relationship between Reactivity and Activity for Derivatives and Analogues of the Duocarmycin and CC-1065 Alkylation Subunits". In: *Journal of the American Chemical Society* 126.1 (2004), pp. 80–81. ISSN: 0002-7863. DOI: 10.1021/ja038162t. URL: http://pubs.acs.org/doi/abs/10.1021/ja038162t.

[175] Vladimir Sharutin. "CCDC 929897: Experimental Crystal Structure Determination". In: *CSD Communication* ||| (2016). DOI: 10.5517/ccdc.csd.cc106mpj.

[176] Wiliam Levason, Baharrudin Sheikh, and Francis P McCullough. "The synthesis and properties of substituted tertiary bismuthine ligands". In: *Journal of Coordination Chemistry* 12.1 (1982), pp. 53–57. ISSN: 0095-8972. DOI: 10.1080/00958978208075842. URL: http://dx.doi.org/10.1080/00958978208075842.

[177] T Ogawa et al. "Enhanced Nucleophilicity of Tris-(2,6-dimethoxyphenyl) bismuthane as Studied by X-ray Crystallography, 170 NM". In: *J. Chem. Soc. Perkin Trans.* 1 (1994), pp. 3479–3483.

[178] A. F.M.Mustafizur Rahman et al. "Effect of π-accepting substituent on the reactivity and spectroscopic characteristics of triarylbismuthanes and triarylbismuth dihalides". In: *Journal of Organometallic Chemistry* 689.21 (2004), pp. 3395–3401. ISSN: 0022328X. DOI: 10.1016/j.jorganchem.2004.07.055.

[179] Christian Gösweiner et al. "Predicting quadrupole relaxation enhancement peaks in proton R 1 -NMRD profiles in solid Bi-aryl compounds from NQR parameters". In: *Molecular Physics* 8976 (2018), pp. 1–11. ISSN: 0026-8976. DOI: 10.1080/00268976.2018.1519201. URL: https://www.tandfonline.com/doi/full/10.1080/00268976.2018.1519201.

[180] Franz Fujara, Danuta Kruk, and Alexei F. Privalov. "Solid state Field-Cycling NMR relaxometry: Instrumental improvements and new applications". In: *Progress in Nuclear Magnetic Resonance Spectroscopy* 82 (2014), pp. 39–69. ISSN: 00796565. DOI: 10.1016/j.pnmrs.2014.08.002. URL: http://dx.doi.org/10.1016/j.pnmrs.2014.08.002http://linkinghub.elsevier.com/retrieve/pii/S0079656514000594.

[181] F. Noack. "NMR field-cycling spectroscopy: principles and a]lications". In: *Progress in Nuclear Magnetic Resonance Spectroscopy* 18.3 (1986), pp. 171–276. ISSN: 00796565. DOI: 10.1016/0079-6565(86)80004-8.

[182] O. Lips et al. "Simultaneous effects of relaxation and polarization transfer in LaF3-type crystals as sources of dynamic information". In: *Solid State Nuclear Magnetic Resonance* 31.3 (2007), pp. 141–152. ISSN: 09262040. DOI: 10.1016/j.ssnmr.2007.04.002.

[183] F. Bonetto, E. Anoardo, and R. Kimmich. "Ultrasound-order director fluctuations interaction in nematic liquid crystals: A nuclear magnetic resonance relaxometry study". In: *The Journal of Chemical Physics* 118.19 (2003), pp. 9037–9043. ISSN: 0021-9606. DOI: 10.1063/1.1566735. URL: http://aip.scitation.org/doi/10.1063/1.1566735.

[184] Eberhard Rommel et al. "Proton spin relaxation dispersion studies of phospholipid membranes". In: *The Journal of Physical Chemistry* 92.10 (1988), pp. 2981–2987. ISSN: 0022-3654. DOI: 10.1021/j100321a053. URL: http://pubs.acs.org/doi/abs/10.1021/j100321a053.

[185] N. Fatkullin, R. Kimmich, and H. W. Weber. "Spin-lattice relaxation of polymers: The memory-function formalism". In: *Physical Review E* 47.6 (1993), pp. 4600–4603. ISSN: 1063651X. DOI: 10.1103/PhysRevE.47.4600.

[186] S. Stapf et al. "Proton and deuteron field-cycling NMR relaxometry of liquids confined in porous glasses". In: *Colloids and Surfaces A: Physicochemical and Engineering Aspects* 115.15 (1996), pp. 107–114. ISSN: 09277757. DOI: 10.1016/0927-7757(96)03610-2.

[187] D. Kruk et al. "Analysis of1H-14N polarization transfer experiments in molecular crystals". In: *Journal of Physics Condensed Matter* 17.3 (2005), pp. 519–533. ISSN: 09538984. DOI: 10.1088/0953-8984/17/3/011.

[188] M Nolte et al. "H-1-N-14 cross-relaxation in trinitrotoluene - a step toward improved landmine detection". In: *J.Phys.D, Appl.Phys.* 35.9 (2002), pp. 939–942. ISSN: 00223727. DOI: 10.1088/0022-3727/35/9/317.

[189] R. Kimmich, W. Nusser, and F. Winter. "In vivo NMR field-cycling relaxation spectroscopy reveals 14N1H relaxation sinks in the backbones of proteins". In: *Plasma Sources Science and Technology* 29.5 (1984), pp. 593–596. ISSN: 00319155. DOI: 10.1088/0031-9155/29/5/011.

[190] Christian Gösweiner, Per-olof Westlund, and Hermann Scharfetter. "Spin–spin relaxation of nuclear quadrupole resonance coherences and the important role of degenerate energy levels". In: *Molecular Physics* 8976 (2020), e1743888. ISSN: 0026-8976. DOI: 10.1080/00268976.2020.1743888. URL: https://doi.org/10.1080/00268976.2020.1743888https://www.tandfonline.com/doi/full/10.1080/00268976.2020.1743888.

[191] Rainer Kimmich. *NMR*. Berlin, Heidelberg: Springer Berlin Heidelberg, 1997. ISBN: 978-3-642-64465-8. DOI: 10.1007/978-3-642-60582-6. URL: http://link.springer.com/10.1007/978-3-642-60582-6.

[192] James McConnell. *The theory of nuclear magnetic relaxation in liquids*. Cambridge: Cambridge University Press, 1987, p. 196. ISBN: 9780521321129.

[193] J. Van Kranendonk. "Theory of quadrupolar nuclear spin-lattice relaxation". In: *Physica* 20.7-12 (1954), pp. 781–800. ISSN: 00318914. DOI: 10.1016/S0031-8914(54)80191-1. URL: http://www.sciencedirect.com/science/article/pii/S0031891454801911.

[194] D. E. Woessner and H. S. Gutowsky. "Nuclear pure quadrupole relaxation and its temperature dependence in solids". In: *The Journal of Chemical Physics* 39.2 (1963), pp. 440–456. ISSN: 00219606. DOI: 10.1063/1.1734268.

[195] J. Van Kranendonk and M. Walker. "Theory of quadrupolar nuclear spin-lattice relaxation due to anharmonic Raman phonon processes". In: *Physical Review Letters* 18.17 (1967), pp. 701–703. ISSN: 00319007. DOI: 10.1103/PhysRevLett.18.701.

[196] R. C. Zamar and C. E. González. "Nuclear quadrupole spin-lattice relaxation in anharmonic molecular crystals". In: *Physical Review B* 51.2 (1995), pp. 932–944. ISSN: 0163-1829. DOI: 10.1103/PhysRevB.51.932. URL: https://link.aps.org/doi/10.1103/PhysRevB.51.932.

[197] Tadashi Tokuhiro. "Effect of hindered rotation on the nuclear quadrupole resonance frequency and the linewidth in trans-1,2-dichloroethane". In: *The Journal of Chemical Physics* 41.2 (1964), pp. 438–444. ISSN: 00219606. DOI: 10.1063/1.1725885.

[198] L. Pang and M. A. Whitehead. "Impurity effect on the 14 N NQR of a polycrystalline ferroelectric Na 1-x K x No 2". In: *Ferroelectrics* 139.1 (1993), pp. 51–55. ISSN: 0015-0193. DOI: 10.1080/00150199308017726. URL: http://www.tandfonline.com/doi/abs/10.1080/00150199308017726.

[199] Janez Seliger, Veselko Žagar, and Tetsuo Asaji. "NQR investigation and characterization of cocrystals and crystal polymorphs". In: *Hyperfine Interactions* 222.1-3 (2013), pp. 1–13. ISSN: 03043843. DOI: 10.1007/s10751-012-0665-9.

[200] N. Sinyavsky, P. Dolinenkov, and G. Kupriyanova. "The T1and T2Relaxation Times Distribution for the35Cl and14N NQR in Micro-composites and in Porous Materials". In: *Applied Magnetic Resonance* 45.5 (2014), pp. 471–482. ISSN: 09379347. DOI: 10.1007/s00723-014-0533-7.

[201] Alan Gregorovič. "14 N NQR lineshape in nanocrystals: An ab initio investigation of urea". In: *The Journal of Chemical Physics* 146.19 (2017), p. 194306. ISSN: 0021-9606. DOI: 10.1063/1.4983484. URL: http://aip.scitation.org/doi/10.1063/1.4983484.

[202] Per-Olof Westlund, Nikolas Benetis, and Håkan Wennerström. "Paramagnetic proton nuclear magnetic relaxation in the Ni 2+ hexa-aquo complex". In: *Molecular Physics* 61.1 (1987), pp. 177–194. ISSN: 0026-8976. DOI: 10.1080/00268978700101061. URL: http://www.tandfonline.com/doi/abs/10.1080/00268978700101061.

[203] Salvatore Califano, Vincenzo Schettino, and Natale Neto. *Lattice Dynamics of Molecular Crystals*. Vol. 26. Lecture Notes in Chemistry. Berlin, Heidelberg: Springer Berlin Heidelberg, 1981. ISBN: 978-3-540-10868-9. DOI: 10.1007/978-3-642-93186-4. URL: http://link.springer.com/10.1007/978-3-642-93186-4.

[204] Luca Catalano and Panče Naumov. "Exploiting rotational motion in molecular crystals". In: *CrystEngComm* 20.39 (2018), pp. 5872–5883. ISSN: 14668033. DOI: 10.1039/c8ce00420j.

[205] H. L. Friedman, M. Holz, and H. G. Hertz. "EPR relaxations of aqueous Ni2+ ion". In: *The Journal of Chemical Physics* 70.7 (1979), pp. 3369–3383. ISSN: 00219606. DOI: 10.1063/1.437922.

[206] Alexander J. Vega and Daniel Fiat. "Relaxation theory and the stochastic Liouville equation". In: *Journal of Magnetic Resonance (1969)* 19.1 (1975), pp. 21–30. ISSN: 00222364. DOI: 10.1016/0022-2364(75)90024-4.

[207] Nicola Salvi. *Dynamic Studies Through Control of Relaxation in NMR Spectroscopy*. Springer Theses. Cham: Springer International Publishing, 2014. ISBN: 978-3-319-06169-6. DOI: 10.1007/978-3-319-06170-2. URL: http://link.springer.com/10.1007/978-3-319-06170-2.

[208] Per-Olof Westlund and Håkan Wennerström. "NMR lineshapes of and nuclei. Chemical exchange effects and dynamic shifts". In: *Journal of Magnetic Resonance (1969)* 50.3 (1982), pp. 451–466. ISSN: 00222364. DOI: 10.1016/0022-2364(82)90008-7. URL: https://linkinghub.elsevier.com/retrieve/pii/0022236482900087.

[209] M. Rubinstein, A. Baram, and Z. Luz. "Electronic and nuclear relaxation in solutions of transition metal ions with spin s= 3/2 and 5/2". In: *Molecular Physics* 20.1 (1971), pp. 67–80. ISSN: 13623028. DOI: 10.1080/00268977100100081.

[210] Donald E. Woessner. "Brownian Motion and Correlation Times". In: *Encyclopedia of Magnetic Resonance*. Chichester, UK: John Wiley & Sons, Ltd, 2007. ISBN: 9780470034590. DOI: 10.1002/9780470034590.emrstm0047. URL: http://doi.wiley.com/10.1002/9780470034590.emrstm0047.

[211] Eugene Paul Wigner. *Gruppentheorie und ihre Anwendung auf die Quantenmechanik der Atomspektren*. Braunschweig: Friedr. Vieweg und Sohn Akt.-Ges., 1931, p. 332. ISBN: 3 528 08353X.

[212] Matteus Lindgren, Aatto Laaksonen, and Per Olof Westlund. "A theoretical spin relaxation and molecular dynamics simulation study of the Gd(H2O)93+ complex". In: *Physical Chemistry Chemical Physics* 11.44 (2009), pp. 10368–10376. ISSN: 14639076. DOI: 10.1039/b907099k.

[213] Christian Bengs and Malcolm H. Levitt. "SpinDynamica: Symbolic and numerical magnetic resonance in a Mathematica environment". In: *Magnetic Resonance in Chemistry* 56.6 (2018), pp. 374–414. ISSN: 1097458X. DOI: 10.1002/mrc.4642.

[214] JOHN CAVANAGH et al. "Relaxation and Dynamic Processes". In: *Protein NMR Spectroscopy* (2007), pp. 333–404. DOI: 10.1016/b978-012164491-8/50007-5.

[215] P.T. Eles and C.A. Michal. "Two-photon excitation in nuclear quadrupole resonance". In: *Chemical Physics Letters* 376.3-4 (2003), pp. 268–273. ISSN: 00092614. DOI: 10.1016/S0009-2614(03)00969-2. URL: https://linkinghub.elsevier.com/retrieve/pii/S0009261403009692.

[216] Philip T. Eles and Carl A. Michal. "Crossed-coil detection of two-photon excited nuclear quadrupole resonance". In: *Journal of Magnetic Resonance* 175.2 (2005), pp. 201–209. ISSN: 10907807. DOI: 10.1016/j.jmr.2005.04.006. URL: https://linkinghub.elsevier.com/retrieve/pii/S1090780705001291.

[217] Lawrence G. Werbelow and David M. Grant. "Intramolecular Dipolar Relaxation in Multispin Systems". In: *Advances in Magnetic and Optical Resonance* 9.C (1977), pp. 189–299. ISSN: 10572732. DOI: 10.1016/B978-0-12-025509-2.50008-7.

[218] A. Abragam and K. Kambe. "Dipolar Broadening of the Quadrupole Resonance Line Width in Zero Applied Field". In: *Physical Review* 91.4 (1953), pp. 894–897. ISSN: 0031-899X. DOI: 10.1103/PhysRev.91.894. URL: https://link.aps.org/doi/10.1103/PhysRev.91.894.

[219] S. N. Popov. "35Cl nuclear quadrupole resonance and the macroscopic superstructure in Hg2Cl2 crystal". In: *Physics of the Solid State* 39.7 (2002), pp. 1143–1146. ISSN: 1063-7834. DOI: 10.1134/1.1130032.

[220] Nirvana B. Caballero et al. "Molecular kinetics of solid and liquid CHCl3". In: *Chemical Physics Letters* 585 (2013), pp. 69–73. ISSN: 00092614. DOI: 10.1016/j.cplett.2013.08.105. arXiv: arXiv:1308.5931v1.

[221] D. Kruk et al. "209 Bi quadrupole relaxation enhancement in solids as a step towards new contrast mechanisms in magnetic resonance imaging". In: *Physical Chemistry Chemical Physics* 20.18 (2018), pp. 12710–12718. ISSN: 1463-9076. DOI: 10.1039/C8CP00993G. URL: http://xlink.rsc.org/?DOI=C8CP00993G.

[222] D. Kruk et al. "Multi-quantum quadrupole relaxation enhancement effects in 209 Bi compounds". In: *The Journal of Chemical Physics* 150.18 (2019), p. 184309. ISSN: 0021-9606. DOI: 10.1063/1.5082007. URL: http://aip.scitation.org/doi/10.1063/1.5082007.

[223] Hermann Scharfetter et al. "Quadrupole enhanced proton relaxation: Proof of principle for a novel extrinsic MRI contrast mechanism". In: *ABSTRACT BOOK EUROMAR Nantes*. 2018, p. 34.

[224] Hermann Scharfetter et al. "Relaxation enhancement in selected Bismuth-Aryl compounds: Promising precursors for novel T1 MRI contrast agents". English. In: *Proc. Intl. Soc. Mag. Reson. Med. 2018*. June 2018.

[225] Danuta Kruk et al. "Estimation of the magnitude of quadrupole relaxation enhancement in the context of magnetic resonance imaging contrast". In: *Journal of Chemical Physics* 150.18 (2019). ISSN: 00219606. DOI: 10.1063/1.5082177.